

**From the Pre-critical Nucleus to Atmospheric Aerosol Particles: Insights from Rotational Spectroscopic, Computational, and Aerosol Characterization Studies**

by

Mohamad H. Al-jabiri

A thesis submitted in partial fulfillment of the requirements for the degree of

Doctor of Philosophy

Department of Chemistry  
University of Alberta

© Mohamad H. Al-jabiri, 2024

# Abstract

Over the past several years in Alberta, the frequency and severity of wildfires has increased and resulted in the loss of lives, destruction of housing, and devastation of large forest areas. A byproduct of these fires are toxic emissions that contain primary aerosols and volatile organic compounds that can lead to the formation of secondary organic aerosols. Atmospheric aerosols are colloidal suspensions of liquid or solid particles in the atmosphere, which can have severe impacts on both human health and climate. The process of secondary organic aerosol formation involves the initial release of volatile organic compounds and their subsequent oxidation by atmospheric species, such as, for example, OH radical, to produce more oxygen-rich compounds of lower volatility. These semi-volatile compounds can agglomerate, i.e., partition from the gas to the particle phase, and form aerosol particles. General aspects of this nucleation process, such as the participation of organic acids, water, sulfuric acid, and ammonia, the formation of a critical nucleus after which particle growth is spontaneous, and the involvement of hydrogen-bonding and dispersion interactions, are known. Specific information about the formation of the initial clusters and complexes, such as the effect of conformational flexibility on the strength and the number of intermolecular interactions, is still not complete.

To study the early stages of nucleation of semi-volatile organic compounds with water or themselves, I utilize jet-cooled Fourier transform microwave spectroscopy and quantum chemical calculations. This combination allows for a detailed analysis of the intra- and intermolecular noncovalent interactions that stabilize specific conformers. My studies have shown that the *cis*-conformation of the carboxylic acid in *para*-aminobenzoic acid, *para*-nitrobenzoic acid, *para*-chlorobenzoic acid, *para*-hydroxybenzoic acid, and vanillic acid is the

lowest energy conformer. Additionally, I found that functional groups in the *para*-position of benzoic acid can affect the structure of the acid group, depending on their ability to donate or withdraw electron density. *ortho*-functional groups may play an indirect role in cluster formation through intramolecular interactions that limit their ability to act as inter-molecular hydrogen bond donor and acceptor, as demonstrated for the case of vanillic acid monohydrate. As a proxy for large semi-volatile organic compounds, benzyl benzoate, an ester with terminal benzyl and phenol groups, was studied. In this molecule, CH $\cdots$ O hydrogen bonding plays a significant role in determining its structural preference in the monomer, while in the dimer,  $\pi$ - $\pi$  stacking structural motifs are central.

Polyvinylchloride, PVC, is an important building material and co-combusts with biomass, such as wood, in house fires. PVC combustion leads to emission of hydrogen chloride and atmospheric aerosol particles, a mixture that becomes more complex in biomass co-combustion scenarios. To gain a better understanding of the influence of PVC on emissions from wildfires, I conducted laboratory based PVC pyrolysis experiments. The resulting hydrogen chloride emissions, aerosol particle size distribution, and aerosol particle optical properties were studied using a range of aerosol characterization instruments and analytical tools. A 61% mass loss was observed after 40 minutes of PVC pyrolysis at 350°C, with an average of 25% of those emissions being gaseous hydrogen chloride. The emitted aerosol particles are predominantly composed of organic compounds that form concentration-dependent agglomerates. These particles have a maximum in the size distribution of approximately 150 nm, falling within the accumulation mode of biomass burning-derived aerosol particles. Additionally, I found that the aerosol particles emitted from PVC pyrolysis have a wavelength-dependent absorption with an absorption Ångstrom coefficient (AAC) between 5.8 and 6.1. That means that these particles that

contain semi-volatile organic compounds preferentially absorb at lower wavelengths compared to soot particles.

# Preface

This thesis is a collection of my completed and ongoing research at the University of Alberta.

The contributions of everybody involved in this research are summarized below.

The study described in Chapter 3 has been published as “Rotational Spectroscopic Studies of *para*-Nitrobenzoic acid, *para*-Aminobenzoic acid, *para*-chlorobenzoic acid, and *para*-hydroxybenzoic acid” by M. H. Al-Jabiri, A.S. Hazrah, A. Insausti, Y. Xu, and W. Jäger, *J. Mol. Spectrosc.*, 2023, **394**,111790. I was responsible for data collection and calculations, analyses, and preparation of the manuscript. A. S. Hazrah assisted in calculations, data analysis, and project discussions. A. Insausti assisted in data collection and analyses. Y. Xu and W. Jäger are the supervisory authors and were involved with concept formation and manuscript composition.

The study described in Chapter 4 has been published as “Conformers of Vanillic Acid and Its Monohydrate: A Rotational Spectroscopic and Theoretical Study” by M. H. Al-Jabiri, A.S. Hazrah, and W. Jäger, *J. Phys. Chem. A.*, 2022, **126**, 6686-6694. I was responsible for project conception, data collection and calculations, analyses, and preparation of the manuscript. A. S. Hazrah assisted in calculations and data analysis. W. Jäger is the supervisory author and was involved in concept formation and manuscript composition.

The study described in Chapter 5 is in the final stage of manuscript edits and will be submitted for publication as “Shapes of Benzyl Benzoate: A Rotational Spectroscopic and Computational Study” by M. H. Al-Jabiri, A. Insausti, C. D. Carlson, J. Ma, M. Anshasi, A.S. Hazrah, Y. Xu, and W. Jäger. I was responsible for project conception, data collection and calculations, analyses, and preparation of the manuscript. A. Insausti, assisted in data collection, calculations, and project discussions. A. S. Hazrah, M. Anshasi assisted in data collection and

calculations. C. D. Carlson and J. Ma assisted in data analysis and calculations. Y. Xu and W. Jäger are the supervisory authors and were involved with concept formation and manuscript composition.

The study described in Chapter 7 is in the initial stages of manuscript preparation and titled “Analyzing Emissions of Pyrolyzed PVC: Measuring Hydrogen Chloride Emissions and Aerosol Properties” by M. H. Al-Jabiri, M. D’Souza, A. H. Moraes, and W. Jäger. I was responsible for project conception, experiment design, measurements, data analysis, and preparation of the manuscript. M. D’Souza assisted in data collection and analysis. A. H. Moraes assisted in data collection, W. Jäger was the supervisory author and was involved with concept formation and manuscript composition.

For my family

# Acknowledgements

I would like to express my deepest gratitude to my supervisor, Prof. Wolfgang Jäger for his support, guidance, and encouragement throughout my research. Your knowledge, advice, and dedication have been instrumental in my research and academic growth. Your mentorship has not only provided me with the skills needed to tackle complex problems but also inspired me to pursue excellence in my work. I am immensely grateful for the time you have spent reviewing my work and providing constructive feedback. I feel incredibly fortunate to have had the opportunity to learn from you. From your Environmental Chemistry I class during my undergraduate studies to the completion of my PhD, the many lessons I have learned from you will continue to guide me throughout my career. Thank you, Wolfgang.

I am grateful to Prof. Yunjie Xu for her invaluable assistance with editing and providing feedback on my papers and presentations. Your meticulous attention to detail and insightful suggestions have greatly enhanced my understanding and research capabilities. Your support and mentorship have been instrumental in my growth as a researcher. I also thank Prof. Alex Brown and Prof. Michael Serpe for taking the time to be on my supervisory committee and providing me with advice and support over the years. I am grateful to Prof. Gabriel Hanna for our many valuable discussions on career and scientific topics over coffee. I thank Prof. Kenneth R. Leopold for agreeing to be my external examiner.

I am deeply thankful to Dr. Matthias Heger for our many scientific discussions, guidance on research topics and support. I also thank Prof. Ran Zhao for being a constant support for career and atmospheric science discussions. I wish to convey my appreciation to Dr. Reza Poopari for his leadership and assistance in developing my instructional abilities. I would like to

sincerely thank the technical staff in the department, especially Dirk Kelm, Farhat Emhemed, Paul Crothers, and Bryce Thomas for their knowledge and mechanical advice. I am immensely appreciative for the support of my past and present colleagues including Craig, Alex, Aran, Reihana, Shyam, Jiarui, Colton, Nate, Amanda M, Mohammed, Arsh, Fan, Guojie, Haolu, Seif, Amanda N, Brittney, Mutasem, Yangqing, Santhosh, Mason, Shauna, and Juliette.

Funding from the Alberta Graduate Excellence Scholarship, Dr. R. Norman and Magda Kemeny Jones Travel Award, Marshall Syska Chemistry Graduate Scholarship, Gunning Research Associate Award, Natural Sciences and Engineering Research Council, and the University of Alberta is gratefully acknowledged.

I am grateful to my Mom, Amale Al-Tamimi, for your love, sacrifices, and belief in me, which have been the foundation of my success. This thesis marks many years of hard work, a journey that I could not have undertaken without the encouragement you have given me to pursue my dreams and ambitions. I am deeply thankful to my siblings Saja, Doha, Zahraa, Zeinab, Mehdi, Sara, as well as my nieces and nephews, for your love and laughter that have brought me joy throughout these years. I also wish to thank my father and mother-in-law, Jerry and Lois, who have provided me with support and encouragement – I am grateful for your presence in my journey. Finally, I am deeply grateful to my wife, Erin, for her unwavering love, patience, and support throughout this journey. Thank you for believing in me, for sharing the joys and hardships, and for always being honest, saying what I need to hear rather than just what I want to hear. After 12 years together, you continue to be my source of strength. This achievement is as much yours as it is mine, and I am profoundly grateful to have you by my side.

# Table of Contents

<b>Chapter 1. Introduction</b> .....	<b>1</b>
<b>Chapter 2. Experimental and Theoretical Methods for the Study of Gas-phase Molecules and Molecular Clusters of Atmospheric Relevance</b> .....	<b>12</b>
2.1. Background.....	12
2.2. Theoretical Tools.....	15
2.3. Rotational Spectroscopy.....	21
2.4. Chirped-Pulsed Fourier Transform Microwave Spectrometer.....	23
2.5. Molecular Supersonic Jet Expansion.....	25
<b>Chapter 3. Rotational Spectroscopic Studies of <i>para</i>-Nitrobenzoic acid, <i>para</i>-Aminobenzoic acid, <i>para</i>-Chlorobenzoic acid, and <i>para</i>-Hydroxybenzoic acid</b> .....	<b>37</b>
3.1. Introduction.....	37
3.2. Methods.....	39
3.2.1. Computational details.....	39
3.2.2. Experiments.....	40
3.3. Results and Discussion.....	41
3.3.1. Computational Results.....	41
3.3.2. Experimental Results.....	46
3.3.3. <i>p</i> -aminoBA.....	47
3.3.4. <i>p</i> -nitroBA.....	49
3.3.5. <i>p</i> -chloroBA.....	52
3.3.6. <i>p</i> -hydroxyBA.....	54
3.3.7. <i>para</i> -substituent Effects.....	57
3.4. Conclusions.....	60
<b>Chapter 4. Conformers of Vanillic Acid and its Monohydrate: A Rotational Spectroscopic and Theoretical Study</b> .....	<b>72</b>
4.1. Introduction.....	72
4.2. Methods.....	74
4.2.1. Experiments.....	74
4.2.2. Computations.....	76
4.3. Results.....	78
4.4. Discussion.....	90
4.4.1. Vanillic Acid Monomer.....	90
4.4.2. Vanillic Acid - Water.....	96
4.5. Atmospheric Implications.....	102
4.6. Conclusions.....	106
<b>Chapter 5. Shapes of Benzyl Benzoate: A Rotational Spectroscopic and Computational Study</b> .....	<b>117</b>

5.1. Introduction.....	117
5.2. Methods.....	119
5.2.1. Computational Details .....	119
5.2.2. Experimental Details.....	120
5.3. Results and Discussion .....	121
5.3.1. Rotational Assignments and Conformational Identification.....	121
5.3.2. Conformational Conversion Cooling .....	130
5.3.3. Experimental Structural Parameters.....	131
5.3.4. Intramolecular Noncovalent Interactions.....	132
5.3.5. BnBz Dimer .....	136
5.3.5.1. Rotational Assignment and Conformational Identification .....	136
5.3.5.2. Noncovalent Interactions in the BnBz Dimer .....	142
5.4. Conclusion .....	145
<b>Chapter 6. Instruments and Techniques to Probe Emissions from PVC Pyrolysis.....</b>	<b>155</b>
6.1. Introduction.....	155
6.2. Thermal Degradation of PVC using a Tube Furnace .....	156
6.3. Thermal Optical Transmission Analysis for Classification of Aerosol particles .....	157
6.4. Colorimetric Analysis for Determination of Hydrogen Chloride Concentration from PVC Pyrolysis.....	159
6.5. Instruments to Probe Aerosol Properties.....	161
6.5.1. Photo-reaction “Smog” Chamber .....	161
6.5.2. Scanning Mobility Particle Sizer .....	162
6.5.3. Aethalometer.....	163
<b>Chapter 7. Analyzing Emissions of Pyrolyzed PVC: Measuring Hydrogen Chloride Emissions and Aerosol Properties .....</b>	<b>170</b>
7.1. Introduction.....	170
7.2. Experimental Methods.....	173
7.2.1. Generation and Sampling of Pyrolysis Emissions .....	173
7.2.2. Emissions Characterization.....	176
7.3. Results and Discussion .....	178
7.3.1. HCl Emissions .....	179
7.3.2. Thermal Optical Analysis .....	180
7.3.3. Size Distribution .....	181
7.3.4. Optical Properties.....	185
7.4. Future Studies .....	188
7.5. Conclusions .....	188
<b>Chapter 8. Conclusions.....</b>	<b>195</b>
<b>Bibliography .....</b>	<b>205</b>
<b>Appendix A.....</b>	<b>243</b>
<b>Appendix B .....</b>	<b>254</b>
<b>Appendix C.....</b>	<b>262</b>

# List of Tables

<b>Table 2.1.</b> Specific $\Delta K_a$ and $\Delta K_c$ selection rules for asymmetric top molecules.....	23
<b>Table 3.1.</b> Sum of electronic energy and zero-point energy relative to the lowest energy conformer and their rotational constants, dipole moments, and nuclear hyper fine quadrupole coupling constants for the cis-trans isomers of p-chloroBA, p-aminoBA, p-nitroBA, p-hydroxyBA and at the B3LYP-D3BJ/def2-TZVP level of theory.....	42
<b>Table 3.2.</b> Experimental spectroscopic parameters and those computed at the B3LYP-D3BJ/def2-TZVP and B2PLYP-D3BJ/def2-TZVP levels of theory for cis-p-aminoBA and cis-p-nitroBA.....	51
<b>Table 3.3.</b> Experimental spectroscopic parameters of cis-p- <sup>35</sup> chloroBA and cis-p- <sup>37</sup> chloroBA and those computed at the B3LYP-D3BJ/def2-TZVP and B2PLYP-D3BJ/def2-TZVP levels of theory.....	53
<b>Table 3.4.</b> Experimental spectroscopic parameters of cis-p-hydroxyBA and those computed at the B3LYP-D3BJ/def2-TZVP level of theory.....	56
<b>Table 3.5.</b> Molecular electrostatic potential of p-chloroBA, p-aminoBA, p-nitroBA, p-hydroxyBA, and benzoic acid (BA) in the trans- conformation where $V_{\min}$ , is the electrostatic potential minimum near the O atom, $V_p$ , the difference between $V_{\min}$ of unsubstituted and substituted benzoic acid in kcal mol <sup>-1</sup> , and $\tau$ , the angle between the aromatic ring and the trans-carboxylic acid at the B3LYP D3BJ/def2-TZVP level of theory.....	58
<b>Table 3.6.</b> Mayer bond order of p-chloroBA, p-aminoBA, p-nitroBA, p-hydroxyBA in the trans- conformation at the B3LYP-D3BJ/def2-TZVP level of theory. Refer to Figure 3.17 for labelling.....	59
<b>Table 4.1.</b> Relative zero-point corrected energies and spectroscopic parameters for vanillic acid conformers obtained at the B3LYP-D3(BJ)/ def2-TZVP level of theory. Refer to Figure 4.4 for description of the conformer labelling.....	79
<b>Table 4.2.</b> Relative zero-point corrected energies and spectroscopic parameters for the four lowest energy vanillic acid monomers obtained at the MP2/aug-cc-pVTZ level of theory. Refer to Figure 4.4 for description of the conformer labelling.....	81

<b>Table 4.3.</b> Relative zero-point corrected energies and spectroscopic parameters of the vanillic acid monohydrate conformers determined at the B3LYP-D3(BJ)/def2-TZVP level of theory. Refer to Figure B.2 for description of the labels of the monohydrate conformers. ....	82
<b>Table 4.4.</b> Relative zero-point corrected energies and spectroscopic parameters for the two lowest energy vanillic acid monohydrate obtained at the MP2/6-311++g(2df,2pd) level of theory. Refer to Figure 4.7 for description of the conformer labelling. ....	85
<b>Table 4.5.</b> Energies and spectroscopic parameters of the two lowest energy conformers of vanillic acid, calculated at the B3LYP-D3(BJ)/def2-TZVP level of theory, together with experimental values. ....	86
<b>Table 4.6.</b> Theoretical (B3LYP-D3(BJ)/def2-TZVP) and experimental spectroscopic parameters and energies for the two lowest energy conformers of the vanillic acid-water complex. ....	87
<b>Table 5.1.</b> Theoretical (B3LYP-D3BJ/def2-TZVP) spectroscopic parameters for the four conformers of BnBz. ....	126
<b>Table 5.2.</b> Theoretical (B3LYP-D3BJ/def2-TZVP) and experimental spectroscopic parameters for the two conformers of BnBz. ....	127
<b>Table 5.3.</b> Experimental rotational constants of the <sup>13</sup> C isotopologues of BnBz-g and BnBz-t. <sup>a</sup> ....	129
<b>Table 5.4.</b> The substitution and theoretical equilibrium structural parameters <sup>a</sup> of BnBz-g. ....	132
<b>Table 5.5</b> Experimental spectroscopic parameters of the BnBz dimer and parameters of four candidate structures, calculated at the B3LYP-D3(BJ)/def2-TZVP level of theory with an energy correction at the CCSD(T)/cc-pVTZ level of theory. ....	140
<b>Table 5.6.</b> Sapt2+/aug-cc-pVDZ results of the BnBz dimer, in of kJ mol <sup>-1</sup> , with negative values signifying attractive contributions to the overall energy and positive values repulsive contributions. Energies are in kJ mol <sup>-1</sup> . ....	144
<b>Table 7.1</b> The mass of PVC pyrolyzed, emission yield (M <sub>PVC</sub> -M <sub>char</sub> )/M <sub>PVC</sub> , and percent HCl in the emissions, M <sub>HCl</sub> /(M <sub>PVC</sub> -M <sub>char</sub> ). ....	180
<b>Table 7.2.</b> Results from the thermal-optical analysis of PVC pyrolysis emissions. ....	181
<b>Table 7.3.</b> The AAC calculated using the two-wavelength ( $\lambda_1, \lambda_2$ ) approximation (Equation (2)) for the different possible combinations of wavelengths. ....	187
<b>Table A.1.</b> Assigned transitions of the cis-p-aminoBA monomer. ....	244
<b>Table A.2.</b> Assigned transitions of the cis-p-nitroBA monomer. ....	246

<b>Table A.3.</b> Assigned transitions of the cis-p- <sup>35</sup> chloroBA monomer. ....	248
<b>Table A.4.</b> Assigned transitions of the cis-p- <sup>37</sup> chlorBA monomer. ....	250
<b>Table A.5.</b> Assigned transitions of the cis-p-hydroxyBA-I monomer. ....	252
<b>Table A.6.</b> Assigned transitions of the cis-p-hydroxyBA-II monomer.....	252
<b>Table B.1.</b> List of the assigned rotational transitions of the VA-I monomer. ....	255
<b>Table B.2.</b> List of the assigned transitions of the VA-II monomer. ....	256
<b>Table B.3.</b> List of the assigned transitions of the VA-I-W monohydrate. ....	259
<b>Table B.4.</b> List of the assigned transitions of the VA-II-W monohydrate.....	261
<b>Table C.1.1.</b> List of assigned rotational transitions of BnBz-g.....	263
<b>Table C.1.2.</b> List of assigned rotational transitions of BnBz-g <sup>13</sup> C1 .....	270
<b>Table C.1.3.</b> List of assigned rotational transitions of BnBz-g <sup>13</sup> C2.....	270
<b>Table C.1.4.</b> List of assigned rotational transitions of BnBz-g <sup>13</sup> C3.....	271
<b>Table C.1.5.</b> List of assigned rotational transitions of BnBz-g <sup>13</sup> C4.....	271
<b>Table C.1.6.</b> List of assigned rotational transitions of BnBz-g <sup>13</sup> C5.....	272
<b>Table C.1.7.</b> List of assigned rotational transitions of BnBz-g <sup>13</sup> C6.....	272
<b>Table C.1.8.</b> List of assigned rotational transitions of BnBz-g <sup>13</sup> C7.....	273
<b>Table C.1.9.</b> List of assigned rotational transitions of BnBz-g <sup>13</sup> C8.....	274
<b>Table C.1.10.</b> List of assigned rotational transitions of BnBz-g <sup>13</sup> C9.....	274
<b>Table C.1.11.</b> List of assigned rotational transitions of BnBz-g <sup>13</sup> C10.....	275
<b>Table C.1.12.</b> List of assigned rotational transitions of BnBz-g <sup>13</sup> C11.....	275
<b>Table C.1.13.</b> List of assigned rotational transitions of BnBz-g <sup>13</sup> C12.....	276
<b>Table C.1.14.</b> List of assigned rotational transitions of BnBz-g <sup>13</sup> C13.....	276
<b>Table C.1.15.</b> List of assigned rotational transitions of BnBz-g <sup>13</sup> C14.....	277
<b>Table C.2.1.</b> List of assigned rotational transitions of BnBz-t.....	278
<b>Table C.2.2.</b> List of assigned rotational transitions of BnBz-t <sup>13</sup> C1 .....	284
<b>Table C.3.</b> Cartesian Coordinates of 14 in BnBz-g obtained through Kraitchman's substitution equation.....	284
<b>Table C.4.</b> Cartesian Coordinates of 4 in BnBz-t obtained through Kraitchman's substitution equation.....	285
<b>Table C.5.</b> List of computationally identified BnBz dimers .....	286
<b>Table C.6.</b> List of assigned rotational transitions of the BnBz dimer .....	290s

# List of Figures

<b>Figure 1.1.</b> Radiative Forcing, in $\text{W/m}^2$ , of atmospheric pollutants. Positive (negative) radiative forcing leads to global heating (cooling). This Figure is displayed unchanged from Figure SPM.5 of the IPCC AR5 climate change 2013 report and for technical details please see the Technical Summary Supplementary Material in the AR5 IPCC report. <sup>16</sup> .....	3
<b>Figure 2.1.</b> a) The equilibrium geometries of the four most stable cis-1,2-cyclohexanediol conformers. The blue dashed lines represent the intramolecular H-bonds. B) A 2D PES scan along two dihedral angles associated with the OH pointing directions at the B3LYP-D3(BJ)/6-311++G(d,p) level of theory. One can see that the conformational conversion barriers from <b>II</b> → <b>I</b> and <b>IV</b> → <b>III</b> are fairly low, leading to the non-observation of <b>II</b> and <b>IV</b> in a jet expansion. Reproduced from Ref. 19.....	18
<b>Figure 2.2.</b> Results of QTAIM and NCI analyses of vanillic acid monohydrate showing how these techniques can supplement each other in analyzing non-covalent interactions. ....	20
<b>Figure 2.3.</b> Diagram that correlates asymmetric top energy levels with those of oblate and prolate symmetric tops for $J = 0, 1, \text{ and } 2$ . The corresponding $JKaKc$ and $JK$ quantum numbers are given, as is Ray's asymmetry parameter that describes the deviation from the symmetric top cases. ....	22
<b>Figure 3.1.</b> The four para-substituted benzoic acids studied here: p-aminoBA, p-nitroBA, p-chloroBA, and p-hydroxyBA. ....	38
<b>Figure 3.2.</b> Geometries of the lowest energy conformers of cis-p-chloroBA, cis-p-aminoBA, cis-p-nitroBA, and cis-p-hydroxyBA at the B3LYP-D3BJ/def2-TZVP level of theory. p-hydroxyBA-II is only $0.2 \text{ kJ mol}^{-1}$ higher in energy than p-hydroxyBA-I.....	43
<b>Figure 3.3.</b> Intrinsic reaction coordinate (IRC) of the cis-trans conversion in p-nitroBA calculated at the B3LYP-D3BJ/def2-TZVP level of theory. In regions of shallow potential where an IRC computation was not feasible, a relaxed dihedral scan was conducted. The zero-point energy corrected interconversion barrier from trans- to the cis-p-aminoBA is about $20 \text{ kJ mol}^{-1}$ .....	43
<b>Figure 3.4.</b> Barrier to interconversion from cis to trans of the p-aminoBA carboxylic acid group at the B3LYP-D3BJ/def2-TZVP level of theory. ....	44

<b>Figure 3.5.</b> Barrier to interconversion from cis to trans of the p-hydroxyBA-II carboxylic acid group at the B3LYP-D3BJ/def2-TZVP level of theory. ....	44
<b>Figure 3.6.</b> Barrier to interconversion from cis to trans of the p-hydroxyBA-I carboxylic acid group at the B3LYP-D3BJ/def2-TZVP level of theory. ....	45
<b>Figure 3.7.</b> Barrier to interconversion from cis to trans of the p- <sup>35</sup> chloroBA carboxylic acid group at the B3LYP-D3BJ/def2-TZVP level of theory. ....	46
<b>Figure 3.8.</b> Stable conformations of trans carboxylic acid of p-chloroBA, p-aminoBA, p-nitroBA, and p-hydroxyBA computed at the B3LYP-D3BJ/def2-TZVP level of theory.....	46
<b>Figure 3.9.</b> Experimental (top) and simulated (bottom) spectrum of p-aminoBA. The simulated spectrum was obtained using calculated rotational constants, dipole moments, and N <sup>14</sup> nuclear quadrupole coupling constants. ....	49
<b>Figure 3.10.</b> Barrier to inversion of the amino group of the cis-p-aminoBA monomer at the B3LYP-D3BJ/def2-TZVP level of theory. ....	50
<b>Figure 3.11.</b> Barrier to nitro internal rotation in cis-p-nitroBA monomer at the B3LYP-D3BJ/def2-TZVP level of theory. ....	52
<b>Figure 3.12.</b> Experimental (top) and simulated (bottom) spectrum of p-nitroBA. The simulated spectrum was obtained using calculated rotational constants, dipole moments, and N <sup>14</sup> nuclear quadrupole coupling constants. ....	53
<b>Figure 3.13.</b> Experimental (top) simulated (bottom) spectrum of p-chloroBA. The simulated spectrum was obtained using calculated rotational constants, dipole moments, and N <sup>14</sup> nuclear quadrupole coupling constants. ....	56
<b>Figure 3.14.</b> Barrier to interconversion from cis-p-hydroxyBA-II to cis-p-hydroxyBA-I through a rotation of the hydroxyl group at the B3LYP-D3BJ/def2-TZVP level of theory.....	58
<b>Figure 3.15.</b> Barrier to interconversion from cis-p-hydroxyBA-II to cis-p-hydroxyBA-I through a rotation of the carboxylic acid group at the B3LYP-D3BJ/def2-TZVP level of theory. ....	59
<b>Figure 3.16.</b> An overview of the experimental (top) and simulated (bottom) rotational spectra of cis-p-hydroxyBA-I and -II. The simulated spectra were obtained using the experimentally determined rotational constants and the predicted dipole moment components at a rotational temperature of 1 K. ....	61
<b>Figure 3.17.</b> The C3-C4-C7-O1 out-of-plane dihedral angle $\tau$ , as a function of the difference of molecular electrostatic potential between the substituted benzoic acid and benzoic acid at the B3LYP-D3BJ/def2-TZVP level of theory in the trans-conformation. ....	63

<b>Figure 4.1.</b> Top trace: The experimental spectrum (black) for vanillic acid. Bottom trace: Simulated (blue and red) spectra of the VA-I and VA-II vanillic acid conformers.....	79
<b>Figure 4.2.</b> Experimental spectrum of the vanillic acid monohydrate (top trace) and the assigned transitions of the lowest energy monohydrates, VA-I-W and VA-II-W (bottom trace). The monomer lines were removed from the experimental spectrum. ....	80
<b>Figure 4.3.</b> Dihedral angles scanned to probe the potential energy surface of the vanillic acid monomer.....	81
<b>Figure 4.4.</b> All vanillic acid monomer conformers found at the B3LYP-D3(BJ)/def2-TZVP level of theory. The configuration of each conformer can be described by three dihedral angles (indicated in the lowest energy conformer) that can be cis (c), trans (t), or eclipsed (e). The relative energies are given in brackets in units of $\text{kJ mol}^{-1}$ .....	83
<b>Figure 4.5.</b> NCI gradient isosurfaces (reduced electron density gradient $s=0.6$ ) visualizing the intra-molecular interactions in the two lowest energy conformers of vanillic acid. The isosurfaces are coloured from red (repulsive) to blue (attractive) according to the product of sign of the second eigenvalue of the Hessian and electron density, $\text{sign}(\lambda_2)\rho$ . ....	84
<b>Figure 4.6.</b> Dihedral angle scan along the interconversion coordinate between the two lowest energy conformers of the vanillic acid monomer, VA-I and VA-II. The respective zero-point energies are indicated.....	85
<b>Figure 4.7.</b> All vanillic acid monohydrate conformers found at the B3LYP-D3(BJ)/def2-TZVP level of theory. The conformers are first grouped by monomer structure and then shown in order of increasing energy. The relative energies with respect to the lowest energy conformer, VA-I-W-1, are given in parentheses in units of $\text{kJ mol}^{-1}$ .....	88
<b>Figure 4.8.</b> NCI reduced electron gradient ( $s=0.6$ ) iso-surface visualizations for the two lowest energy vanillic acid – water conformers.....	92
<b>Figure 4.9.</b> Bond (blue) and ring (red) critical points in the two lowest energy conformers of the vanillic acid monomer from QTAIM analyses. ....	92
<b>Figure 4.10.</b> Bond (blue) and ring (red) critical points in the two lowest energy conformers of the vanillic acid monohydrate from QTAIM analyses. ....	93
<b>Figure 4.11.</b> IBSI values for the indicated fragment interactions in the VA-I and VA-II conformers of vanillic acid.....	93
<b>Figure 4.12.</b> IBSI values for the indicated fragment interactions for the two lowest energy vanillic acid monohydrate conformers.....	94

<b>Figure 4.13.</b> Conversion pathways between conformers of the vanillic acid monomer. The values in parenthesis are the relative energies with respect to the lowest energy conformer in $\text{kJ mol}^{-1}$ and the values between conformers are the barrier heights to interconversion, also in $\text{kJ mol}^{-1}$ .....	96
<b>Figure 4.14.</b> Intrinsic reaction coordinate scan of the methyl internal rotation in the VA-I monomer. The intrinsic reaction coordinate is in units of $\text{amu} \times \text{bohr}$ . To emphasize the asymmetry of the potential a dotted line is placed at the saddle point ( $\text{IRC} = 0$ ). .....	99
<b>Figure 4.15.</b> Intrinsic reaction coordinate scan of the methyl internal rotation in the VA-II monomer. The intrinsic reaction coordinate is in units of $\text{amu} \times \text{bohr}$ . To emphasize the asymmetry of the potential a dotted line is placed at the saddle point ( $\text{IRC} = 0$ ). .....	100
<b>Figure 4.16.</b> Change in dipole moment components as a function of the wagging motion of the free hydrogen in VA-I-W monohydrate.....	103
<b>Figure 4.17.</b> Change in dipole moment components as a function of the wagging motion of the free hydrogen in VA-II-W monohydrate.....	104
<b>Figure 4.18.</b> Potential energy curve of the wagging motion of the free hydrogen of the water moiety in VA-I-W. The zero-point energy (horizontal line) is well above the potential barrier at planarity. All values were obtained at the B3LYP-D3(BJ)/def2-TZVP level of theory. ....	105
<b>Figure 4.19.</b> Potential energy curve of the wagging motion of the free hydrogen of the water moiety in VA-II-W. The zero-point energy (horizontal line) is well above the potential barrier at planarity. All values were obtained at the B3LYP-D3(BJ)/def2-TZVP level of theory. ....	106
<b>Figure 4.20.</b> Intrinsic reaction coordinate scan of the methyl internal rotation in the VA-I-W-1 monohydrate. The intrinsic reaction coordinate is in units of $\text{amu} \times \text{bohr}$ . To emphasize the asymmetry a dotted line is placed at the saddle point ( $\text{IRC} = 0$ ).....	108
<b>Figure 4.21.</b> Intrinsic reaction coordinate scan of the methyl internal rotation in the VA-II-W-1 monohydrate. The intrinsic reaction coordinate is in units of $\text{amu} \times \text{bohr}$ . To emphasize the asymmetry a dotted line is placed at the saddle point ( $\text{IRC} = 0$ ).....	109
<b>Figure 4.22.</b> Abundance of vanillic acid monohydrate relative to the vanillic acid monomer in the atmosphere between 01. January 2018 to 01. January 2021, at the University of Alberta, Edmonton, Alberta, Canada. The data were computed from experimental rotational constants, measured temperature and pressure, and calculated vibrational frequencies and dissociation energies. See the text for details. ....	112

<b>Figure 5.1.</b> The four dihedral angles, $\tau_1$ to $\tau_4$ , associated with the flexibility of BnBz and the atom numbering.....	129
<b>Figure 5.2.</b> The relaxed 1D-PES scan along the $\tau_2$ dihedral angle. The optimized geometries of BnBz-t, BnBz-g, and the related transition states are shown. The dihedral angle values for ( $\tau_1$ , $\tau_2$ , $\tau_3$ , $\tau_4$ ) for BnBz-t and BnBz-g are ( $89.4^\circ$ , $180^\circ$ , $180^\circ$ , $0.0^\circ$ ) and ( $92.3^\circ$ , $-88.6^\circ$ , $177.6^\circ$ , $-1.8^\circ$ ), respectively. ....	129
<b>Figure 5.3.</b> The relaxed 1D-PES scans starting with BnBz-g along $\tau_1$ , $\tau_3$ , and $\tau_4$ . ....	131
<b>Figure 5.4.</b> The relaxed 1D-PES scans starting with BnBz-t along $\tau_1$ , $\tau_3$ , and $\tau_4$ . ....	132
<b>Figure 5.5.</b> Stable conformers of BnBz and their relative energies to the lowest energy conformer (BnBz-g). ....	133
<b>Figure 5.6.</b> Experimental spectrum with argon, helium, and neon as carrier gases. ....	135
<b>Figure 5.7.</b> The QTAIM, NCI, and IBSI analyses of the two observed BnBz conformers. The calculations were done at the B3LYP-D3BJ/def2-TZVP level of theory. The isosurfaces in the NCI plots have reduced electron density gradient $s=0.6$ . The intrinsic bond strength indices between atom pairs are indicated for BnBz-g and BnBz-t.....	142
<b>Figure 5.8.</b> The NCI plots of the three optimized geometries of benzyl benzoate (BnBz), ethyl benzyl benzoate (eBnBz), and propyl benzyl benzoate (pBnBz). ....	143
<b>Figure 5.9.</b> Examples of structure within the $g^-g^+$ family. ....	144
<b>Figure 5.10.</b> Examples of structure within the tt family. ....	145
<b>Figure 5.11.</b> Examples of structure within the tg family with minimal distortion of the monomer subunits. ....	145
<b>Figure 5.12.</b> Examples of structure within the tg family with the trans subunit distorted from its monomer configuration. ....	146
<b>Figure 5.13.</b> Results from a) a QTAIM analysis and b) an NCI analysis of the BnBz-tg-1 dimer.....	146
<b>Figure 5.14.</b> Intrinsic bond strength indices between atom pairs in the BnBz-tg-1 dimer. ....	147
<b>Figure 5.15.</b> Visualization of results from NCI analyses of BnBz- $g^-g^+$ -5, BnBz-tg-1, BnBz-tg-2, BnBz-tg-8.....	150
<b>Figure 5.16.</b> QTAIM results of BnBz- $g^-g^+$ -5, BnBz-tg-1, BnBz-tg-2, BnBz-tg-8 with the $\pi$ - $\pi$ and $CH\cdots\pi$ bond critical points, ring critical points, and cage critical points removed for clarity.....	151

<b>Figure 6.1.</b> Schematic of experimental setup utilized in Chapter 7 to study the emissions resulting from PVC pyrolysis.....	160
<b>Figure 6.2.</b> Custom built tube furnace utilized in Chapter 7 for the pyrolysis of PVC. ....	161
<b>Figure 6.3.</b> Thermogram of an EC/OC analysis of PVC. The blue and red traces are the temperature and transmittance respectively. The signal from the flame-ionization (FID) detector is shown in purple. Regions where peaks of organic carbon (OC), pyrolytic carbon (PC), and elemental carbon (EC) are shown. The last peak in the thermogram is a methane calibration peak.....	163
<b>Figure 7.1.</b> The overall experimental set up to study the emissions form pyrolysis of PVC piping.....	178
<b>Figure 7.2.</b> The HCl trap used to capture gaseous HCl by bubbling the emissions through 2M NaOH solution. ....	180
<b>Figure 7.3.</b> Colorimetric calibration curves for the determination of HCl concentration from the HCl trap. The error in the fit is one standard deviation of the last digit.....	181
<b>Figure 7.4.</b> Measurements of size distribution of PVC pyrolyzed at 350°C at onset of heating. The SMPS scans takes 2 minutes per scan and the scans are labelled by the start time of the scan relative to the start of the tube furnace.....	186
<b>Figure 7.5.</b> a) The total particle concentration emitted by the thermal degradation of PVC at 350°C as a function of pyrolysis time. b) The corresponding mean particle mobility diameter of the aerosol size distribution measured directly from the tube furnace. Experiments 1 and 2 were done under the same conditions; for experiment 3, the emissions flow was interrupted for 30 s, 11 min after onset of heating. ....	187
<b>Figure 7.6.</b> The change in the mean mobility diameter of aerosol particles in the smog chamber. Measurements began after injection of aerosol particles into the smog chamber ended (40 minutes). ....	188
<b>Figure 7.7.</b> The number densities of particles with diameters ( $D_p$ ) of 151.2 nm, 250.3 nm, 552.3 nm, and 850.5 nm throughout experiment. The numbers in brackets are the errors in units of the last digit. ....	189
<b>Figure 7.8.</b> The absorption ( $Babs$ ) of PVC pyrolyzed emission, in $Mm^{-1}$ , at different wavelengths ( $\lambda$ ) in nm, is fit as a power law relationship to determine the absorption Ångstrom coefficients (AAC), a unitless parameter. The errors of the fitted parameters are given in brackets in units of the last digit.....	190

# List of Symbols

$A$	Surface area (Chapter 6)
$A, B, C$	Rotational constants
$b_{ATN}$	Attenuation coefficient
$B$	Absorption coefficients
$D_p$	Particle diameter
$D_0$	Dissociation energy
$E_{pulse}$	Electric field strength of the chirped pulse
$e$	Equatorial
$g$	Gauche
$\hat{H}_{rot}$	Hamiltonian operator for a rigid molecule
$h$	Planck's constant
$\hbar$	Reduced Planck's constant
$I_a, I_b, I_c$	Moments of inertia about principal axes
$I_0$	Light intensity through particle free filter
$I$	Light intensity through aerosol-filled filter
$J$	Rotational angular momentum quantum number
$\hat{J}_a, \hat{J}_b, \hat{J}_c$	Angular momentum about principal axes
$K_{a(c)}$	Quantum number at the oblate (prolate) limit
$K_H$	Dissociation constant benzoic acid
$K_p$	Equilibrium constant of complexation
$K_R$	Dissociation constant of substituted benzoic acid
MAE	Mass-specific absorption cross-section

$M_{\text{PVC}}$	Mass of PVC
$M_{\text{char}}$	Mass of PVC char
$N$	Total number of transitions
$n$	Mol fraction
$P^c$	Percent abundance
$ P $	Magnitude of the polarization response
$Q_x$	Partition function for $x$ species (Chapter 4)
$Q$	Flow rate
$R$	Ideal gas constant
$r_e$	Equilibrium structure
$r_s$	Substitution structure
$t$	Trans
$V_{\text{min}}$	Local minimum in electrostatic potential
$\alpha$	Sweep rate
$\Delta E$	Relative energy
$\Delta E_0$	Relative zero-point corrected energy
$\Delta G$	Sum of Gibbs free energy and electronic energy
$\Delta_J, \Delta_{JK}, \Delta_K, \delta_J, \text{ and } \delta_K$	Quartic centrifugal distortion constants
$\Delta I$	Inertial defect
$\Delta N_0$	Population difference between two energy levels
$\Delta t$	Change in time
$\kappa$	Ray's asymmetry parameter
$\rho$	Electron density distribution
$\tau$	Dihedral angle
$\mu_{a,b,c}$	Dipole moment components

$\mu_{ab}$	Transition dipole moment
$\sigma$	Standard deviation of the fit
$\sigma_R$	Hammett constant
$\lambda$	Wavelength
$\chi$	Nuclear quadrupole coupling constant (Chapter 2/3)
$\chi$	Equilibrium constant of complexation (Chapter 4)

# List of Abbreviations

AAC	Absorption Ångström exponent
AC	Activated charcoal
AQHI	Air quality health index
ATN	Attenuation
AWG	Arbitrary wave form generator
BA	Benzoic acid
BC	Black carbon
BCP	Bond critical point
BJ	Becke-Johnson damping
BnBz	Benzyl benzoate
BrC	Brown carbon
BSSE	Basis set super position error
B3LYP	Becke, 3-parameter, Lee-Yang-Parr
CPC	Condensation particle counter
CP-FTMW	Chirped pulse Fourier transform microwave spectroscopy
CREST	Conformer rotamer ensemble sampling tool
DMA	Differential mobility analyzer
DOAS	Differential optical absorption spectroscopy
D3	Dispersion correction 3 <sup>rd</sup> iteration
EC	Elemental carbon
FID	Free induction decay (Chapter 2/3/4/5)
FID	Flame ionization detector (Chapter 6)
FTMW	Fourier transform microwave spectroscopy

GFN2-xTB	Geometry, frequency, non-covalent, extended tight binding
IBSI	Intrinsic bond strength index
IPCC	Intergovernmental panel on climate change
IRC	Intrinsic reaction coordination
LIM	Power limiter
LNA	Low noise amplifier
MP2	Møller-Plesset perturbation theory
NCI	Non-covalent interactions
NEB	Nudged elastic band
OC	Organic carbon
PAX	Photo-acoustic extinciometer
PC	Pyrolytic carbon
PCB	Polychlorinated biphenyls
PD	Parallel displaced
PES	Potential energy surface
PFA	Perfluoroalkoxy
PM	Particulate matter
PVC	Polyvinyl chloride
QTAIM	Quantum theory of atoms in molecules
RCP	Ring critical point
RDG	Reduced density gradient
SAPT	Symmetry adapted perturbation theory
SMPS	Scanning mobility particle sizer
SOA	Secondary organic aerosol
SVOC	Semi-volatile organic compound

SW	Single-pull single-throw switch
TS	Transition state
TT	Tilted t-shape
TWT	Traveling wave tube amplifier
VA	Vanillic acid
VOC	Volatile organic compound
ZPE	Zero-point energy

# 1

## Introduction

Atmospheric aerosols are a colloidal suspension of solid or liquid particles in air<sup>1</sup> that can impact human health<sup>2</sup> and Earth's climate.<sup>3</sup> When discussing the health effects of atmospheric aerosols, we often refer to them as particulate matter (PM). In a health context, concentrations of PM<sub>10</sub> (particulate matter with an aerodynamic diameter less than or equal to 10  $\mu\text{m}$ ) and PM<sub>2.5</sub> (particulate matter with an aerodynamic diameter less than or equal to 2.5  $\mu\text{m}$ ) are often reported because they have a high lung penetration capacity<sup>4,5</sup> and a long residence time in the atmosphere. In fact, common air quality health indices such as the AQHI, the air quality health index used in Canada<sup>6</sup> that provides a measure of the potential health implications due to exposure to poor air quality, incorporate at least one if not both categories.<sup>7</sup> The consequences of overexposure to PM include an increase in cardiovascular morbidity and mortality and are a focus of environmental and health government policy.<sup>4</sup> PM<sub>2.5</sub> and PM<sub>10</sub> are size categories and their mass concentrations, in  $\mu\text{g}/\text{m}^3$ , are often reported and used as a standard for exposure because it can be readily measured using filter-based techniques.<sup>8</sup> Additionally, PM is not a single compound but a mixture of different chemical species where the composition, and therefore toxicity, is influenced by the PM source.<sup>9</sup> For instance, PM from combustion sources such as biomass burning has higher toxicity than PM from non-combustion sources such as road dust.<sup>9</sup> Even solid PM can be found in a mixture of states and not just as pure solid. For instance, soot from biomass burning is emitted as a solid; however, low volatile organic compounds

(VOCs) that are emitted simultaneously can condense onto the aerosol particle to form a core-shell structure<sup>10</sup> like a ball left outside overnight that collects a morning dew. The liquid coat of such a structure can act as a reaction vessel, bringing molecules and oxidants into closer proximity, resulting in the possible formation of toxic compounds.<sup>11</sup> To mitigate the health impacts of PM, a multidisciplinary approach is needed. For instance, countries in the global south commonly burn garbage due to a lack of economic support, resulting in the emission of toxic PM and an estimated 270,000 premature deaths per year globally.<sup>12</sup> An understanding of the emissions and the evolution of their physical properties, such as size and mass, during their atmospheric lifetime is needed to direct policy and engineering strategies to provide alternative approaches to open waste burning.

Atmospheric aerosols impact climate by scattering and absorbing solar radiation directly and indirectly.<sup>13</sup> For instance, aerosols derived from biomass burning, such as soot, are able to directly absorb solar radiation<sup>14</sup> and after aging in the atmosphere can indirectly interact with solar radiation by acting as cloud condensation nuclei.<sup>15</sup> Radiative forcing, the difference in energy flux between incoming solar radiation and radiative emissions back into space at the top of the atmosphere,<sup>13</sup> is a measure of the potential impact of atmospheric pollutants on our climate, including atmospheric aerosols. The Intergovernmental Panel on Climate Change (IPCC) evaluates the individual contributions of compounds to radiative forcing; the results are published in the IPCC Reports (see Figure 1.1).<sup>16</sup> Some classes of pollutants can contribute to both heating and cooling (see Figure 1.1), and aerosols have such an ability with the largest variability. The variability in the impact of atmospheric aerosols depends on physical properties of the constituent particles, such as composition, morphology, and size, all of which may change over their lifetime in the atmosphere, adding uncertainty to their impact on Earth's radiative

budget.<sup>16</sup> For instance, brown carbon (BrC) aerosols which are emitted from biomass burning and preferentially absorb wavelengths in the ultraviolet and visible regions, can bleach, i.e., lose their ability to absorb radiation,<sup>17</sup> making their impact spatially and temporally dependent. The impact of emissions on climate is further complicated when sources are in close proximity so that the composition of the emissions will be uniquely influenced by the co-emissions into the environment. For instance, open waste burning commonly occurs in the presence of biomass which will release BrC, soot, and VOCs. If plastics such as PVC are also present in the waste products, a chlorine radical source is immediately available for oxidation of the BrC and the VOCs.

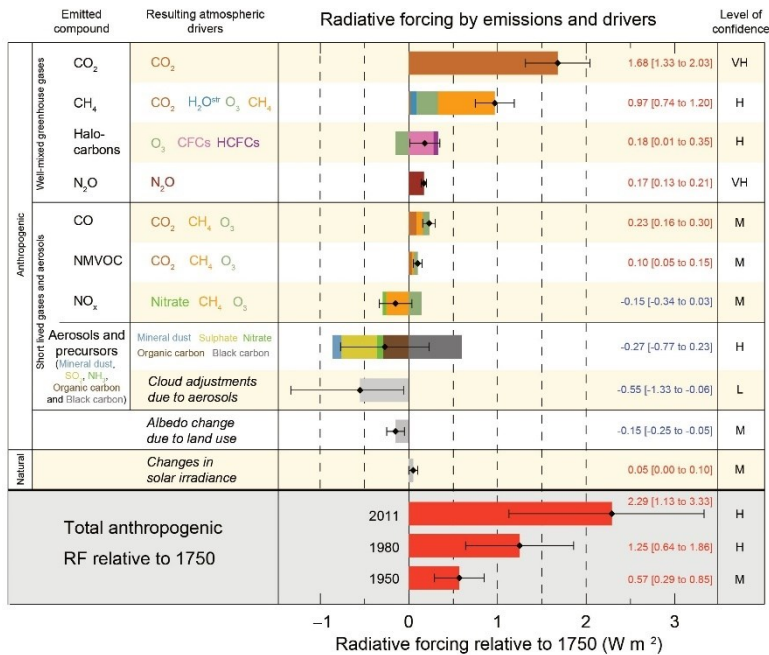


**Figure 1.1.** Radiative forcing estimates in 2011 relative to 1750 and aggregated uncertainties for the main drivers of climate change. Values are global average radiative forcing (RF14), partitioned according to the emitted compounds or processes that result in a combination of drivers. The best estimates of the net radiative forcing are shown as black diamonds with corresponding uncertainty intervals; the numerical values are provided on the right of the figure, together with the confidence level in the net forcing (VH – very high, H – high, M – medium, L – low, VL – very low). Albedo forcing due to black carbon on snow and ice is included in the black carbon aerosol bar. Small forcings due to contrails (0.05 W m<sup>-2</sup>, including contrail induced cirrus), and HFCs, PFCs and SF<sub>6</sub> (total 0.03 W m<sup>-2</sup>) are not shown. Concentration-based RFs for gases can be obtained by summing the like-coloured bars. Volcanic forcing is not included as its episodic nature makes it difficult to compare to other forcing mechanisms. Total anthropogenic radiative forcing is provided for three different years relative to 1750. For further technical details, including uncertainty ranges associated with individual components and processes, see the Technical Summary Supplementary Material. {8.5; Figures 8.14–8.18; Figures TS.6 and TS.7}. This Figure is displayed unchanged from Figure SPM.5 of the IPCC AR5 climate change 2013 report and for technical details please see the Technical Summary Supplementary Material in the AR5 IPCC report.<sup>16</sup> (Reprinted with permission from ref 16. Copyright 2013 Intergovernmental Panel on Climate Change)

Biogenic atmospheric aerosols are either emitted directly from the biosphere, such as pollen or plant debris, or can be secondary organic aerosols (SOAs) formed from VOCs emitted by plants, such as terpenes. Anthropogenic atmospheric aerosols, on the other hand, are aerosols emitted into the atmosphere by human activity, such as open waste burning, and are the targets of government policy.<sup>18</sup> To make meaningful policies that target health and climate, knowledge of how atmospheric aerosols form and how their physical properties change thereafter is important. Atmospheric aerosols, if directly emitted into the atmosphere from their source, are called primary atmospheric aerosols (for example, sea-spray aerosols and soot from biomass burning). Primary aerosol particles can provide a surface for aerosol growth through condensation of atmospherically relevant species.<sup>19</sup> In the absence of such a surface, atmospheric aerosols may form through gas-to-particle conversion processes, such as nucleation, and are called secondary atmospheric aerosols.<sup>20,21</sup> Nucleation can be described as a two-step kinetic process where the first step is the formation of the critical nucleus, the smallest cluster that, once formed, can grow spontaneously. The second step is then spontaneous aerosol growth.<sup>22</sup> It is known that the critical nucleus is stabilized by intermolecular interactions, such as van der Waals interactions and hydrogen bonding.<sup>23</sup> However, details about the structural and conformational preferences and the types of noncovalent interactions that stabilize the initial cluster are still not fully understood. Further complicating our understanding of new particle formation is the variability in the chemical species that are emitted and their involvement in nucleation.<sup>21</sup>

VOCs are a large class of compounds that are emitted anthropogenically or biogenically and are known to play a crucial role in aerosol nucleation and growth,<sup>24</sup> and even enhance atmospheric aerosol formation.<sup>25</sup> For instance, the addition of 0.04 ppb of benzoic acid can result in a 5-fold enhancement in the formation of sulfate aerosol particles.<sup>25</sup> This is thought to be a

result of organic compounds, and in particular organic acids, that provide the necessary stability to the initial cluster while still allowing for further complexation.<sup>22</sup> Initially emitted VOCs can continuously partition between the gas phase and the particle phase; however, in both the particle phase and the gas phase, VOCs can be oxidized and form lower volatile compounds that will preferentially remain in the particle phase.<sup>24</sup> The now lower volatility VOCs will form aerosol particles or become incorporated into particles through non-covalent interactions.<sup>24</sup> Both pathways depend on non-covalent interactions, and an understanding of such interactions between VOCs and nucleation partners may lead to a greater understanding of the formation of the critical nuclei.

In this thesis, I utilize an interdisciplinary approach to study 1) the initial steps in the formation of pre-critical nuclei from VOCs and 2) the physical properties, and their evolution, of emissions from PVC co-pyrolysis, which may depend on semi-volatile organic compounds (SVOCs) and VOCs. In the first part of my thesis, I present my studies of non-covalent interactions involved in the formation of pre-critical nuclei from SVOCs with a focus on benzoic acid derivatives emitted into the atmosphere from anthropogenic or natural sources such as forest fires. I utilize a dual theoretical and experimental approach involving quantum chemical calculations and Fourier transform microwave (FTMW) spectroscopy to study the structural motifs that may dictate how the critical nucleus forms and evolves. In the second part of my thesis, I describe the first steps of a study of co-pyrolysis of polyvinyl chloride (PVC) and biomass. The focus is on determining the size and optical properties of aerosol particles from PVC pyrolysis emissions and quantification of hydrogen chloride emissions during the pyrolysis. I also utilized a photoreaction chamber and various instruments for aerosol particle

characterization to investigate the aging of the emitted aerosol particles in the presence of semi-volatile organic compounds (SVOCs).

In Chapter 2, I describe the method of Fourier transform microwave spectroscopy, a gas phase spectroscopy, and how it can be utilized to extract structural information about the pre-critical nucleus. In Chapter 3, I present a gas phase study of low-volatility benzoic acid derivatives, which contain a nitro-, amino-, chloro-, or hydroxy- functional group in the para-position relative to the carboxylic acid, to understand the influence of functionalization on the structure and dynamics of benzoic acids derivatives. In Chapter 4, I present my study of vanillic acid and its complexation with one water molecule, a major nucleation partner, to understand the initial steps in hydrate formation, the initial steps in the condensational growth of low volatile organic compounds. In Chapter 5, I transition to a study of benzyl benzoate, a biogenic VOC, and its dimer, to probe how large VOCs behave in aggregation processes and the influence of flexibility and non-covalent interactions between aromatic subunits on dimer formation. In Chapter 6, I describe the instruments I have used to characterize the emissions from PVC pyrolysis and to study the aging of aerosol particles from the pyrolysis. In Chapter 7, I describe my study of PVC pyrolysis to probe the emitted aerosol particles and to determine physical properties of the particles. In Chapter 8, I present an overview of my research results and their major conclusions.

## References

- (1) Hinds, W. C. *Aerosol Technology: Properties, Behavior, and Measurement of Airborne Particles*; John Wiley & Sons, 1999.
- (2) Almetwally, A. A.; Bin-Jumah, M.; Allam, A. A. Ambient Air Pollution and Its Influence on Human Health and Welfare: An Overview. *Environ Sci Pollut Res* **2020**, *27* (20), 24815–24830. <https://doi.org/10.1007/s11356-020-09042-2>.
- (3) Li, J.; Carlson, B. E.; Yung, Y. L.; Lv, D.; Hansen, J.; Penner, J. E.; Liao, H.; Ramaswamy, V.; Kahn, R. A.; Zhang, P.; Dubovik, O.; Ding, A.; Lacis, A. A.; Zhang, L.; Dong, Y. Scattering and Absorbing Aerosols in the Climate System. *Nat Rev Earth Environ* **2022**, *3* (6), 363–379. <https://doi.org/10.1038/s43017-022-00296-7>.
- (4) Bernstein, J. A.; Alexis, N.; Barnes, C.; Bernstein, I. L.; Nel, A.; Peden, D.; Diaz-Sanchez, D.; Tarlo, S. M.; Williams, P. B.; Bernstein, J. A. Health Effects of Air Pollution. *Journal of Allergy and Clinical Immunology* **2004**, *114* (5), 1116–1123. <https://doi.org/10.1016/j.jaci.2004.08.030>.
- (5) Kim, K.-H.; Kabir, E.; Kabir, S. A Review on the Human Health Impact of Airborne Particulate Matter. *Environment International* **2015**, *74*, 136–143. <https://doi.org/10.1016/j.envint.2014.10.005>.
- (6) Canada, E. and C. C. *About the Air Quality Health Index*. <https://www.canada.ca/en/environment-climate-change/services/air-quality-health-index/about.html> (accessed 2024-04-04).
- (7) Stieb, D. M.; Burnett, R. T.; Smith-Doiron, M.; Brion, O.; Shin, H. H.; Economou, V. A. New Multipollutant, No-Threshold Air Quality Health Index Based on Short-Term Associations Observed in Daily Time-Series Analyses. *Journal of the Air & Waste*

- Management Association* **2008**, 58 (3), 435–450. <https://doi.org/10.3155/1047-3289.58.3.435>.
- (8) *Methods for Measurement of Filterable PM10 and PM2.5 and Measurement of Condensable PM Emissions From Stationary Sources*. Federal Register. <https://www.federalregister.gov/documents/2010/12/21/2010-30847/methods-for-measurement-of-filterable-pm10-and-pm25-and-measurement-of-condensable-pm-emissions-from> (accessed 2024-03-20).
- (9) Park, M.; Joo, H. S.; Lee, K.; Jang, M.; Kim, S. D.; Kim, I.; Borlaza, L. J. S.; Lim, H.; Shin, H.; Chung, K. H.; Choi, Y.-H.; Park, S. G.; Bae, M.-S.; Lee, J.; Song, H.; Park, K. Differential Toxicities of Fine Particulate Matters from Various Sources. *Sci Rep* **2018**, 8 (1), 17007. <https://doi.org/10.1038/s41598-018-35398-0>.
- (10) Unga, F.; Choël, M.; Derimian, Y.; Deboudt, K.; Dubovik, O.; Goloub, P. Microscopic Observations of Core-Shell Particle Structure and Implications for Atmospheric Aerosol Remote Sensing. *Journal of Geophysical Research: Atmospheres* **2018**, 123 (24), 13,944–13,962. <https://doi.org/10.1029/2018JD028602>.
- (11) Kameda, T.; Azumi, E.; Fukushima, A.; Tang, N.; Matsuki, A.; Kamiya, Y.; Toriba, A.; Hayakawa, K. Mineral Dust Aerosols Promote the Formation of Toxic Nitropolycyclic Aromatic Compounds. *Sci Rep* **2016**, 6 (1), 24427. <https://doi.org/10.1038/srep24427>.
- (12) Saikawa, E.; Wu, Q.; Zhong, M.; Avramov, A.; Ram, K.; Stone, E. A.; Stockwell, C. E.; Jayarathne, T.; Panday, A. K.; Yokelson, R. J. Garbage Burning in South Asia: How Important Is It to Regional Air Quality? *Environ. Sci. Technol.* **2020**, 54 (16), 9928–9938. <https://doi.org/10.1021/acs.est.0c02830>.

- (13) Haywood, J.; Boucher, O. Estimates of the Direct and Indirect Radiative Forcing Due to Tropospheric Aerosols: A Review. *Reviews of Geophysics* **2000**, *38* (4), 513–543. <https://doi.org/10.1029/1999RG000078>.
- (14) Brown, H.; Liu, X.; Pokhrel, R.; Murphy, S.; Lu, Z.; Saleh, R.; Mielonen, T.; Kokkola, H.; Bergman, T.; Myhre, G.; Skeie, R. B.; Watson-Paris, D.; Stier, P.; Johnson, B.; Bellouin, N.; Schulz, M.; Vakkari, V.; Beukes, J. P.; van Zyl, P. G.; Liu, S.; Chand, D. Biomass Burning Aerosols in Most Climate Models Are Too Absorbing. *Nat Commun* **2021**, *12* (1), 277. <https://doi.org/10.1038/s41467-020-20482-9>.
- (15) Friebel, F.; Lobo, P.; Neubauer, D.; Lohmann, U.; Drossaert van Dusseldorp, S.; Mühlhofer, E.; Mensah, A. A. Impact of Isolated Atmospheric Aging Processes on the Cloud Condensation Nuclei Activation of Soot Particles. *Atmospheric Chemistry and Physics* **2019**, *19* (24), 15545–15567. <https://doi.org/10.5194/acp-19-15545-2019>.
- (16) Intergovernmental Panel on Climate Change. *Climate Change 2013 – The Physical Science Basis: Working Group I Contribution to the Fifth Assessment Report of the Intergovernmental Panel on Climate Change*; Cambridge University Press: Cambridge, 2014. <https://doi.org/10.1017/CBO9781107415324>.
- (17) Hems, R. F.; Schnitzler, E. G.; Liu-Kang, C.; Cappa, C. D.; Abbatt, J. P. D. Aging of Atmospheric Brown Carbon Aerosol. *ACS Earth Space Chem.* **2021**, *5* (4), 722–748. <https://doi.org/10.1021/acsearthspacechem.0c00346>.
- (18) Canada, E. and C. C. *Greenhouse gases and aerosols monitoring*. <https://www.canada.ca/en/environment-climate-change/services/climate-change/greenhouse-gases-aerosols-monitoring.html> (accessed 2024-03-20).

- (19) Riipinen, I.; Yli-Juuti, T.; Pierce, J. R.; Petäjä, T.; Worsnop, D. R.; Kulmala, M.; Donahue, N. M. The Contribution of Organics to Atmospheric Nanoparticle Growth. *Nature Geosci* **2012**, *5* (7), 453–458. <https://doi.org/10.1038/ngeo1499>.
- (20) Kulmala, M.; Kerminen, V.-M.; Petäjä, T.; J. Ding, A.; Wang, L. Atmospheric Gas-to-Particle Conversion: Why NPF Events Are Observed in Megacities? *Faraday Discussions* **2017**, *200* (0), 271–288. <https://doi.org/10.1039/C6FD00257A>.
- (21) Lee, S.-H.; Gordon, H.; Yu, H.; Lehtipalo, K.; Haley, R.; Li, Y.; Zhang, R. New Particle Formation in the Atmosphere: From Molecular Clusters to Global Climate. *Journal of Geophysical Research: Atmospheres* **2019**, *124* (13), 7098–7146. <https://doi.org/10.1029/2018JD029356>.
- (22) Zhang, R. Getting to the Critical Nucleus of Aerosol Formation. *Science* **2010**, *328* (5984), 1366–1367. <https://doi.org/10.1126/science.1189732>.
- (23) Zhang, R.; Khalizov, A.; Wang, L.; Hu, M.; Xu, W. Nucleation and Growth of Nanoparticles in the Atmosphere. *Chem. Rev.* **2012**, *112* (3), 1957–2011. <https://doi.org/10.1021/cr2001756>.
- (24) Tröstl, J.; Chuang, W. K.; Gordon, H.; Heinritzi, M.; Yan, C.; Molteni, U.; Ahlm, L.; Frege, C.; Bianchi, F.; Wagner, R.; Simon, M.; Lehtipalo, K.; Williamson, C.; Craven, J. S.; Duplissy, J.; Adamov, A.; Almeida, J.; Bernhammer, A.-K.; Breitenlechner, M.; Brilke, S.; Dias, A.; Ehrhart, S.; Flagan, R. C.; Franchin, A.; Fuchs, C.; Guida, R.; Gysel, M.; Hansel, A.; Hoyle, C. R.; Jokinen, T.; Junninen, H.; Kangasluoma, J.; Keskinen, H.; Kim, J.; Krapf, M.; Kürten, A.; Laaksonen, A.; Lawler, M.; Leiminger, M.; Mathot, S.; Möhler, O.; Nieminen, T.; Onnela, A.; Petäjä, T.; Piel, F. M.; Miettinen, P.; Rissanen, M. P.; Rondo, L.; Sarnela, N.; Schobesberger, S.; Sengupta, K.; Sipilä, M.; Smith, J. N.; Steiner, G.; Tomè,

A.; Virtanen, A.; Wagner, A. C.; Weingartner, E.; Wimmer, D.; Winkler, P. M.; Ye, P.; Carslaw, K. S.; Curtius, J.; Dommen, J.; Kirkby, J.; Kulmala, M.; Riipinen, I.; Worsnop, D. R.; Donahue, N. M.; Baltensperger, U. The Role of Low-Volatility Organic Compounds in Initial Particle Growth in the Atmosphere. *Nature* **2016**, *533* (7604), 527–531.

<https://doi.org/10.1038/nature18271>.

- (25) Zhang, R.; Suh, I.; Zhao, J.; Zhang, D.; Fortner, E. C.; Tie, X.; Molina, L. T.; Molina, M. J. Atmospheric New Particle Formation Enhanced by Organic Acids. *Science* **2004**, *304* (5676), 1487–1490. <https://doi.org/10.1126/science.1095139>.

# 2

## Experimental and Theoretical Methods for the Study of Gas-phase Molecules and Molecular Clusters of Atmospheric Relevance

### 2.1. Background

The formation of secondary organic aerosol particles can occur via the atmospheric oxidation of biogenic or anthropogenic volatile organic compounds. The products of the initial oxidation steps are typically lower volatility compounds that can begin to aggregate with other atmospheric species such as water, sulfuric acid, ammonia and other organic compounds. These oxidation products can contain OH, carbonyl, and carboxyl groups, in addition to double bonds and aromatic moieties, for example. These can all participate in intermolecular interactions which are the driving force for the partitioning of atmospheric species from the gas into the condensed, particle phase.

Organic acids, such as vanillic acid and benzoic acid derivatives, are thought to play an important role in atmospheric aerosol particle formation.<sup>1</sup> To complement the aerosol and smog chamber research activities, I also carried out rotational spectroscopic studies of the related acids. These acids can occur as several conformers,<sup>2,3</sup> offering multiple intermolecular binding

sites. The formation of a mono-hydrate, for example, increases the conformational space significantly and produces further intermolecular binding sites for the aggregation to continue. One main goal of my thesis research is to first probe the conformational landscape and internal dynamics of these atmospherically-relevant species in their isolated form, i.e., in the gas phase, and then follow the initial steps of their self-aggregation and aggregation with water molecules to explore the effects of non-covalent intermolecular interactions on the conformational preferences and dynamics. These aggregates may be important precursors to nucleation and eventual formation of aerosol particles in the atmosphere.<sup>4</sup>

High-resolution rotational spectroscopy, coupled with a supersonic jet expansion, has been utilized extensively for studies of structural and dynamic properties of diverse molecular systems, catering to varied research interests.<sup>5-7</sup> For example, the onset of microscopic superfluidity<sup>8</sup> was traced by rotational spectroscopy of highly fluxional doped helium clusters;<sup>9,10</sup> the early fundamental rotational studies of chiral molecules and their non-covalently bonded chiral molecular pairs<sup>11-13</sup> have led to the practical application of rotational spectroscopy for enantiomeric excess determination.<sup>14</sup> More directly related to my thesis work are the rotational spectroscopic studies of organic acids and their water containing clusters, such as methanesulfonic acid (a common component found in marine aerosols),<sup>15</sup> H<sub>2</sub>SO<sub>4</sub>,<sup>16</sup> pyruvic acid,<sup>17</sup> o-toluic acid,<sup>18</sup> and oxalic acid.<sup>19</sup> Detailed analyses of the conformational preferences, proton tunneling dynamics, and non-covalent interactions provide the molecular foundation to further explore their roles as aerosol nucleation intermediates and chemical intermediates in physicochemical processes in the atmosphere.<sup>6</sup> In our research group, we have targeted another family of volatile organic compounds: namely alcohols. Some examples are cis-1,2-cyclohexanediol,<sup>20</sup> perillyl alcohol,<sup>21</sup> 2,2,3,3,3-pentafluoro-1-propanol,<sup>22</sup> and 4,4,4-trifluoro-1-

butanol.<sup>23</sup> We extensively mapped out the rich conformational landscapes of these alcohols and thoroughly investigated the associated large-amplitude motions including proton tunneling. Moving one step further to explore how self-aggregation and interaction with water can influence the structural properties and further binding abilities of these alcohols, we also studied the associated hydrogen-bonded complexes.<sup>24–26</sup>

In general, cavity-based Fourier transform microwave (FTMW) and broadband chirped pulse FTMW (CP-FTMW) spectrometers, coupled with a pulsed supersonic jet expansion, are the most common instruments utilized in laboratories around the world for rotational spectroscopic studies. The pulsed jet expansion offers not only a very low rotational temperature (typically a few Kelvin), therefore greatly enhanced sensitivity, but also a straightforward way to synthesize the desired non-covalently bonded molecular complexes. These points will be further elaborated in Section 2.6. The cavity-based<sup>27</sup> and CP-FTMW<sup>28</sup> instruments in our laboratory offer excellent high-resolution capability, with corresponding full widths at half height of 15 and 150 kHz, respectively. Consequently, the experimental rotational spectra contain accurate information about molecular structure and are very sensitive to only the slightest structural variations. The details of the CP-FTMW instrument used in the current thesis research will be described in a later section, together with the sensitivity improvements made in the last few years. It is particularly exciting to point out that with this instrument developed in our laboratory, we are now able to access increasingly larger molecular systems, for example, hexafluoroisopropanol trimer,<sup>29</sup> trimer of propylene oxide,<sup>30</sup> and 3-methylcatechol $\cdots$ water<sub>n</sub> (n=1-5).<sup>28</sup> These successes have inspired my thesis work on benzyl benzoate, a member of a different group of volatile organic compounds, and its homodimer, which rank among the largest molecular species investigated using rotational spectroscopy.

It is worth to point out that a recorded experimental microwave spectrum often contains rotational spectra of several conformers of an isolated monomer and multiple non-covalently bound complexes containing the monomer subunit(s). As a result, experimental rotational spectra taken with the CP-FTMW spectrometer typically comprise several thousands of lines within the small frequency range of a few gigahertz. Consequently, assigning transitions to rotational quantum numbers and to a particular molecular species or conformer is often extremely challenging. In dealing with increasingly large, flexible organic molecules, including those investigated in this thesis, the support of multiple theoretical tools is essential. For example, assistance with theoretical conformational searches and help from electronic structure calculations are commonly needed to predict molecular structures of possible conformers, their relative energies, and conversion barriers between conformers to aid the assignment. Additionally, to enrich our understanding of the molecular systems, further theoretical tools are utilized.

In the following, I first describe the theoretical tools used in the current studies. Then, I introduce some basic terms used in rotational spectroscopy. Finally, I discuss the CP-FTMW spectrometer and the supersonic jet expansions, which we apply to measure rotational spectra.

## **2.2. Theoretical Tools**

Before going into the theoretical details, it is helpful to briefly address the definition of conformer. Conformers of a molecule can be generated by internal rotations about a single bond, and molecular samples can often contain several conformers, depending on outcomes of synthetic processes and barriers to interconversion. In molecular complexes and clusters, the term conformer is often used in a less restrictive manner and includes species with intermolecular interactions between different binding sites of the constituent monomers.

To aid a spectral assignment, one needs to simulate the rotational spectrum of a potential conformer of interest. To do that it is necessary to obtain the associated theoretical rotational constants and permanent dipole moment components of the optimized geometry. To optimize the candidate geometry of a molecular monomer or its complex of interest, we apply electronic structure calculations as implemented in the ORCA<sup>31</sup> and/or Gaussian<sup>16</sup> suites of programs.<sup>32</sup> Typically, we used the combination of B3LYP<sup>33</sup>-D3<sup>34</sup> (BJ)<sup>35</sup> functional with different basis sets, such as 6-311++G(d,p)<sup>36</sup> and def2-TZVP.<sup>37</sup> Here, D3 denotes Grimme's dispersion correction<sup>33</sup> and BJ is the Becke-Johnson damping function.<sup>34</sup> These combinations have been utilized extensively by our group for a variety of molecular systems from those dominated by weak dispersion<sup>38,39</sup> to strong hydrogen bonding interactions.<sup>40,41</sup> Additionally, frequency calculations are done at the same level to verify that the identified conformer is not a transition state, through the absence of imaginary frequencies, and to obtain zero-point-energy (ZPE) corrections.

Relative energies (either the ZPE corrected energies or Gibbs free energies) obtained from these calculations are important to estimate the relative abundances of conformers and the possibility for experimental detection. Based on the large number of molecular systems reported, the aforementioned levels of theory generally provide reasonable rotational constants (within a few percent) and dipole moment components (usually consistent ordering) to guide the rotational spectroscopic assignment. It has been noted in some recent publications that large amplitude motions associated with potential barriers may lead to drastically different a-, b- and c-type transition intensities compared to those predicted, for example, for some chiral molecule-water complexes.<sup>42,43</sup> Such observation implies that some spectroscopic properties predicted at a potential minimum may be very different from those observed in the ground vibrational state.

Below I address theoretical approaches to locate conformers of monomers and complexes on the multidimensional potential energy surface.

To assign a dense experimental CP-FTMW spectrum, it is necessary to consider all the possible species including their potential conformers. Possible species can be identified based on the experimental conditions (samples used, different carrier gases, source temperature, etc.) and lines of known species can then be removed from the spectrum using the previously assigned rotational spectra. To facilitate the spectroscopic assignments of the species of interest, it is highly desirable to first identify theoretically all low energy conformers of a molecular target.

For a simple system with limited flexibility such as para-chlorobenzoic acid, described in Chapter 3, chemical intuition can be used to identify possible conformers. For conformationally more flexible systems, two strategies can be used to find the possible minima. For example, in the case of cis-1,2-cyclohexanediol,<sup>20</sup> a simple cyclic vicinal diol, there are two flexible dihedral angles which are related to the OH pointing directions of the two hydroxyl groups. To find the possible conformers, a relaxed, two-dimensional potential energy surface scan along these two angles was generated. This was done by performing a relaxed scan, where two dihedral angles, H-O1-C1-C2 and H-O2-C2-C1, were stepped in 9° increments, from 0° to 360° while performing an optimization of the other structure parameters. The resulting energy values obtained from the 40x40 relaxed scan were used to produce the potential energy surface shown in Figure 2.1. As one can see, four distinct conformers I-IV exhibiting different intramolecular OH...OH binding topologies were identified. Furthermore, one can also read out the interconversion barriers between conformers, equipping one with an overview of conformers which may or may not be detectable in a supersonic jet expansion (vide infra). A similar strategy was used for the study of vanillic acid described in Chapter 4.

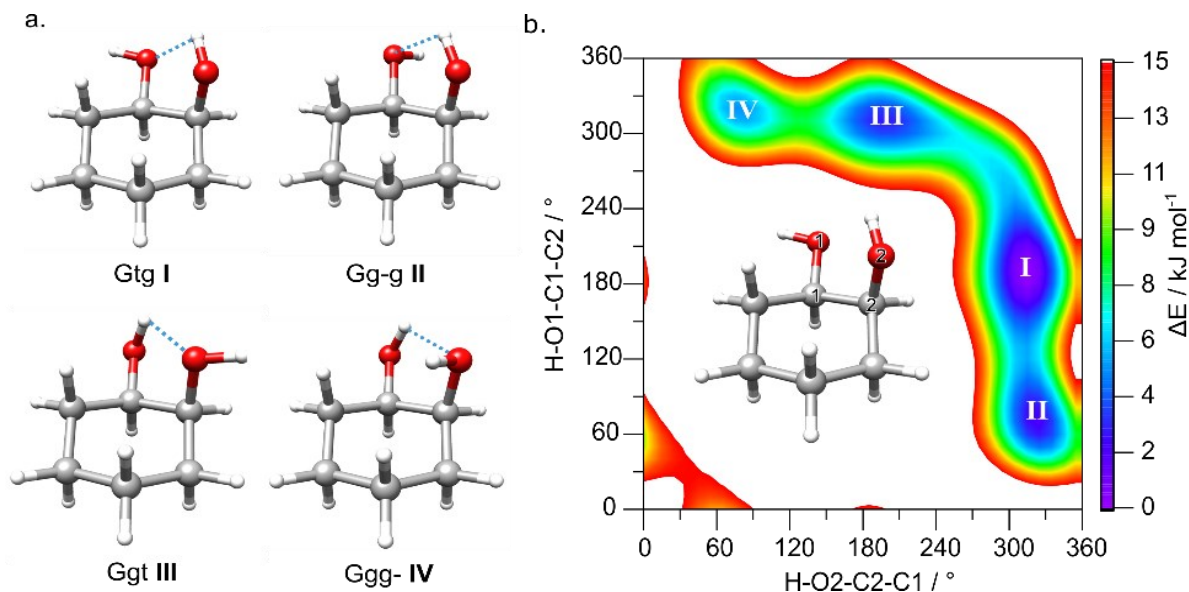


**Figure 2.1.** a) The equilibrium geometries of the four most stable cis-1,2-cyclohexanediol conformers. The blue dashed lines represent the intramolecular H-bonds. B) A 2D PES scan along two dihedral angles associated with the OH pointing directions at the B3LYP-D3(BJ)/6-311++G(d,p) level of theory. One can see that the conformational conversion barriers from **II**→**I** and **IV**→**III** are fairly low, leading to the non-observation of **II** and **IV** in a jet expansion. Reproduced from Ref. 20.

For molecular systems with even greater flexibility a relaxed scan method is not practical. Generally, the second strategy is applied by utilizing Grimme's conformer rotamer ensemble sampling tool<sup>44</sup> (CREST) program. CREST is an automated potential energy surface exploration program, that can be used to find minima on the multi-dimensional potential energy surface which correspond to molecular conformers.<sup>44</sup> The CREST program utilizes the semiempirical GFN-xTB<sup>45</sup> method, making the search for conformations computationally cost effective. For example, I was involved in a chirality recognition infrared spectroscopic study of homo- and heterochiral protonated dimers of asparagine with serine and with valine where thousands of CREST candidates were identified.<sup>46</sup> In Chapter 5, the CREST program was used to explore the potential energy landscape of the benzyl benzoate dimer and 128 conformers were identified.

To gain further insights into the role of non-covalent interactions in cluster formation, it is useful to determine binding energies, identify different types of interactions, such as hydrogen-bonding,  $\pi$ -stacking, and van der Waals interactions, and partition binding energies into contributions from electrostatic, induction, and dispersion forces.<sup>47-49</sup> The total binding energy between two subunits can be determined using the supermolecular approach, where the energies of the subunits are subtracted from that of the complex or cluster. The counterpoise correction<sup>50</sup> can be applied to correct for basis set superposition error. Symmetry adapted perturbation theory (SAPT) is a method to decompose the binding energy into contributions from dispersion, induction, exchange, and electrostatic interactions.<sup>51</sup>

To provide qualitative and semi-quantitative insights into intermolecular interactions, topological analyses of the electron density distribution,  $\rho$ , obtained from electronic structure calculations, are useful. In my studies, I have used Bader's quantum theory of atoms in molecules (QTAIM)<sup>52</sup> and non-covalent interactions (NCI) analyses.<sup>49</sup> In QTAIM, both covalent and non-covalent bonds between atoms are identified by bond-critical points, where the electron density is a minimum along the path of steepest descent of  $\rho$  between two nuclei (bond path) and a maximum perpendicularly to the bond path (second-order saddle point).<sup>53</sup> Other critical points exist and are classified as nuclear, ring, and cage critical points, depending on whether  $\rho$  is a maximum, a first-order saddle point, or a minimum.<sup>53</sup> From properties at the bond critical point, such as  $\rho$  and the Laplacian, i.e., the trace of the second order derivative matrix of  $\rho$ , bonds can be classified as covalent, hydrogen-bond, or van der Waals interaction<sup>54</sup> and hydrogen bond energies can be estimated.<sup>55</sup> It is known that weak hydrogen bonds, such as the weak intramolecular hydrogen bonds in vanillic acid monohydrate (see Figure 3), are often not indicated by a bond critical point in a QTAIM analysis<sup>56</sup> and an NCI analysis can provide a more intuitive

picture of the non-covalent interactions. The NCI method also utilizes the electron density to identify weak interactions, but uses less stringent criteria than QTAIM. In NCI, small values of the reduced density gradient, RDG, given in Equation (1), at low electron densities indicate weak interactions (see the spikes in the left-hand part of Figure 2.2).<sup>49</sup>

$$RDG = \frac{1}{2(3\pi^2)^{\frac{1}{3}}} \left( \frac{|\nabla\rho|}{\rho^{\frac{4}{3}}} \right) \quad (1)$$

The strength of the interaction is given by the magnitude of the electron density for a given low value (spike) of the RDG and the sign of the second eigenvalue of the hessian of electron density  $\text{sign}(\lambda_2)$  is used to identify whether the interaction is repulsive ( $\text{sign}(\lambda_2) > 0$ ), attractive ( $\text{sign}(\lambda_2) < 0$ ), or van der Waals ( $\text{sign}(\lambda_2) \sim 0$ ).<sup>49</sup> This is also indicated with color coding, i.e., red (repulsive), blue (attractive), or green (van der Waals); see Figure 2.2.

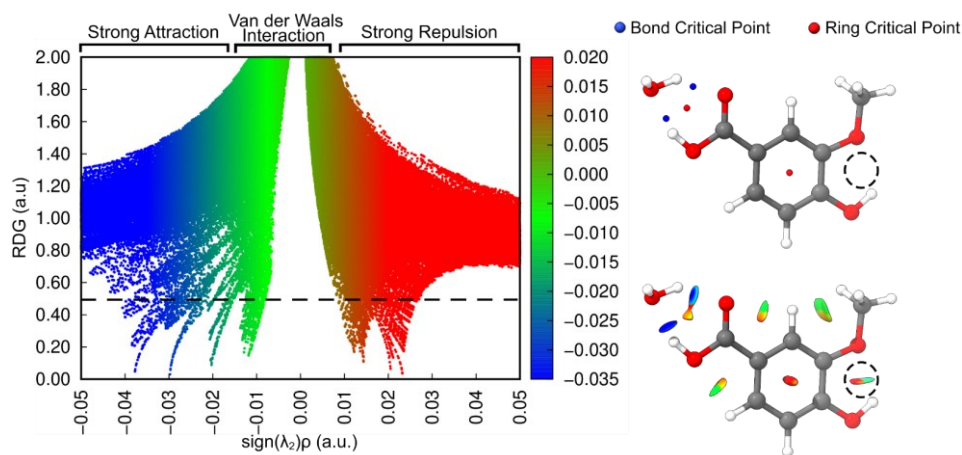


**Figure 2.2.** Results of QTAIM and NCI analyses of vanillic acid monohydrate showing how these techniques can supplement each other in analyzing non-covalent interactions.

### 2.3. Rotational Spectroscopy

The rotational energy levels of a molecule are obtained by solving the time-independent Schrödinger equation governing rotational motion. The Hamiltonian operator for a rigid molecule is given by

$$\hat{H}_{rot} = \frac{1}{2} \left( \frac{\hat{J}_a^2}{I_a} + \frac{\hat{J}_b^2}{I_b} + \frac{\hat{J}_c^2}{I_c} \right). \quad (2)$$

Here, the  $\hat{J}_a^2$ ,  $\hat{J}_b^2$ , and  $\hat{J}_c^2$  are the angular momentum operators and  $I_a$ ,  $I_b$ , and  $I_c$  are the principal moments of inertia.<sup>57</sup> The energies of the resulting energy levels are usually expressed in terms of rotational constants  $A$ ,  $B$ , and  $C$  which are defined as

$$A = \frac{\hbar^2}{2I_a}, B = \frac{\hbar^2}{2I_b}, C = \frac{\hbar^2}{2I_c}. \quad (3)$$

Here,  $\hbar = \frac{h}{2\pi}$  with  $h$  being Planck's constant. For asymmetric top molecules, such as those described in this thesis,  $A > B > C$ . For semi-rigid molecules, centrifugal distortion of the structure of the rotating molecule must be taken into account. For example, Watson's A-reduction fourth order centrifugal distortion constants,  $\Delta_J$ ,  $\Delta_{JK}$ ,  $\Delta_K$ ,  $\delta_J$ , and  $\delta_K$ , can be regarded as corrections to the rotational constants.<sup>57</sup> The rotational energy levels of an asymmetric top molecule are labelled in this thesis with the quantum numbers  $J_{K_a K_c}$ .<sup>58</sup> Here,  $J$  is the (good) total angular momentum quantum number and  $K_a, K_c$  are pseudo quantum numbers that relate to the  $K$  quantum number in the limiting oblate and prolate symmetric top cases. The labelling scheme is indicated in Figure 2.3, in which the asymmetric top energy levels are correlated to those of the prolate and oblate symmetric tops. Also indicated in Figure 2.3 is Ray's asymmetry parameter  $\kappa$ , which describes the degree of deviation from the symmetric top cases.

$$\kappa = \frac{2B - A - C}{A - C} \quad (4)$$

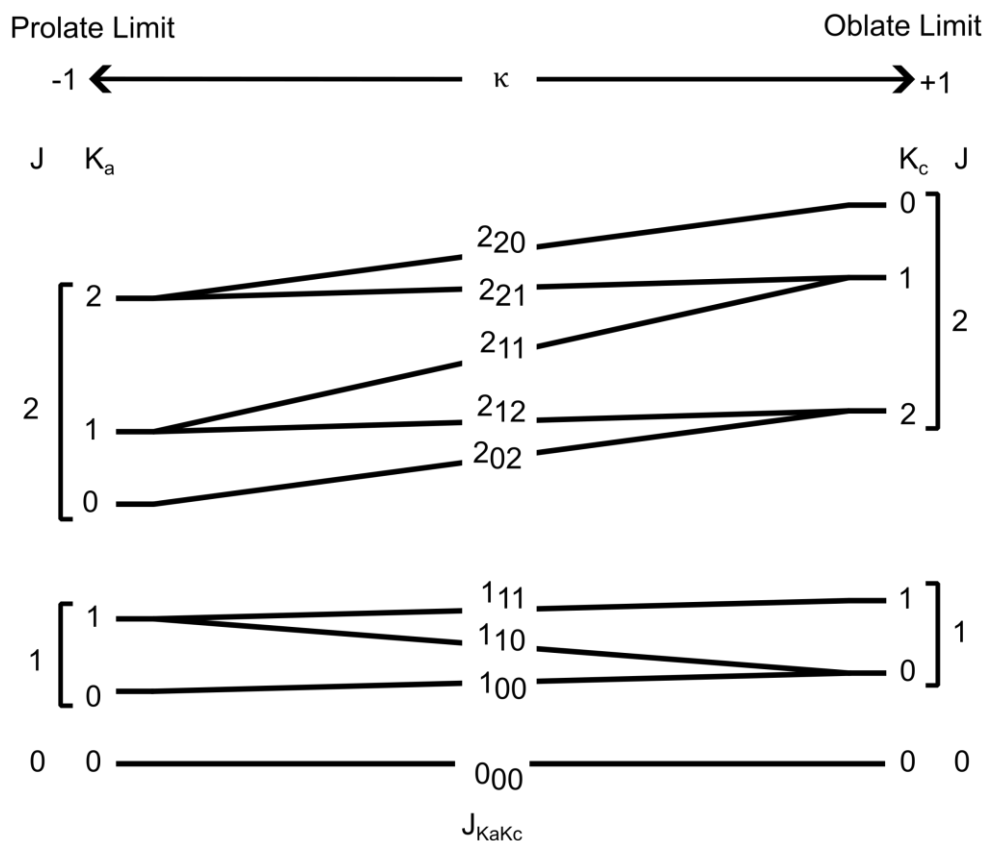


**Figure 2.3.** Diagram that correlates asymmetric top energy levels with those of oblate and prolate symmetric tops for  $J = 0, 1,$  and  $2$ . The corresponding  $J_{K_a K_c}$  and  $J_K$  quantum numbers are given, as is Ray's asymmetry parameter that describes the deviation from the symmetric top cases.

In general, three types of transitions, designated as  $a$ -,  $b$ -, or  $c$ -type, can occur depending on whether the transition is driven by dipole moment components,  $\mu_a$ ,  $\mu_b$ , or  $\mu_c$ , along the  $a$ -,  $b$ -, or  $c$ -principal inertial axis, respectively. Specific selection rules are  $\Delta J = 0, \pm 1$  and those given in Table 2.1 for  $\Delta K_a$  and  $\Delta K_c$ .

**Table 2.1.** Specific  $\Delta K_a$  and  $\Delta K_c$  selection rules for asymmetric top molecules

Types of transitions	Dipole moment components	$\Delta K_a$	$\Delta K_c$
<i>a</i> -type	$\mu_a \neq 0$	0 (even)	$\pm 1$ (odd)
<i>b</i> -type	$\mu_b \neq 0$	$\pm 1$ (odd)	$\pm 1$ (odd)
<i>c</i> -type	$\mu_c \neq 0$	$\pm 1$ (odd)	0 (even)

## 2.4. Chirped-Pulsed Fourier Transform Microwave Spectrometer

I used a CP-FTMW spectrometer for the rotational spectroscopic studies described in this thesis. The first CP-FTMW spectrometer was developed in 2008 by the Pate group at the University of Virginia and made possible by the rapid development of high speed electronic components.<sup>7,59</sup> The design of our 2-6 GHz CP-FTMW spectrometer<sup>60,61</sup> is based on the 2-8 GHz CP-FTMW instrument first reported by Perez *et al.*<sup>62</sup> An overview of the 2-6 GHz chirped pulse spectrometer can be seen in Figure 2.4 and some important details are provided below

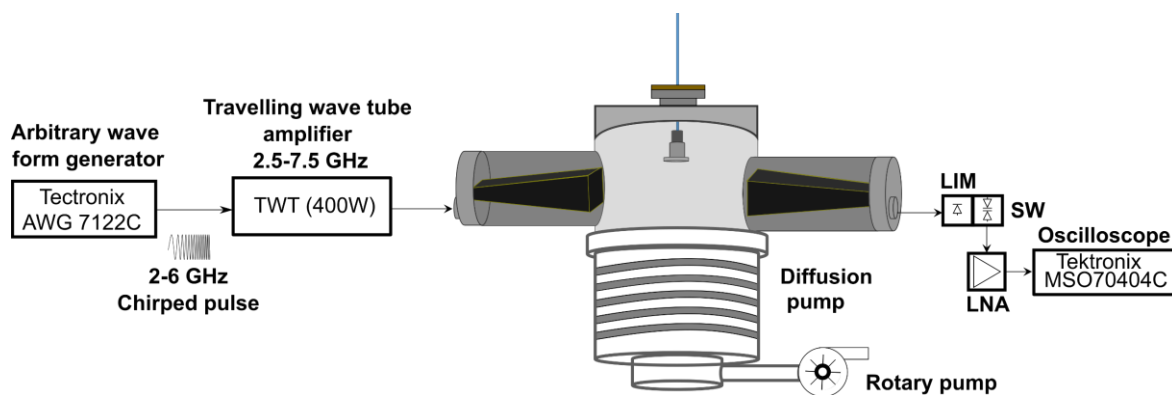


**Figure 2.4.** Overview of the chirped pulse Fourier Transform microwave spectrometer at the University of Alberta where LIM is a power limiter, SW a single-pull single-throw switch, and LNA a low noise amplifier.

The instrument is based on a pulsed excitation - spontaneous emission technique. A 4  $\mu$ s long microwave excitation pulse is scanned rapidly through a large frequency range (2 – 6 GHz) (“chirped pulse”) and irradiates the expansion-cooled molecular sample. If the microwave pulse sweeps over a molecular transition frequency of an allowed transition, a superposition state is

generated that is composed of the two stationary states involved in the transition. Classically, this non-stationary superposition state corresponds to an oscillating dipole moment that emits electromagnetic radiation with the transition frequency. This coherent spontaneous emission signal can be recorded in the time domain with a fast oscilloscope and then Fourier transformed to yield the rotational spectrum in the frequency domain. The power of this method lies in the ability to record transitions over a wide spectral range (in our case 2 to 6 GHz) simultaneously in a single shot. The signal intensity is proportional to the macroscopic sample polarization, which is given by<sup>7</sup>

$$|P| = \frac{2 \cdot |\mu_{ab}|^2 \cdot E_{pulse} \cdot \Delta N_0}{\hbar} \cdot \left(\frac{\pi}{\alpha}\right)^{\frac{1}{2}}. \quad (5)$$

Here,  $\mu_{ab}$  is the transition dipole moment,  $E_{pulse}$  is the electric field strength of the chirped pulse,  $\Delta N_0$  is the population difference between the two energy levels,  $\hbar$  is the reduced Planck's constant, and  $\alpha$  is the sweep rate of the chirped pulse.

The experiment begins with a pulsed expansion of a sample gas mixture into a vacuum chamber that is maintained at a pressure of ca.  $10^{-6}$  torr under no-load conditions. A 4  $\mu$ s long chirped pulse from 2-6 GHz is then generated by a 12 Gs  $s^{-1}$  arbitrary wave form generator (Tektronix AWG7122C) and amplified by a 2.5 - 7.5 GHz travelling wave tube (TWT) amplifier (IFI GT7525-400). The amplified chirped pulse is broadcasted onto the molecular expansion via a horn antenna (Q-par QW-SL-2-18-N-HG-R) that is mounted perpendicularly to the molecular flight path. The resulting molecular emission signal (free-induction decay, FID) is detected by a second horn antenna. Following the detection horn antenna is a PIN diode power limiter followed by a PIN diode switch that protects the 25 GS  $s^{-1}$  fast oscilloscope (Tektronix MS07404C) from the high-power chirped pulse until the excitation pulse has dissipated (ca. 250 ns). A low noise MW amplifier (Miteq AMF-5F-02000600-13-10) is placed after the PIN diode

switch to amplify the molecular signal. The molecular signal is digitized at a rate of 25 GS s<sup>-1</sup> with the fast oscilloscope and recorded for 20 μs or 40 μs. Both the AWG and the oscilloscope are phase-locked to a 10 MHz Rb standard (SRS FS725), making coherent averaging of the molecular time signal possible. During a single molecular gas pulse 6 excitation-detection acquisition cycles are possible. The repetition rate of the pulsed molecular expansion is 2 s<sup>-1</sup>, so that a typical experiment with 10<sup>6</sup> averaging cycles takes about 24 h.

## **2.5. Molecular Supersonic Jet Expansion**

The sample is introduced into the spectrometer via a pulsed molecular expansion. The expansion is generated with a pulsed nozzle (General Valve, Series 9) with a nozzle orifice of 0.8 mm. The nozzle is operated at a repetition rate of 2 Hz and the duration of the molecular pulse is several 100 μs. The sample consists typically of 1 % molecular monomer(s) and He, Ne, or Ar as carrier gas at a total pressure of several atm. For the investigation of low vapour pressure substances, a modified heated nozzle cap<sup>63</sup> with a sample reservoir was built. The whole nozzle cap body can be heated up to about 150°C.

The use of a molecular expansion rather than a static gas sample has several advantages. Collisions of the molecule under investigation with noble gas atoms of the carrier gas leads to cooling. The process, however, is highly non-equilibrium and results in translational temperatures in the millikelvin range, rotational temperatures of ~1-2 K, and higher conformational and vibrational temperatures.<sup>64,65</sup> The low rotational temperature has the effect of squeezing the population into lower rotational energy levels. This leads to decongestion of the rotational spectrum and to greatly enhanced line intensity because of increase in populations and population differences. The line width is determined by the detection time, as the emitting molecules move through the interaction zone of the receiving horn antenna. Finally, the large

number of the collisions at the edge of the exit channel leads to the formation of the targeted molecular complexes and clusters which are subsequently stabilized in the collision-free environment of the molecular expansion.

Because of the different cooling efficiencies of He, Ne, and Ar, one can use different carrier gases to probe the conversion barrier between conformers. For instance, in Chapter 5, when changing the carrier gas from He to Ne and then to Ar, there is a decrease in the relative population of the higher energy *trans* conformer of the benzyl benzoate (BnBz) monomer because of the higher cooling efficiency of the heavier carrier gases.

## References

- (1) Zhang, R.; Suh, I.; Zhao, J.; Zhang, D.; Fortner, E. C.; Tie, X.; Molina, L. T.; Molina, M. J. Atmospheric New Particle Formation Enhanced by Organic Acids. *Science* **2004**, *304* (5676), 1487–1490. <https://doi.org/10.1126/science.1095139>.
- (2) Al-Jabiri, M. H.; Hazrah, A. S.; Insausti, A.; Xu, Y.; Jäger, W. Rotational Spectroscopic Studies of Para-Nitrobenzoic Acid, Para-Aminobenzoic Acid, Para-Chlorobenzoic Acid, and Para-Hydroxybenzoic Acid. *J. Mol. Spectrosc.* **2023**, *394*, 111790. <https://doi.org/10.1016/j.jms.2023.111790>.
- (3) Al-Jabiri, M. H.; Hazrah, A. S.; Jäger, W. Conformers of Vanillic Acid and Its Monohydrate: A Rotational Spectroscopic and Theoretical Study. *J. Phys. Chem. A* **2022**. <https://doi.org/10.1021/acs.jpca.2c05120>.
- (4) Knopf, D. A.; Alpert, P. A.; Wang, B. The Role of Organic Aerosol in Atmospheric Ice Nucleation: A Review. *ACS Earth Space Chem.* **2018**, *2* (3), 168–202. <https://doi.org/10.1021/acsearthspacechem.7b00120>.
- (5) Xu, Y.; Wijngaarden, J. V.; Jäger, W. Microwave Spectroscopy of Ternary and Quaternary van Der Waals Clusters. *Int. Rev. Phys. Chem.* **2005**, *24* (2), 301–338. <https://doi.org/10.1080/01442350500252039>.
- (6) Leopold, K. R. Hydrated Acid Clusters. *Annu. Rev. Phys. Chem.* **2011**, *62* (Volume 62, 2011), 327–349. <https://doi.org/10.1146/annurev-physchem-032210-103409>.
- (7) Park, G. B.; Field, R. W. Perspective: The First Ten Years of Broadband Chirped Pulse Fourier Transform Microwave Spectroscopy. *J. Chem. Phys.* **2016**, *144* (20), 200901. <https://doi.org/10.1063/1.4952762>.

- (8) Tang, J.; Xu, Y.; McKellar, A. R. W.; Jäger, W. Quantum Solvation of Carbonyl Sulfide with Helium Atoms. *Science* **2002**, *297* (5589), 2030–2033.  
<https://doi.org/10.1126/science.1073718>.
- (9) McKellar, A. R. W.; Xu, Y.; Jäger, W. Spectroscopic Exploration of Atomic Scale Superfluidity in Doped Helium Nanoclusters. *Phys. Rev. Lett.* **2006**, *97* (18), 183401.  
<https://doi.org/10.1103/PhysRevLett.97.183401>.
- (10) Song, X.; Xu, Y.; Roy, P.-N.; Jäger, W. Rotational Spectrum, Potential Energy Surface, and Bound States of the Weakly Bound Complex He–N<sub>2</sub>O. *J. Chem. Phys.* **2004**, *121* (24), 12308–12314. <https://doi.org/10.1063/1.1819875>.
- (11) King, A. K.; Howard, B. J. A Microwave Study of the Hetero-Chiral Dimer of Butan-2-ol. *Chem. Phys. Lett.* **2001**, *348* (3), 343–349. [https://doi.org/10.1016/S0009-2614\(01\)01121-6](https://doi.org/10.1016/S0009-2614(01)01121-6).
- (12) Borho, N.; Xu, Y. Rotational Spectrum of a Chiral  $\alpha$ -Hydroxyester: Conformation Stability and Internal Rotation Barrier Heights of Methyl Lactate. *Phys. Chem. Chem. Phys.* **2007**, *9* (11), 1324–1328. <https://doi.org/10.1039/B608561J>.
- (13) Thomas, J.; Sunahori, F. X.; Borho, N.; Xu, Y. Chirality Recognition in the Glycidol···Propylene Oxide Complex: A Rotational Spectroscopic Study. *Chem. Eur. J.* **2011**, *17* (16), 4582–4587. <https://doi.org/10.1002/chem.201003536>.
- (14) Pate, B. H.; Evangelisti, L.; Caminati, W.; Xu, Y.; Thomas, J.; Patterson, D.; Perez, C.; Schnell, M. Chapter 17 - Quantitative Chiral Analysis by Molecular Rotational Spectroscopy. In *Chiral Analysis (Second Edition)*; Polavarapu, P. L., Ed.; Elsevier, 2018; pp 679–729. <https://doi.org/10.1016/B978-0-444-64027-7.00019-7>.

- (15) Huff, A. K.; Love, N.; Leopold, K. R. Microwave and Computational Study of Methanesulfonic Acid and Its Complex with Water. *J. Phys. Chem. A* **2023**, *127* (16), 3658–3667. <https://doi.org/10.1021/acs.jpca.3c01395>.
- (16) Fiacco, D. L.; Hunt, S. W.; Leopold, K. R. Microwave Investigation of Sulfuric Acid Monohydrate. *J. Am. Chem. Soc.* **2002**, *124* (16), 4504–4511. <https://doi.org/10.1021/ja012724w>.
- (17) Schnitzler, E. G.; Seifert, N. A.; Ghosh, S.; Thomas, J.; Xu, Y.; Jäger, W. Hydration of the Simplest  $\alpha$ -Keto Acid: A Rotational Spectroscopic and Ab Initio Study of the Pyruvic Acid–Water Complex. *Phys. Chem. Chem. Phys.* **2017**, *19* (6), 4440–4446. <https://doi.org/10.1039/C6CP08741H>.
- (18) Schnitzler, E. G.; Zenchyzen, B. L. M.; Jäger, W. Rotational Spectroscopy of the Atmospheric Photo-Oxidation Product o-Toluic Acid and Its Monohydrate. *Phys. Chem. Chem. Phys.* **2015**, *18* (1), 448–457. <https://doi.org/10.1039/C5CP06073G>.
- (19) Schnitzler, E. G.; Badran, C.; Jäger, W. Contrasting Effects of Water on the Barriers to Decarboxylation of Two Oxalic Acid Monohydrates: A Combined Rotational Spectroscopic and Ab Initio Study. *J. Phys. Chem. Lett.* **2016**, *7* (7), 1143–1147. <https://doi.org/10.1021/acs.jpcclett.6b00278>.
- (20) Ma, J.; Insausti, A.; Al-Jabiri, M. H.; Carlson, C. D.; Jäger, W.; Xu, Y. Unlocking a New Hydrogen-Bonding Marker: C–O Bond Shortening in Vicinal Diols Revealed by Rotational Spectroscopy. *J. Chem. Phys.* **2024**, *160* (15), 154304. <https://doi.org/10.1063/5.0203123>.
- (21) Xie, F.; Seifert, N. A.; Heger, M.; Thomas, J.; Jäger, W.; Xu, Y. The Rich Conformational Landscape of Perillyl Alcohol Revealed by Broadband Rotational Spectroscopy and

- Theoretical Modelling. *Phys. Chem. Chem. Phys.* **2019**, *21* (28), 15408–15416.  
<https://doi.org/10.1039/C9CP03028J>.
- (22) Wu, B.; Seifert, N. A.; Insausti, A.; Ma, J.; Oswald, S.; Jäger, W.; Xu, Y. 2,2,3,3,3-Pentafluoro-1-Propanol and Its Dimer: Structural Diversity, Conformational Conversion, and Tunnelling Motion. *Phys. Chem. Chem. Phys.* **2022**, *24* (24), 14975–14984.  
<https://doi.org/10.1039/D2CP01895K>.
- (23) Lu, T.; Xie, F.; Seifert, N. A.; Jäger, W.; Xu, Y. Conformational Landscape and Intricate Conformational Relaxation Paths of 4,4,4-Trifluoro-1-Butanol: Rotational Spectroscopy and Quantum Chemical Calculations. *J. Mol. Struct.* **2020**, *1217*, 128359.  
<https://doi.org/10.1016/j.molstruc.2020.128359>.
- (24) Lu, T.; Xie, F.; Seifert, N. A.; Mejlej, R. H.; Jäger, W.; Xu, Y. Binary Conformers of a Flexible, Long-Chain Fluoroalcohol: Dispersion Controlled Selectivity and Relative Abundances in a Jet. *Phys. Chem. Chem. Phys.* **2024**, *26* (14), 10538–10545.  
<https://doi.org/10.1039/D4CP00401A>.
- (25) Thomas, J.; Xu, Y. Chirality Synchronization in Trifluoroethanol Dimer Revisited: The Missing Heterochiral Dimer. *J. Phys. Chem. Lett.* **2014**, *5* (11), 1850–1855.  
<https://doi.org/10.1021/jz500718f>.
- (26) Thomas, J.; Seifert, N. A.; Jäger, W.; Xu, Y. A Direct Link from the Gas to the Condensed Phase: A Rotational Spectroscopic Study of 2,2,2-Trifluoroethanol Trimers. *Angew. Chem. Int. Ed.* **2017**, *56* (22), 6289–6293. <https://doi.org/10.1002/anie.201612161>.
- (27) Xu, Y.; Jäger, W. High Resolution Spectroscopy of Ne and Ar Containing Noble Gas Clusters. *J. Chem. Phys.* **1997**, *107* (13), 4788–4796. <https://doi.org/10.1063/1.474842>.

- (28) Hazrah, A. S.; Insausti, A.; Ma, J.; Al-Jabiri, M. H.; Jäger, W.; Xu, Y. Wetting vs Droplet Aggregation: A Broadband Rotational Spectroscopic Study of 3-Methylcatechol···Water Clusters. *Angew. Chem. Int. Ed.* **2023**, *62* (44), e202310610.  
<https://doi.org/10.1002/anie.202310610>.
- (29) Oswald, S.; Seifert, N. A.; Bohle, F.; Gawrilow, M.; Grimme, S.; Jäger, W.; Xu, Y.; Suhm, M. A. The Chiral Trimer and a Metastable Chiral Dimer of Achiral Hexafluoroisopropanol: A Multi-Messenger Study. *Angew. Chem. Int. Ed.* **2019**, *58* (15), 5080–5084.  
<https://doi.org/10.1002/anie.201813881>.
- (30) Xie, F.; Fusè, M.; Hazrah, A. S.; Jäger, W.; Barone, V.; Xu, Y. Discovering the Elusive Global Minimum in a Ternary Chiral Cluster: Rotational Spectra of Propylene Oxide Trimer. *Angew. Chem. Int. Ed.* **2020**, *59* (50), 22427–22430.  
<https://doi.org/10.1002/anie.202010055>.
- (31) Neese, F.; Wennmohs, F.; Becker, U.; Riplinger, C. The ORCA Quantum Chemistry Program Package. *J. Chem. Phys.* **2020**, *152* (22), 224108.  
<https://doi.org/10.1063/5.0004608>.
- (32) Frisch, M. J.; Trucks, G. W.; Schlegel, H. B.; Scuseria, G. E.; Robb, M. A.; Cheeseman, J. R.; Scalmani, G.; Barone, V.; Petersson, G. A.; Nakatsuji, H.; Li, X.; Caricato, M.; Marenich, A. V.; Bloino, J.; Janesko, B. G.; Gomperts, R.; Mennucci, B.; Hratchian, H. P.; Ortiz, J. V.; Izmaylov, A. F.; Sonnenberg, J. L.; Williams; Ding, F.; Lipparini, F.; Egidi, F.; Goings, J.; Peng, B.; Petrone, A.; Henderson, T.; Ranasinghe, D.; Zakrzewski, V. G.; Gao, J.; Rega, N.; Zheng, G.; Liang, W.; Hada, M.; Ehara, M.; Toyota, K.; Fukuda, R.; Hasegawa, J.; Ishida, M.; Nakajima, T.; Honda, Y.; Kitao, O.; Nakai, H.; Vreven, T.; Throssell, K.; Montgomery Jr., J. A.; Peralta, J. E.; Ogliaro, F.; Bearpark, M. J.; Heyd, J. J.;

- Brothers, E. N.; Kudin, K. N.; Staroverov, V. N.; Keith, T. A.; Kobayashi, R.; Normand, J.; Raghavachari, K.; Rendell, A. P.; Burant, J. C.; Iyengar, S. S.; Tomasi, J.; Cossi, M.; Millam, J. M.; Klene, M.; Adamo, C.; Cammi, R.; Ochterski, J. W.; Martin, R. L.; Morokuma, K.; Farkas, O.; Foresman, J. B.; Fox, D. J. Gaussian 16 Rev. C.01, 2016.
- (33) Becke, A. D. A New Mixing of Hartree–Fock and Local Density-functional Theories. *J. Chem. Phys.* **1993**, *98* (2), 1372–1377. <https://doi.org/10.1063/1.464304>.
- (34) Grimme, S.; Antony, J.; Ehrlich, S.; Krieg, H. A Consistent and Accurate Ab Initio Parametrization of Density Functional Dispersion Correction (DFT-D) for the 94 Elements H-Pu. *J. Chem. Phys.* **2010**, *132* (15), 154104. <https://doi.org/10.1063/1.3382344>.
- (35) Becke, A. D.; Johnson, E. R. A Density-Functional Model of the Dispersion Interaction. *J. Chem. Phys.* **2005**, *123* (15), 154101. <https://doi.org/10.1063/1.2065267>.
- (36) Frisch, M. J.; Pople, J. A.; Binkley, J. S. Self-consistent Molecular Orbital Methods 25. Supplementary Functions for Gaussian Basis Sets. *J. Chem. Phys.* **1984**, *80* (7), 3265–3269. <https://doi.org/10.1063/1.447079>.
- (37) Schäfer, A.; Huber, C.; Ahlrichs, R. Fully Optimized Contracted Gaussian Basis Sets of Triple Zeta Valence Quality for Atoms Li to Kr. *J. Chem. Phys.* **1994**, *100* (8), 5829–5835. <https://doi.org/10.1063/1.467146>.
- (38) Ma, J.; Insausti, A.; Hazrah, A. S.; Xu, Y. Deciphering the Non-Covalent Interactions in the Furan···hexane Complex Using Rotational Spectroscopy and Theoretical Analyses. *J. Chem. Phys.* **2023**, *159* (13), 134302. <https://doi.org/10.1063/5.0166935>.
- (39) Wu, B.; Seifert, N. A.; Oswald, S.; Jäger, W.; Xu, Y. Rotational Spectrum and Molecular Structures of the Binary Aggregates of 1,1,1,3,3,3-Hexafluoro-2-Propanol with Ne and Ar. *J. Phys. Chem. A* **2021**, *125* (24), 5355–5364. <https://doi.org/10.1021/acs.jpca.1c03757>.

- (40) Insausti, A.; Ma, J.; Yang, Q.; Xie, F.; Xu, Y. Rotational Spectroscopy of 2-Furoic Acid and Its Dimer: Conformational Distribution and Double Proton Tunneling. *Chem. Phys. Chem.* **2022**, *23* (12), e202200176. <https://doi.org/10.1002/cphc.202200176>.
- (41) Wu, B.; Hazrah, A. S.; Seifert, N. A.; Oswald, S.; Jäger, W.; Xu, Y. Higher-Energy Hexafluoroisopropanol···Water Isomer and Its Large Amplitude Motions: Rotational Spectra and DFT Calculations. *J. Phys. Chem. A* **2021**, *125* (48), 10401–10409. <https://doi.org/10.1021/acs.jpca.1c09058>.
- (42) Carlson, C. D.; Hazrah, A. S.; Mason, D.; Yang, Q.; Seifert, N. A.; Xu, Y. Alternating 1-Phenyl-2,2,2-Trifluoroethanol Conformational Landscape With the Addition of One Water: Conformations and Large Amplitude Motions. *J. Phys. Chem. A* **2022**, *126* (40), 7250–7260. <https://doi.org/10.1021/acs.jpca.2c05803>.
- (43) Gall, J. T. A.; Thomas, J.; Xie, F.; Wang, Z.; Jäger, W.; Xu, Y. Rotational Spectroscopy of the Methyl Glycidate–Water Complex: Conformation and Water and Methyl Rotor Tunnelling Motions. *Phys. Chem. Chem. Phys.* **2017**, *19* (43), 29508–29515. <https://doi.org/10.1039/C7CP05464E>.
- (44) Pracht, P.; Bohle, F.; Grimme, S. Automated Exploration of the Low-Energy Chemical Space with Fast Quantum Chemical Methods. *Phys. Chem. Chem. Phys.* **2020**, *22* (14), 7169–7192. <https://doi.org/10.1039/C9CP06869D>.
- (45) Bannwarth, C.; Caldeweyher, E.; Ehlert, S.; Hansen, A.; Pracht, P.; Seibert, J.; Spicher, S.; Grimme, S. Extended Tight-Binding Quantum Chemistry Methods. *WIREs Comput. Mol. Sci.* **2021**, *11* (2), e1493. <https://doi.org/10.1002/wcms.1493>.

- (46) Wang, H.; Heger, M.; Al-Jabiri, M. H.; Xu, Y. Vibrational Spectroscopy of Homo- and Heterochiral Amino Acid Dimers: Conformational Landscapes. *Molecules* **2022**, *27* (1), 38. <https://doi.org/10.3390/molecules27010038>.
- (47) Seifert, N. A.; Hazrah, A. S.; Jäger, W. The 1-Naphthol Dimer and Its Surprising Preference for  $\pi$ - $\pi$  Stacking over Hydrogen Bonding. *J. Phys. Chem. Lett.* **2019**, *10* (11), 2836–2841. <https://doi.org/10.1021/acs.jpcclett.9b00646>.
- (48) Fatima, M.; Steber, A. L.; Poblitzki, A.; Pérez, C.; Zinn, S.; Schnell, M. Rotational Signatures of Dispersive Stacking in the Formation of Aromatic Dimers. *Angew. Chem.* **2019**, *131* (10), 3140–3145. <https://doi.org/10.1002/ange.201812556>.
- (49) Johnson, E. R.; Keinan, S.; Mori-Sánchez, P.; Contreras-García, J.; Cohen, A. J.; Yang, W. Revealing Noncovalent Interactions. *J. Am. Chem. Soc.* **2010**, *132* (18), 6498–6506. <https://doi.org/10.1021/ja100936w>.
- (50) Boys, S. F.; Bernardi, F. The Calculation of Small Molecular Interactions by the Differences of Separate Total Energies. Some Procedures with Reduced Errors. *Mol. Phys.* **1970**, *19* (4), 553–566. <https://doi.org/10.1080/00268977000101561>.
- (51) Parker, T. M.; Burns, L. A.; Parrish, R. M.; Ryno, A. G.; Sherrill, C. D. Levels of Symmetry Adapted Perturbation Theory (SAPT). I. Efficiency and Performance for Interaction Energies. *J. Chem. Phys.* **2014**, *140* (9), 094106. <https://doi.org/10.1063/1.4867135>.
- (52) Bader, R. F. W. A Quantum Theory of Molecular Structure and Its Applications. *Chem. Rev.* **1991**, *91* (5), 893–928. <https://doi.org/10.1021/cr00005a013>.

- (53) Matta, C. F.; Boyd, R. J. An Introduction to the Quantum Theory of Atoms in Molecules. In *The Quantum Theory of Atoms in Molecules*; John Wiley & Sons, Ltd, 2007; pp 1–34.  
<https://doi.org/10.1002/9783527610709.ch1>.
- (54) Koch, U.; Popelier, P. L. A. Characterization of C-H-O Hydrogen Bonds on the Basis of the Charge Density. *J. Phys. Chem.* **1995**, *99* (24), 9747–9754.  
<https://doi.org/10.1021/j100024a016>.
- (55) Mata, I.; Alkorta, I.; Espinosa, E.; Molins, E. Relationships between Interaction Energy, Intermolecular Distance and Electron Density Properties in Hydrogen Bonded Complexes under External Electric Fields. *Chem. Phys. Lett.* **2011**, *507* (1), 185–189.  
<https://doi.org/10.1016/j.cplett.2011.03.055>.
- (56) Lane, J. R.; Contreras-García, J.; Piquemal, J.-P.; Miller, B. J.; Kjaergaard, H. G. Are Bond Critical Points Really Critical for Hydrogen Bonding? *J. Chem. Theory Comput.* **2013**, *9* (8), 3263–3266. <https://doi.org/10.1021/ct400420r>.
- (57) Gordy, W.; Cook, R. L. *Microwave Molecular Spectra*; Wiley: New York, 1970.
- (58) Townes, C. H.; Schawlow, A. L. *Microwave Spectroscopy*; Courier Corporation, 2013.
- (59) Brown, G. G.; Dian, B. C.; Douglass, K. O.; Geyer, S. M.; Shipman, S. T.; Pate, B. H. A Broadband Fourier Transform Microwave Spectrometer Based on Chirped Pulse Excitation. *Rev. Sci. Instrum.* **2008**, *79* (5), 053103. <https://doi.org/10.1063/1.2919120>.
- (60) Seifert, N. A.; Thomas, J.; Jäger, W.; Xu, Y. Rotational Spectra and Theoretical Study of Tetramers and Trimers of 2-Fluoroethanol: Dramatic Intermolecular Compensation for Intramolecular Instability. *Phys. Chem. Chem. Phys.* **2018**, *20* (43), 27630–27637.  
<https://doi.org/10.1039/C8CP05653F>.

- (61) Carlson, C. D.; Seifert, N. A.; Heger, M.; Xie, F.; Thomas, J.; Xu, Y. Conformational Dynamics of 1-Phenyl-2,2,2-Trifluoroethanol by Rotational Spectroscopy and *Ab Initio* Calculations. *J. Mol. Spectrosc.* **2018**, *351*, 62–67.  
<https://doi.org/10.1016/j.jms.2018.07.006>.
- (62) Pérez, C.; Lobsiger, S.; Seifert, N. A.; Zaleski, D. P.; Temelso, B.; Shields, G. C.; Kisiel, Z.; Pate, B. H. Broadband Fourier Transform Rotational Spectroscopy for Structure Determination: The Water Heptamer. *Chem. Phys. Lett.* **2013**, *571*, 1–15.  
<https://doi.org/10.1016/j.cplett.2013.04.014>.
- (63) Xie, F.; Seifert, N. A.; Jäger, W.; Xu, Y. Conformational Panorama and Chirality Controlled Structure–Energy Relationship in a Chiral Carboxylic Acid Dimer. *Angew. Chem. Int. Ed.* **2020**, *59* (36), 15703–15710. <https://doi.org/10.1002/anie.202005685>.
- (64) Borho, N.; Xu, Y. Molecular Recognition in 1 : 1 Hydrogen-Bonded Complexes of Oxirane and Trans-2,3-Dimethyloxirane with Ethanol: A Rotational Spectroscopic and *Ab Initio* Study. *Phys. Chem. Chem. Phys.* **2007**, *9* (32), 4514–4520.  
<https://doi.org/10.1039/B705746F>.
- (65) Xie, F.; Ng, X.; Seifert, N. A.; Thomas, J.; Jäger, W.; Xu, Y. Rotational Spectroscopy of Chiral Tetrahydro-2-Furoic Acid: Conformational Landscape, Conversion, and Abundances. *J. Chem. Phys.* **2018**, *149* (22), 224306. <https://doi.org/10.1063/1.5063683>.

# 3

## Rotational Spectroscopic Studies of *para*-Nitrobenzoic acid, *para*-Aminobenzoic acid, *para*-Chlorobenzoic acid, and *para*-Hydroxybenzoic acid

### 3.1. Introduction

Benzoic acid, the simplest stable aromatic carboxylic acid, is naturally present in plant and animal tissues.<sup>1</sup> It is also one of the most common organic acids in Earth's atmosphere and plays an important role in atmospheric chemistry, for example as an anthropogenic precursor to secondary organic aerosol formation.<sup>2-4</sup> In general, benzoic acid and its derivatives are widely used for the production of a range of products from antimicrobial food preservatives, pharmaceuticals, to insect repellents.<sup>1,5-7</sup> For example, *para*-hydroxybenzoic acid has antibacterial and antifungal properties,<sup>8</sup> while OH substitution at the *ortho* position gives salicylic acid, a precursor for many anti-inflammatory drugs.<sup>9</sup> Other examples of the many singly substituted benzoic acid derivatives with varying functionalities include *para*-aminobenzoic acid, a topical agent for sunburn prevention,<sup>10</sup> *para*-nitrobenzoic acid, an anesthetic drug precursor,<sup>11</sup> and *para*-chlorobenzoic acid, a hydroxyl radical probe.<sup>12</sup>

Due to its importance, benzoic acid has been the subject of many rotational,<sup>13,14</sup> vibrational,<sup>15</sup> and electronic<sup>16</sup> spectroscopic studies. In this paper, we describe our rotational

spectroscopic and theoretical investigation of four different substituted benzoic acids, i.e., *para*-aminobenzoic acid (*p*-aminoBA), *para*-nitrobenzoic acid (*p*-nitroBA), *para*-chlorobenzoic acid (*p*-chloroBA), and *para*-hydroxybenzoic acid (*p*-hydroxyBA) (see Figure 3.1). While *p*-aminoBA,<sup>17,18</sup> *p*-nitroBA,<sup>19</sup> *p*-chloroBA,<sup>20</sup> and *p*-hydroxyBA<sup>21</sup> have been investigated in the condensed phase using infrared and Raman spectroscopy, no high resolution spectroscopic studies have been reported for any of them. One motivation to study these benzoic acid derivatives is to examine conformational distributions and how different substituents influence local electronic properties in these four molecules. Jet-cooled chirped-pulse Fourier transform microwave (CP-FTMW) spectroscopy is well suited for this purpose.<sup>22</sup> In particular, one can obtain not only experimentally determined rotational constants which are markers of particular structures and conformers but also hyperfine constants, such as nuclear quadrupole coupling constants which contain information about the local electronic/chemical environment of a quadrupolar nucleus. Furthermore, we have on-going interest in how the substitution in the *para* position of benzoic acid will influence the double proton tunneling in binary complexes of substituted benzoic acids and if these changes can be modelled using Jacobi field instanton theory.<sup>23,24</sup> To achieve that goal, a detailed characterization of the monomeric species is an important first step.

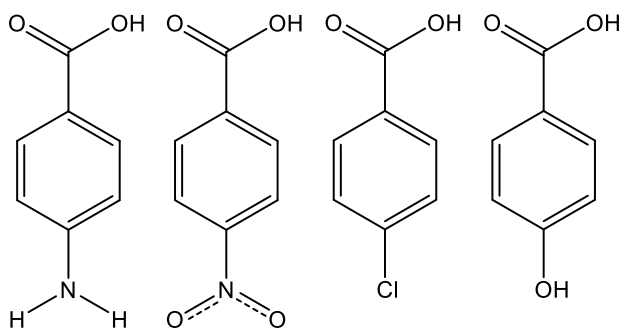


**Figure 3.1.** The four para-substituted benzoic acids studied here: *p*-aminoBA, *p*-nitroBA, *p*-chloroBA, and *p*-hydroxyBA.

## 3.2. Methods

### 3.2.1. Computational details

The electronic structure calculations, optimizations, and frequency calculations were done using the Gaussian16 program suite.<sup>25</sup> Chemical intuition and reasonable structural parameters were used to construct initial trial geometries which were then optimized at the B3LYP-D3BJ/def2-TZVP level of theory.<sup>26</sup> In some instances, nuclear quadrupole coupling constants calculated at the B3LYP-D3BJ/def2-TZVPD level of theory did not agree well with the experimental values and the B2PLYP-D3BJ/cc-pCVTZ level of theory was used instead.<sup>27</sup> Frequency calculations were used to confirm the prediction of minima through the absence of imaginary vibrational frequencies. For each species two or more minima were identified. To map the trajectories between minima and locate the transition states, we applied the nudged elastic band (NEB) method,<sup>28</sup> which has been used recently to explore large amplitude motions and tunnelling paths in a water containing complex.<sup>29</sup> The NEB calculations were performed at the B3LYP-D3BJ/def2-TZVPD level of theory using the ORCA software.<sup>30</sup> In one instance an intrinsic reaction coordinate (IRC) calculation was performed, using Gaussian 16, to better trace the shape of the barrier. The transition states identified were then further optimized at the B3LYP-

D3BJ/def2-TZVP or B2PLYP-D3BJ/cc-pCVTZ level using the Berny algorithm in Gaussian16 and confirmed to be transition states by the frequency calculations. Additionally, Multiwfn<sup>31</sup> was used to determine values for minima on the molecular electrostatic potential surface and calculate Mayer bond order<sup>32</sup> indices. Finally, we utilized both Western's Pgopher program<sup>33</sup> and Pickett's SPCAT/SPFIT<sup>34</sup> suite for spectral simulations to aid the assignments and also for the final spectroscopic fitting procedures.

### 3.2.2. Experiments

The rotational spectra of *p*-aminoBA, *p*-nitroBA, *p*-chloroBA, and *p*-hydroxyBA were measured using a 2 to 6 GHz chirp-pulse Fourier transform microwave spectrometer<sup>35</sup> that is based on the design by Pate and co-workers.<sup>36</sup> A 12 GS/s arbitrary waveform generator is used to generate a 1  $\mu$ s chirp pulse in the 2-6 GHz range which is then amplified by a traveling wave tube amplifier and broadcasted into the vacuum chamber by a transmitting horn antenna. The excitation pulse intercepts a molecular beam perpendicularly and the subsequent free induction decays (FIDs) were detected by a receiving horn antenna, which faces the broadcasting antenna, digitized using a 25 GS/s oscilloscope, averaged, and finally Fourier transformed to obtain the spectrum.

The substituted benzoic acid sample was placed in a reservoir inside a custom-built nozzle cap<sup>37</sup> of a General Valve, Series 9, pulsed nozzle and heated to 170°C in all cases to achieve a sufficient vapour pressure. Helium was used as a carrier gas at a backing pressure of 280 kPa in all cases. Twelve 20  $\mu$ s long FIDs were recorded per molecular pulse. A total of 711k, 692k, 643k, and 631k FIDs were acquired for *p*-aminoBA, *p*-nitroBA, *p*-chloroBA, and *p*-hydroxyBA, respectively.

### 3.3. Results and Discussion

#### 3.3.1. Computational Results

In total, 2, 2, 2, and 4 conformers were identified theoretically for *p*-aminoBA, *p*-nitroBA, *p*-chloroBA, and *p*-hydroxyBA, respectively. The associated spectroscopic constants and relative energies are summarized in Table 3.1. In all four molecular systems, the global minimum structure possesses a *cis*-conformation of the carboxylic acid group (see Figure 3.2); the calculated rotational constants, nuclear quadrupole coupling constants, and dipole moment components are given in Table 3.2 for *cis-p*-aminoBA and *cis-p*-nitroBA, Table 3.3 for *cis-p*-<sup>35</sup>chloroBA and *cis-p*-<sup>37</sup>chloroBA, and Table 3.4 for *cis-p*-hydroxyBA-I and *cis-p*-hydroxyBA-II. A dominant *cis*-conformation of the carboxylic group has also been found in benzoic acid,<sup>13</sup> *para*- and *ortho*-toluic acid,<sup>38,39</sup> and vanillic acid,<sup>40</sup> whereas a preference for the *trans*-conformation, supported by an intramolecular COOH $\cdots$ O bond, was reported for tetrahydro-2-furoic acid<sup>41</sup> and *o*-anisic acid.<sup>42</sup> In proline<sup>43</sup> and glutamine,<sup>44</sup> the *trans*-conformation has been shown to be stabilized by a COOH $\cdots$ N intramolecular interaction. The *trans*-conformers of the four acids studied here are separated from the respective *cis*-conformers by an interconversion barrier of about 20 kJ mol<sup>-1</sup>. See Figure 3.3 for *p*-nitroBA and Figures 3.4, 3.5, 3.6, and 3.7 for the other cases. The relatively high barrier prevents conformational cooling in the molecular expansion,<sup>45</sup> but the relative population of the *trans*-conformer at the source temperature (170 °C) is calculated to be only 0.2%, which is too low to be detectable in our experiments. For the *cis*-conformers, all atoms are in one plane, except the H-atoms of the amino group in *p*-aminoBA. For the *trans*-conformers, the carboxylic acid groups are pushed slightly out-of-plane (see Figure 3.8) so that there is a rather flat ( $\sim 1$  kJ mol<sup>-1</sup>) local maximum at the planar *trans*-conformation (see Figure 3.3).

**Table 3.1.** Sum of electronic energy and zero-point energy relative to the lowest energy conformer and their rotational constants, dipole moments, and nuclear hyper fine quadrupole coupling constants for the cis-trans isomers of *p*-chloroBA, *p*-aminoBA, *p*-nitroBA, *p*-hydroxyBA and at the B3LYP-D3BJ/def2-TZVP level of theory.

	$\Delta E_0^a$ / kJ mol <sup>-1</sup>	$\Delta G_0^b$ / kJ mol <sup>-1</sup>	<i>A</i> / MHz	<i>B</i> / MHz	<i>C</i> / MHz	$ \mu_a $ / Debye	$ \mu_b $ / Debye	$ \mu_c $ / Debye	$\chi_{aa}$ / MHz	$\chi_{bb}-\chi_{cc}$ / MHz
<i>cis-p</i> - <sup>35</sup> chloroBA	0	0	3892.4	554.6	485.4	0	1.4	0	-75.1	8.9
<i>trans-p</i> - <sup>35</sup> chloroBA	26.2	24.9	3858.2	551.9	486.4	2.7	2.3	0.8	-75.6	8.6
<i>cis-p</i> - <sup>37</sup> chloroBA	0	0	3892.4	541.2	475.1	0	1.4	0	-59.2	7.0
<i>trans-p</i> - <sup>37</sup> chloroBA	26.2	25.0	3858.2	538.6	476.0	2.7	2.3	0.8	-59.6	6.7
<i>cis-p</i> -aminoBA	0	0	3860.3	795.7	660.0	3.9	1.4	0.8	2.5	6.9
<i>trans-p</i> -aminoBA	25.0	23.8	3827.2	791.7	660.5	6.5	2.3	0.1	2.5	6.8
<i>cis-p</i> -nitroBA	0	0	3014.1	474.5	409.9	3.3	1.4	0	-1.2	-1.1
<i>trans-p</i> -nitroBA	27.1	26.2	2991.1	472.0	411.5	0.6	2.2	0.9	-1.2	-1.0
<i>cis-p</i> -hydroxyBA-I	0	0	3877.8	793.8	658.9	2.0	0.1	0	–	–
<i>trans-p</i> -hydroxyBA-I	25.3	24.0	3844.7	789.4	659.7	4.6	1.0	0.8	–	–
<i>cis-p</i> -hydroxBA-II	0	0	3877.7	793.7	658.8	2.0	2.7	0	–	–
<i>trans-p</i> -hydroxyBA-II	26.1	24.8	3843.9	789.0	660.0	4.6	3.6	0.6	–	–

<sup>a</sup> Sum of electronic and zero-point energy relative to the lowest energy conformer.

<sup>b</sup> Sum of Gibbs free energy and electronic energy relative to the lowest energy conformer

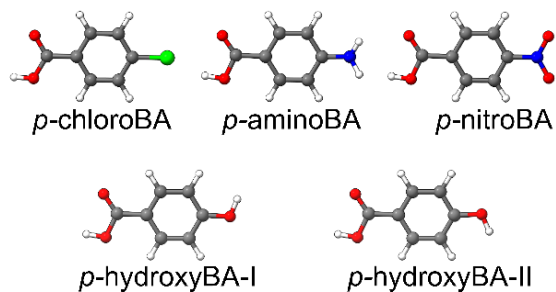


**Figure 3.2.** Geometries of the lowest energy conformers of *cis-p*-chloroBA, *cis-p*-aminoBA, *cis-p*-nitroBA, and *cis-p*-hydroxyBA at the B3LYP-D3BJ/def2-TZVP level of theory. *p*-hydroxyBA-II is only 0.2 kJ mol<sup>-1</sup> higher in energy than *p*-hydroxyBA-I.

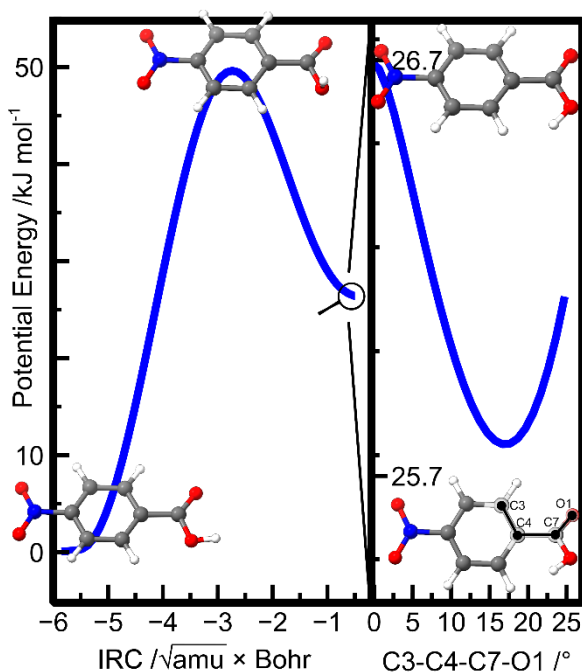


**Figure 3.3.** Intrinsic reaction coordinate (IRC) of the *cis-trans* conversion in *p*-nitroBA calculated at the B3LYP-D3BJ/def2-TZVP level of theory. In regions of shallow potential where an IRC computation was not feasible, a relaxed dihedral scan was conducted. The zero-point energy corrected interconversion barrier from *trans*- to the *cis-p*-aminoBA is about 20 kJ mol<sup>-1</sup>.

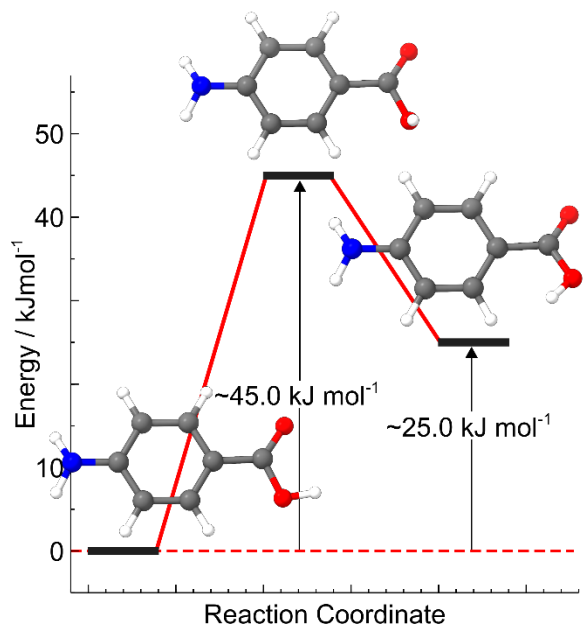


**Figure 3.4.** Barrier to interconversion from cis to trans of the *p*-aminoBA carboxylic acid group at the B3LYP-D3BJ/def2-TZVP level of theory.

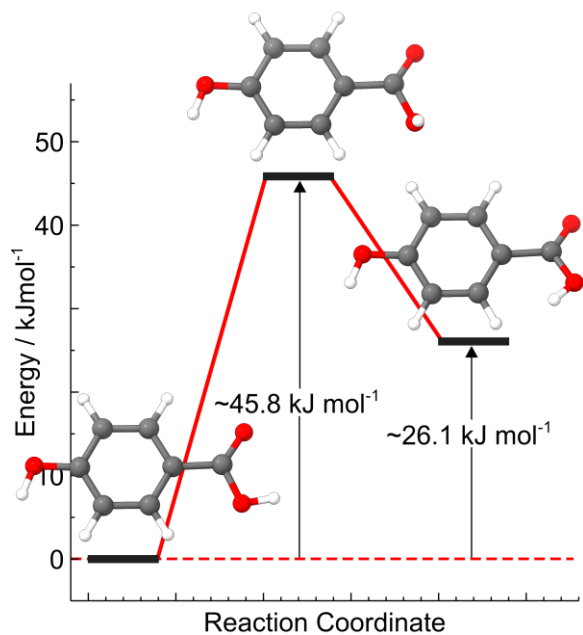


**Figure 3.5.** Barrier to interconversion from cis to trans of the *p*-hydroxyBA-II carboxylic acid group at the B3LYP-D3BJ/def2-TZVP level of theory.

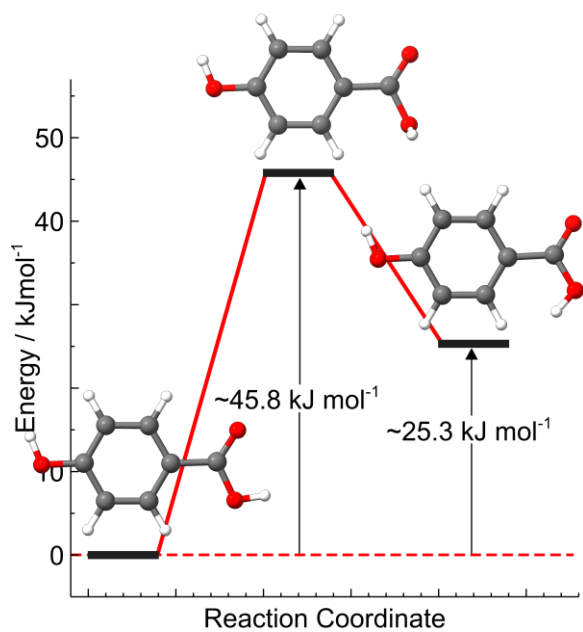


**Figure 3.6.** Barrier to interconversion from cis to trans of the *p*-hydroxyBA-I carboxylic acid group at the B3LYP-D3BJ/def2-TZVP level of theory.

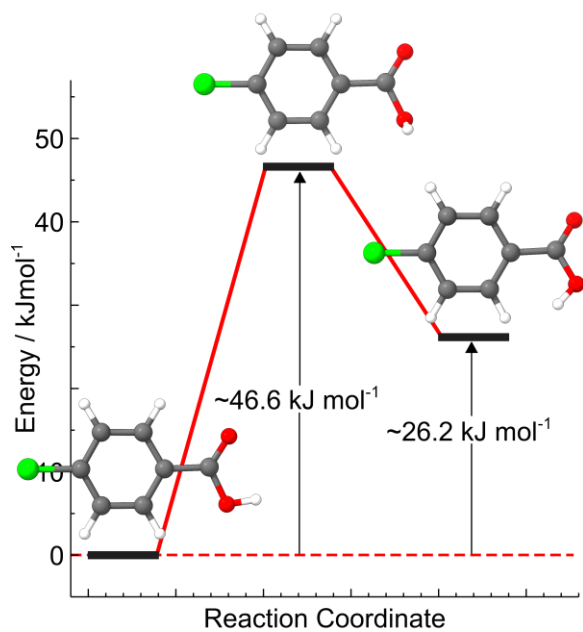


**Figure 3.7.** Barrier to interconversion from cis to trans of the *p*-<sup>35</sup>chloroBA carboxylic acid group at the B3LYP-D3BJ/def2-TZVP level of theory.

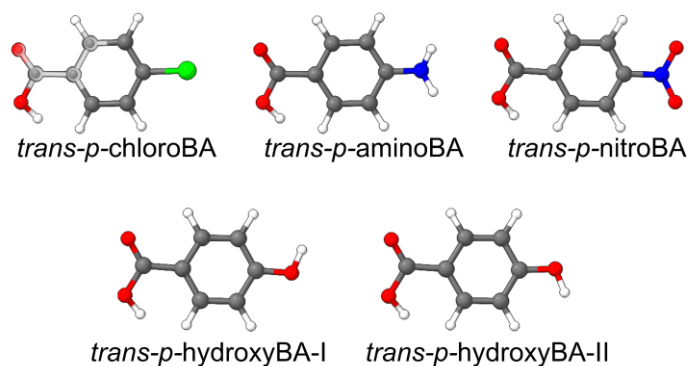


**Figure 3.8.** Stable conformations of *trans* carboxylic acid of *p*-chloroBA, *p*-aminoBA, *p*-nitroBA, and *p*-hydroxyBA computed at the B3LYP-D3BJ/def2-TZVP level of theory.

### 3.3.2. Experimental Results

The rotational quantum number assignments were straightforward because of the high quality B3LYP-D3BJ/def2-TZVP predicted rotational constants which were found to be less than 1% off those derived from the experimental data. Watson's S-reduction Hamiltonian<sup>46</sup> in its  $I'$  representation was used to fit the rotational constants to the experimental transition frequencies. We were not able to determine any centrifugal distortion constants as a result of the relative rigidity of the molecules and the relatively low J-quantum numbers of the observed transitions. The experimental rotational constants are collected and compared to the corresponding calculated values in Table 3.2 for *cis-p*-aminoBA and *cis-p*-nitroBA, Table 3.3 for *cis-p*-<sup>35</sup>chloroBA and *cis-p*-<sup>37</sup>chloroBA, and Table 3.4 for *cis-p*-hydroxyBA-I and *cis-p*-hydroxyBA-II. No rare isotopologues except those with <sup>35</sup>Cl and <sup>37</sup>Cl of *cis-p*-chloroBA were identified in this study because of the low volatility of the samples and the resulting low signal-to-noise ratio in the experimental spectra. Below, we describe the interesting specifics to each of the substituted benzoic acids studied here.

### 3.3.3. *p*-aminoBA

All atoms of *cis-p*-aminoBA, except the two hydrogen atoms of the amino group, are in one plane. Two equivalent equilibrium structures related to the position of the hydrogen atoms on one side or the other with respect to the molecular plane exist, suggesting the possibility of an inversion tunnelling motion similar to the cases of aniline<sup>47,48</sup> and *N,N*-dimethylaniline.<sup>49</sup> The rotational spectrum and the assigned transitions of *p*-aminoBA are given in Figure 3.9 and Table A.1 of the Appendix A (A), respectively. Experimentally, no tunnelling splittings were observed in the rotational transitions, similar to the case of *para*-aminobenzonitrile<sup>50</sup> and several ester derivatives of *para*-aminobenzoic acid.<sup>51</sup> To gain further insight into the energy profile along the NH<sub>2</sub> wagging coordinate, a NEB calculation was employed to find the transition state. The planar transition state structure identified was optimized and its zero-point corrected energy was found to be 0.8 kJ mol<sup>-1</sup> below that of the minimum energy structure (see Figure 3.10). This means that the NH<sub>2</sub> wagging motion is a barrierless large amplitude motion, rather than a tunnelling motion. As a result, the  $\mu_c$  dipole moment component averages out, and *c*-type transitions could not be observed. In an analogous computational procedure for aniline we found a 0.7 kJ mol<sup>-1</sup> barrier to the NH<sub>2</sub> wagging motion, consistent with the observation of tunnelling splittings in the experimental spectra.<sup>47,48</sup> Splitting of rotational transitions due to the <sup>14</sup>N nuclear quadrupole moment could be resolved, and were analysed to yield <sup>14</sup>N nuclear quadrupole coupling constants which are given in Table 3.2. The theoretical values of the <sup>14</sup>N nuclear quadrupole coupling constants are within 15 % of the experimental constants. Calculation of the <sup>14</sup>N nuclear quadrupole coupling constants at the B2PLYP-D3BJ/cc-pCVTZ level (see the next section, *p*-nitroBA, for details) improved the agreement marginally (Table 3.2). Note that the

theoretical values are for the calculated equilibrium geometry and were not averaged over the  $\text{NH}_2$  large amplitude wagging motion.

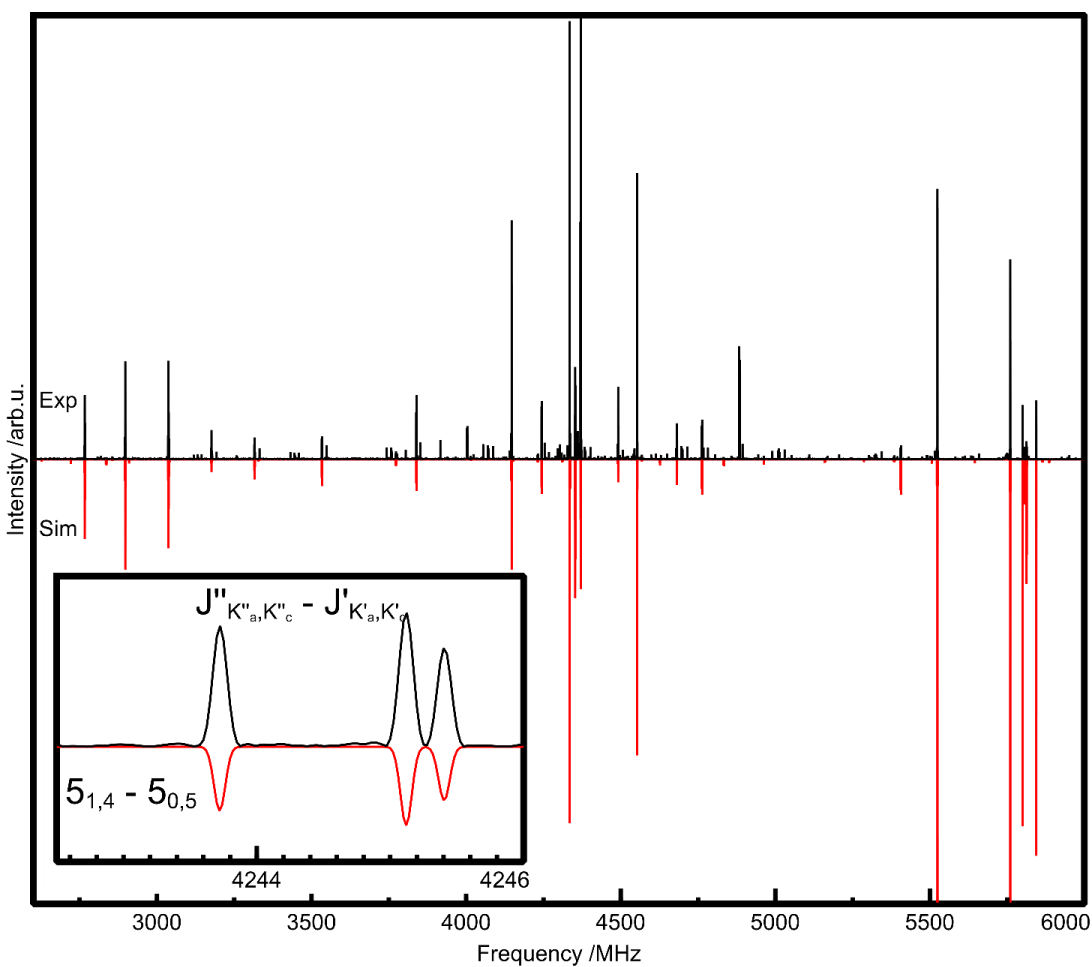


**Figure 3.9.** Experimental (top) and simulated (bottom) spectrum of *p*-aminoBA. The simulated spectrum was obtained using calculated rotational constants, dipole moments, and  $\text{N}^{14}$  nuclear quadrupole coupling constants.

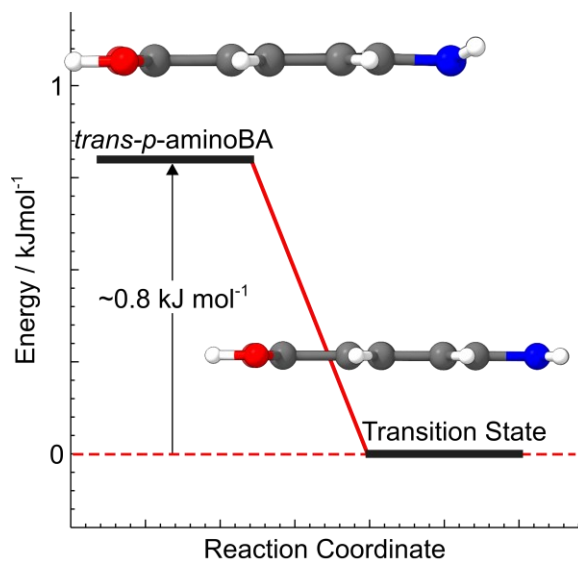


**Figure 3.10.** Barrier to inversion of the amino group of the *cis-p*-aminoBA monomer at the B3LYP-D3BJ/def2-TZVP level of theory.

### 3.3.4. *p*-nitroBA

For *cis-p*-nitroBA, all atoms are in the same plane in the equilibrium structure. A similar planar nitro-conformation was also reported for nitrobenzene,<sup>52</sup> and the nitro-conformation is known to only deviate from its planarity in the presence of bulky adjacent functional groups.<sup>53</sup> The barrier for internal rotation of the nitro group about its  $C_2$  axis was calculated to be  $19.9 \text{ kJ mol}^{-1}$  (see Figure 3.11), much too high to cause an observable tunnelling splitting in the rotational spectrum. The rotational spectrum and assigned transitions are given in Figure 3.12 and Table A.2 of the Appendix A, respectively. The experimental  $^{14}\text{N}$  nuclear quadrupole coupling constants are given in Table 3.2, together with their calculated values. Interestingly, the deviation between calculated and experimental  $\chi_{bb} - \chi_{cc}$  is  $> 120 \%$ . The experimental  $\chi_{aa}$ ,  $\chi_{bb}$ , and  $\chi_{cc}$  values determined here for *cis-p*-nitroBA are within 10% of those of related systems, such as nitrobenzene<sup>54</sup> and *p*-nitroanisole.<sup>55</sup> In addition, the  $^{14}\text{N}$  nuclear quadrupole coupling constants of *p*-nitroanisole at the B3LYP-D3BJ/def2-TZVP level show similar discrepancies to the

experimental values as in the case of *cis-p*-nitroBA studied here. We also performed the corresponding calculations for nitrobenzene and a similar picture emerged. Difficulties in calculating the  $^{14}\text{N}$  nuclear quadrupole coupling constants in substituted nitrobenzenes were noted before,<sup>56,57</sup> and can be attributed to electron delocalization involving the nitro group. The double-hybrid functional B2PLYP with long-range dispersion corrections has been shown to provide high accuracy for many chemically relevant properties.<sup>58</sup> For example, the infrared frequency pattern of a steroid containing multiple C=O and C=C double bonds was predicted correctly by using the double hybrid B2PLYP functional whereas the B3LYP functional failed.<sup>59</sup> We therefore calculated the  $^{14}\text{N}$  nuclear quadrupole coupling constants at the B2PLYP-D3BJ/cc-pCVTZ level, as also suggested in Ref. <sup>56</sup>. The B2PLYP results are summarized in Table 3.2 and agree with the experimental coupling constants now within tens of kHz; for example, the deviation for  $\chi_{\text{bb}} - \chi_{\text{cc}}$  is now only about 70 kHz (~15 %).

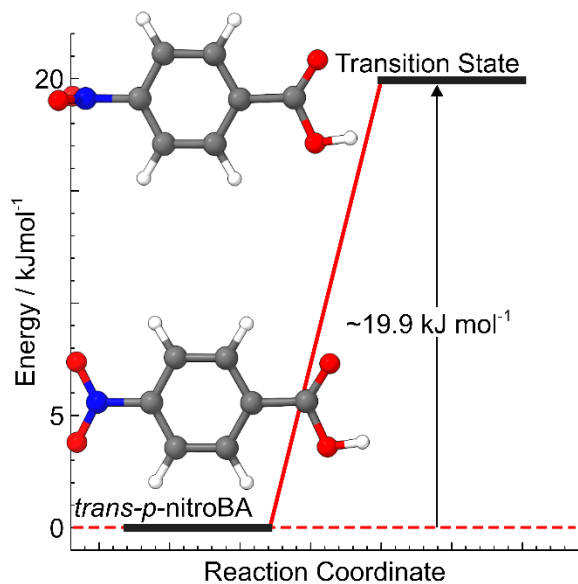


**Figure 3.11.** Barrier to nitro internal rotation in *cis-p*-nitroBA monomer at the B3LYP-D3BJ/def2-TZVP level of theory.

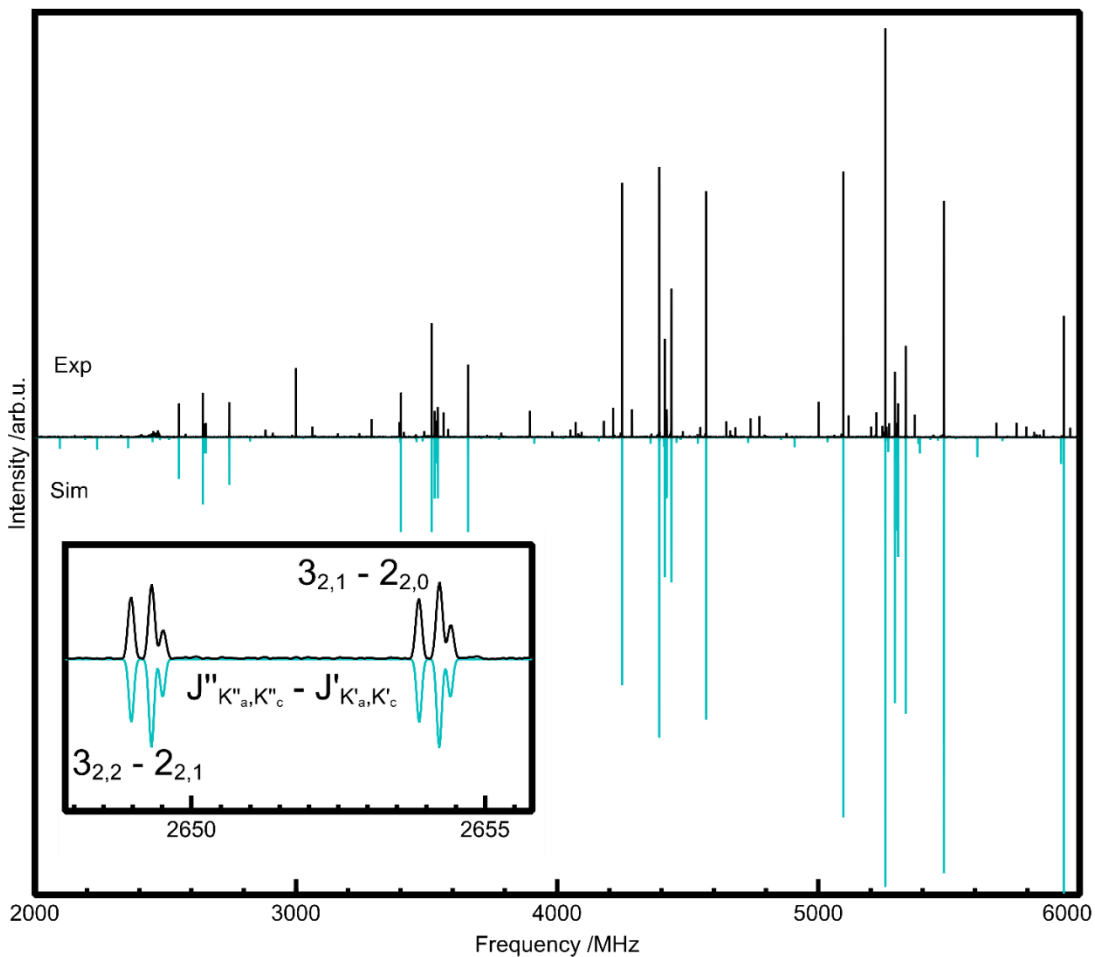


**Figure 3.12.** Experimental (top) and simulated (bottom) spectrum of *p*-nitroBA. The simulated spectrum was obtained using calculated rotational constants, dipole moments, and N<sup>14</sup> nuclear quadrupole coupling constants.

**Table 3.2.** Experimental spectroscopic parameters and those computed at the B3LYP-D3BJ/def2-TZVP and B2PLYP-D3BJ/def2-TZVP levels of theory for *cis-p*-aminoBA and *cis-p*-nitroBA.

	<i>cis-p</i> -aminoBA			<i>cis-p</i> -nitroBA		
	B3LYP	B2PLYP	Experiment	B3LYP	B2PLYP	Experiment
<i>A</i> /MHz	3860.3	3856.7	3833.8376(5)	3014.1	3001.7	2987.2012(6)
<i>B</i> /MHz	795.7	795.1	793.20495(9)	474.5	474.6	473.79165(8)

$C$ /MHz	659.9	659.5	657.79676(9)	409.9	409.8	409.28824(8)
$\chi_{aa}$ /MHz	2.45	2.41	2.430(2)	-1.24	-1.04	-1.093(3)
$\chi_{bb}-\chi_{cc}$ /MHz	7.05	6.71	6.17(1)	-1.07	-0.35	-0.471(5)
$ \mu_a ,  \mu_b ,  \mu_c $ /D	3.9, 1.4, 0.8	3.5, 1.4, 0.9	$ \mu_a  >  \mu_b , \mu_c$ not obs. <sup>a</sup>	3.4, 1.4, 0.0	3.1, 1.3, 0.0	$ \mu_a  >  \mu_b , \mu_c$ not obs. <sup>a</sup>
$N^b$	-	-	82	-	-	76
$\sigma^c$ /kHz	-	-	3.9	-	-	5.9

<sup>a</sup> Relative magnitudes of dipole moment components, estimated from signal strengths.

<sup>b</sup> Total number of transitions used in the fit. <sup>c</sup> Standard deviation of the fit.

### 3.3.5. *p*-chloroBA

The rotational spectrum of both the  $^{35}\text{Cl}$  and  $^{37}\text{Cl}$  isotopologues is provided in Figure 3.13, where the inset shows the nuclear quadrupole hyperfine splittings of the  $J_{K_a, K_c}=4_{1,3}-4_{0,4}$  transitions. The assigned rotational transitions can be found in Tables A.3 and A.4. The chlorine nuclear quadrupole hyperfine structures of the  $^{35}\text{Cl}$  and  $^{37}\text{Cl}$  isotopologues could be resolved and were analysed. The experimental Cl nuclear quadrupole coupling constants are given in Table 3.3, staying within 33% of the values from the B3LYP-D3BJ/def2-TZVP calculations. Calculations at the B2PLYP-D3BJ/def2-TZVP level improve the agreement with experiment markedly to within 8% (see Table 3.3). The Cl nuclear quadrupole coupling constants may be compared to those of chlorobenzene, being -71.2359(13), 38.2153(15), 33.0205(15) and -56.1445(16), 30.1200(27), 26.0244(27) for  $\chi_{aa}$ ,  $\chi_{bb}$ , and  $\chi_{cc}$  of  $^{35}\text{Cl}$  and  $^{37}\text{Cl}$  chlorobenzene, respectively.<sup>60</sup> We compare the  $\chi_{cc}$  constants since the *c*-inertial axes are perpendicular to the molecular plane in both *cis-p*-chloroBA and chlorobenzene and find that they differ by less than 2 %, an indication that the electronic structure at the Cl nucleus is only slightly affected by the carboxyl group in the *para* position.

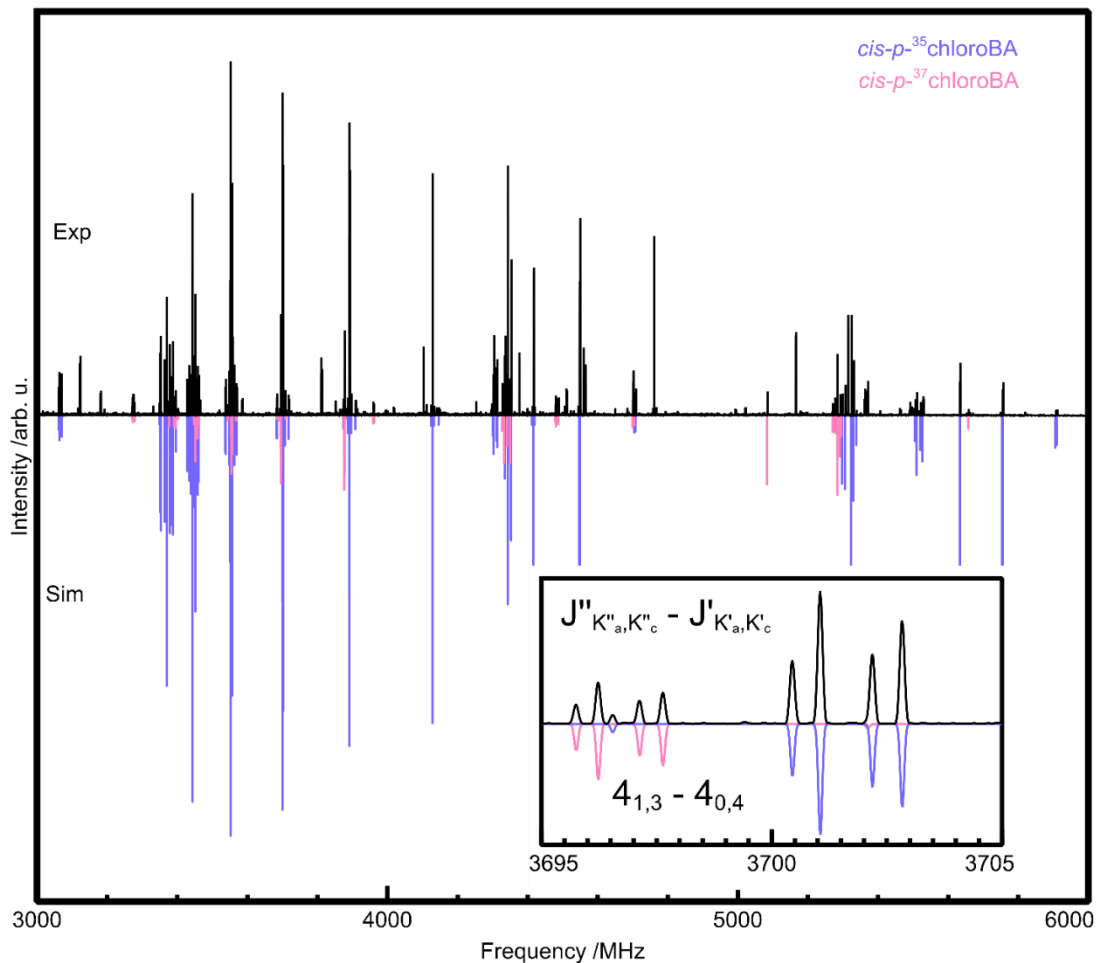


**Figure 3.13.** Experimental (top) simulated (bottom) spectrum of *p*-chloroBA. The simulated spectrum was obtained using calculated rotational constants, dipole moments, and  $N^{14}$  nuclear quadrupole coupling constants.

**Table 3.3.** Experimental spectroscopic parameters of *cis-p*- $^{35}$ chloroBA and *cis-p*- $^{37}$ chloroBA and those computed at the B3LYP-D3BJ/def2-TZVP and B2PLYP-D3BJ/def2-TZVP levels of theory.

	<i>cis-p</i> - $^{35}$ chloroBA			<i>cis-p</i> - $^{37}$ chloroBA		
	B3LYP	B2PLYP	Experiment	B3LYP	B2PLYP	Experiment
$A$ /MHz	3892.4	3886.2	3860.8602(4)	3892.4	3886.2	3860.8374(4)

$B$ /MHz	554.6	554.7	554.75032(7)	541.1	541.3	541.3831(1)
$C$ /MHz	485.4	485.4	485.2542(1)	475.1	475.1	474.99536(9)
$\chi_{aa}$ /MHz	-75.08	-72.22	-71.445(3)	-59.17	-56.92	-56.321(4)
$\chi_{bb}-\chi_{cc}$ /MHz	8.93	7.22	6.705(6)	7.04	5.69	5.278(6)
$ \mu_a ,  \mu_b ,  \mu_c $ /D	0.0, 1.4, 0.0	0.2, 1.3, 0.0	only $\mu_b$ obs.	0.0, 1.4, 0.0	0.2, 1.3, 0.0	only $\mu_b$ obs.
$N^a$	-	-	103	-	-	58
$\sigma^b$ /kHz	-	-	3.9	-	-	3.6

<sup>a</sup> Total number of transitions used in the fit.

<sup>b</sup> Standard deviation of the fit.

### 3.3.6. *p*-hydroxyBA

There are two low energy conformers of *cis-p*-hydroxyBA which differ by the orientation of the *para*-substituted hydroxyl group (Figure 3.2) and are labelled I and II, according to their relative energy ordering. The higher energy conformer, *cis-p*-hydroxyBA-II, has the hydrogen of the hydroxyl group pointing in the opposite direction of the carbonyl group and is 0.2 kJ mol<sup>-1</sup> higher in energy. A rotation of the *para*-positioned hydroxyl group of *cis-p*-hydroxyBA-II by 180° leads to *cis-p*-hydroxyBA-I with a barrier of 17.5 kJ mol<sup>-1</sup>. The conversion from *cis-p*-hydroxyBA-II to *cis-p*-hydroxyBA-I can also result from a rotation of the carboxylic acid group by 180° which has a barrier of 31.8 kJ mol<sup>-1</sup>. The results are summarized in Figures 3.14 and 3.15. The large conformational conversion barrier leads to negligible conformational cooling in the supersonic jet expansion and both conformers could be observed in the experimental spectrum. The Boltzmann population ratios based on the relative free energies and the source temperature of 170 °C are 51.5 % and 48.5 % for *cis-p*-hydroxyBA-I and -II, respectively. From experiment we

find similar abundances of both conformers, in agreement with the very low value of the calculated relative energy and the high barrier to conformational interconversion.

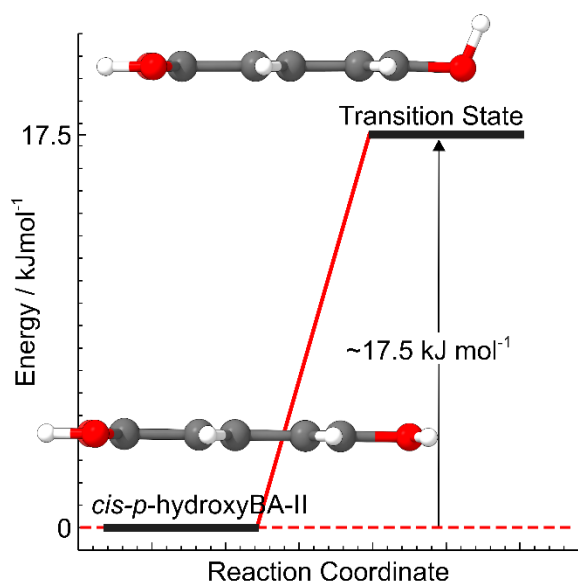


**Figure 3.14.** Barrier to interconversion from *cis-p*-hydroxyBA-II to *cis-p*-hydroxyBA-I through a rotation of the hydroxyl group at the B3LYP-D3BJ/def2-TZVP level of theory.

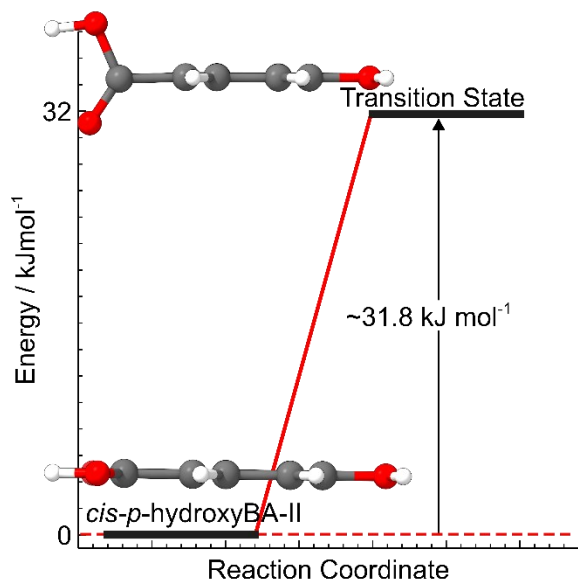


**Figure 3.15.** Barrier to interconversion from *cis-p*-hydroxyBA-II to *cis-p*-hydroxyBA-I through a rotation of the carboxylic acid group at the B3LYP-D3BJ/def2-TZVP level of theory.

**Table 3.4.** Experimental spectroscopic parameters of *cis-p*-hydroxyBA and those computed at the B3LYP-D3BJ/def2-TZVP level of theory.

	<i>cis-p</i> -hydroxyBA-I		<i>cis-p</i> -hydroxyBA-II	
	B3LYP	Experiment	B3LYP	Experiment
$\Delta E_0^a$ /kJ mol <sup>-1</sup>	0	-	0.2	-
$A$ /MHz	3877.8	3849.2(1)	3877.7	3849.6925(9)
$B$ /MHz	793.8	791.5517(2)	793.7	791.4800(2)
$C$ /MHz	658.9	656.9212(1)	658.9	656.8753(2)
$ \mu_a ,  \mu_b ,  \mu_c $ /D	2.0, 0.1, 0.0	only $\mu_a$ obs. <sup>b</sup>	2.0, 2.7, 0.0	$ \mu_a  \sim  \mu_b $ , $\mu_c$ not obs. <sup>b</sup>
$N^c$	-	19	-	36
$\sigma^d$ /kHz	-	3.2	-	3.8

<sup>a</sup> Zero-point energy corrected energy relative to the lowest energy conformer.

<sup>b</sup> Relative magnitudes of dipole moment components, estimated from signal strengths.

<sup>c</sup> Total number of transitions used in the fit.

<sup>d</sup> Standard deviation of the fit.

The orientation of the hydroxyl group has a significant impact on the *b*-dipole moment component, which is rather small ( $\sim 0.1$  D) for *cis-p*-hydroxyBA-I and much larger (2.7 D) for *cis-p*-hydroxyBA-II (see Table 3.4.). Consequently, only *a*-type transitions were observed for *cis-p*-hydroxyBA-I in the experimental spectrum, whereas for *cis-p*-hydroxyBA-II, both *a*-type and *b*-type transitions were observed. As a result, the *A* rotational constant of *cis-p*-hydroxyBA-I has a relatively large error associated with it. An overview of the experimental rotational spectra of *cis-p*-hydroxyBA-I and -II is shown in Figure 3.16. Note that the *a*-type transitions of *cis-p*-hydroxyBA-I and -II are at very similar frequencies and appear to be on top of each other at the

wide frequency scale of the figure. The assigned rotational transitions are given in Tables A.5 and A.6 of the Appendix for *cis-p*-hydroxyBA-I and *cis-p*-hydroxyBA-II, respectively.

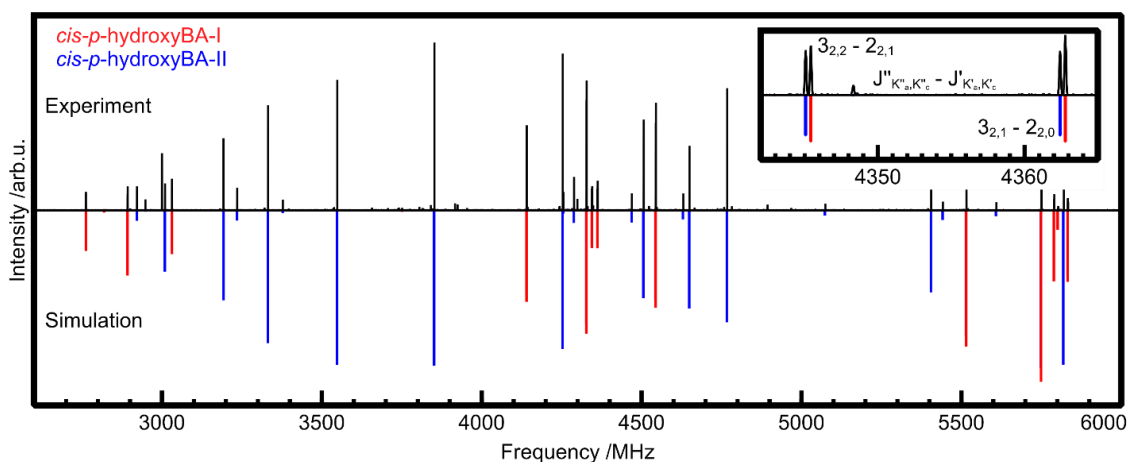


**Figure 3.16.** An overview of the experimental (top) and simulated (bottom) rotational spectra of *cis-p*-hydroxyBA-I and -II. The simulated spectra were obtained using the experimentally determined rotational constants and the predicted dipole moment components at a rotational temperature of 1 K.

### 3.3.7. *para*-substituent Effects

In the *cis*-conformers of the *para*-substituted benzoic acid monomers all atoms of the carboxylic acid group are in the aromatic ring plane. However, we noticed in the results from the electronic structure calculations of the *trans*-conformers that the carboxylic acid group rotates out of the aromatic ring plane which we attribute to a COO-H $\cdots$ H-C close contact. The C3-C4-C7-O1 dihedral angle  $\tau$ , see Figure 3.3, varies between 18.1° and 26.1° depending on the substituent group in the *para*-position. It is reasonable to assume that the variation in out-of-plane angle is a result of the effect of the *para*-substituent, specifically its electron-withdrawing or electron-donating effect, on the electronic structure in the carboxylic acid environment. Hammett recognized such substituent effects on the reactivity of *meta*- and *para*-substituted benzoic acids and introduced an empirical constant, the Hammett constant  $\sigma_R$ , to rank their reactivity against unsubstituted benzoic acid.<sup>61,62</sup> For the dissociation reaction of benzoic acids, the Hammett

constant is defined as  $\sigma_R = \log \frac{K_R}{K_H}$ , where  $K_H$  and  $K_R$  are the dissociation constants of benzoic acid and substituted benzoic acid, respectively. Sayyed and Suresh<sup>63</sup> found that the local minimum,  $V_{\min}$ , in the electrostatic potential near the O atom of the carboxylic OH group in *meta* and *para*-substituted *cis*-benzoic acids correlates well with the corresponding Hammett substitution constants. For *para* substituted benzoic acids, the difference between  $V_{\min}$  values and the corresponding value of unsubstituted benzoic acid is labelled  $V_p$ . We determined  $V_p$  values at the B3LYP D3BJ/def2-TZVP level of theory (see Table 3.5) and plot the dihedral angle  $\tau$  against those values in Figure 3.16. There is a strong correlation between  $\tau$  and  $V_p$ , such that electron withdrawing groups, in general those that lead to positive  $V_p$  values, cause a larger excursion of the carboxylic acid group from planarity with the aromatic ring. In a perhaps oversimplified view, the now more acidic proton of the carboxyl group experiences greater electrostatic repulsion from the *ortho* H-atom.

**Table 3.5.** Molecular electrostatic potential of *p*-chloroBA, *p*-aminoBA, *p*-nitroBA, *p*-hydroxyBA, and benzoic acid (BA) in the *trans*- conformation where  $V_{\min}$ , is the electrostatic potential minimum near the O atom,  $V_p$ , the difference between  $V_{\min}$  of unsubstituted and substituted benzoic acid in kcal mol<sup>-1</sup>, and  $\tau$ , the angle between the aromatic ring and the *trans*-carboxylic acid at the B3LYP D3BJ/def2-TZVP level of theory.

	$V_{\min} / \text{kcal mol}^{-1}$	$V_p / \text{kcal mol}^{-1}$	$\tau / ^\circ$
BA	-20.688	0	0
<i>p</i> -nitroBA	-9.851	10.837	26.1
<i>p</i> -chloroBA	-17.198	3.49	22.7
<i>p</i> -hydroxyBA-II	-22.179	-1.491	20.2
<i>p</i> -hydroxyBA-I	-22.772	-2.084	19.3
<i>p</i> -aminoBA	-26.893	-6.205	18.1

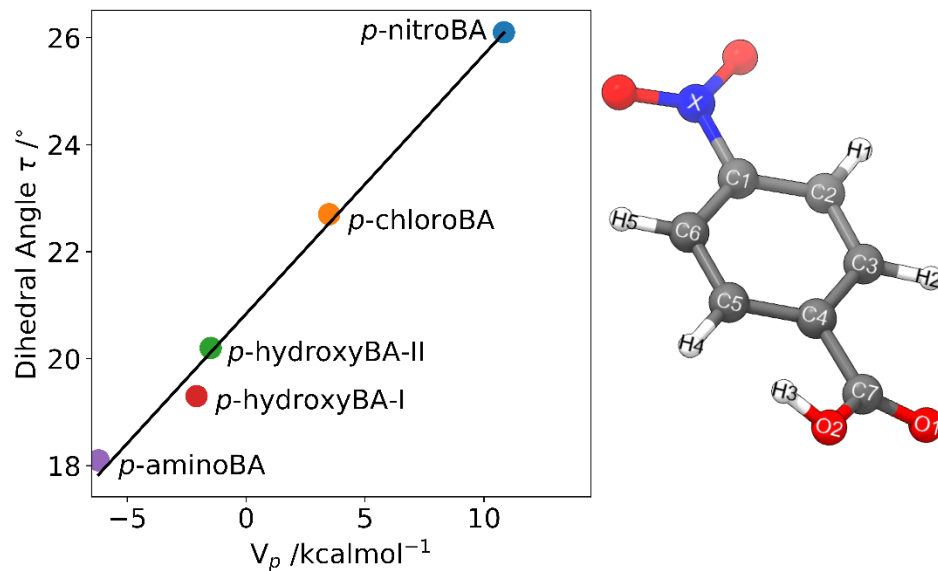


**Figure 3.17.** The C3-C4-C7-O1 out-of-plane dihedral angle  $\tau$ , as a function of the difference of molecular electrostatic potential between the substituted benzoic acid and benzoic acid at the B3LYP-D3BJ/def2-TZVP level of theory in the trans-conformation.

**Table 3.6.** Mayer bond order of p-chloroBA, p-aminoBA, p-nitroBA, p-hydroxyBA in the trans-conformation at the B3LYP-D3BJ/def2-TZVP level of theory. Refer to Figure 3.17 for labelling.

	<i>trans-p-nitroBA</i>	<i>trans-p-35chloroBA</i>	<i>trans-p-hydroxyBA-II</i>	<i>trans-p-hydroxyBA-I</i>	<i>trans-p-aminoBA</i>
C1-C2	1.4014	1.3439	1.3549	1.3229	1.3166
C2-C3	1.3948	1.3963	1.4421	1.4188	1.4940
C3-C4	1.3939	1.3901	1.3778	1.4032	1.3826
C4-C5	1.3444	1.3390	1.3487	1.3288	1.3324
C5-C6	1.4470	1.4442	1.4538	1.4844	1.5278
C6-C1	1.4366	1.3753	1.3473	1.3869	1.3474
C7-C4	0.9502	0.9561	0.9668	0.9672	0.9754

O1-C7	2.0946	2.0921	2.0900	2.0878	2.0868
O2-C7	1.2135	1.2109	1.2056	1.2086	1.2043
O2-H3	0.8714	0.8733	0.8753	0.8749	0.8763
C2-H1	0.9351	0.9730	0.9792	0.9546	0.9624
C3-H2	0.957613	0.950955	0.95605	0.935355	0.951431
C5-H4	0.932293	0.932768	0.92463	0.939495	0.938065
C6-H5	0.924034	0.965071	0.950957	0.969827	0.955296
C1-X	0.967062	0.966253	1.149043	1.149338	1.090209

The changes in electron density with substitution can also be quantified by assessing  $\pi$ -electron delocalization and bond orders.<sup>64</sup> Using the Mayer bond order index, we find that the C-COOH bond order decreases with the presence of more efficient electron withdrawing groups in the *para*-position (see Table 3.6). The decrease of the C-COOH bond order suggests a decrease in  $\pi$ -bonding characteristic and greater torsional flexibility about the bond so that the steric effects of the COO-H $\cdots$ H-C close contact are better able to push the carboxylic group further out-of-plane.

### 3.4. Conclusions

Four *para*-substituted benzoic acids, i.e., *p*-aminoBA, *p*-nitroBA, *p*-chloroBA, and *p*-hydroxyBA, were studied experimentally and computationally using chirp-pulse Fourier transform microwave spectroscopy and electronic structure calculations. In all cases, the computed minimum energy conformations contain a planar carboxylic acid group in its *cis*-conformation and these were experimentally identified. The *trans*-conformers are at least 23 kJ

mol<sup>-1</sup> higher in energy and the carboxylic acid group was identified in the computations to be out-of-plane with respect to the benzene ring. The electron donating or withdrawing nature of the *para*-substituents is shown to influence the out-of-plane angle of the carboxylic acid group. The calculated barriers between equivalent conformations and different conformers are in accord with the absence of tunneling splittings in the spectra and the observation of two conformers in the case of *para*-hydroxyBA. The nuclear quadrupole hyperfine structures of <sup>35</sup>Cl and <sup>37</sup>Cl *cis-p*-chloroBA were measured and analyzed to yield Cl nuclear quadrupole coupling constants. The corresponding B2PLYP-D3BJ/def2-TZVP calculated parameters are in reasonable agreement with the experimental ones. The calculated <sup>14</sup>N nuclear quadrupole coupling constants are also in reasonable agreement with the experimental values for *cis-p*-aminoBA, but in the case of *cis-p*-nitroBA it was necessary to utilize the B2PLYP functional to reduce the discrepancy between experiment and calculations.

## References

- (1) Del Olmo, A.; Calzada, J.; Nuñez, M. Benzoic Acid and Its Derivatives as Naturally Occurring Compounds in Foods and as Additives: Uses, Exposure, and Controversy. *Crit. Rev. Food Sci. Nutr.* **2017**, *57* (14), 3084–3103.  
<https://doi.org/10.1080/10408398.2015.1087964>.
- (2) Schnitzler, E. G.; Jäger, W. The Benzoic Acid–Water Complex: A Potential Atmospheric Nucleation Precursor Studied Using Microwave Spectroscopy and Ab Initio Calculations. *Phys. Chem. Chem. Phys.* **2014**, *16* (6), 2305–2314. <https://doi.org/10.1039/C3CP54486A>.
- (3) Ho, K. F.; Lee, S. C.; Ho, S. S. H.; Kawamura, K.; Tachibana, E.; Cheng, Y.; Zhu, T. Dicarboxylic Acids, Ketocarboxylic Acids,  $\alpha$ -Dicarbonyls, Fatty Acids, and Benzoic Acid in Urban Aerosols Collected during the 2006 Campaign of Air Quality Research in Beijing (CAREBeijing-2006). *J. Geophys. Res. Atmospheres* **2010**, *115* (D19).  
<https://doi.org/10.1029/2009JD013304>.
- (4) Duan, X.; Song, X.; Shi, R.; Wang, X.; Chen, S.; Zhao, S. A Theoretical Perspective on the Structure and Thermodynamics of Secondary Organic Aerosols from Toluene: Molecular Hierarchical Synergistic Effects. *Environ. Sci. Nano* **2022**, *9* (3), 1052–1063.  
<https://doi.org/10.1039/D1EN00959A>.
- (5) Chipley, J. R. Sodium Benzoate and Benzoic Acid. In *Antimicrobials in food*; CRC Press, 2020; pp 41–88.
- (6) Marwan, A. G.; Nagel, C. W. Quantitative Determination of Infinite Inhibition Concentrations of Antimicrobial Agents. *Appl. Environ. Microbiol.* **1986**, *51* (3), 559–561.  
<https://doi.org/10.1128/aem.51.3.559-561.1986>.

- (7) Marwan, A. G.; Nagel, C. W. Microbial Inhibitors of Cranberries. *J. Food Sci.* **1986**, *51* (4), 1009–1013. <https://doi.org/10.1111/j.1365-2621.1986.tb11220.x>.
- (8) Chaudhary, J.; Jain, A.; Manuja, R.; Sachdeva, S. A Comprehensive Review on Biological Activities of P-Hydroxy Benzoic Acid and Its Derivatives. *Int. J. Pharm. Sci. Rev. Res.* **2013**, *22*.
- (9) Clissold, S. P. Aspirin and Related Derivatives of Salicylic Acid. *Drugs* **1986**, *32* (4), 8–26. <https://doi.org/10.2165/00003495-198600324-00003>.
- (10) Pathak, M. A.; Fitzpatrick, T. B.; Frenk, E. Evaluation of Topical Agents That Prevent Sunburn — Superiority of Para-Aminobenzoic Acid and Its Ester in Ethyl Alcohol. *N. Engl. J. Med.* **1969**, *280* (26), 1459–1463. <https://doi.org/10.1056/NEJM196906262802607>.
- (11) Maki, T.; Takeda, K. Benzoic Acid and Derivatives. In *Ullmann's Encyclopedia of Industrial Chemistry*; John Wiley & Sons, Ltd, 2000. [https://doi.org/10.1002/14356007.a03\\_555](https://doi.org/10.1002/14356007.a03_555).
- (12) Pi, Y.; Schumacher, J.; Jekel, M. The Use of Para-Chlorobenzoic Acid (pCBA) as an Ozone/Hydroxyl Radical Probe Compound. *Ozone Sci. Eng.* **2005**, *27* (6), 431–436. <https://doi.org/10.1080/01919510500349309>.
- (13) Onda, M.; Asai, M.; Takise, K.; Kuwae, K.; Hayami, K.; Kuroe, A.; Mori, M.; Miyazaki, H.; Suzuki, N.; Yamaguchi, I. Microwave Spectrum of Benzoic Acid. *J. Mol. Struct.* **1999**, *482–483*, 301–303. [https://doi.org/10.1016/S0022-2860\(98\)00675-9](https://doi.org/10.1016/S0022-2860(98)00675-9).
- (14) Godfrey, P. D.; McNaughton, D. Structural Studies of Aromatic Carboxylic Acids via Computational Chemistry and Microwave Spectroscopy. *J. Chem. Phys.* **2013**, *138* (2), 024303. <https://doi.org/10.1063/1.4773347>.

- (15) Kim, Y.; Machida, K. Vibrational Spectra, Normal Vibrations and Infrared Intensities of Six Isotopic Benzoic Acids. *Spectrochim. Acta Part Mol. Spectrosc.* **1986**, *42* (8), 881–889. [https://doi.org/10.1016/0584-8539\(86\)80206-9](https://doi.org/10.1016/0584-8539(86)80206-9).
- (16) Baum, J. C.; McClure, D. S. The Ultraviolet Transitions of Benzoic Acid. 1. Interpretation of the Singlet Absorption Spectrum. *J. Am. Chem. Soc.* **1979**, *101* (9), 2335–2339. <https://doi.org/10.1021/ja00503a016>.
- (17) Cismesia, A. P.; Nicholls, G. R.; Polfer, N. C. Amine vs. Carboxylic Acid Protonation in Ortho-, Meta-, and Para-Aminobenzoic Acid: An IRMPD Spectroscopy Study. *J. Mol. Spectrosc.* **2017**, *332*, 79–85. <https://doi.org/10.1016/j.jms.2016.10.020>.
- (18) Borah, B.; Gomti Devi, Th. Vibrational Study on the Molecular Interaction of L-Proline and Para-Aminobenzoic Acid. *J. Mol. Struct.* **2020**, *1203*, 127396. <https://doi.org/10.1016/j.molstruc.2019.127396>.
- (19) Badilescu, S.; Ashrit, P. V.; Truong, V.-V.; Badilescu, I. I. Enhanced Infrared ATR Spectra of O-, m-, and p-Nitrobenzoic Acid with Ag Films. *Appl. Spectrosc.* **1989**, *43* (3), 549–552. <https://doi.org/10.1366/0003702894202850>.
- (20) Sundaraganesan, N.; Anand, B.; Meganathan, C.; Joshua, B. D. FT-IR, FT-Raman Spectra and Ab Initio HF, DFT Vibrational Analysis of p-Chlorobenzoic Acid. *Spectrochim. Acta. A. Mol. Biomol. Spectrosc.* **2008**, *69* (3), 871–879. <https://doi.org/10.1016/j.saa.2007.05.051>.
- (21) Steill, J. D.; Oomens, J. Gas-Phase Deprotonation of p-Hydroxybenzoic Acid Investigated by IR Spectroscopy: Solution-Phase Structure Is Retained upon ESI. *J. Am. Chem. Soc.* **2009**, *131* (38), 13570–13571. <https://doi.org/10.1021/ja903877v>.

- (22) Park, G. B.; Field, R. W. Perspective: The First Ten Years of Broadband Chirped Pulse Fourier Transform Microwave Spectroscopy. *J. Chem. Phys.* **2016**, *144* (20), 200901.  
<https://doi.org/10.1063/1.4952762>.
- (23) Eraković, M.; Vaillant, C. L.; Cvitaš, M. T. Instanton Theory of Ground-State Tunneling Splittings with General Paths. *J. Chem. Phys.* **2020**, *152* (8), 084111.  
<https://doi.org/10.1063/1.5145278>.
- (24) Mil'nikov, G. V.; Nakamura, H. Practical Implementation of the Instanton Theory for the Ground-State Tunneling Splitting. *J. Chem. Phys.* **2001**, *115* (15), 6881–6897.  
<https://doi.org/10.1063/1.1406532>.
- (25) Frisch, M. J.; Trucks, G. W.; Schlegel, H. B.; Scuseria, G. E.; Robb, M. A.; Cheeseman, J. R.; Scalmani, G.; Barone, V.; Petersson, G. A.; Nakatsuji, H.; Li, X.; Caricato, M.; Marenich, A. V.; Bloino, J.; Janesko, B. G.; Gomperts, R.; Mennucci, B.; Hratchian, H. P.; Ortiz, J. V.; Izmaylov, A. F.; Sonnenberg, J. L.; Williams; Ding, F.; Lipparini, F.; Egidi, F.; Goings, J.; Peng, B.; Petrone, A.; Henderson, T.; Ranasinghe, D.; Zakrzewski, V. G.; Gao, J.; Rega, N.; Zheng, G.; Liang, W.; Hada, M.; Ehara, M.; Toyota, K.; Fukuda, R.; Hasegawa, J.; Ishida, M.; Nakajima, T.; Honda, Y.; Kitao, O.; Nakai, H.; Vreven, T.; Throssell, K.; Montgomery Jr., J. A.; Peralta, J. E.; Ogliaro, F.; Bearpark, M. J.; Heyd, J. J.; Brothers, E. N.; Kudin, K. N.; Staroverov, V. N.; Keith, T. A.; Kobayashi, R.; Normand, J.; Raghavachari, K.; Rendell, A. P.; Burant, J. C.; Iyengar, S. S.; Tomasi, J.; Cossi, M.; Millam, J. M.; Klene, M.; Adamo, C.; Cammi, R.; Ochterski, J. W.; Martin, R. L.; Morokuma, K.; Farkas, O.; Foresman, J. B.; Fox, D. J. Gaussian 16 Rev. C.01, 2016.

- (26) Grimme, S.; Ehrlich, S.; Goerigk, L. Effect of the Damping Function in Dispersion Corrected Density Functional Theory. *J. Comput. Chem.* **2011**, *32* (7), 1456–1465. <https://doi.org/10.1002/jcc.21759>.
- (27) Pritchard, B. P.; Altarawy, D.; Didier, B.; Gibson, T. D.; Windus, T. L. New Basis Set Exchange: An Open, Up-to-Date Resource for the Molecular Sciences Community. *J. Chem. Inf. Model.* **2019**, *59* (11), 4814–4820. <https://doi.org/10.1021/acs.jcim.9b00725>.
- (28) Ásgeirsson, V.; Birgisson, B. O.; Bjornsson, R.; Becker, U.; Neese, F.; Riplinger, C.; Jónsson, H. Nudged Elastic Band Method for Molecular Reactions Using Energy-Weighted Springs Combined with Eigenvector Following. *J. Chem. Theory Comput.* **2021**, *17* (8), 4929–4945. <https://doi.org/10.1021/acs.jctc.1c00462>.
- (29) Carlson, C. D.; Hazrah, A. S.; Mason, D.; Yang, Q.; Seifert, N. A.; Xu, Y. Alternating 1-Phenyl-2,2,2-Trifluoroethanol Conformational Landscape With the Addition of One Water: Conformations and Large Amplitude Motions. *J. Phys. Chem. A* **2022**, *126* (40), 7250–7260. <https://doi.org/10.1021/acs.jpca.2c05803>.
- (30) Neese, F.; Wennmohs, F.; Becker, U.; Riplinger, C. The ORCA Quantum Chemistry Program Package. *J. Chem. Phys.* **2020**, *152* (22), 224108. <https://doi.org/10.1063/5.0004608>.
- (31) Lu, T.; Chen, F. Multiwfn: A Multifunctional Wavefunction Analyzer. *J. Comput. Chem.* **2012**, *33* (5), 580–592. <https://doi.org/10.1002/jcc.22885>.
- (32) Matito, E.; Poater, J.; Solà, M.; Duran, M.; Salvador, P. Comparison of the AIM Delocalization Index and the Mayer and Fuzzy Atom Bond Orders. *J. Phys. Chem. A* **2005**, *109* (43), 9904–9910. <https://doi.org/10.1021/jp0538464>.

- (33) Western, C. M. PGOPHER: A Program for Simulating Rotational, Vibrational and Electronic Spectra. *J. Quant. Spectrosc. Radiat. Transf.* **2017**, *186*, 221–242.  
<https://doi.org/10.1016/j.jqsrt.2016.04.010>.
- (34) Pickett, H. M. The Fitting and Prediction of Vibration-Rotation Spectra with Spin Interactions. *J. Mol. Spectrosc.* **1991**, *148* (2), 371–377. [https://doi.org/10.1016/0022-2852\(91\)90393-O](https://doi.org/10.1016/0022-2852(91)90393-O).
- (35) Seifert, N. A.; Thomas, J.; Jäger, W.; Xu, Y. Rotational Spectra and Theoretical Study of Tetramers and Trimers of 2-Fluoroethanol: Dramatic Intermolecular Compensation for Intramolecular Instability. *Phys. Chem. Chem. Phys.* **2018**, *20* (43), 27630–27637.  
<https://doi.org/10.1039/C8CP05653F>.
- (36) Pérez, C.; Lobsiger, S.; Seifert, N. A.; Zaleski, D. P.; Temelso, B.; Shields, G. C.; Kisiel, Z.; Pate, B. H. Broadband Fourier Transform Rotational Spectroscopy for Structure Determination: The Water Heptamer. *Chem. Phys. Lett.* **2013**, *571*, 1–15.  
<https://doi.org/10.1016/j.cplett.2013.04.014>.
- (37) Xie, F.; Seifert, N. A.; Jäger, W.; Xu, Y. Conformational Panorama and Chirality Controlled Structure–Energy Relationship in a Chiral Carboxylic Acid Dimer. *Angew. Chem. Int. Ed.* **2020**, *59* (36), 15703–15710. <https://doi.org/10.1002/anie.202005685>.
- (38) Schnitzler, E. G.; Zenchyzen, B. L. M.; Jäger, W. Rotational Spectroscopy of the Atmospheric Photo-Oxidation Product o-Toluic Acid and Its Monohydrate. *Phys. Chem. Chem. Phys.* **2015**, *18* (1), 448–457. <https://doi.org/10.1039/C5CP06073G>.
- (39) Schnitzler, E. G.; Seifert, N. A.; Kusuma, I.; Jäger, W. Rotational Spectroscopy of P-Toluic Acid and Its 1:1 Complex with Water. *J. Phys. Chem. A* **2017**, *121* (45), 8625–8631.  
<https://doi.org/10.1021/acs.jpca.7b08984>.

- (40) Al-Jabiri, M. H.; Hazrah, A. S.; Jäger, W. Conformers of Vanillic Acid and Its Monohydrate: A Rotational Spectroscopic and Theoretical Study. *J. Phys. Chem. A* **2022**, *126* (38), 6686–6694. <https://doi.org/10.1021/acs.jpca.2c05120>.
- (41) Perera, A. S.; Cheramy, J.; Poopari, M. R.; Xu, Y. Aggregation of Lactic Acid in Cold Rare-Gas Matrices and the Link to Solution: A Matrix Isolation-Vibrational Circular Dichroism Study. *Phys. Chem. Chem. Phys.* **2019**, *21* (7), 3574–3584. <https://doi.org/10.1039/C8CP04748K>.
- (42) Macario, A.; Blanco, S.; Thomas, J.; Xu, Y.; López, J. C. Competition Between Intra- and Intermolecular Hydrogen Bonding: O-Anisic Acid···Formic Acid Heterodimer. *Chem. – Eur. J.* **2019**, *25* (53), 12325–12331. <https://doi.org/10.1002/chem.201902086>.
- (43) Lesarri, A.; Mata, S.; Cocinero, E. J.; Blanco, S.; López, J. C.; Alonso, J. L. The Structure of Neutral Proline. *Angew. Chem. Int. Ed.* **2002**, *41* (24), 4673–4676. <https://doi.org/10.1002/anie.200290012>.
- (44) León, I.; Alonso, E. R.; Mata, S.; Cabezas, C.; Alonso, J. L. Unveiling the Neutral Forms of Glutamine. *Angew. Chem.* **2019**, *131* (45), 16148–16153. <https://doi.org/10.1002/ange.201907222>.
- (45) Ruoff, R. S.; Klots, T. D.; Emilsson, T.; Gutowsky, H. S. Relaxation of Conformers and Isomers in Seeded Supersonic Jets of Inert Gases. *J. Chem. Phys.* **1990**, *93* (5), 3142–3150. <https://doi.org/10.1063/1.458848>.
- (46) Watson, J. K. G. In *Vibrational spectra and structure*; Durig, J. R., Ed.; Elsevier: Amsterdam, 1977; Vol. 6, p 1.

- (47) Lister, D. G.; Tyler, J. K.; Høg, J. H.; Larsen, N. W. The Microwave Spectrum, Structure and Dipole Moment of Aniline. *J. Mol. Struct.* **1974**, *23* (2), 253–264.  
[https://doi.org/10.1016/0022-2860\(74\)85039-8](https://doi.org/10.1016/0022-2860(74)85039-8).
- (48) Ye, E.; Chandrasekaran, K.; Bettens, R. P. A. Millimeter Wave Measurement and Assignment of the Rotational Spectrum of Aniline. *J. Mol. Spectrosc.* **2005**, *229* (1), 54–56.  
<https://doi.org/10.1016/j.jms.2004.08.011>.
- (49) Bird, R. G.; Neill, J. L.; Alstadt, V. J.; Young, J. W.; Pate, B. H.; Pratt, D. W. Ground State <sup>14</sup>N Quadrupole Couplings in the Microwave Spectra of N,N'-Dimethylaniline and 4,4'-Dimethylaminobenzonitrile. *J. Phys. Chem. A* **2011**, *115* (34), 9392–9398.  
<https://doi.org/10.1021/jp111075r>.
- (50) Betz, T.; Zinn, S.; Graneek, J. B.; Schnell, M. Nuclear Quadrupole Coupling Constants of Two Chemically Distinct Nitrogen Atoms in 4-Aminobenzonitrile. *J. Phys. Chem. A* **2014**, *118* (28), 5164–5169. <https://doi.org/10.1021/jp410964w>.
- (51) Insausti, A.; Calabrese, C.; Parra, M.; Usabiaga, I.; Vallejo-López, M.; Écija, P.; Basterretxea, F. J.; Grabow, J.-U.; Caminati, W.; Lesarri, A.; Cocinero, E. J. Conformational Impact of Aliphatic Side Chains in Local Anaesthetics: Benzocaine, Butamben and Isobutamben. *Chem. Commun.* **2020**, *56* (45), 6094–6097.  
<https://doi.org/10.1039/D0CC00760A>.
- (52) Høg, J. H.; Nygaard, L.; Ole Sørensen, G. Microwave Spectrum and Planarity of Nitrobenzene. *J. Mol. Struct.* **1971**, *7* (1), 111–121. [https://doi.org/10.1016/0022-2860\(71\)90012-3](https://doi.org/10.1016/0022-2860(71)90012-3).

- (53) Omelchenko, I. V.; Shishkin, O. V.; Gorb, L.; Hill, F. C.; Leszczynski, J. Properties, Aromaticity, and Substituents Effects in Poly Nitro- and Amino-Substituted Benzenes. *Struct. Chem.* **2012**, *23* (5), 1585–1597. <https://doi.org/10.1007/s11224-012-9971-8>.
- (54) Heineking, N.; Dreizler, H. Nitrogen Quadrupole Coupling Constants of Nitrobenzene and O-Nitrophenol. *Berichte Bunsenges. Für Phys. Chem.* **1993**, *97* (5), 663–665. <https://doi.org/10.1002/bbpc.19930970504>.
- (55) Graneek, J. B.; Pérez, C.; Schnell, M. Structural Determination and Population Transfer of 4-Nitroanisole by Broadband Microwave Spectroscopy and Tailored Microwave Pulses. *J. Chem. Phys.* **2017**, *147* (15), 154306. <https://doi.org/10.1063/1.4991902>.
- (56) Roucou, A.; Kleiner, I.; Goubet, M.; Bteich, S.; Mouret, G.; Bocquet, R.; Hindle, F.; Meerts, W. L.; Cuisset, A. Towards the Detection of Explosive Taggants: Microwave and Millimetre-Wave Gas-Phase Spectroscopies of 3-Nitrotoluene. *ChemPhysChem* **2018**, *19* (9), 1056–1067. <https://doi.org/10.1002/cphc.201701266>.
- (57) Baweja, S.; Antonelli, E.; Hussain, S.; Fernández-Ramos, A.; Kleiner, I.; Nguyen, H. V. L.; Sanz, M. E. Revealing Internal Rotation and  $^{14}\text{N}$  Nuclear Quadrupole Coupling in the Atmospheric Pollutant 4-Methyl-2-Nitrophenol: Interplay of Microwave Spectroscopy and Quantum Chemical Calculations. *Molecules* **2023**, *28* (5), 2153. <https://doi.org/10.3390/molecules28052153>.
- (58) Schwabe, T.; Grimme, S. Double-Hybrid Density Functionals with Long-Range Dispersion Corrections: Higher Accuracy and Extended Applicability. *Phys. Chem. Chem. Phys.* **2007**, *9* (26), 3397–3406. <https://doi.org/10.1039/B704725H>.

- (59) Yang, Y.; Krin, A.; Cai, X.; Poopari, M. R.; Zhang, Y.; Cheeseman, J. R.; Xu, Y. Conformations of Steroid Hormones: Infrared and Vibrational Circular Dichroism Spectroscopy. *Molecules* **2023**, *28* (2), 771. <https://doi.org/10.3390/molecules28020771>.
- (60) Dorosh, O.; Białkowska-Jaworska, E.; Kisiel, Z.; Pszczółkowski, L. New Measurements and Global Analysis of Rotational Spectra of Cl-, Br-, and I-Benzene: Spectroscopic Constants and Electric Dipole Moments. *J. Mol. Spectrosc.* **2007**, *246* (2), 228–232. <https://doi.org/10.1016/j.jms.2007.09.010>.
- (61) Hansch, Corwin.; Leo, A.; Taft, R. W. A Survey of Hammett Substituent Constants and Resonance and Field Parameters. *Chem. Rev.* **1991**, *91* (2), 165–195. <https://doi.org/10.1021/cr00002a004>.
- (62) Hammett, L. P. The Effect of Structure upon the Reactions of Organic Compounds. Benzene Derivatives. *J. Am. Chem. Soc.* **1937**, *59* (1), 96–103. <https://doi.org/10.1021/ja01280a022>.
- (63) Sayyed, F. B.; Suresh, C. H. Quantification of Substituent Effects Using Molecular Electrostatic Potentials: Additive Nature and Proximity Effects. *New J. Chem.* **2009**, *33* (12), 2465–2471. <https://doi.org/10.1039/B9NJ00333A>.
- (64) Wang, X.; Liu, Z.; Yan, X.; Lu, T.; Zheng, W.; Xiong, W. Bonding Character, Electron Delocalization, and Aromaticity of Cyclo[18]Carbon (C18) Precursors, C18-(CO)<sub>n</sub> (N=6, 4, and 2): Focusing on the Effect of Carbonyl (-CO) Groups. *Chem. – Eur. J.* **2022**, *28* (7), e202103815. <https://doi.org/10.1002/chem.202103815>.

# 4

## Conformers of Vanillic Acid and its Monohydrate: A Rotational Spectroscopic and Theoretical Study

### 4.1. Introduction

On average, 19,600 km<sup>2</sup> of forested area is burned in wildfire events every year in Canada.<sup>1</sup> During these events the release of primary aerosol particles and secondary organic aerosol (SOA) precursors, such as soot,<sup>2</sup> volatile organic compounds (VOC),<sup>3</sup> and a host of other inorganic and organic compounds,<sup>1</sup> results in a decrease in air quality,<sup>4</sup> leading to a variety of impacts on climate and human health.<sup>5,6</sup> A common fuel source in wildfire combustion is wood which is composed of lignin, cellulose, and hemicellulose.<sup>7</sup> The incomplete combustion of lignin produces several products including organic acids such as syringic acid, cinnamic acid, and vanillic acid<sup>3</sup> which are thought to enhance SOA formation.<sup>8</sup>

SOA particles develop through a nucleation process where the initial formation of a critical nucleus is followed by a period of spontaneous growth.<sup>8</sup> The compositions and structures of the critical nuclei are highly varied, but it is known that molecules such as sulfuric acid, water, ammonia, and organic acids participate in their formation.<sup>9</sup> To generate a critical nucleus, a pre-critical nucleus must first form where the smallest such entity is a molecular dimer.<sup>8</sup> An important characteristic of these pre-critical nuclei is that they have conformational flexibility

which can help to maximize their intermolecular interactions while still stabilizing the initial cluster, usually through strong hydrogen bonds. This conformational flexibility can be seen in sulfuric acid-organic acid dimers where strong and medium-strong hydrogen bonds greatly stabilize the dimer while allowing for a free OH site on the sulfuric acid unit to form larger clusters.<sup>8</sup> The flexibility and binding sites of the organic acids also play roles in forming pre-critical nuclei by providing more hydrogen bonding donor and acceptor sites which is influenced by the conformational flexibility and the available functional groups.

Vanillic acid, a biomass burning product, is released during the combustion of soft and hard wood.<sup>10</sup> During wildfire events, vanillic acid is released in significant quantities into the atmosphere; concentrations of  $6.5 \mu\text{g m}^{-3}$  have been measured in biomass burning events in the Amazon.<sup>11</sup> The concentration information can be used, in conjunction with that of other aromatic acids, to identify the fuel source (type of tree burning) and conditions (humidity, temperature) in past wildfire events by comparing the concentrations of the released aromatic acids.<sup>10</sup> Soot and aerosol from large wildfire events, such as the 2018 British Columbia wildfires which destroyed 1.35 million hectares of forest,<sup>12</sup> can travel long distances and deposit on glaciers in the Arctic and surrounding regions, where they can be preserved allowing for the extraction of information about historical wildfire trends.<sup>10,13</sup> Even VOCs with relatively short atmospheric lifetimes, such as vanillic acid,<sup>14</sup> can undergo long-range transport by their incorporation into aerosol particles.<sup>15</sup> For example, monomeric aromatics such as toluene and xylene have lifetimes of a few days or less in the atmosphere,<sup>16</sup> with the exception of benzene, but they can undergo long range transport via aerosol particles.<sup>15</sup>

Vanillic acid plays important roles as a biomass burning tracer,<sup>3</sup> wildfire proxy,<sup>13</sup> brown carbon constituent,<sup>17</sup> and in aerosol growth and nucleation.<sup>8</sup> Intermolecular interactions between

vanillic acid and other atmospheric constituents, such as other organic acids, sulfuric acid, ammonia, and water, affect its atmospheric lifetime and determine how vanillic acid participates in aerosol particle formation.<sup>15</sup> Here, we describe a rotational spectroscopic study of the vanillic acid monomer and its monohydrate to shed light on conformational flexibility and hydrogen bonding energetics. Fourier transform microwave (FTMW) spectroscopy in conjunction with electronic structure calculations is well suited for such a study, as demonstrated in past work on, for instance, *o*- and *p*-toluic acid and their water complexes,<sup>18,19</sup> oxalic acid<sup>20</sup> and its mono- and di-hydrates,<sup>21</sup> and cinnamic acid.<sup>22</sup>

## **4.2. Methods**

### **4.2.1. Experiments**

A 2 to 6 GHz chirped-pulse (cp) FTMW spectrometer, which is based on the design by the Pate group,<sup>23</sup> was used to record the spectra of vanillic acid and its hydrate. This spectrometer is equipped with a 12 GS s<sup>-1</sup> arbitrary waveform generator used to generate a 2 to 6 GHz chirped pulse that is then amplified by a traveling wave tube amplifier.<sup>24</sup> The amplified chirped pulse is introduced into a vacuum chamber via a horn antenna that is mounted perpendicularly to a molecular beam expansion and antiparallel to a detecting horn antenna. The chirped pulse excites rotational transitions in the 2 to 6 GHz range and a macroscopic polarization is achieved.<sup>23</sup> The subsequent free induction decay is measured after the excitation pulse has dissipated by a fast, 25 GS s<sup>-1</sup>, oscilloscope. The free induction decays are averaged and then Fourier transformed into the frequency domain.

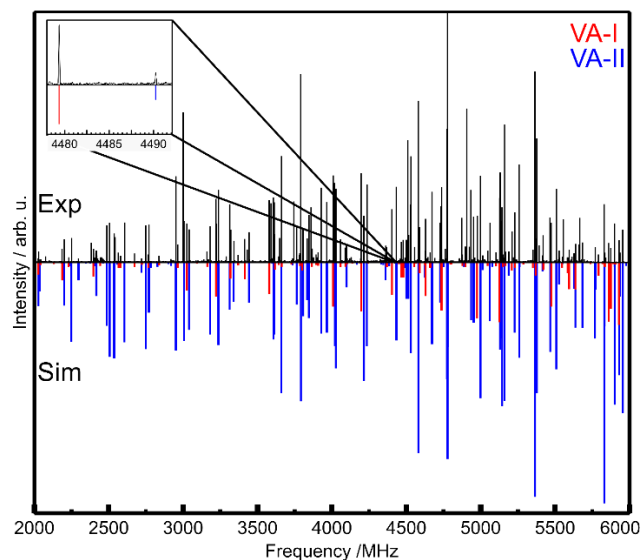


**Figure 4.1.** Top trace: The experimental spectrum (black) for vanillic acid. Bottom trace: Simulated (blue and red) spectra of the VA-I and VA-II vanillic acid conformers.

Vanillic acid was placed into the sample reservoir of a home-built nozzle cap for a General Valve, Series 9, pulsed nozzle and heated to 170 °C. Helium was used as a carrier gas at a backing pressure of 40 psi to introduce vanillic acid into the sample region via a supersonic jet expansion. A total of 734,000 spectra were acquired and averaged to increase the signal to noise ratio of the monomer spectrum (Figure 4.1). The spectrum of vanillic acid monohydrate was acquired under similar conditions, except that the carrier gas was a mixture of water vapour and helium. A total of 724,000 spectra were acquired and averaged for the monohydrate (Figure 4.2).

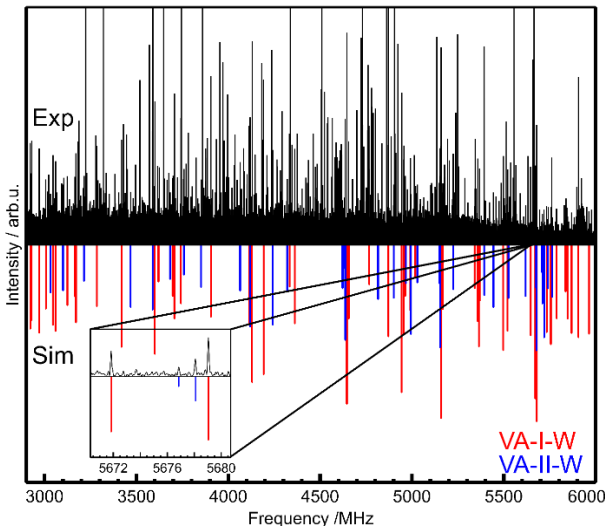


**Figure 4.2.** Experimental spectrum of the vanillic acid monohydrate (top trace) and the assigned transitions of the lowest energy monohydrates, VA-I-W and VA-II-W (bottom trace). The monomer lines were removed from the experimental spectrum.

#### 4.2.2. Computations

All electronic structure calculations in this report utilized the Gaussian16 program suite<sup>25</sup> to investigate the energetics and conformational diversity of vanillic acid and the vanillic acid - water complex. The calculations were done at different levels of theory, i.e. at the DFT B3LYP-D3(BJ)/def2-TZVP level<sup>26,27</sup> and using second order Møller-Plesset perturbation theory, MP2, with the aug-cc-pVTZ and 6-311++g(2df,2pd) basis sets.<sup>28</sup> The potential energy landscape of vanillic acid was analyzed by performing relaxed scans about distinct dihedral angles of an initial optimized structure (see Figure 4.3) to obtain further stable configurations. The scans were done by fixing one dihedral angle which was incremented by  $6^\circ$  for 60 steps to cover a range of  $360^\circ$ . At each step, a structure optimization (except the stepped dihedral angle) was done to obtain an energy profile of the rotation coordinate. When a minimum energy configuration was found the dihedral angle was fixed and another dihedral angle was scanned. This process was repeated until no more minimum energy configurations could be found. To assess if all the minimum energy

structures were located, Grimme's Conformer-Rotamer Ensemble Sampling Tool<sup>29</sup> (CREST) was used to further probe the conformational landscape of vanillic acid, but no additional conformers were found. Dihedral angle scans were also used to locate transition states which were identified by the presence of a vibrational mode with an imaginary frequency; in some instances, the transition state structure was optimized. For the case of the methyl internal rotation, the transition states were located using the Synchronous Transit-guided Quasi-Newton method as implemented in Gaussian (keyword QST3).<sup>30</sup>

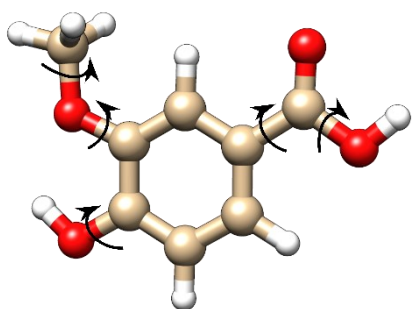


**Figure 4.3.** Dihedral angles scanned to probe the potential energy surface of the vanillic acid monomer.

For the vanillic acid-water complex, an initial CREST search was conducted where the starting structure was made up of the lowest energy vanillic acid conformer and a water molecule forming a six-membered ring with the carboxylic acid group. Additional conformers were found using higher energy vanillic acid monomers in the starting structure. Following the conformational search, geometry optimizations were done at the B3LYP-D3(BJ)/ def2-TZVP level of theory.

Anharmonic calculations were done to obtain centrifugal distortions constants and the spectroscopic parameters were obtained by using the keyword “output = Pickett” in Gaussian 16.<sup>31</sup> The calculated rotational constants for the minimum energy structures were used in

Pgopher<sup>32</sup> to simulate rotational spectra to guide the assignment of transitions in the experimental spectra.

The noncovalent interactions were visualized and analyzed using quantum theory of atoms in molecules (QTAIM)<sup>33</sup> and non-covalent interactions (NCI)<sup>34</sup> approaches, as implemented in Multiwfn,<sup>35</sup> and IGMPLOT.<sup>36–39</sup>

### 4.3. Results

Twelve minima were found on the potential energy surface of vanillic acid, see Figure 4.4, spanning an energy range of 51 kJ mol<sup>-1</sup>; their relative zero-point corrected energies, dipole moment components, and rotational constants are listed in Table 4.1. The conformers are labelled as follows. VA-I indicates that the carbonyl oxygen of the acid group is close to the methoxy group and VA-II that the acid hydroxyl group is close to the methoxy group. The following letter labels specify the orientation of the hydroxy, methoxy, and carboxylic acid groups, respectively, and the dihedral angles are defined in Figure 4.5. The first letter indicates whether the OH group points towards (cis, c) or away from (trans, t) the methoxy group. The second letter describes if the methoxy group points in the same direction (cis, c) or away from (eclipsed, e) the neighboring ring H-atom and the third describes the cis-trans isomerism of the carboxylic acid group. The two lowest-energy conformers, VA-I-c-c-c and VA-II-c-c-c, and the corresponding interconversion path are shown Figure 4.6. In VA-I-c-c-c, the carboxylic acid moiety is in the plane of the aromatic ring and the carbonyl group is closest to the meta-methoxy group. A rotation of the carboxylic acid group of VA-I-c-c-c by 180° results in a conversion to VA-II-c-c-c where the hydroxyl group is closest to the meta-methoxy group (see Figure 4.6). For the remainder of the paper VA-I and VA-II will be used to refer to the two lowest energy conformers VA-I-c-c-c and VA-II-c-c-c, respectively. VA-I and VA-II (relative energies of 0.0

and  $1.8 \text{ kJ mol}^{-1}$ , respectively) are stabilized by an intramolecular hydrogen bond between the hydroxyl H-atom and the methoxy O-atom. Intramolecular hydrogen bonds are not present in the next two higher energy conformers and as a result their relative energies are significantly higher, with  $17.9 \text{ kJ mol}^{-1}$  and  $19.1 \text{ kJ mol}^{-1}$ , respectively. The remaining conformers are at least  $23 \text{ kJ mol}^{-1}$  higher in energy and are not expected to be detectable in our experiments.<sup>40</sup> For the four lowest energy conformers, energies, rotational constants, and dipole moment components calculated at the MP2/aug-cc-pVTZ level are given in Table 4.2.

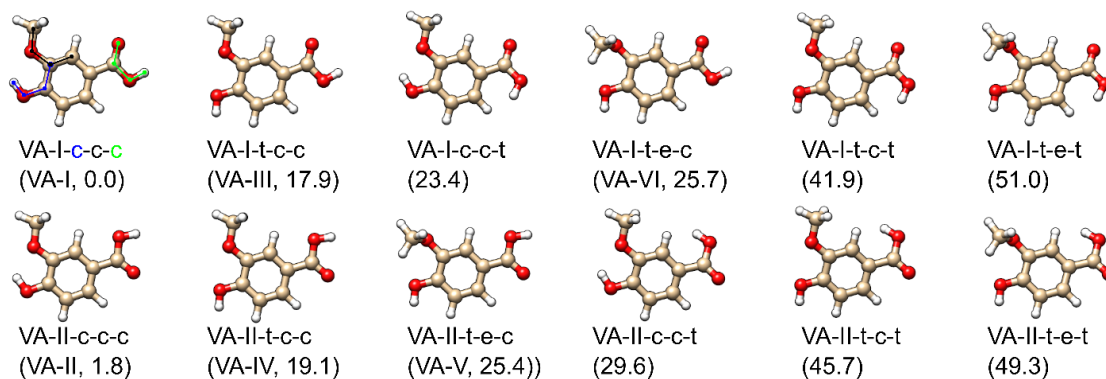


**Figure 4.4.** All vanillic acid monomer conformers found at the B3LYP-D3(BJ)/ def2-TZVP level of theory. The configuration of each conformer can be described by three dihedral angles (indicated in the lowest energy conformer) that can be cis (c), trans (t), or eclipsed (e). The relative energies are given in brackets in units of  $\text{kJ mol}^{-1}$ .

**Table 4.1.** Relative zero-point corrected energies and spectroscopic parameters for vanillic acid conformers obtained at the B3LYP-D3(BJ)/ def2-TZVP level of theory. Refer to Figure 4.4 for description of the conformer labelling.

	$\Delta E_0^a / \text{kJ mol}^{-1}$	$ \mu_a  / \text{D}$	$ \mu_b  / \text{D}$	$ \mu_c  / \text{D}$	A/ MHz	B/ MHz	C/ MHz
VA-I-c-c-c (VA-I)	0	1.54	0.81	0	1586.77	646.88	460.88
VA-II-c-c-c (VA-II)	1.8	2.39	3.43	0	1569.40	653.12	462.55
VA-I-t-c-c (VA-III)	17.9	0.85	1.86	0	1563.90	651.19	461.10
VA-II-t-c-c (VA-IV)	19.1	1.75	0.75	0	1547.84	657.50	462.83
VA-I-c-c-t	23.4	3.79	0.80	0.76	1574.93	647.00	462.32

VA-II-t-e-c (VA-V)	25.4	2.38	0.75	1.08	1858.49	589.27	458.87
VA-I-t-e-c (VA-VI)	25.7	1.53	3.39	1.44	1881.89	584.25	457.26
VA-II-c-c-t	29.6	5.23	3.36	0.87	1565.42	646.18	463.44
VA-I-t-c-t	41.9	3.16	3.44	0.72	1553.04	650.83	462.75
VA-II-t-c-t	45.7	4.61	0.70	0.95	1545.45	650.49	463.65
VA-II-t-e-t	49.3	5.25	0.85	0.02	1863.61	581.26	459.78
VA-I-t-e-t	51.0	3.88	4.95	0.75	1873.25	584.35	457.31

<sup>a</sup> Sum of electronic and zero-point energy relative to the lowest energy conformer.

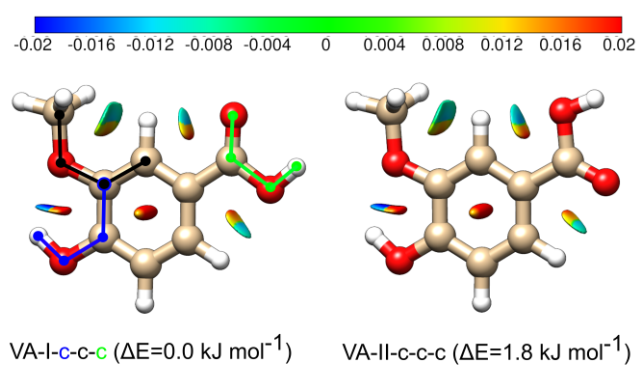


**Figure 4.5.** NCI gradient isosurfaces (reduced electron density gradient  $s=0.6$ ) visualizing the intra-molecular interactions in the two lowest energy conformers of vanillic acid. The isosurfaces are coloured from red (repulsive) to blue (attractive) according to the product of sign of the second eigenvalue of the Hessian and electron density,  $\text{sign}(\lambda_2)\rho$ .

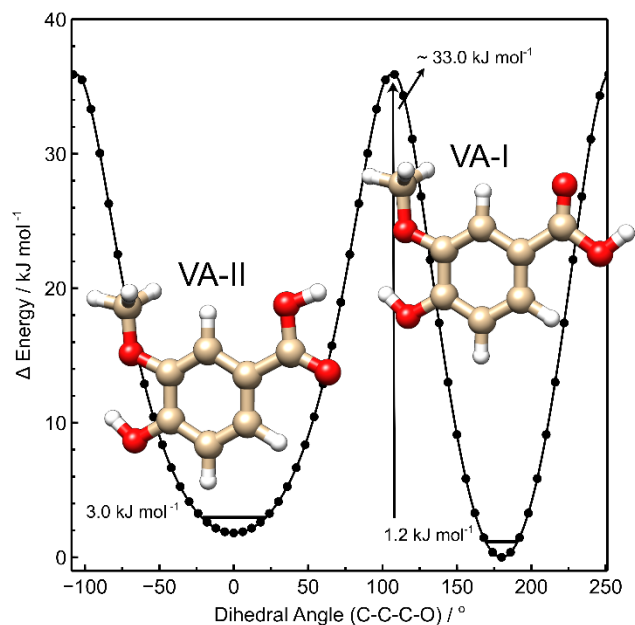


**Figure 4.6.** Dihedral angle scan along the interconversion coordinate between the two lowest energy conformers of the vanillic acid monomer, VA-I and VA-II. The respective zero-point energies are indicated.

**Table 4.2.** Relative zero-point corrected energies and spectroscopic parameters for the four lowest energy vanillic acid monomers obtained at the MP2/aug-cc-pVTZ level of theory. Refer to Figure 4.4 for description of the conformer labelling.

	VA-I-c-c-c (VA-I)	VA-II-c-c-c (VA- II)	VA-I-t-c-c (VA- III)	VA-II-t-c-c (VA-IV)
$\Delta E_0^a / \text{kJ mol}^{-1}$	0	1.7	18.1	19.3
$\Delta G^b / \text{kJ mol}^{-1}$	0	1.5	18.0	19.1
P <sup>c</sup> / %	59.6	39.7	0.4	0.3
A / MHz	1586.69	1571.32	1567.54	1553.41
B / MHz	649.72	655.48	653.27	659.12
C / MHz	462.32	463.90	462.45	464.13
$ \mu_a / \mu_b / \mu_c /\text{Debye}$	1.21/ 1.02/ 0	1.98/ 3.44/ 0	0.58/ 1.59/ 0	1.40/ 0.82/ 0

<sup>a</sup> Sum of electronic and zero-point energy relative to the lowest energy conformer.

<sup>b</sup> Sum of Gibbs free energy and electronic energy relative to the lowest energy conformer.

<sup>c</sup> Percent abundance calculated using relative free energy at a nozzle temperature of 443.15 K.

For the monohydrate, 28 theoretical conformers were identified; their relative zero-point corrected energies, dipole moment components, and rotational constants are listed in Table 4.3. Conformers of the vanillic acid - water complex are designated using the monomer labels described above and an additional label signifying the energy ordering within that subgroup (see Figure 4.7). The two lowest energy conformers, VA-I-W-1 and VA-II-W-1 contain the VA-I and VA-II monomer structure, respectively, with the carboxylic acid forming a six-membered ring with the water molecule. We will refer to VA-I-W-1 and VA-II-W-1 as VA-I-W and VA-II-W for the remainder of the text. The zero-point corrected energy difference between VA-I-W and VA-II-W is 0.9 kJ mol<sup>-1</sup>. The remaining conformers are at least 10 kJ mol<sup>-1</sup> higher in energy and are not expected to be detectable in our experiments.<sup>41</sup> Energies, rotational constants, and dipole moment components for the two lowest energy monohydrate conformers, calculated at the MP2/6-311++g(2df,2pd) level are given in Table 4.4.

**Table 4.3.** Relative zero-point corrected energies and spectroscopic parameters of the vanillic acid monohydrate conformers determined at the B3LYP-D3(BJ)/ def2-TZVP level of theory. Refer to Figure B.2 for description of the labels of the monohydrate conformers.

	$\Delta E_0^a$ / kJ mol <sup>-1</sup>	$ \mu_a $ / D	$ \mu_b $ / D	$ \mu_c $ / D	A/ MHz	B/ MHz	C/ MHz
VA-I-W-1	0.0	1.42	2.15	1.35	1521.75	396.09	315.14
VA-I-W-2	10.2	0.20	0.39	0.93	936.33	610.86	370.77
VA-I-W-3	17.2	1.44	1.31	1.49	1495.82	435.91	342.96
VA-I-W-4	24.8	0.17	2.93	1.36	960.25	488.99	325.12
VA-I-W-5	26.7	3.63	1.70	0.95	1122.18	472.33	343.34
VA-II-W-1	0.9	1.44	2.59	1.34	1503.86	399.34	316.40
VA-II-W-3	19.2	2.33	3.86	1.50	1478.87	439.02	344.27
VA-II-W-2	19.3	3.67	3.96	1.31	1159.17	472.10	336.48
VA-II-W-4	22.8	0.86	2.29	0.64	920.81	607.07	377.45
VA-II-W-5	26.9	0.43	5.62	1.42	972.82	485.81	325.16
VA-III-W-1	17.7	1.04	0.58	1.35	1503.85	397.88	315.49
VA-III-W-2	28.7	5.08	2.45	0.00	992.19	477.28	323.42

VA-III-W-3	29.6	0.00	2.46	1.00	929.97	612.01	370.22
VA-III-W-4	37.2	1.06	3.19	1.10	1523.53	413.11	326.82
VA-III-W-5	44.1	1.81	0.57	0.77	1114.75	473.73	340.79
VA-IV-W-1	18.4	1.13	0.15	1.34	1487.16	401.07	316.74
VA-IV-W-2	29.8	4.71	0.29	0.01	1004.17	475.85	324.01
VA-IV-W-3	35.7	2.04	1.65	1.26	1144.81	475.75	337.07
VA-IV-W-4	38.2	0.13	0.76	1.13	1500.06	416.95	328.10
VA-IV-W-5	41.4	1.20	0.66	0.95	918.91	605.25	379.25
VA-V-W-1	25.0	1.85	1.73	0.08	1760.60	369.68	311.09
VA-V-W-2	34.7	5.77	1.53	0.77	1088.40	455.05	327.21
VA-V-W-3	41.8	1.97	0.16	2.24	1264.29	444.40	335.87
VA-V-W-4	50.7	0.85	1.03	0.91	1185.60	498.17	450.67
VA-VI-W-1	25.3	1.81	1.85	2.65	1791.70	366.60	309.87
VA-VI-W-2	35.2	5.88	4.28	1.15	1080.06	455.43	326.68
VA-VI-W-3	44.6	1.28	4.12	2.73	1002.54	548.85	362.45
VA-VI-W-4	45.6	1.37	3.73	3.25	1491.87	413.08	360.43

---

<sup>a</sup> Sum of electronic and zero-point energy relative to the lowest energy conformer.

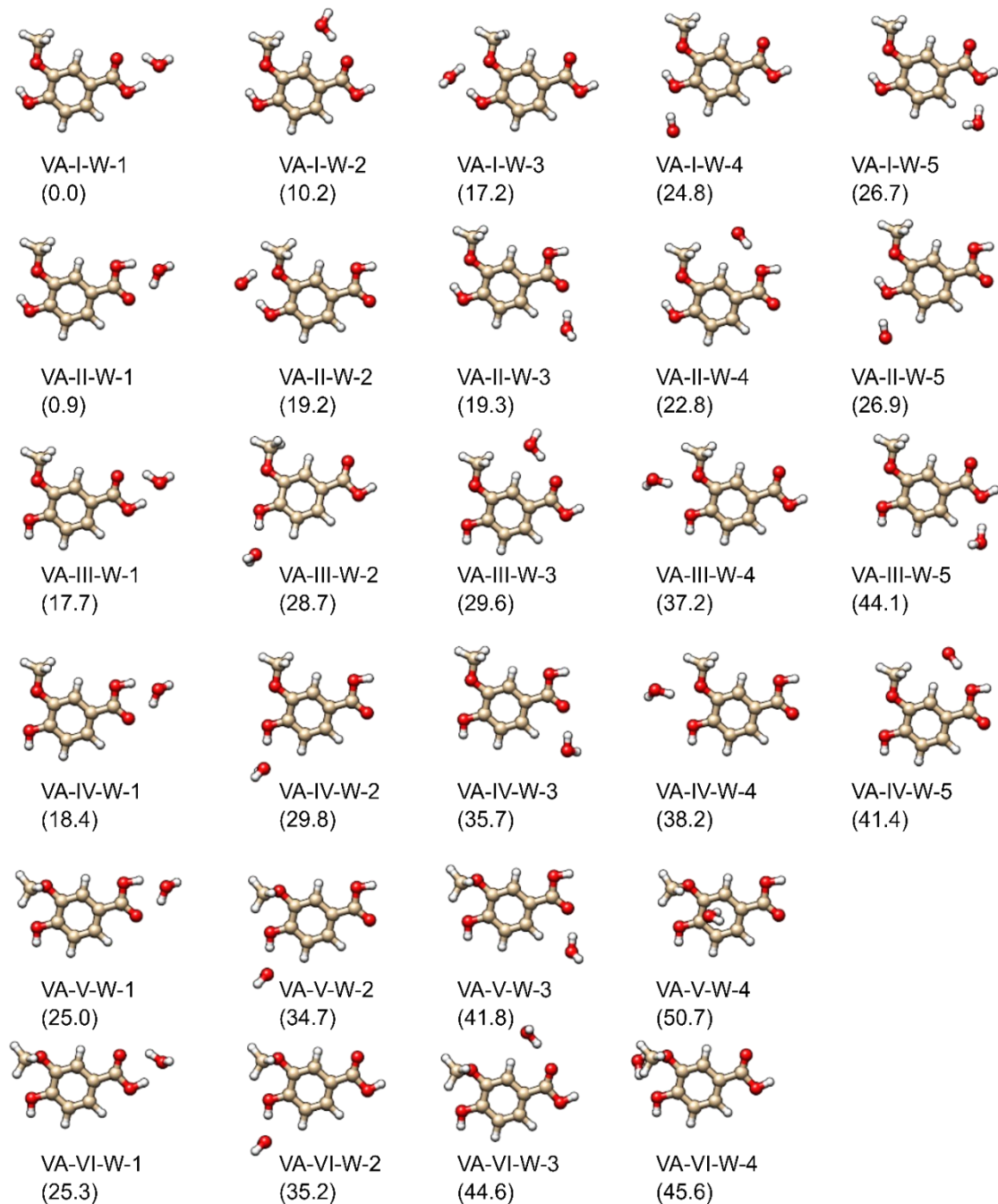


**Figure 4.7.** All vanillic acid monohydrate conformers found at the B3LYP-D3(BJ)/ def2-TZVP level of theory. The conformers are first grouped by monomer structure and then shown in order of increasing energy. The relative energies with respect to the lowest energy conformer, VA-I-W-1, are given in parentheses in units of  $\text{kJ mol}^{-1}$ .

**Table 4.4.** Relative zero-point corrected energies and spectroscopic parameters for the two lowest energy vanillic acid monohydrate obtained at the MP2/6-311++g(2df,2pd) level of theory. Refer to Figure 4.7 for description of the conformer labelling.

	VA-I-W-1	VA-II-W-1
$\Delta E_0^a$ / kJ mol <sup>-1</sup>	0	0.8
$\Delta G^b$ /kJ mol <sup>-1</sup>	0	0.8
P <sup>c</sup> / %	55.5	44.5
A/ MHz	1529.29	1509.487
B/ MHz	398.02	401.57
C/ MHz	316.66	318.03
$ \mu_a / \mu_b / \mu_c $ / Debye	0.82/ 2.35/ 1.23	0.90/ 2.72/ 1.28

<sup>a</sup> Sum of electronic and zero-point energy relative to the lowest energy conformer.

<sup>b</sup> Sum of Gibbs free energy and electronic energy relative to the lowest energy conformer.

<sup>c</sup> Percent abundance calculated using relative free energy at a nozzle temperature of 443.15 K.

To assign the experimental spectrum, the calculated rotational constants for the low energy conformers of vanillic acid and its monohydrate were used as a guide. It was relatively straightforward to assign transitions of VA-I, VA-II and VA-I-W, VA-II-W, an indication of the high quality of the calculated molecular structures. The transition frequencies, together with rotational quantum number assignments are given in Tables B.1 and B.2 for VA-I and VAI, respectively. The corresponding data for VA-I-W and VA-II-W are listed in Tables B.3 and B.4, respectively. P<sub>gopher</sub><sup>32</sup> was used to fit the spectra of these four species to yield rotational and centrifugal distortion constants using Watson's A-reduction Hamiltonian.<sup>42</sup> Some centrifugal distortion constants could not be determined in the fits; their values were fixed at DFT values. The resulting rotational constants and centrifugal distortion constants are given Tables 4.5 and 4.6 for the monomers and monohydrates, respectively. Only *a*- and *b*-type and no *c*-type

transitions were observed for VA-I and VA-II and for the monohydrates. For both the monomers and the monohydrates, minor isotopologues could not be observed, mainly as a result of the low vapour pressure of the sample.

**Table 4.5.** Energies and spectroscopic parameters of the two lowest energy conformers of vanillic acid, calculated at the B3LYP-D3(BJ)/def2-TZVP level of theory, together with experimental values.

	VA-I		VA-II	
	Theory	Experiment	Theory	Experiment
$\Delta E_0^a$ /kJ mol <sup>-1</sup>	0	-	1.8	-
$\Delta G^b$ /kJ mol <sup>-1</sup>	0	-	1.8	-
$P^c$ /%	61.2	-	37.9	-
$A$ /MHz	1586.77	1583.26700(70)	1569.40	1566.06789(41)
$B$ /MHz	646.88	645.54975(21)	653.12	651.68909(21)
$C$ /MHz	460.88	460.16912(22)	462.55	461.80909(18)
$ \mu_a / \mu_b / \mu_c $ Debye	1.54/ 0.81/ 0	$\mu_a > \mu_b, \mu_c = 0$	2.39/ 3.43/ 0	$\mu_a < \mu_b, \mu_c = 0$
$\Delta_J$ /kHz	0.0088	0.0117(33)	0.0091	0.0073(25)
$\Delta_{JK}$ /kHz	0.013	0.026(13)	0.014	0.0173(67)
$\Delta_K$ /kHz	0.077	0.104(69)	0.072	0.071(29)
$\delta_J$ /kHz	0.0028	[0.0028] <sup>d</sup>	0.0029	0.00334(62)
$\delta_K$ /kHz	0.028	0.0089(17)	0.028	0.033(10)
$\Delta I^e$ /amu·Å <sup>2</sup>	-3.20	-3.82	-3.22	-3.85
$\sigma^f$ /kHz	-	4.71	-	4.60
$N$ ( $a$ -/ $b$ -/ $c$ -type)	-	31/ 48/ 0	-	34/ 66/ 0

<sup>a</sup> Sum of electronic and zero-point energy relative to the lowest energy conformer.

<sup>b</sup> Sum of Gibbs free energy and electronic energy relative to the lowest energy conformer.

<sup>c</sup> Percent abundance calculated using relative free energy at a nozzle temperature of 170 °C.

<sup>d</sup> Parameter fixed at calculated value.

<sup>e</sup> Inertial defect  $\Delta I = I_c - I_a - I_b$ .

<sup>f</sup> Root-mean-square deviation of the fit.

**Table 4.6.** Theoretical (B3LYP-D3(BJ)/def2-TZVP) and experimental spectroscopic parameters and energies for the two lowest energy conformers of the vanillic acid-water complex.

	VA-I-W		VA-II-W	
	Theory	Experiment	Theory	Experiment
$\Delta E_0$ <sup>a</sup> /kJ mol <sup>-1</sup>	0	-	0.9	-
$\Delta G$ <sup>b</sup> /kJ mol <sup>-1</sup>	0	-	0.9	-
$P$ <sup>c</sup> /%	56.1	-	43.8	-
$A$ /MHz	1521.75	1519.54252(38)	1503.86	1500.37400(39)
$B$ /MHz	396.09	392.56157(37)	399.33	396.01444(18)
$C$ /MHz	315.14	312.88031(30)	316.40	314.23772(15)
$ \mu_a / \mu_b / \mu_c $ Debye	1.42/ 2.15/ 1.35	$\mu_a < \mu_b, \mu_c = 0$	1.44/ 2.59/ 1.34	$\mu_a < \mu_b, \mu_c = 0$
$\Delta_J$ /kHz	0.0052	0.0106(22)	0.052	[0.052] <sup>d</sup>
$\Delta_{JK}$ /kHz	0.020	[0.020] <sup>d</sup>	0.022	[0.022] <sup>d</sup>
$\Delta_K$ /kHz	0.089	[0.089] <sup>d</sup>	0.086	[0.086] <sup>d</sup>
$\delta_J$ /kHz	0.0013	0.00185(63)	0.0013	[0.0013] <sup>d</sup>
$\delta_K$ /kHz	0.027	[0.027] <sup>d</sup>	0.028	[0.028] <sup>d</sup>
$\Delta I$ <sup>e</sup> /amu·Å <sup>2</sup>	-4.36	-4.73	-4.34	-4.73
$\sigma$ <sup>e</sup> /kHz	-	6.41	-	6.82
$N(a-/ b-/ c\text{-type})$	-	52/ 3/ 0	-	32/ 1/ 0)

<sup>a</sup> Sum of electronic and zero-point energies relative to the lowest energy conformer.

<sup>b</sup> Sum of Gibbs free energy and electronic energy relative to the lowest energy conformer.

<sup>c</sup> Percent abundance calculated using the relative free energy at a nozzle temperature of 170 °C.

<sup>d</sup> Fixed at calculated value.

<sup>e</sup> Inertial defect  $\Delta I = I_c - I_a - I_b$ .

<sup>f</sup> Root-mean-square deviation of the fit.

NCI reduced electron gradient iso-surface visualizations for the low-energy monomer and monohydrate conformers are given in Figures 4.5 and 4.8, respectively. The results from QTAIM analyses, including bond and ring critical points, can be found in Figures 4.9 and 4.10. Intrinsic bond strength index, IBSI, calculations were done with IGMPLOT<sup>39,43</sup> to compare the strengths of the weak bonds in both monomers and hydrates. The results are in Figures 4.11 and 4.12.

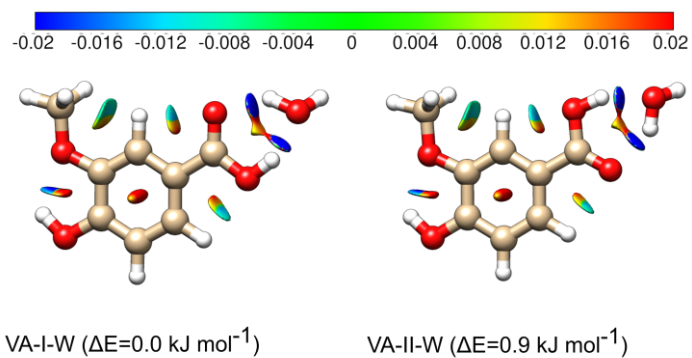


**Figure 4.8.** NCI reduced electron gradient ( $s=0.6$ ) iso-surface visualizations for the two lowest energy vanillic acid – water conformers.

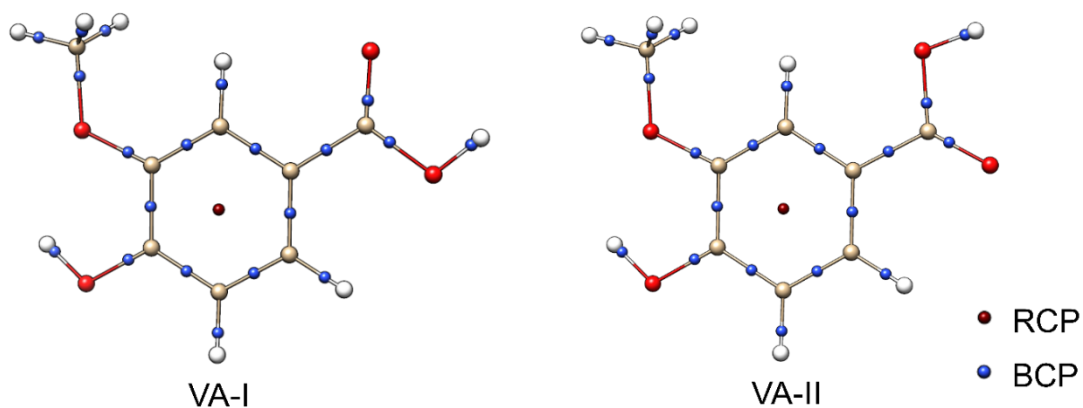


**Figure 4.9.** Bond (blue) and ring (red) critical points in the two lowest energy conformers of the vanillic acid monomer from QTAIM analyses.

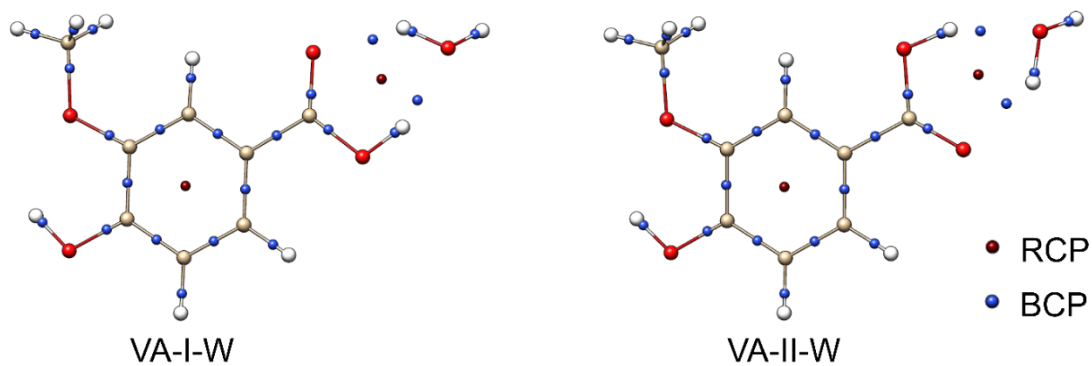


**Figure 4.10.** Bond (blue) and ring (red) critical points in the two lowest energy conformers of the vanillic acid monohydrate from QTAIM analyses.

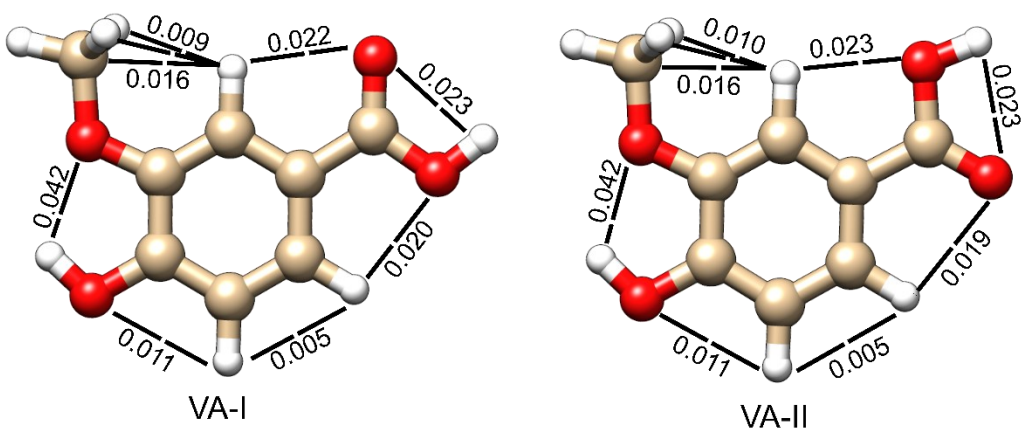


**Figure 4.11.** IBSI values for the indicated fragment interactions in the VA-I and VA-II conformers of vanillic acid.

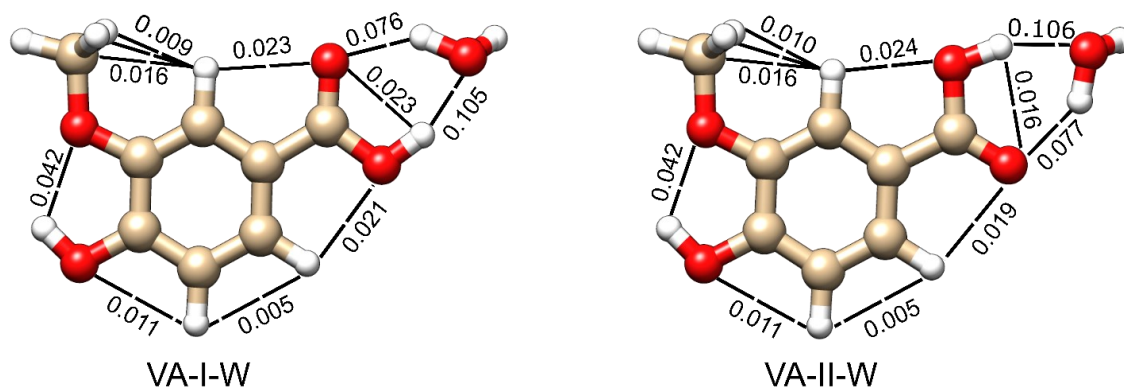


**Figure 4.12.** IBSI values for the indicated fragment interactions for the two lowest energy vanillic acid monohydrate conformers.

## 4.4. Discussion

### 4.4.1. Vanillic Acid Monomer

Out of the 12 theoretical conformers of vanillic acid, 10 have relative energies higher than 17 kJ mol<sup>-1</sup> and are predicted to have a combined population of < 1% at the nozzle temperature of 170 °C. Accordingly, only the two lowest energy conformers VA-I and VA-II could be identified in the experimental spectrum. The theoretical rotational constants of VA-I and VA-II differ by only ~1.1 % but the differences between experimental and theoretical rotational constants are even smaller (< 0.2 %), making the conformer assignment unambiguous. We note that the inertial defects (Table 4.5) can be attributed mainly to the out-of-plane H-atoms of the methyl group. The experimental values are slightly more negative than the calculated ones as a result of out-of-plane low-frequency vibrations.

From the source temperature, the calculated energy difference between the two conformers, and magnitudes of the calculated dipole moment components, we determined intensity ratios  $I(\text{VA-I}):I(\text{VA-II})$  of 1:2.4 and 1:18 for *a*- and *b*-type transitions, respectively. This is in qualitative agreement with the corresponding experimental intensity ratios of 1:0.7 and

1:6.1 and provides further confirmation of the conformer assignment. That the agreement is not better is likely the result of dipole moment averaging over large amplitude motions (*vide infra*). The calculated conversion barrier from VA-II to VA-I (Figure 4.5) is 33 kJ mol<sup>-1</sup> and we have assumed that interconversion between VA-II and VA-I is not possible under the jet expansion conditions.<sup>40</sup>

In the monomer, the conversion paths between the four lowest energy conformers have barriers greater than 15 kJ mol<sup>-1</sup> (see Figure 4.13 for conversion barriers between monomer conformers), and that is attributable to relatively strong intra-molecular interactions as well as resonance stabilization of the, in most cases, planar heavy atom structures. The energy differences between some groups of conformers can also be traced back to intra-molecular interactions. For example, NCI plots (Figure 4.5) show that the two lowest energy conformers, VA-I and VA-II are stabilized by a hydrogen bonding interaction between the hydroxyl and methoxy groups; VA-I-t-c-c and VA-II-t-c-c lack this interaction and are ~17 kJ mol<sup>-1</sup> and ~19 kJ mol<sup>-1</sup> higher in energy, respectively.

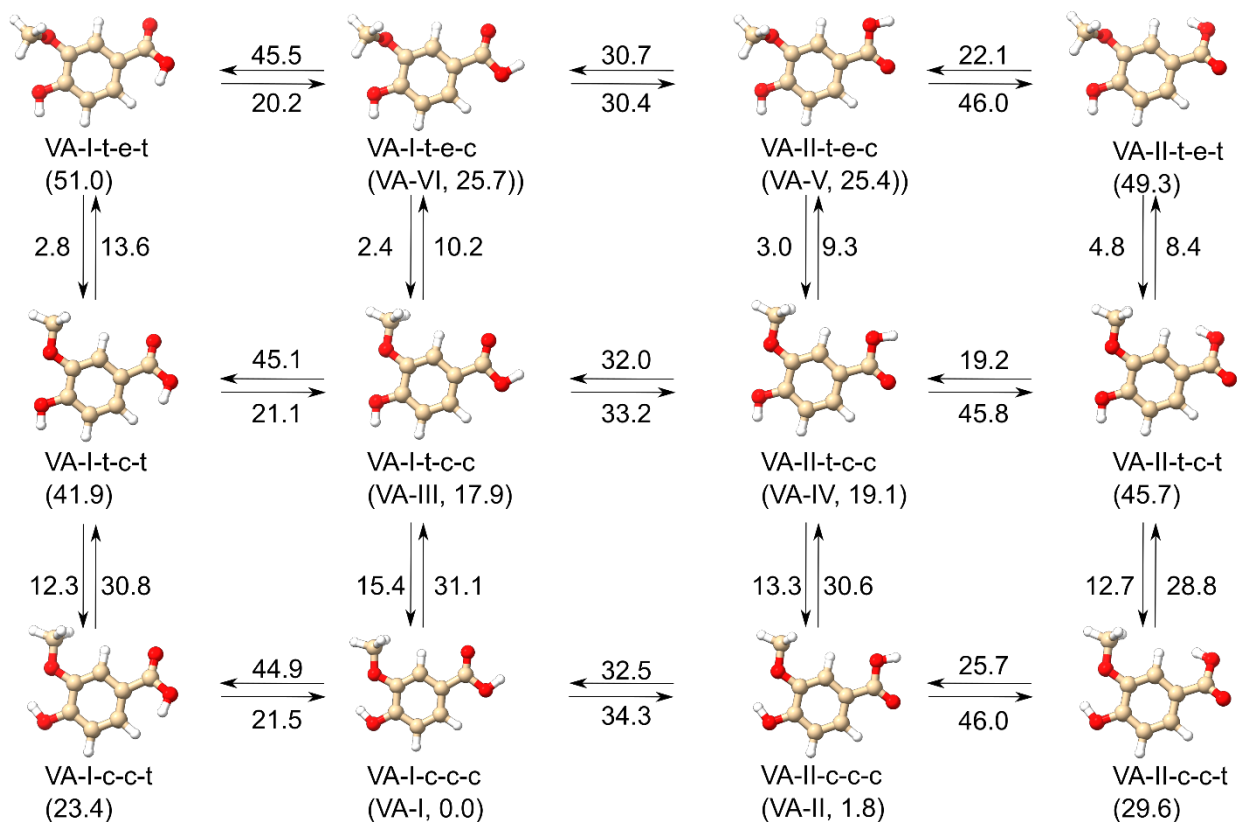


**Figure 4.13.** Conversion pathways between conformers of the vanillic acid monomer. The values in parenthesis are the relative energies with respect to the lowest energy conformer in kJ mol<sup>-1</sup> and the values between conformers are the barrier heights to interconversion, also in kJ mol<sup>-1</sup>.

The NCI analyses indicate other, weaker attractive interactions between the methyl group and ring H-atom and between the O-atoms of the carboxyl group and the respective ring H-atoms in both VA-I and VA-II (see Figure 4.5). For similar molecules, for example vanillin, ethyl vanillin, 2-methoxyphenol,<sup>44</sup> and acetovanillone,<sup>42</sup> analogous intra-molecular hydrogen bonds were identified and the O-H...O-CH<sub>3</sub> bond lengths are all in the range between 2.062 and 2.080 Å, which is in good agreement with VA-I and VA-II values of 2.073 and 2.091 Å. The strengths of the weak intra-molecular interactions can be quantified using the IBSI<sup>39</sup> which is based on an analysis of the electron density distribution with the independent gradient model (IGM). The

IBSI of a bond is correlated to the local bond stretching force constant and can be used to assess relative bond strengths.<sup>39</sup> The IBSI values of the weak intra-molecular interactions in VA-I and VA-II are given in Figure 4.11. The IBSI values are all in the non-covalent region of the scale provided by Klein et al.,<sup>39</sup> and the OH...O-CH<sub>3</sub> interaction is clearly the strongest. Its IBSI value of 0.042 may be compared with those of the hydrogen bond and O-H covalent bond of the H-bond acceptor molecule in the water dimer (0.059 and 1.394, respectively) and the weak and strong hydrogen bonds in the acyclic formic acid dimer (0.020 and 0.091, respectively) and the OH...O-CH<sub>3</sub> bond can be classified as a moderately strong hydrogen bond. The two weak interactions involving the carboxyl O-atoms are, with IBSI values of 0.022 and 0.020, significantly weaker and the interactions involving the methyl group are even weaker (IBSI = 0.009).

It is interesting, that none of the weak intra-molecular interactions identified in the NCI plots are indicated as bond critical point in the results of the QTAIM analyses<sup>33,35</sup> (Figure 4.5). This absence of a BCP in QTAIM analyses in such instances has been noted previously in 1,2-ethanediol<sup>45</sup> and allyl alcohol,<sup>46</sup> for example. Lane et al. attribute this lack of BCP to the stringent conditions of the QTAIM procedure that results in the exclusion of weaker hydrogen bonds.<sup>45</sup>

The absence of methyl internal rotor tunneling splittings in the experimental spectra suggests a relatively high barrier to methyl internal rotation. This is similar to the cases of *o*-vanillin, vanillin, ethyl vanillin, acetovanillin, for example, where also no methoxy methyl tunneling splitting was observed.<sup>44,47,48</sup> The high barrier can be a result of the weak bonding interaction between the C-atom of the methyl group and the neighbouring ring H-atom (see the corresponding electron isodensity surface in Figure 4.5) at the minimum energy configuration

and the steric repulsion between a methyl H-atom and the ring H-atom that approach very closely at the methyl rotation transition state. Electronic structure calculations were performed to confirm the high methyl rotation barrier. Relaxed scans of a dihedral angle involving a methyl group H-atom along the methyl internal rotation coordinate did not produce smooth potential energy curves. Instead, we first determined the transition state of the methyl rotation using the QST3 keyword in Gaussian and performed then an intrinsic reaction coordinate calculation using the IRC keyword. Interestingly, in the transition state the methoxy O-atom and the methyl C-atom are forced out of the ring plane because of the strong steric repulsion between methyl group and ring H-atom. As a consequence, the IRC potential energy curves are not symmetric about the transition state, as can be seen in Figures 4.14 and 4.15. The zero-point energy corrected barriers to the methyl internal rotation are 11.1 and 11.2 kJ mol<sup>-1</sup> for the VA-I and VA-II conformers, respectively, which is in the high barrier limit, so that indeed no lines splittings are expected to be observable in the experimental spectra.

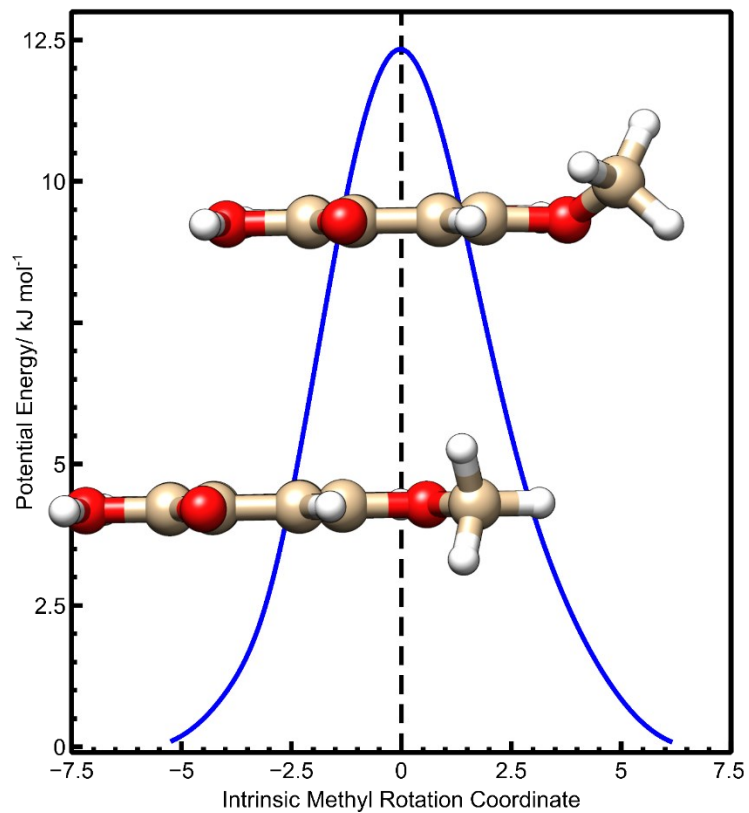


**Figure 4.14.** Intrinsic reaction coordinate scan of the methyl internal rotation in the VA-I monomer. The intrinsic reaction coordinate is in units of  $\sqrt{amu} \times bohr$ . To emphasize the asymmetry of the potential a dotted line is placed at the saddle point (IRC = 0).

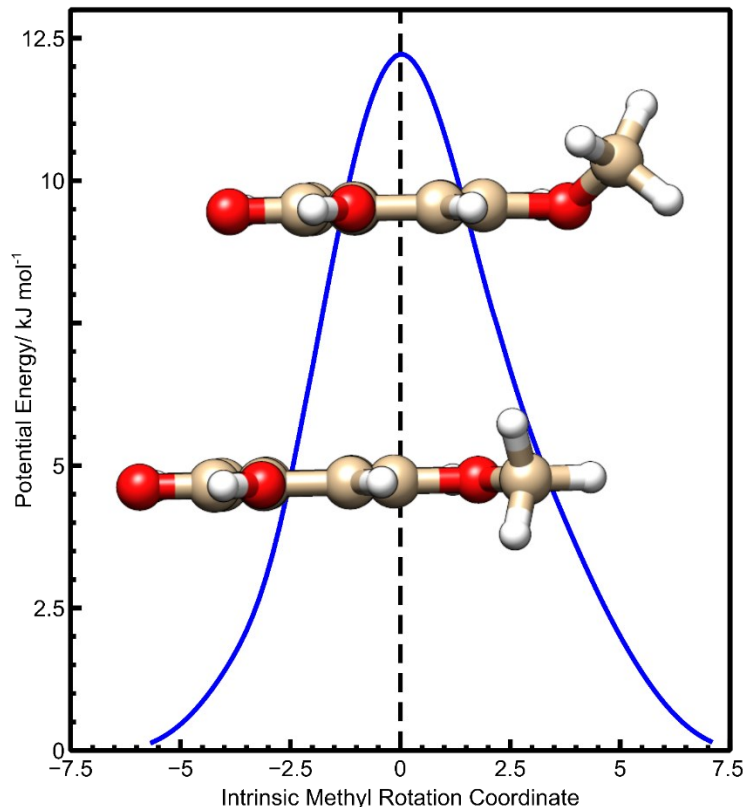


**Figure 4.15.** Intrinsic reaction coordinate scan of the methyl internal rotation in the VA-II monomer. The intrinsic reaction coordinate is in units of  $\sqrt{amu} \times bohr$ . To emphasize the asymmetry of the potential a dotted line is placed at the saddle point (IRC = 0).

#### 4.4.2. Vanillic Acid - Water

The lowest energy vanillic acid-water complexes contain the two lowest energy vanillic acid monomers, VA-I and VA-II, and form a six-membered ring between the carboxylic acid group and the water molecule (see Figure 4.8). This bonding motif is similar to that of other carboxylic acid monohydrates such as benzoic acid-water,<sup>49</sup> *p*- and *o*-toluic acid – water,<sup>18,19</sup> and oxalic acid-water,<sup>21</sup> for example. All the remaining higher energy vanillic acid-water complexes that were found in the conformational searches are given in Figure 4.7. Only the two lowest energy conformers of the vanillic acid-water complex, VA-I-W and VA-II-W were observed in the experiments. The higher energy conformers account for less than < 1 % population at the

elevated nozzle temperature and are not expected to be detectable. A total of 55 (34) transitions was assigned for VA-I-W (VA-II-W) with an RMS error of 6.41 kHz (6.82 kHz) (Table 4.5). The percent deviation between experimental and computed rotational constants is less than 1 % at the B3LYP-D3(BJ)/def2-TZVP level of theory for both conformers. The inertial defects of the monohydrates (Table 4.5) are more negative than those of the monomers, which is attributable to the wagging motion of the free H-atom of the water unit.

In the experimental monohydrate spectra, both *a*-type and *b*-type transitions were observed for both conformers; no *c*-type transitions were detected, despite sizeable calculated *c*-dipole moment components at the equilibrium geometry (see Table 4.6). The lack of *c*-type transitions in our spectra is explained by a large amplitude wagging motion of the free water H-atom from above to below the heavy atom plane of vanillic acid, leading to a cancellation of the  $\mu_c$  dipole moment component (see Figures 4.16, 4.17). This has previously been also observed in benzoic acid - water,<sup>49</sup> *o*-toluic acid - water,<sup>18</sup> *p*-toluic acid - water complexes,<sup>19</sup> for example. A potential energy curve corresponding to the free H-atom wagging motion was constructed by first determining the planar transition state of the wagging motion and then executing an IRC scan to the minimum. The potential past the minimum was mapped out by scanning a dihedral angle involving the free H-atom of the water unit. The resulting potential curves are shown in Figures 4.18 and Figure 4.19. The calculated zero-point energy (ZPE) of the resulting two-well potentials lies above the transition state making the wagging motion a barrier-less motion resulting in an average planar structure (except the methyl H-atoms).

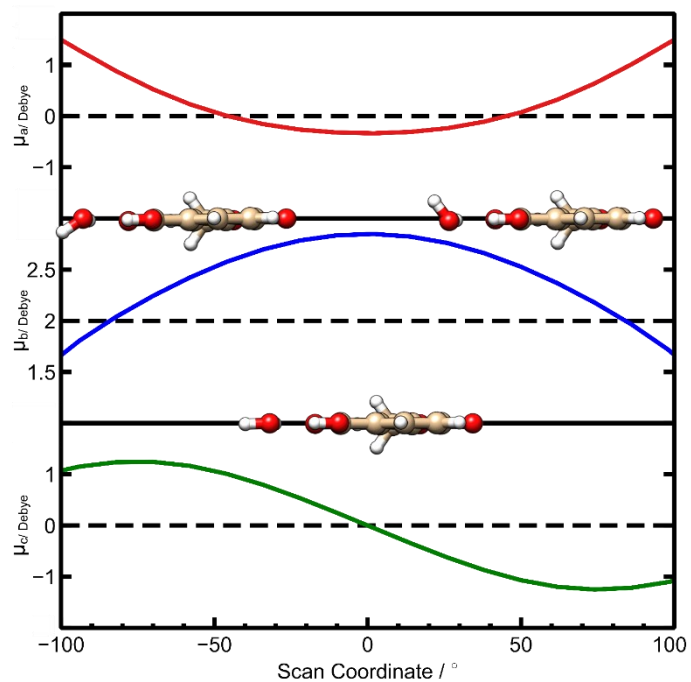


**Figure 4.16.** Change in dipole moment components as a function of the wagging motion of the free hydrogen in VA-I-W monohydrate.

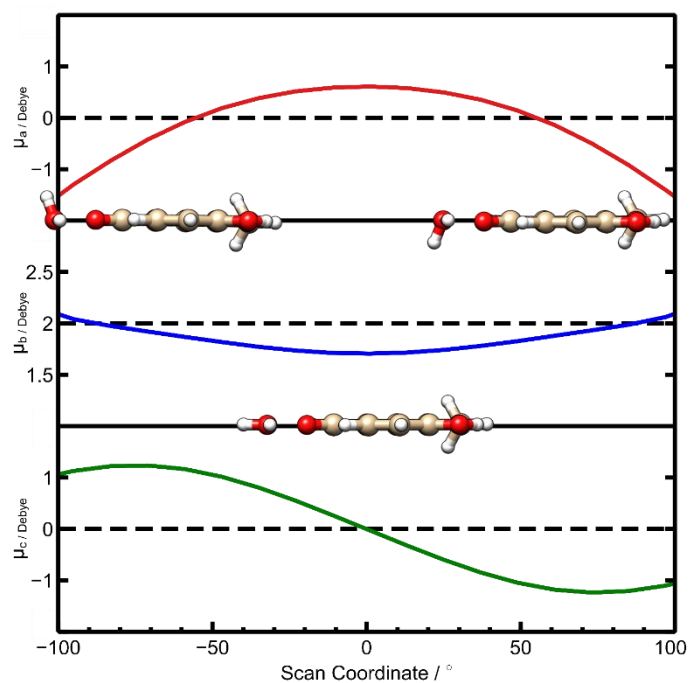


**Figure 4.17.** Change in dipole moment components as a function of the wagging motion of the free hydrogen in VA-II-W monohydrate.

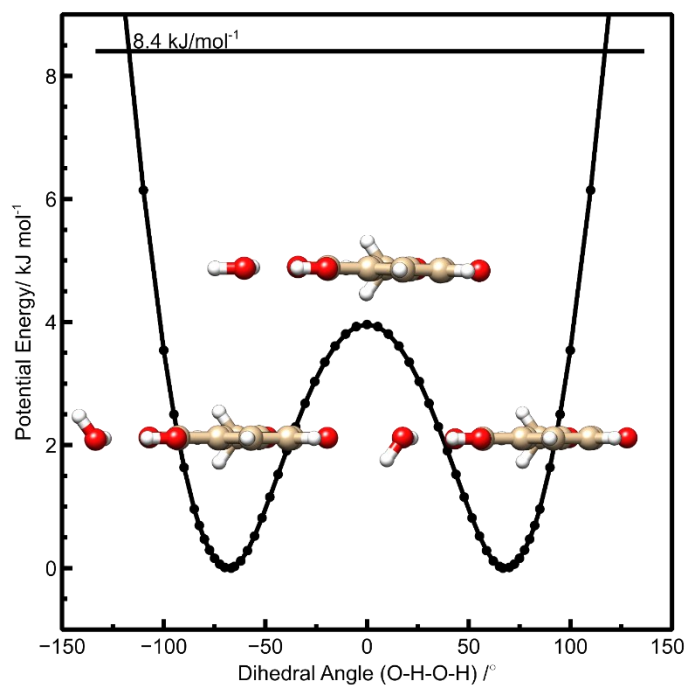


**Figure 4.18.** Potential energy curve of the wagging motion of the free hydrogen of the water moiety in VA-I-W. The zero-point energy (horizontal line) is well above the potential barrier at planarity. All values were obtained at the B3LYP-D3(BJ)/def2-TZVP level of theory.

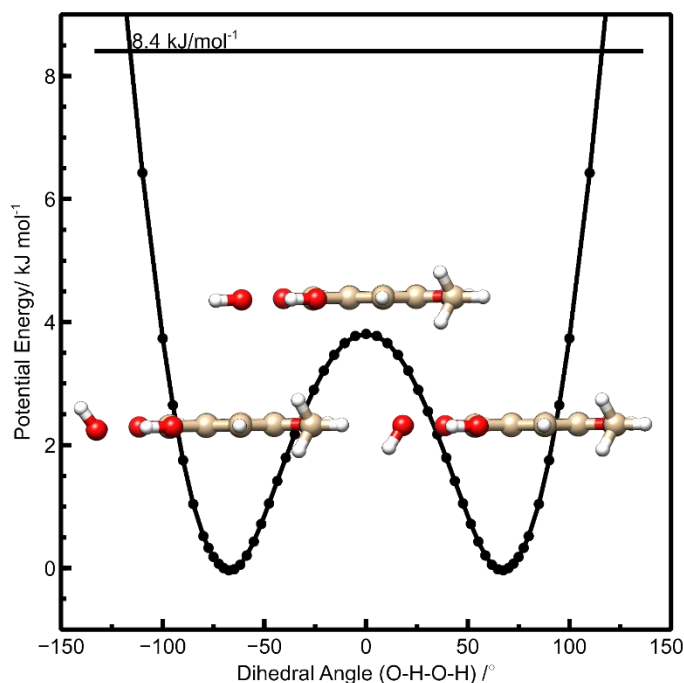


**Figure 4.19.** Potential energy curve of the wagging motion of the free hydrogen of the water moiety in VA-II-W. The zero-point energy (horizontal line) is well above the potential barrier at planarity. All values were obtained at the B3LYP-D3(BJ)/def2-TZVP level of theory.

The results from the QTAIM analyses and the NCI reduced electron gradient iso-surfaces of the two lowest energy monohydrates are shown in Figure 4.12 and Figure 4.8, respectively. Similar to the vanillic acid monomers, no bond critical points were found for the intra-monomer interactions in the results from the QTAIM analyses (Figure 4.9). Two bond critical points and a ring critical point appear as a result of the interaction of the carboxylic acid group and the water molecule forming a six-membered ring. From the NCI plots, one can see that these hydrogen bond interactions are stronger than the  $\text{OH}\cdots\text{O}-\text{CH}_3$  intra-monomer interaction. Strong hydrogen bonds are confirmed by the IBSI values of 0.076 for the bond between the carbonyl O-atom and the water H-atom and 0.105 for the bond between the hydroxyl H-atom and the water O-atom. Unsurprisingly, the  $\text{OH}\cdots\text{O}-\text{CH}_3$  interaction (IBSI = 0.042) is not affected by the complexation with the water molecule at the relatively distant carboxylic acid site. Potential energy curves for

the methyl internal rotation were constructed (see Figures 4.20 and 4.21), following the same procedure as for the monomers. The barrier shapes and heights (12.1 and 12.3 kJ mol<sup>-1</sup> for VA-I-W and VA-II-W, respectively) are very similar to those of the monomers and thus also barely affected by the water unit.

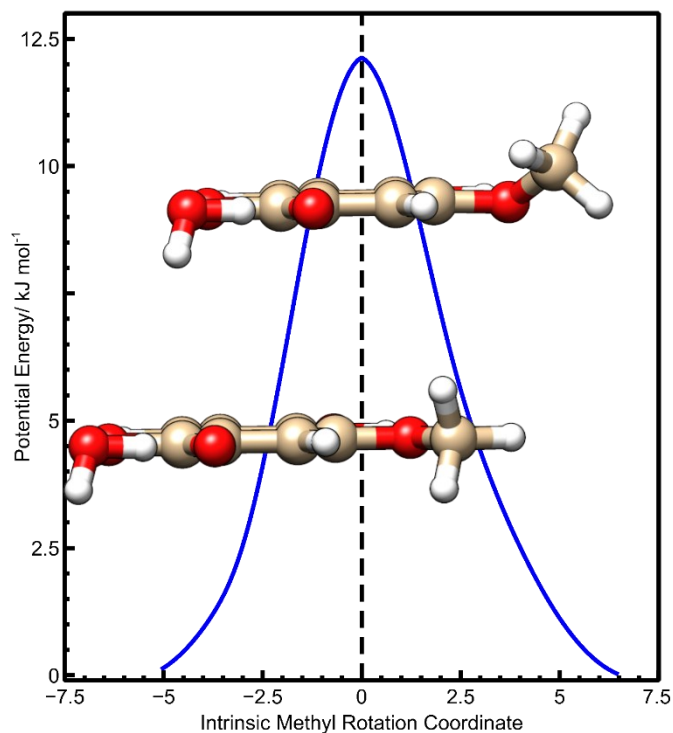


**Figure 4.20.** Intrinsic reaction coordinate scan of the methyl internal rotation in the VA-I-W-1 monohydrate. The intrinsic reaction coordinate is in units of  $\sqrt{amu} \times bohr$ . To emphasize the asymmetry a dotted line is placed at the saddle point (IRC = 0).

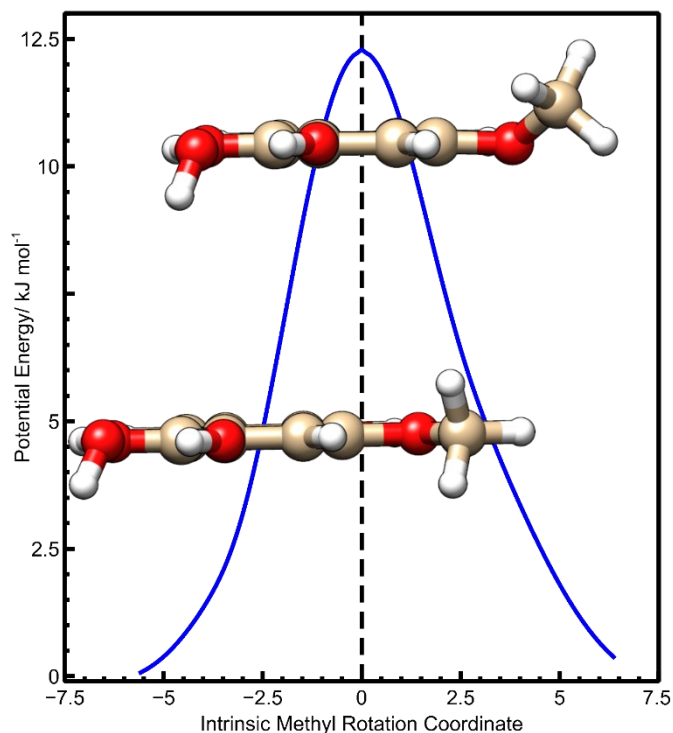


**Figure 4.21.** Intrinsic reaction coordinate scan of the methyl internal rotation in the VA-II-W-1 monohydrate. The intrinsic reaction coordinate is in units of  $\sqrt{amu} \times bohr$ . To emphasize the asymmetry a dotted line is placed at the saddle point (IRC = 0).

#### 4.5. Atmospheric Implications

To investigate the possible atmospheric implications of the vanillic acid monohydrate, we evaluate thermodynamic abundances of the two experimentally assigned water complexes using equilibrium constants of complexation,  $K_p$ . The equilibrium constants were computed directly from partition functions and dissociation energies:

$$K_p = 2 \frac{Q_{A-B}(T)}{Q_A(T)Q_B(T)} e^{\frac{D_0}{RT}} \quad (1)$$

Here,  $R$  is the gas constant in  $J \text{ mol}^{-1} \text{ K}^{-1}$ ,  $T$  is temperature in K, and  $D_0$  is the dissociation energy in  $J \text{ mol}^{-1}$ . The pre-factor of two is included to reflect the wagging motion of the non-bonded hydrogen atom of the water molecule, resulting in mirror images.<sup>50,51</sup> Dissociation energies were obtained by subtracting the difference between the zero-point energy corrections of the

monomers and monohydrates from the counterpoise corrected interaction energies. In this study we used daily average ambient temperature measurements from January 1st, 2018, to January 1st, 2021. The measurements were obtained from the Earth and Atmospheric Sciences (EAS) weather station,<sup>52</sup> located at the University of Alberta, Edmonton, Alberta, Canada.  $Q_A(T)$  and  $Q_B(T)$  are the total partition functions for water and vanillic acid, and  $Q_{A-B}(T)$  is the total partition function for the vanillic acid-water complex.

The total partition function for each species is the product of the electronic, vibrational, rotational, and translational partition functions. The electronic partition function is equal to one for each species, as the excited electronic states are sufficiently high in energy, such that they are inaccessible at the relevant temperatures. The vibrational, rotational, and translational partition functions are all temperature dependent, and were calculated for each daily ambient temperature measurement. The vibrational partition function is given by the product of the partition function for each vibrational mode, where each vibrational mode partition function is inversely proportional to the respective vibrational mode frequency. The vibrational frequencies for VA-I, VA-II, VA-I-W, and VA-II-W were obtained from harmonic frequency calculations at the B3LYP-D3(BJ)/def2-TZVP level of theory. In addition to temperature, the rotational partition function is dependent on rotational constants and symmetry number. The rotational constants used for VA-I, VA-II, VA-I-W, and VA-II-W are reported in Tables 4.5 and 4.6. The rotational constants of water were taken from a previous study.<sup>53</sup> The rotational symmetry number for all species is one, with the exception of water possessing a symmetry number of two. The translational partition function for each species is simply computed from its mass and temperature.

The percentage of vanillic acid that occurs as hydrate conformer  $i$  in the atmosphere,  $\chi_i$ , is dependent on the equilibrium constant of complexation and the concentration of water vapour:

$$\chi_i = K_{p,i} \left[ \frac{p(H_2O)}{p_a} \right] 100\% \quad (2)$$

Here  $p(H_2O)$  is the partial pressure of water, and  $p_a$  is the ambient air pressure. Ambient air pressure measurements were obtained from the EAS weather station, while the partial pressure of water was calculated using the vapour pressure parameterization of the World Meteorological Organization.<sup>54</sup> The total percentage of hydrated vanillic acid is presented in Figure 4.22 and is calculated from

$$\chi = n_i \chi_i + n_j \chi_j \quad (3)$$

Here,  $n_{i,j}$  is the mol fraction of hydrate  $i$  and  $j$ . The average mol fraction and average yearly hydrate percentage, mol fraction weighted, for VA-I-W (VA-II-W) are 0.58 (0.42) and 14.1% (15.1%), respectively. The higher hydrate abundance of the less energetically stable VA-II-W complex is a consequence of the higher dissociation energy ( $D_{0_{VA-I-W}} = 40.1 \text{ kJ mol}^{-1}$  and  $D_{0_{VA-II-W}} = 41.1 \text{ kJ mol}^{-1}$ ). The total yearly average hydrate percentage is 29.2% and the changes between the summer and winter months are not very large (see Figure 4.22) with a yearly standard deviation of 0.7%. The percentage of hydrated vanillic acid is the highest (lowest) during the summer (winter) months, when  $p(H_2O)$  is at its highest (lowest) and  $K_p$  is at its lowest (highest).

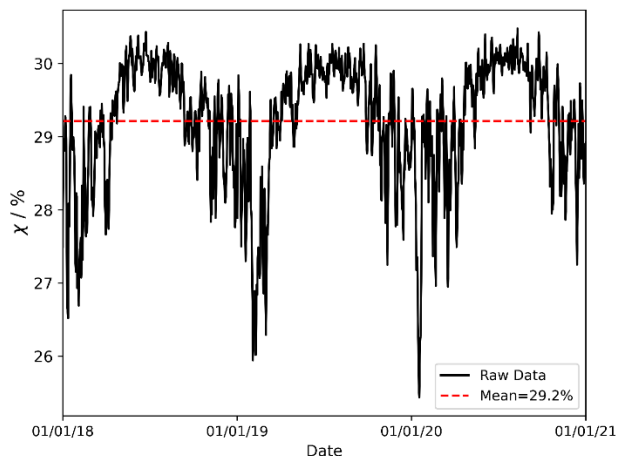


**Figure 4.22.** Abundance of vanillic acid monohydrate relative to the vanillic acid monomer in the atmosphere between 01. January 2018 to 01. January 2021, at the University of Alberta, Edmonton, Alberta, Canada. The data were computed from experimental rotational constants, measured temperature and pressure, and calculated vibrational frequencies and dissociation energies. See the text for details.

To understand how the VA-I-W and VA-II-W complexes relate to other atmospherically relevant systems, we make a comparison to the monohydrates of benzoic acid<sup>55</sup> and ortho-toluic acid,<sup>56</sup> two systems which can undergo complexation with water at their respective carboxylic acid groups. At the MP2/6-311++G(2df,2pd) level, the yearly abundance average for benzoic acid and ortho-toluic acid monohydrates is ~1% and ~0.1%, respectively. This relatively large difference in vanillic acid hydrate abundance compared to benzoic acid and ortho-toluic acid is most likely a consequence of the different levels of theory used in this study, and more specifically, the effect the level of theory has on the dissociation energy,  $D_0$ . In benzoic acid and ortho-toluic acid, the dissociation energy is ~30 kJ mol<sup>-1</sup> (MP2/6-311++G(2df,2pd)), while in vanillic acid the dissociation energy is ~40 kJ mol<sup>-1</sup> (B3LYP-D3(BJ)/def2-TZVP). This 10 kJ mol<sup>-1</sup> difference leads to ~60-fold increase in the equilibrium constant for vanillic acid.

Recalculating the dissociation energies for the VA-I-W and VA-II-W complexes at the MP2/6-

311++G(2df,2pd) level of theory, the dissociation energies become 31.0 kJ mol<sup>-1</sup> and 31.9 kJ mol<sup>-1</sup>, respectively. The average abundance values for VA-I-W and VA-II-W with the new dissociation values are then 0.49% and 0.70%, respectively. With the mol fraction included, the total average vanillic acid hydrate abundance is 0.57%, which is similar to the benzoic acid and ortho-toluic acid results. With the alarming increase of biomass burning due to forest fires, and concurrent increase in vanillic acid emission, its monohydrate may be currently of more atmospheric interest than the monohydrates of benzoic acid and ortho-toluic acid, despite the similarities in relative hydrate abundance. These results not only provide valuable thermodynamic insights, but also further enhance our understanding of gas-phase clusters containing organic acids and water in the atmosphere.

#### **4.6. Conclusions**

Vanillic acid is an important by-product of biomass burning of soft and hard wood. It plays a significant role in aerosol formation, i.e., nucleation and growth and is, in addition, used as a biomass tracer to help reconstruct historical biomass burning trends. The structure of vanillic acid was studied using a combination of electronic structure calculations and cp-FTMW spectroscopy. Twelve conformers of vanillic acid were found computationally using a combination of relaxed scans and the CREST computational tool and the two lowest energy conformers were identified in the experimental spectra. Intra-molecular hydrogen bonds play a significant role in the relative stabilities of the monomer conformers. These weak intra-molecular bonds were analyzed using QTAIM and NCI analyses as well as IBSI values from IGMPlot analyses. A similar approach was taken to study the vanillic acid-water complex and a total of 28 conformers were found computationally. The two lowest energy conformers were identified experimentally and the intra-molecular interactions in the monohydrates are similar to those in

the vanillic acid monomers. The carboxyl group forms a six-membered ring with the water molecule and is stabilized by strong hydrogen bonds. The absence of *c*-type transitions in the vanillic acid monohydrate is a result of a large amplitude wagging motion of the free hydrogen of the water moiety, which averages out the *c*-dipole moment component. The atmospheric abundances of the vanillic acid-water complex relative to the monomer were calculated and are found to be very sensitive to the level of theory as they depend strongly on the calculated dissociation energy.

## References

- (1) Hanes, C. C.; Wang, X.; Jain, P.; Parisien, M.-A.; Little, J. M.; Flannigan, M. D. Fire-Regime Changes in Canada over the Last Half Century. *Can. J. For. Res.* **2019**, *49* (3), 256–269. <https://doi.org/10.1139/cjfr-2018-0293>.
- (2) Andreae, M. O.; Andreae, T. W.; Annegarn, H.; Beer, J.; Cachier, H.; Le Canut, P.; Elbert, W.; Maenhaut, W.; Salma, I.; Wienhold, F. G.; Zenker, T. Airborne Studies of Aerosol Emissions from Savanna Fires in Southern Africa: 2. Aerosol Chemical Composition. *J. Geophys. Res. Atmos.* **1998**, *103* (D24), 32119–32128. <https://doi.org/10.1029/98JD02280>.
- (3) Simoneit, B. R. T. Biomass Burning — a Review of Organic Tracers for Smoke from Incomplete Combustion. *Appl. Geochemistry* **2002**, *17* (3), 129–162. [https://doi.org/10.1016/S0883-2927\(01\)00061-0](https://doi.org/10.1016/S0883-2927(01)00061-0).
- (4) McClure, C. D.; Jaffe, D. A. US Particulate Matter Air Quality Improves except in Wildfire-Prone Areas. *PNAS* **2018**, *115* (31), 7901–7906. <https://doi.org/10.1073/pnas.1804353115>.
- (5) Park, M.; Joo, H. S.; Lee, K.; Jang, M.; Kim, S. D.; Kim, I.; Borlaza, L. J. S.; Lim, H.; Shin, H.; Chung, K. H.; Choi, Y.-H.; Park, S. G.; Bae, M.-S.; Lee, J.; Song, H.; Park, K. Differential Toxicities of Fine Particulate Matters from Various Sources. *Sci. Rep.* **2018**, *8* (1), 17007. <https://doi.org/10.1038/s41598-018-35398-0>.
- (6) Fuzzi, S.; Baltensperger, U.; Carslaw, K.; Decesari, S.; Denier van der Gon, H.; Facchini, M. C.; Fowler, D.; Koren, I.; Langford, B.; Lohmann, U.; Nemitz, E.; Pandis, S.; Riipinen, I.; Rudich, Y.; Schaap, M.; Slowik, J. G.; Spracklen, D. V.; Vignati, E.; Wild, M.; Williams, M.; Gilardoni, S. Particulate Matter, Air Quality and Climate: Lessons Learned

- and Future Needs. *Atmos. Chem. Phys.* **2015**, *15* (14), 8217–8299.  
<https://doi.org/10.5194/acp-15-8217-2015>.
- (7) PETERSEN, R. C. The Chemical Composition of Wood. In *The Chemistry of Solid Wood*; Advances in Chemistry; American Chemical Society, 1984; Vol. 207, pp 57–126.  
<https://doi.org/10.1021/ba-1984-0207.ch002>.
- (8) Zhang, R. Getting to the Critical Nucleus of Aerosol Formation. *Science* **2010**, *328* (5984), 1366–1367. <https://doi.org/10.1126/science.1189732>.
- (9) Lee, S.-H.; Gordon, H.; Yu, H.; Lehtipalo, K.; Haley, R.; Li, Y.; Zhang, R. New Particle Formation in the Atmosphere: From Molecular Clusters to Global Climate. *J Geophys. Res. Atmos.* **2019**, *124* (13), 7098–7146. <https://doi.org/10.1029/2018JD029356>.
- (10) Wan, X.; Kawamura, K.; Ram, K.; Kang, S.; Loewen, M.; Gao, S.; Wu, G.; Fu, P.; Zhang, Y.; Bhattarai, H.; Cong, Z. Aromatic Acids as Biomass-Burning Tracers in Atmospheric Aerosols and Ice Cores: A Review. *Environ. Pollut.* **2019**, *247*, 216–228.  
<https://doi.org/10.1016/j.envpol.2019.01.028>.
- (11) bin Abas, M. R.; Simoneit, B. R. T.; Elias, V.; Cabral, J. A.; Cardoso, J. N. Composition of Higher Molecular Weight Organic Matter in Smoke Aerosol from Biomass Combustion in Amazonia. *Chemosphere* **1995**, *30* (5), 995–1015. [https://doi.org/10.1016/0045-6535\(94\)00442-W](https://doi.org/10.1016/0045-6535(94)00442-W).
- (12) Service, B. W. *Wildfire Season Summary - Province of British Columbia*.  
<https://www2.gov.bc.ca/gov/content/safety/wildfire-status/about-bcws/wildfire-history/wildfire-season-summary> (accessed 2021-09-28).

- (13) Grieman, M. M.; Aydin, M.; McConnell, J. R.; Saltzman, E. S. Burning-Derived Vanillic Acid in an Arctic Ice Core from Tunu, Northeastern Greenland. *Clim. Past* **2018**, *14* (11), 1625–1637. <https://doi.org/10.5194/cp-14-1625-2018>.
- (14) Liu, C.; Zeng, C. Heterogeneous Kinetics of Methoxyphenols in the OH-Initiated Reactions under Different Experimental Conditions. *Chemosphere* **2018**, *209*, 560–567. <https://doi.org/10.1016/j.chemosphere.2018.06.131>.
- (15) Donahue, N. M.; Chuang, W.; Epstein, S. A.; Kroll, J. H.; Worsnop, D. R.; Robinson, A. L.; Adams, P. J.; Pandis, S. N.; Donahue, N. M.; Chuang, W.; Epstein, S. A.; Kroll, J. H.; Worsnop, D. R.; Robinson, A. L.; Adams, P. J.; Pandis, S. N. Why Do Organic Aerosols Exist? Understanding Aerosol Lifetimes Using the Two-Dimensional Volatility Basis Set. *Environ. Chem.* **2013**, *10* (3), 151–157. <https://doi.org/10.1071/EN13022>.
- (16) Cabrera-Perez, D.; Taraborrelli, D.; Sander, R.; Pozzer, A. Global Atmospheric Budget of Simple Monocyclic Aromatic Compounds. *Atmos. Chem. Phys.* **2016**, *16* (11), 6931–6947. <https://doi.org/10.5194/acp-16-6931-2016>.
- (17) Yan, J.; Wang, X.; Gong, P.; Wang, C.; Cong, Z. Review of Brown Carbon Aerosols: Recent Progress and Perspectives. *Sci. Total Env.* **2018**, *634*, 1475–1485. <https://doi.org/10.1016/j.scitotenv.2018.04.083>.
- (18) Schnitzler, E. G.; Zenchyzen, B. L. M.; Jäger, W. Rotational Spectroscopy of the Atmospheric Photo-Oxidation Product o-Toluic Acid and Its Monohydrate. *Phys. Chem. Chem. Phys.* **2015**, *18* (1), 448–457. <https://doi.org/10.1039/C5CP06073G>.
- (19) Schnitzler, E. G.; Seifert, N. A.; Kusuma, I.; Jäger, W. Rotational Spectroscopy of P-Toluic Acid and Its 1:1 Complex with Water. *J. Phys. Chem. A* **2017**, *121* (45), 8625–8631. <https://doi.org/10.1021/acs.jpca.7b08984>.

- (20) Godfrey, P. D.; Mirabella, M. J.; Brown, R. D. Structural Studies of Higher Energy Conformers by Millimeter-Wave Spectroscopy: Oxalic Acid. *J. Phys. Chem. A* **2000**, *104* (2), 258–264. <https://doi.org/10.1021/jp992499t>.
- (21) Schnitzler, E. G.; Badran, C.; Jäger, W. Contrasting Effects of Water on the Barriers to Decarboxylation of Two Oxalic Acid Monohydrates: A Combined Rotational Spectroscopic and Ab Initio Study. *J. Phys. Chem. Lett.* **2016**, *7* (7), 1143–1147. <https://doi.org/10.1021/acs.jpcclett.6b00278>.
- (22) Cortijo, V.; Alonso, E. R.; Mata, S.; Alonso, J. L. Conformational Map of Phenolic Acids. *J. Phys. Chem. A* **2018**, *122* (2), 646–651. <https://doi.org/10.1021/acs.jpca.7b08882>.
- (23) Pérez, C.; Lobsiger, S.; Seifert, N. A.; Zaleski, D. P.; Temelso, B.; Shields, G. C.; Kisiel, Z.; Pate, B. H. Broadband Fourier Transform Rotational Spectroscopy for Structure Determination: The Water Heptamer. *Chem. Phys. Lett.* **2013**, *571*, 1–15. <https://doi.org/10.1016/j.cplett.2013.04.014>.
- (24) Seifert, N. A.; Thomas, J.; Jäger, W.; Xu, Y. Rotational Spectra and Theoretical Study of Tetramers and Trimers of 2-Fluoroethanol: Dramatic Intermolecular Compensation for Intramolecular Instability. *Phys. Chem. Chem. Phys.* **2018**, *20* (43), 27630–27637. <https://doi.org/10.1039/C8CP05653F>.
- (25) Frisch, M. J.; Trucks, G. W.; Schlegel, H. B.; Scuseria, G. E.; Robb, M. A.; Cheeseman, J. R.; Scalmani, G.; Barone, V.; Petersson, G. A.; Nakatsuji, H.; Li, X.; Caricato, M.; Marenich, A. V.; Bloino, J.; Janesko, B. G.; Gomperts, R.; Mennucci, B.; Hratchian, H. P.; Ortiz, J. V.; Izmaylov, A. F.; Sonnenberg, J. L.; Williams, Ding, F.; Lipparini, F.; Egidi, F.; Goings, J.; Peng, B.; Petrone, A.; Henderson, T.; Ranasinghe, D.; Zakrzewski, V. G.; Gao, J.; Rega, N.; Zheng, G.; Liang, W.; Hada, M.; Ehara, M.; Toyota, K.; Fukuda, R.;

Hasegawa, J.; Ishida, M.; Nakajima, T.; Honda, Y.; Kitao, O.; Nakai, H.; Vreven, T.; Throssell, K.; Montgomery Jr., J. A.; Peralta, J. E.; Ogliaro, F.; Bearpark, M. J.; Heyd, J. J.; Brothers, E. N.; Kudin, K. N.; Staroverov, V. N.; Keith, T. A.; Kobayashi, R.; Normand, J.; Raghavachari, K.; Rendell, A. P.; Burant, J. C.; Iyengar, S. S.; Tomasi, J.; Cossi, M.; Millam, J. M.; Klene, M.; Adamo, C.; Cammi, R.; Ochterski, J. W.; Martin, R. L.; Morokuma, K.; Farkas, O.; Foresman, J. B.; Fox, D. J. *Gaussian 16 Rev. C.01*; Wallingford, CT, 2016.

- (26) Grimme, S.; Ehrlich, S.; Goerigk, L. Effect of the Damping Function in Dispersion Corrected Density Functional Theory. *J. Comput. Chem.* **2011**, *32* (7), 1456–1465. <https://doi.org/10.1002/jcc.21759>.
- (27) Weigend, F.; Ahlrichs, R. Balanced Basis Sets of Split Valence, Triple Zeta Valence and Quadruple Zeta Valence Quality for H to Rn: Design and Assessment of Accuracy. *Phys. Chem. Chem. Phys.* **2005**, *7* (18), 3297–3305. <https://doi.org/10.1039/B508541A>.
- (28) Kendall, R. A.; Dunning, T. H.; Harrison, R. J. Electron Affinities of the First-row Atoms Revisited. Systematic Basis Sets and Wave Functions. *J. Chem. Phys.* **1992**, *96* (9), 6796–6806. <https://doi.org/10.1063/1.462569>.
- (29) Pracht, P.; Bohle, F.; Grimme, S. Automated Exploration of the Low-Energy Chemical Space with Fast Quantum Chemical Methods. *Phys. Chem. Chem. Phys.* **2020**, *22* (14), 7169–7192. <https://doi.org/10.1039/C9CP06869D>.
- (30) Peng, C.; Bernhard Schlegel, H. Combining Synchronous Transit and Quasi-Newton Methods to Find Transition States. *Isr. J. Chem.* **1993**, *33* (4), 449–454. <https://doi.org/10.1002/ijch.199300051>.

- (31) Pickett, H. M. The Fitting and Prediction of Vibration-Rotation Spectra with Spin Interactions. *J. Mol. Spectrosc.* **1991**, *148* (2), 371–377. [https://doi.org/10.1016/0022-2852\(91\)90393-O](https://doi.org/10.1016/0022-2852(91)90393-O).
- (32) Western, C. M. PGOPHER: A Program for Simulating Rotational, Vibrational and Electronic Spectra. *J. Quant. Spectrosc. Radiat. Transf.* **2017**, *186*, 221–242. <https://doi.org/10.1016/j.jqsrt.2016.04.010>.
- (33) Bader, R. F. W. A Quantum Theory of Molecular Structure and Its Applications. *Chem. Rev.* **1991**, *91* (5), 893–928. <https://doi.org/10.1021/cr00005a013>.
- (34) Johnson, E. R.; Keinan, S.; Mori-Sánchez, P.; Contreras-García, J.; Cohen, A. J.; Yang, W. Revealing Noncovalent Interactions. *J. Am. Chem. Soc.* **2010**, *132* (18), 6498–6506. <https://doi.org/10.1021/ja100936w>.
- (35) Lu, T.; Chen, F. Multiwfn: A Multifunctional Wavefunction Analyzer. *J. Comput. Chem.* **2012**, *33* (5), 580–592. <https://doi.org/10.1002/jcc.22885>.
- (36) Lefebvre, C.; Rubez, G.; Khartabil, H.; Boisson, J.-C.; Contreras-García, J.; Hénon, E. Accurately Extracting the Signature of Intermolecular Interactions Present in the NCI Plot of the Reduced Density Gradient versus Electron Density. *Phys. Chem. Chem. Phys.* **2017**, *19* (27), 17928–17936. <https://doi.org/10.1039/C7CP02110K>.
- (37) Lefebvre, C.; Khartabil, H.; Boisson, J.-C.; Contreras-García, J.; Piquemal, J.-P.; Hénon, E. The Independent Gradient Model: A New Approach for Probing Strong and Weak Interactions in Molecules from Wave Function Calculations. *Chem. Phys. Chem.* **2018**, *19* (6), 724–735. <https://doi.org/10.1002/cphc.201701325>.

- (38) Ponce-Vargas, M.; Lefebvre, C.; Boisson, J.-C.; Hénon, E. Atomic Decomposition Scheme of Noncovalent Interactions Applied to Host–Guest Assemblies. *J. Chem. Inf. Model.* **2020**, *60* (1), 268–278. <https://doi.org/10.1021/acs.jcim.9b01016>.
- (39) Klein, J.; Khartabil, H.; Boisson, J.-C.; Contreras-García, J.; Piquemal, J.-P.; Hénon, E. New Way for Probing Bond Strength. *J. Phys. Chem. A* **2020**, *124* (9), 1850–1860. <https://doi.org/10.1021/acs.jpca.9b09845>.
- (40) Xie, F.; Seifert, N. A.; Heger, M.; Thomas, J.; Jäger, W.; Xu, Y. The Rich Conformational Landscape of Perillyl Alcohol Revealed by Broadband Rotational Spectroscopy and Theoretical Modelling. *Phys. Chem. Chem. Phys.* **2019**, *21* (28), 15408–15416. <https://doi.org/10.1039/C9CP03028J>.
- (41) Borho, N.; Xu, Y. Molecular Recognition in 1 : 1 Hydrogen-Bonded Complexes of Oxirane and Trans-2,3-Dimethyloxirane with Ethanol: A Rotational Spectroscopic and Ab Initio Study. *Phys. Chem. Chem. Phys.* **2007**, *9* (32), 4514. <https://doi.org/10.1039/b705746f>.
- (42) Watson, J. K. G. In *Vibrational spectra and structure*; Durig, J. R., Ed.; Elsevier: Amsterdam, 1977; Vol. 6, p 1.
- (43) *IGMPlot: a program revealing non-covalent interactions*. <http://igmpplot.univ-reims.fr/> (accessed 2021-11-18).
- (44) Cocinero, E. J.; Lesarri, A.; Écija, P.; Grabow, J.-U.; Fernández, J. A.; Castaño, F. Conformational Equilibria in Vanillin and Ethylvanillin. *Phys. Chem. Chem. Phys.* **2010**, *12* (39), 12486–12493. <https://doi.org/10.1039/C0CP00585A>.
- (45) Lane, J. R.; Contreras-García, J.; Piquemal, J.-P.; Miller, B. J.; Kjaergaard, H. G. Are Bond Critical Points Really Critical for Hydrogen Bonding? *J. Chem. Theory Comput.* **2013**, *9* (8), 3263–3266. <https://doi.org/10.1021/ct400420r>.

- (46) Miller, B. J.; Lane, J. R.; Kjaergaard, H. G. Intramolecular OH $\cdots\pi$  Interactions in Alkenols and Alkynols. *Phys. Chem. Chem. Phys.* **2011**, *13* (31), 14183–14193. <https://doi.org/10.1039/C1CP21190K>.
- (47) Cocinero, E. J.; Basterretxea, F. J.; Écija, P.; Lesarri, A.; Fernández, J. A.; Castaño, F. Conformational Behaviour, Hydrogen Bond Competition and Intramolecular Dynamics in Vanillin Derivatives: Acetovanillone and 6-Hydroxy-3-Methoxyacetophenone. *Phys. Chem. Chem. Phys.* **2011**, *13* (29), 13310–13318. <https://doi.org/10.1039/C0CP02418J>.
- (48) Cocinero, E. J.; Lesarri, A.; Écija, P.; Basterretxea, F.; Fernández, J. A.; Castaño, F. Competing Hydrogen Bonding in Methoxyphenols: The Rotational Spectrum of o-Vanillin. *J. Mol. Spectrosc.* **2011**, *267* (1), 112–117. <https://doi.org/10.1016/j.jms.2011.02.009>.
- (49) Schnitzler, E. G.; Jäger, W. The Benzoic Acid–Water Complex: A Potential Atmospheric Nucleation Precursor Studied Using Microwave Spectroscopy and Ab Initio Calculations. *Phys. Chem. Chem. Phys.* **2014**, *16* (6), 2305–2314. <https://doi.org/10.1039/C3CP54486A>.
- (50) Ouyang, B.; Howard, B. J. High-Resolution Microwave Spectroscopic and Ab Initio Studies of Propanoic Acid and Its Hydrates. *J. Phys. Chem. A* **2008**, *112* (36), 8208–8214.
- (51) Fernández-Ramos, A.; Ellingson, B. A.; Meana-Pañeda, R.; Marques, J.; Truhlar, D. G. Symmetry Numbers and Chemical Reaction Rates. *Theor. Chem. Acc.* **2007**, *118* (4), 813–826.
- (52) *EAS Weather Station | Earth and Atmospheric Sciences*. <https://www.ualberta.ca/earth-sciences/facilities/weather.html> (accessed 2022-03-08).
- (53) Messer, J. K.; De Lucia, F. C.; Helminger, P. The Pure Rotational Spectrum of Water Vapor—a Millimeter, Submillimeter, and Far Infrared Analysis. *Int. J. infrared millim. waves* **1983**, *4* (4), 505–539.

- (54) Organization, W. M. *Guide to Instruments and Methods of Observation*; WMO Geneva, 2018; Vol. 1.
- (55) G. Schnitzler, E.; Jäger, W. The Benzoic Acid–Water Complex: A Potential Atmospheric Nucleation Precursor Studied Using Microwave Spectroscopy and Ab Initio Calculations. *Phys. Chem. Chem. Phys.* **2014**, *16* (6), 2305–2314. <https://doi.org/10.1039/C3CP54486A>.
- (56) Schnitzler, E. G.; Zenchyzen, B. L.; Jäger, W. Rotational Spectroscopy of the Atmospheric Photo-Oxidation Product o-Toluic Acid and Its Monohydrate. *Phys. Chem. Chem. Phys.* **2016**, *18* (1), 448–457.

# 5

## Shapes of Benzyl Benzoate: A Rotational Spectroscopic and Computational Study

### 5.1. Introduction

Non-covalent interactions between aromatic molecules have long fascinated researchers in physics, chemistry, biology, and materials science.<sup>1,2</sup> Their important roles in, for example, organic photovoltaic devices,<sup>3</sup> single-molecule charge transport<sup>1</sup> and the design of molecular motors,<sup>4</sup> are increasingly recognized. In larger, more extensive aromatic systems, the structural motifs with the  $\pi$ - $\pi$  stacking (face-to-face) between aromatic rings are prevalent in biological contexts and the aforementioned applications. However, some unusual binary structural motifs in these larger aromatic systems have also been reported. For example, in the case of the perylene bisimide dimers formed in helium nanodroplets,<sup>5</sup> several binding motifs featuring two aromatic planes perpendicular to each other were observed. The physical origin of  $\pi$ - $\pi$  stacking interactions has been widely debated. Computational analyses of small aromatic systems by Grimme and others<sup>6,7</sup> suggest that  $\pi$ - $\pi$  stacking is merely topologically favored, owing to additive dispersive forces and a reduction in Pauli exchange repulsion. These authors advocated using the term as a positional descriptor rather than implying a distinct type of force or interaction.

Jet-cooled rotational spectroscopic studies of aromatic complexes are crucial for validating the theoretical results, particularly since they can provide detailed structural and dynamical information without the perturbation of environmental effects, such as solvents, for a direct comparison with theoretical predictions. For instance, Arunan and Gutowsky<sup>8</sup> first reported the rotational spectrum of the benzene dimer, which was later analyzed in detail by Schnell et al.<sup>9</sup> Their analysis revealed a global minimum with a T-shape geometry, featuring CH $\cdots\pi$  interactions. Moreover, the analysis uncovered that the nearly free internal rotation of the benzene ring located in the cap is the tunneling process responsible for the quartet splittings of the rotational transitions initially reported, highlighting the rich information contained in the rotational spectrum.<sup>9</sup> The second minimum structure, i.e., the  $\pi$ - $\pi$  stacking geometry with two parallel and displaced benzene rings, was predicted to be only 0.4 kJ mol<sup>-1</sup> less stable than the global minimum,<sup>10</sup> although it was not observed in the jet-cooled rotational spectroscopic experiments.<sup>8,9</sup> More recently, rotational spectroscopic studies have demonstrated that both substituents and the size of the aromatic subunits can have profound effects on the energy ordering of different binding motifs. For example, while the phenol dimer exhibits a linear hydrogen bonding motif,<sup>11</sup> the 1-naphthol dimer was shown to adopt a V-shaped, partially overlapping  $\pi$ - $\pi$  stacked structure with no canonical hydrogen bonds between the subunits.<sup>12</sup>

The molecular target of the current work is benzyl benzoate (BnBz), a flexible aromatic ester (RC(=O)-O-R') containing two benzene rings. BnBz is emitted by several plants, including Orchids,<sup>13</sup> Violets,<sup>14</sup> and *Mirabilis Jalapa*.<sup>15</sup> Its roles, such as pollinator attraction and defense against white backed planthoppers (insects that inhibit plant growth in the Japonica rice plants), have also been investigated.<sup>15</sup> Additionally, BnBz is an active ingredient in non-agricultural pesticides and is used as a remedy against scabies, a parasitic skin infection.<sup>16</sup> While BnBz is a

naturally occurring volatile organic compound, its potential role in the formation of secondary organic aerosols (SOAs) has not yet been explored, although one of its precursors, benzyl alcohol, has been studied in relation to the SOA formation.<sup>17</sup> So far, no structural information on BnBz has been reported. One may anticipate that detailed structural information facilitated by the intramolecular non-covalent interactions of BnBz would be beneficial for understanding its biological properties and its potential role in the SOA formation.

In this study, we employed jet-cooled chirped pulse Fourier transform microwave (CP-FTMW) spectroscopy in combination with computations to explore the conformational landscape and non-covalent intramolecular interactions in BnBz. Specifically, our aim was to gain insight into how the two separate aromatic groups of BnBz interact with each other and how the balance of various interactions, including the CH $\cdots$ O contacts, leads to the formation of different structural motifs. Additionally, we compared the conformational diversity of BnBz with that of the benzene dimer, where the two aromatic subunits are independent of each other, to understand the role of the bridging ester functional group. Furthermore, we detected and assigned the rotational spectra of extensive <sup>13</sup>C isotopologues of the observed BnBz conformers, utilizing the resulting rotational constants to establish the corresponding conformer geometries.

## **5.2. Methods**

### **5.2.1. Computational Details**

We applied CREST (Conformer-Rotamer Ensemble Sampling Tool)<sup>18</sup> by Grimme and co-workers to strive for an as complete as possible sampling of the conformational space of BnBz. This conformational searching tool has been utilized to explore conformational landscapes of highly flexible organic molecules such as perillyl alcohol<sup>19</sup> and tetrahydro-2-furoic acid<sup>20</sup> where even more subtle conformational variations associated with the OH pointing directions and the

ring puckering conformations were effectively captured. Twenty-eight CREST structural candidates were generated within an energy window of 25 kJ mol<sup>-1</sup> and subsequently screened using CREGEN in CREST to generate two distinct geometry candidates. These two were optimized at the B3LYP<sup>21</sup>-D3BJ/def2-TZVP level with the D3 empirical dispersion corrections<sup>22</sup> and Becke-Johnson damping.<sup>23</sup> In addition, harmonic frequency calculations were also carried out to verify true minimum nature of the optimized geometries and provide the corresponding zero-point corrected energies. All final geometry optimizations and frequency calculations were performed using the Gaussian16 program package.<sup>24</sup> The relevant keywords used are summarized in Point C.1, Appendix C (C). Additionally, relaxed one-dimension (1D) potential energy surface (PES) scans were also carried out at the same level of theory to examine possible conformational interconversion barriers.

The Quantum Theory of Atoms in Molecules (QTAIM)<sup>25</sup> and Non-covalent interactions (NCI)<sup>26</sup> approaches, as implemented in Multiwfn,<sup>27</sup> were applied to further examine the intramolecular non-covalent interactions in BnBz. Furthermore, atom pair interaction strengths were evaluated using the intrinsic bond strength index (IBSI),<sup>28</sup> as implemented in IGMPLOT.<sup>29</sup> For spectral simulation and spectroscopic fitting, Western's Pgopher program<sup>30</sup> and Pickett's SPCAT/SPFIT<sup>31</sup> suite were used.

### **5.2.2. Experimental Details**

A BnBz sample (99% purity) was obtained from Sigma Aldrich and used without further purification. BnBz was placed directly inside a custom-built nozzle cap<sup>32</sup> of a General Valve, Series 9, pulsed nozzle and heated to 145 °C. Helium, neon, and argon were used as carrier gases at a backing pressure of 276, 345, and 345 kPa, respectively. Rotational spectra in the 2 to 6 GHz range were measured with a custom built CP-FTMW spectrometer,<sup>33,34</sup> based on the design by

Pate and coworkers.<sup>35</sup> Briefly, a 4  $\mu$ s long chirped-pulse, from 2 to 6 GHz, was generated using a 12 GS/s arbitrary waveform generator and amplified with a travelling wave tube amplifier. The amplified MW pulse ( $\sim$ 100 W) was then broadcasted into the vacuum chamber via a horn antenna and intercepted a molecular expansion perpendicularly. The free induction decay (FIDs) of the molecular emission signals were collected by the receiving horn antenna, positioned oppositely to the broadcasting horn antenna. The FIDs were digitized with a 25 GS/s oscilloscope, averaged, and Fourier transformed to produce the frequency spectra. A total of 2.3, 1.5, and 0.15 million FIDs were collected with helium, neon and argon, respectively.

### 5.3. Results and Discussion

#### 5.3.1. Rotational Assignments and Conformational Identification

The CREST conformational search produced two low energy BnBz conformers. Generally, the conformational flexibility of BnBz is associated with the four dihedral angles,  $\tau_1$  to  $\tau_4$ , corresponding to rotation about the four  $\sigma$  bonds in BnBz, as also shown in Figure 5.1. For completeness, we also carried out additional manual 1D-PES scans along these angles (vide infra). To view these geometries, we started with the hypothetical planar BnBz geometry. As it turned out, in both low energy conformers, the benzoate ( $C_6H_5-COO$ ) portion remained planar and so did the benzyl ( $C_6H_5-CH_2$ ) group. Rotating the benzene ring of benzyl by  $90^\circ$  led to the second most stable conformer, BnBz-*t*. BnBz-*t* has a symmetry plane ( $C_6H_5-COO-CH_2$ ) which bisects the benzene ring of benzyl. Next, we rotated the benzyl group of BnBz-*t* along  $\tau_2$ . This resulted in the corresponding 1D-PES scan depicted in Figure 5.2, together with the optimized geometries of BnBz-*g* and BnBz-*t* and the associated transition states (TSs). Rotating the benzyl group of BnBz-*t* along  $\tau_2$  in the forward direction (large  $\tau$  values) led to the most stable conformer, BnBz-*g*, which has a *gauche*<sup>+</sup> configuration, whereas the rotation in the backward

direction generated the mirror image of BnBz-g, which has a *gauche*- configuration. Similarly, rotating forward through TS2 also produced the *gauche*- configuration of BnBz-g. Since we cannot tell the pair of the mirror images apart using rotational spectroscopy, we decided to name them simply as BnBz-g, a chiral conformer.

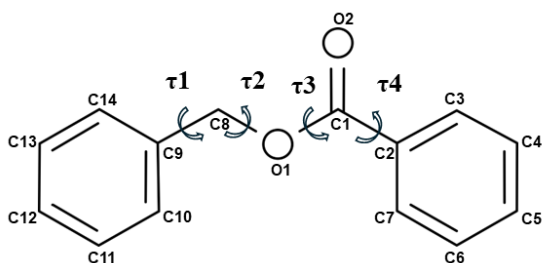


**Figure 5.1.** The four dihedral angles,  $\tau_1$  to  $\tau_4$ , associated with the flexibility of BnBz and the atom numbering.

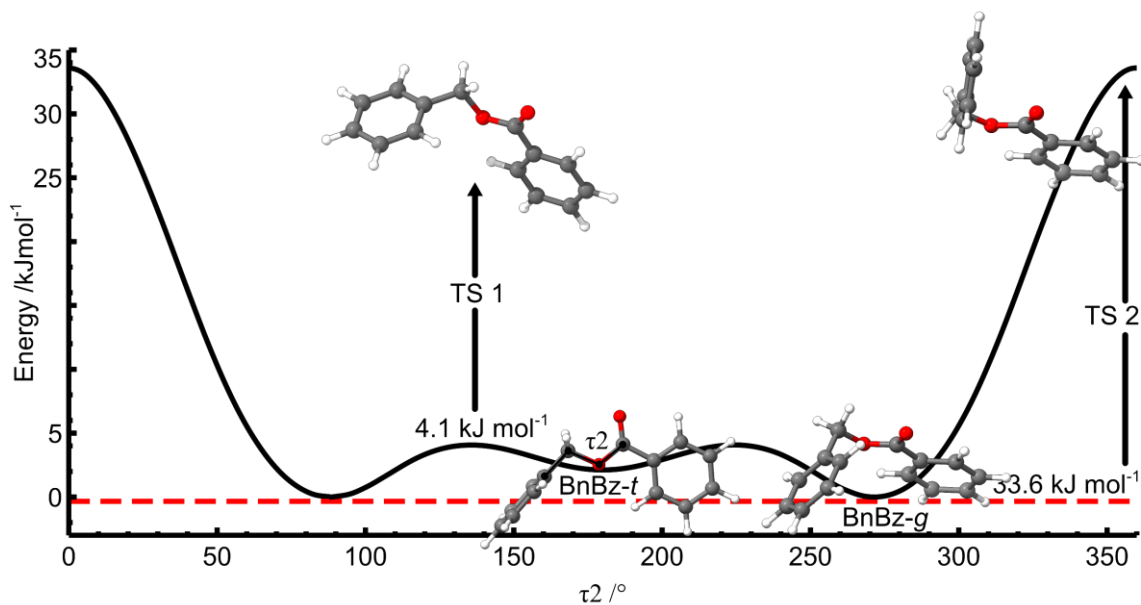


**Figure 5.2.** The relaxed 1D-PES scan along the  $\tau_2$  dihedral angle. The optimized geometries of BnBz-*t*, BnBz-*g*, and the related transition states are shown. The dihedral angle values for ( $\tau_1$ ,  $\tau_2$ ,  $\tau_3$ ,  $\tau_4$ ) for BnBz-*t* and BnBz-*g* are (89.4°, 180°, 180°, 0.0°) and (92.3°, -88.6°, 177.6°, -1.8°), respectively.

BnBz-*g* is approximately  $1.0 \text{ kJ mol}^{-1}$  more stable than BnBz-*t* and is connected to the latter via a conversion barrier of  $4.1 \text{ kJ mol}^{-1}$ . The relaxed 1D-PES scans of BnBz-*g* along the  $\tau_1$ ,  $\tau_3$ , and  $\tau_4$  are shown in Figure 5.3, while the corresponding values of BnBz-*t* are shown in Figure 5.4. The potential energy scans along  $\tau_1$  and  $\tau_3$ , are barriers to rotation of  $4.6 \text{ kJ mol}^{-1}$  and  $25.4 \text{ kJ mol}^{-1}$  respectively for BnBz-*g* and  $3.1 \text{ kJ mol}^{-1}$  and  $27.4 \text{ kJ mol}^{-1}$  for BnBz-*t*. The potential energy scans of  $\tau_4$  for BnBz-*g* and BnBz-*t* shows that the peripheral structure (atoms that do not make up  $\tau_4$ ), relax to what appears to be two stable high energy conformation along the  $\tau_4$  scan, see Figure 5.3 and Figure 5.4. The structures at those minima were further optimized and their frequencies calculated to confirm that these are stable conformers that were previously unidentified by CREST. These conformers were unidentified by CREST because of the energy cut off window which suggests a higher energy window needs to be used for a more comprehensive conformational search. Note that the  $\tau_4$  scan for BnBz-*g* and BnBz-*t* leads to the same high energy minima. The two high energy conformers along with the two found by CREST can be seen Figure 5.5. The two new high energy minima are named BnBz-PD and BnBz-TT because their structures are reminiscent of a parallel displaced (PD)  $\pi$ - $\pi$  stacking<sup>36</sup> and a tilted T-shape<sup>9</sup> (TT). The computational spectroscopic parameters and energy ordering can be seen Table 5.1. In these scans, no new low energy conformers were identified.

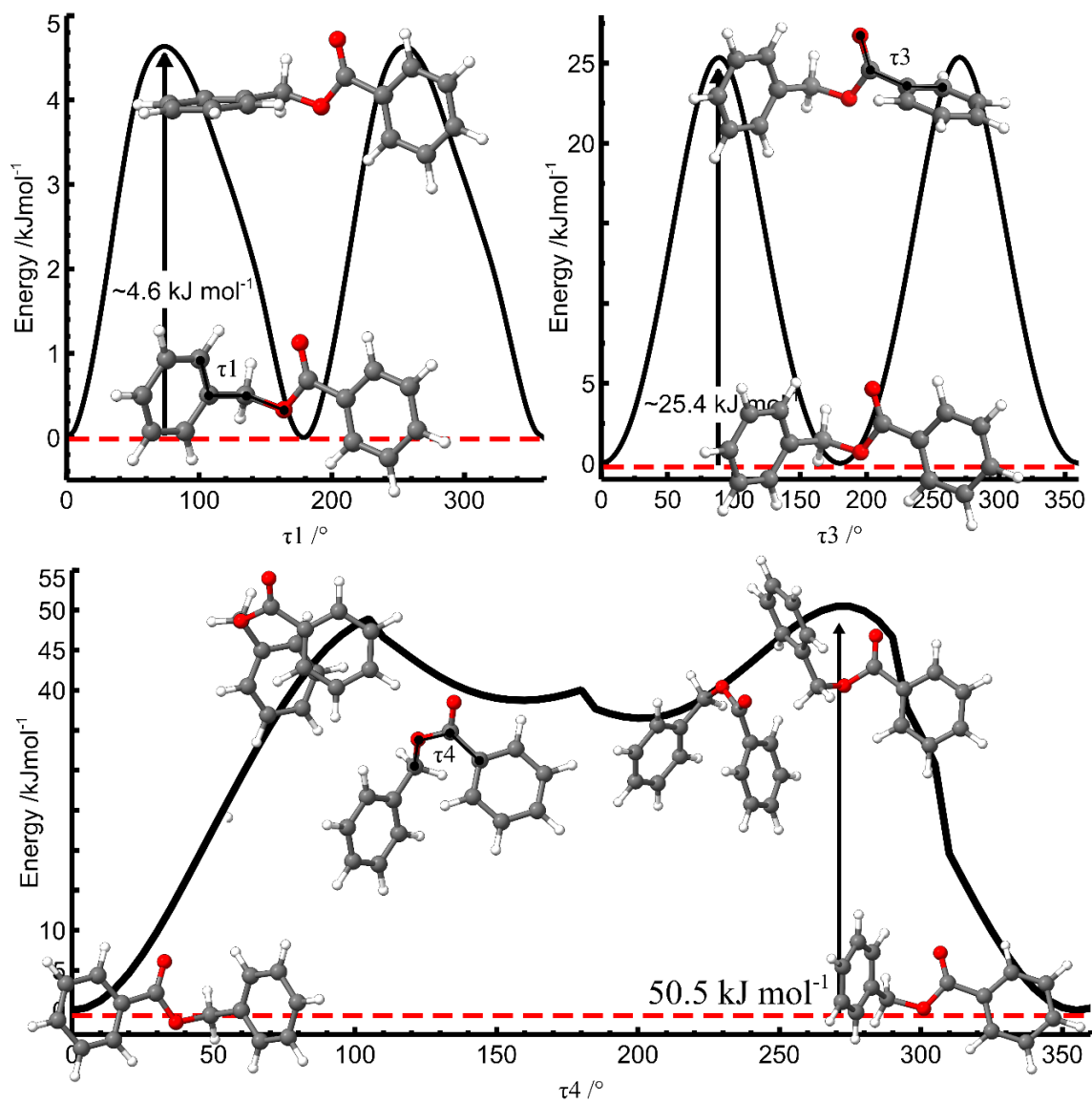


**Figure 5.3.** The relaxed 1D-PES scans starting with BnBz-g along  $\tau_1$ ,  $\tau_3$ , and  $\tau_4$ .

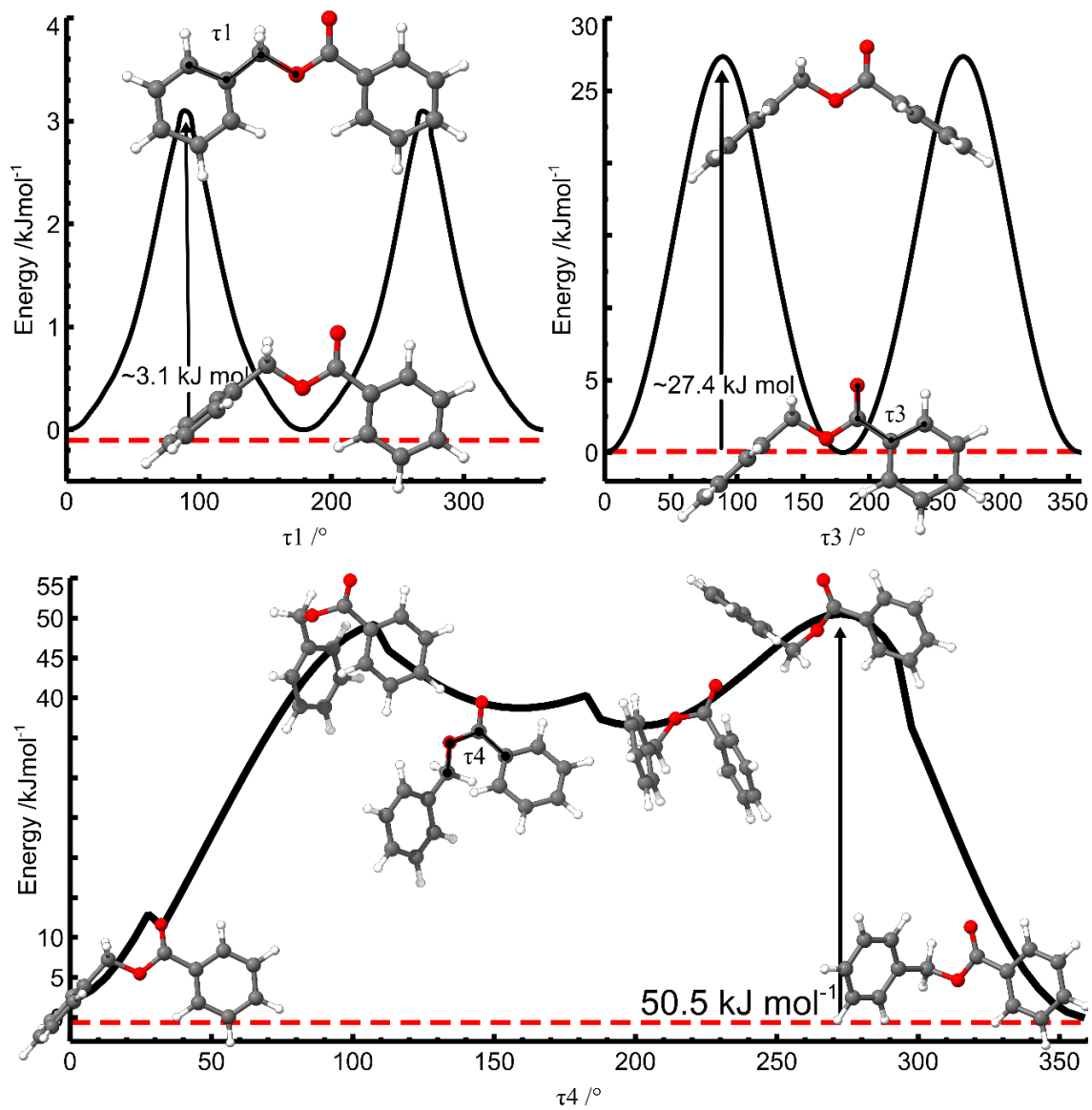


**Figure 5.4.** The relaxed 1D-PES scans starting with BnBz-t along  $\tau_1$ ,  $\tau_3$ , and  $\tau_4$ .

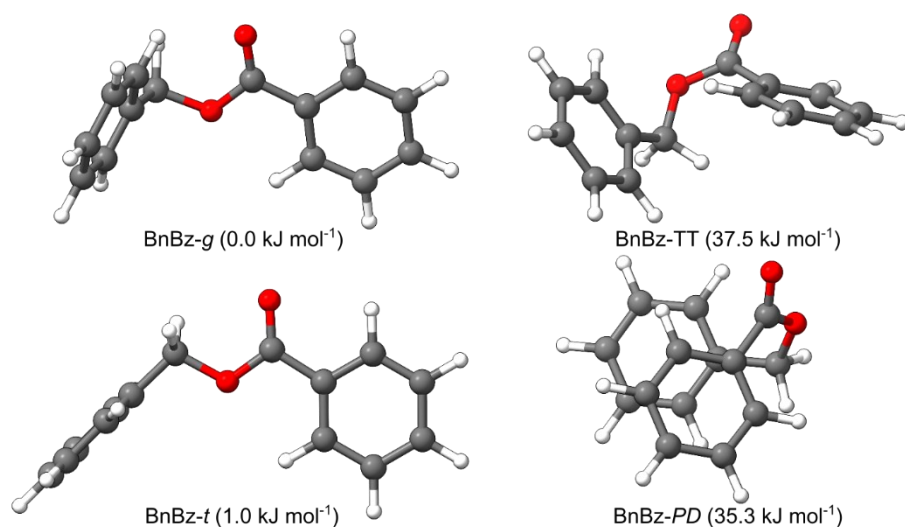


**Figure 5.5.** Stable conformers of BnBz and their relative energies to the lowest energy conformer (BnBz-g).

**Table 5.1.** Theoretical (B3LYP-D3BJ/def2-TZVP) spectroscopic parameters for the four conformers of BnBz.

	BnBz-g	BnBz-t	BnBz-PD	BnBz-TT
$\Delta E^a$ /kJ mol <sup>-1</sup>	0	1.0	35.3	37.5
$\Delta G^b$ /kJ mol <sup>-1</sup>	1.8	0.0	39.1	39.2
$P^c$ /%	37.1	62.9	0	0
$A$ /MHz	1243.8	1297.4	725.4	908.8
$B$ /MHz	252.5	233.1	527.7	362.8
$C$ /MHz	244.1	212.5	400.6	289.6
$\Delta J$ /kHz	0.0303	0.0073	0.2907	0.1095
$\Delta K$ /kHz	2.079	0.4061	0.7491	0.7833
$\Delta_{JK}$ /kHz	-0.219	0.222	-0.824	-0.482
$\delta_J$ /kHz	-0.00143	0.0015	0.0902	0.0290
$\delta_K$ /kHz	-0.0781	-0.6759	0.0622	0.0985
$ \mu_a ,  \mu_b ,  \mu_c $ /Debye	0.3, 1.8, 0.1	0.6, 2.2, 0.0	1.0, 3.9, 2.2	1.4, 4.1, 1.6

<sup>a</sup> Relative zero-point energy corrected energy.

<sup>b</sup> Relative Gibbs free energy at 298 K.

<sup>c</sup> Percent abundance based on the Gibbs free energies at the source temperature of 413 K.

A dense, broadband rotational spectrum of BnBz in a helium expansion was obtained. To aid the spectral assignment, the predicted spectroscopic properties of the two low energy conformers including rotational constants, dipole moment components, quartic centrifugal distortion constants and relative energies are summarized in Table 5.2. Both BnBz-*g* and BnBz-*t* were predicted to have strong *b*-type transitions, while BnBz-*t* also exhibits weaker *c*-type transitions. The simulated spectrum of BnBz-*t* showed characteristic dense Q-branch  $K_a = 2 \leftarrow 1$  transitions centered at  $\sim 2960$  MHz and even denser Q-branch  $K_a = 3 \leftarrow 2$  transitions centered at  $\sim 4935$  MHz, whereas the dense Q-branch  $K_a = 3 \leftarrow 2$  transitions of BnBz-*t* appeared around  $\sim 5380$  MHz, See Figure 5.6. The assigned transitions were fitted using SPFIT<sup>31</sup> and the resulting spectroscopic constants of both conformers are summarized in Table 5.2, while the corresponding observed transition frequencies are provided in Table C.1.1 for BnBz-*g* and Table C.2.1 for BnBz-*t*.

**Table 5.2.** Theoretical (B3LYP-D3BJ/def2-TZVP) and experimental spectroscopic parameters for the two conformers of BnBz.

	BnBz- <i>g</i>		BnBz- <i>t</i>	
	Theory	Experiment	Theory	Experiment
$\Delta E^a$ /kJ mol <sup>-1</sup>	0	-	1.0	-
$\Delta G^b$ /kJ mol <sup>-1</sup>	1.8	-	0	-
$B_f^c$ /%	37.1	-	62.9	-
<i>A</i> /MHz	1243.8	1237.04842(10)	1297.4	1300.43887(14)
<i>B</i> /MHz	252.5	254.192472(24)	233.1	232.458052(39)
<i>C</i> /MHz	244.1	245.864530(23)	212.5	212.028730(38)
$\Delta_J$ /kHz	0.0303	0.030730(48)	0.00728	0.00709(10)
$\Delta_K$ /kHz	2.079	1.9071(25)	0.406	0.0841(43)

$\Delta_{JK}$ /kHz	-0.219	-0.16157(29)	0.222	0.66155(58)
$\delta_J$ /kHz	-0.00143	-0.0016756(84)	0.00151	0.001556(17)
$\delta_K$ /kHz	-0.0781	-0.0275(20)	-0.676	-1.7393(38)
$ \mu_a ,  \mu_b ,  \mu_c $ /Debye	0.3, 1.8, 0.1	N, Y, N	0.6, 2.2, 0.0	Y, Y, N, $ \mu_a  <  \mu_b $
$N^d$	-	271	-	256
$\sigma^e$		3.0		3.7

<sup>a</sup> Zero-point energy corrected relative energy.

<sup>b</sup> Relative Gibbs free energy at 298 K.

<sup>c</sup> Percent abundance based on the Gibbs free energies at the source temperature of 413 K.

<sup>d</sup> Number of transitions included in the fit.

<sup>e</sup> Standard deviation of the fit.

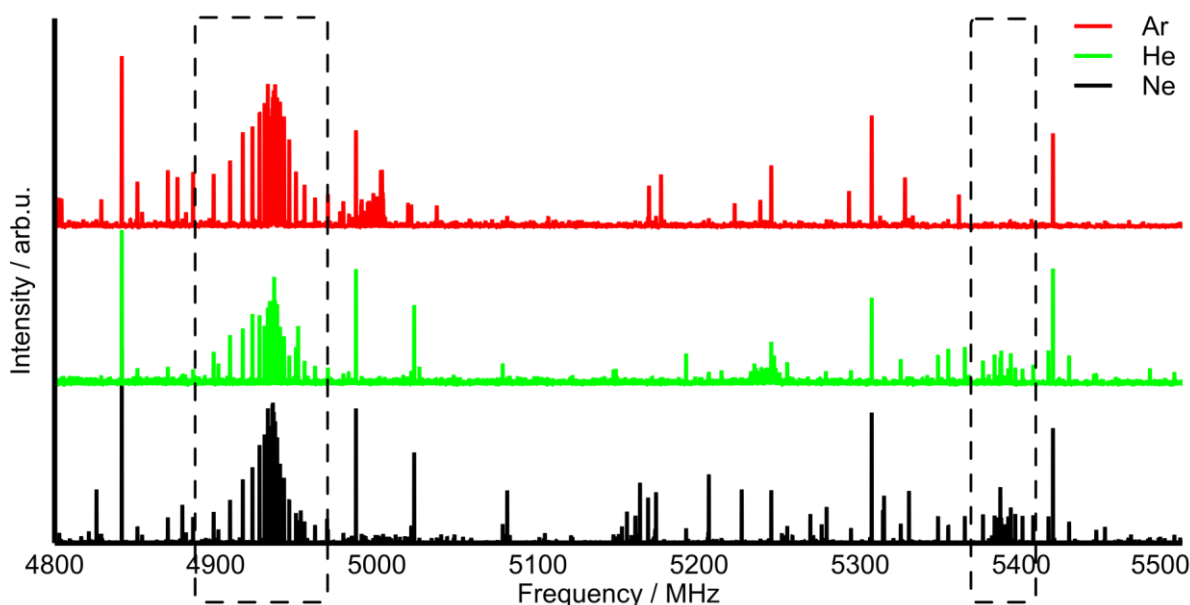


**Figure 5.6.** Experimental spectrum with argon, helium, and neon as carrier gases.

After removing the transitions belong to BnBz-*g* and BnBz-*t*, there are still many transitions with signal-to-noise ratio larger than 5 left. We were able to further assign rotational spectra of a total of 14  $^{13}\text{C}$  isotopologues of BnBz-*g* and two  $^{13}\text{C}$  isotopologues of BnBz-*t*. The experimental rotational transition frequencies are listed in Table C1.2-C1.15 for the  $^{13}\text{C}$  isotopologues of BnBz-*g*, while the corresponding frequencies of the two  $^{13}\text{C}$  isotopologues of

BnBz-*t* are provided in Tables C.2.2 and C.2.3. The resulting fitted rotational constants are summarized in Table 5.3 for all the isotopologues of BnBz-*g* and BnBz-*t*. As can be seen in Table 5.2, the difference between the respective theoretical and experimental rotational constants is less than 1%. In addition, the relative intensity trend of the different types of transitions is consistent with the theoretical electric dipole components (see Table 5.2). While the rotational spectrum of the  $^{13}\text{C}$  isotope at every single C atom in BnBz-*g* were observed and assigned, the weaker intensity of the less abundance BnBz-*t* makes it difficult to achieve the same. On the other hand, for BnBz-*t*, the presence of the symmetry plane which bisects the benzyl benzene ring, makes C10 and C14, and C11 and C13 (see Figure 5.1 for atom numbering), equivalent to each other, leading to a natural abundance of  $\sim 2\%$  for the  $^{13}\text{C}$  substitution at these particular C positions. This explains why only two  $^{13}\text{C}$  isotopologues of BnBz-*t* were observed experimentally. The extensive isotopic data, together with the other pieces of evidence discussed above, unambiguously confirmed the identities of the observed conformers.

**Table 5.3.** Experimental rotational constants of the  $^{13}\text{C}$  isotopologues of BnBz-*g* and BnBz-*t*.<sup>a</sup>

	$^{13}\text{C}1$ BnBz- <i>g</i>	$^{13}\text{C}2$ BnBz- <i>g</i>	$^{13}\text{C}3$ BnBz- <i>g</i>	$^{13}\text{C}4$ BnBz- <i>g</i>
<i>A</i>	1234.54256(82)	1236.9391(11)	1232.78545(77)	1232.88921(53)
<i>B</i>	254.08319(57)	253.65852(16)	253.08531(19)	251.89566(19)
<i>C</i>	245.74986(28)	245.36364(14)	244.72618(15)	243.78381(12)
<i>N</i>	19	16	14	19
$\sigma$	6.7	7.1	6.4	5.2
	$^{13}\text{C}5$ BnBz- <i>g</i>	$^{13}\text{C}6$ BnBz- <i>g</i>	$^{13}\text{C}7$ BnBz- <i>g</i>	$^{13}\text{C}8$ BnBz- <i>g</i>
<i>A</i>	1233.68021(68)	1229.49934(87)	1232.76566(43)	1228.18973(59)
<i>B</i>	251.51428(13)	252.47036(29)	253.42196(10)	253.62269(14)
<i>C</i>	243.37838(14)	243.96126(18)	244.997387(87)	245.67699(11)
<i>N</i>	17	15	21	19
$\sigma$	6.2	6.9	4.5	5.9
	$^{13}\text{C}9$ BnBz- <i>g</i>	$^{13}\text{C}10$ BnBz- <i>g</i>	$^{13}\text{C}11$ BnBz- <i>g</i>	$^{13}\text{C}12$ BnBz- <i>g</i>
<i>A</i>	1235.87707(93)	1231.73132(71)	1229.53634(50)	1230.72915(63)
<i>B</i>	253.47104(63)	253.13109(16)	252.309449(65)	251.70806(12)
<i>C</i>	245.23547(32)	244.69426(12)	243.897811(60)	243.75592(11)
<i>N</i>	16	19	16	18
$\sigma$	7.3	6.2	3.0	5.6

	$^{13}\text{C13}$ BnBz-g	$^{13}\text{C14}$ BnBz-g	$^{13}\text{C10/14}$ BnBz-t	$^{13}\text{C11/13}$ BnBz-t
<i>A</i>	1230.59739(64)	1233.57342(56)	1295.6489(34)	1293.7989(15)
<i>B</i>	252.32416(16)	253.25631(14)	231.3263(42)	230.4763(22)
<i>C</i>	244.18256(11)	244.85867(11)	211.2224(17)	210.46637(88)
<i>N</i>	21	21	10	9
$\sigma$	5.9	5.8	5.9	4.6

<sup>a</sup> *A*, *B*, and *C* are rotational constants in MHz, *N* is the number of transitions included in the fit,  $\sigma$  is the standard deviation of the fit in kHz. All quartic centrifugal distortion constants are fixed at the corresponding values of the parent species.

### 5.3.2. Conformational Conversion Cooling

Experimentally, it was possible to estimate the percentage abundances of the two detected conformers based on the observed rotational transition intensities, estimated rotational temperature, and the theoretical electric dipole moment components. A rotation temperature of 1 K was estimated for the experiments carried out with helium, neon, and argon carrier gas, while the sample source temperature was kept at 140 °C. Using the strong *b*-type transitions in the 2.5-5.5 GHz region, the percentage abundances of BnBz-g:BnBz-t were estimated to be 80:20, 90:10, and 100:0 in helium, neon, and argon, respectively. Clearly, heavier rare gas provides significantly more effective conformational cooling, resulting noticeable relative decrease in the BnBz-t intensity and finally its non-observation in argon, see Figure 5.6. These observations provide unambiguous experimental evidence that BnBz-g is the global minimum. It is interesting to note that while the zero-point energy corrected energies place BnBz-g as more stable than BnBz-t, the free energies suggest the opposite ordering. Logically, one would use the free energies for estimating population abundance in this case, although free energy or relative free energy values are known to have considerable uncertainties. Therefore, it is unclear which conformer would be more stable before the actual experiment. These results highlight the important role such conformation-specific studies play in benchmarking theoretical energy terms.

Furthermore, the experimental results with different carrier gases demonstrated that the conformational conversion barrier from BnBz-*t* to BnBz-*g* is relatively low. Indeed, the relaxed 1D-PES scan along the  $\tau_2$  dihedral angle (Figure 5.2) shows that the interconversion barrier from BnBz-*t* to BnBz-*g* is  $\sim 1.9$  kJ mol<sup>-1</sup>, lower than the empirical cutoff value of 4.8 kJ mol<sup>-1</sup> proposed by Ruoff et al.<sup>37</sup> On the other hand, it has been increasingly recognized that other factors, such as interconversion barrier width and the number of involved heavy atoms, may also play noticeable role in cooling efficiency as demonstrated in, for example, jet-cooled rotational spectroscopic study of vicinal diols<sup>38</sup> and fluoroalcohols and their complexes.<sup>39,40</sup> This helped to explain why BnBz-*t* was observed in helium expansion in the first place.

### 5.3.3. Experimental Structural Parameters

Using the experimental rotational constants of the 15 assigned C isotopologues of BnBz-*g*, we carried out substitution structural analyses,  $r_s$ . The experimental rotational constants and their uncertainties of the parent and <sup>13</sup>C rare isotopologues of BnBz-*g* were directly utilized for the substitution structural analyses using the Kraitchman's equations.<sup>41,42</sup> The Cartesian coordinates in the parent principal inertia axis system of every substituted carbon atoms were calculated using the KRA and EVAL programs,<sup>27</sup> and the results are summarized in Table C.3, along with their Costain errors. The associated bond lengths, angles, and dihedral angles of BnBz-*g* are summarized in Table 5.3., as well as the corresponding theoretical  $r_e$  values. Similar analyses were carried out for BnBz-*t* with the substitution coordinates listed in Table C.4, Appendix C and the  $r_s$ , and  $r_e$  structural parameters also summarized in Table 5.3. In general, the  $r_s$  structural parameters exhibit a good agreement with the theoretical equilibrium values, since the substitution procedure helps to remove some effects caused by the vibrational contributions.

**Table 5.4.** The substitution and theoretical equilibrium structural parameters<sup>a</sup> of BnBz-*g*

	BnBz- <i>g</i>		BnBz- <i>t</i>	
	$r_s$	$r_e$	$r_s$	$r_e$
r(C1-C2)	1.523(7)	1.487		1.487
r(C2-C3)	1.40(1)	1.395		1.395
r(C3-C4)	1.395(2)	1.388		1.386
r(C4-C5)	1.386(4)	1.391		1.391
r(C5-C6)	1.411(7)	1.391		1.391
r(C6-C7)	1.386(5)	1.386		1.388
r(C7-C2)	1.38(1)	1.395		1.395
r(C8-C9)	1.521(8)	1.501		1.497
r(C9-C10)	1.44(8)	1.395		1.393
r(C10-C11)	1.383(4)	1.389	1.32(3)	1.389
r(C11-C12)	1.412(4)	1.390		1.390
r(C12-C13)	1.373(5)	1.390		1.390
r(C13-C14)	1.394(7)	1.389	1.32(3)	1.389
r(C14-C9)	1.36(7)	1.394		1.393
∠(C2-C1-C8)	145.1(5)	145.1		145.7
∠(C9-C8-C1-C2)	104(3)	98.5		0.0
∠(C10-C9-C8-C1)	-113.0(4)	-118.5		-89.4

<sup>a</sup>  $r_s$ ,  $r_e$  are substituted, and theoretical equilibrium (at the B3LYP-D3BJ/def2-TZVP level) structural parameters. The bond lengths are in unit of Å and the angle values are in °. The atom numbers are provided in Figure 5.1. The errors in the parentheses are derived from the Costain errors listed in Tables C.3 and C.4.

### 5.3.4. Intramolecular Noncovalent Interactions

As shown in Figure 5.1, rotation of the benzyl group along  $\tau_2$  generates the two low energy BnBz conformers. While BnBz-*t* has the benzyl and benzoate groups extending in opposite directions, the two benzene rings were brought closer to each other in BnBz-*g*. To gain further insight into how intramolecular non-covalent interactions, among other factors, help to stabilize BnBz-*g* relative to BnBz-*t*, we carried out the QTAIM, NCI, and IBSI analyses. The results for these two conformers are depicted in Figure 5.7. In the QTAIM plots, only one bond critical point (BCP) for intramolecular interaction, associated with the ring H (of benzoate

benzene) $\cdots$ O=C contact, was identified for BnBz-*g*, while none was found for BnBz-*t*, highlighting certain limitations with the QTAIM approach. In the NCI plots, multiple attractive contacts, in green to blue colors, were identified. The orientation of the benzyl group in BnBz-*g* is mainly stabilized by an intramolecular hydrogen bond between the carbonyl O and a methylene H, as well as other weaker attractive interactions including the ring H (of benzoate benzene) $\cdots$ O=C, ring H (of the benzyl benzene) $\cdots$ O=C, and ring H (of benzoate benzene) $\cdots$ O(ester) interactions. In BnBz-*t*, three of the aforementioned attractive interactions are also present although to a lesser degree, while the C-H(of the benzyl benzene ring) $\cdots$ O=C interaction is missing. We note that the intramolecular hydrogen bond between the carbonyl O and the methylene H is missing a bond critical point in the corresponding QTAIM plot.

More recently, a new way, i.e., IBSI, was proposed to characterize bond strength, including non-covalent bonds.<sup>21</sup> Based on an analysis of the local electron density distribution with the independent gradient model,<sup>43</sup> IBSI quantifies the relative strength of a bond with a single value which is correlated to its local bond stretching force constant. This approach was successfully utilized to evaluate the weak intramolecular interactions in vanillic acid<sup>44</sup> and in 1- and 2-naphthol<sup>45</sup> monomers. The IBSI values of BnBz all fall in the noncovalent scale provided in the pervious benchmarks<sup>21</sup> and follow the same relative NCI strength trend revealed by the NCI analysis. For example, the strongest interaction between the carbonyl O and a methylene H by the NCI analysis has the highest IBSI value of 0.027. Similarly, the other weaker interactions in BnBz-*g* and BnBz-*t*, uncovered in the NCI analysis, have the IBSI values ranging from 0.015 to 0.023. Overall, both NCI and IBSI analyses provide a consistent intramolecular non-covalent interaction picture where the intramolecular hydrogen bond between the carbonyl O and a methylene H is largely responsible for the preference of BnBz-*g* over BnBz-*t*.

In both low energy BnBz monomer conformers, no indication of  $\pi$ - $\pi$  or CH $\cdots\pi$  interactions was provided by any of the analyses utilized here. This is presumably because the short C(=O)-O bridge imposes strong steric effect, preventing a close approach of the two aromatic rings. The higher energy conformers however appear to have  $\pi$ - $\pi$  or CH $\cdots\pi$  interactions. This observation leads us to wonder if the monomer of BnBz was more flexible, would these interactions be involved in the lowest energy conformer. By adding one and two methylene groups to BnBz, we form ethyl benzyl benzoate (eBnBz) and propyl benzyl benzoate (pBnBz), respectively. Geometry optimizations at the B3LYP-D3BJ/def2-TZVP level provide two structural candidates and the subsequent NCI analyses of them are shown in Figure 5.8. Interestingly, the benzene rings begin to approach each other to form a folded parallel displaced  $\pi$ - $\pi$  stacking configuration in eBnBz. The longer chain flexibility affords pBnBz to form a fully folded parallel displaced  $\pi$ - $\pi$  stacking structure where a blanket of  $\pi$ - $\pi$  stacking attractive interactions was identified in the NCI plot. It would be of considerable interest to experimentally probe these larger molecular systems in the same series to appreciate the competition among different factors which lead to the very different geometrical outcomes including the  $\pi$ - $\pi$  stacking conformations for the benzyl benzoate series.

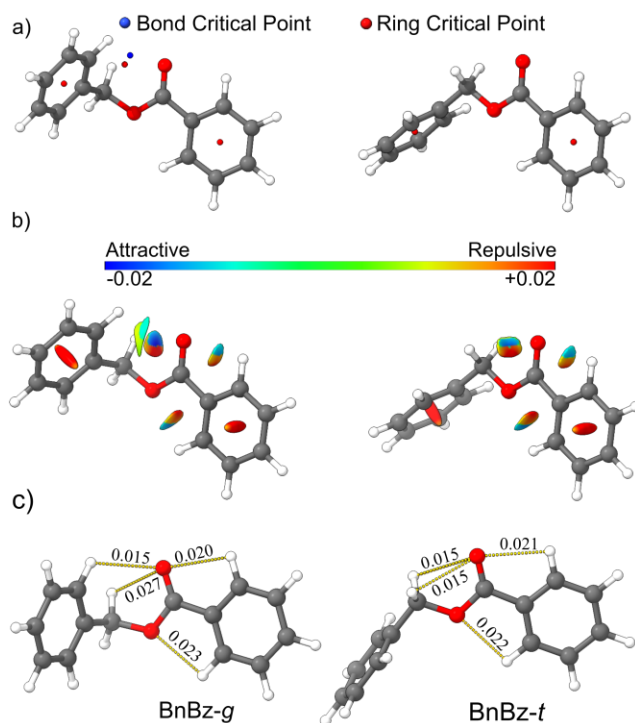


**Figure 5.7.** The QTAIM, NCI, and IBSI analyses of the two observed BnBz conformers. The calculations were done at the B3LYP-D3BJ/def2-TZVP level of theory. The isosurfaces in the NCI plots have reduced electron density gradient  $s=0.6$ . The intrinsic bond strength indices between atom pairs are indicated for BnBz-*g* and BnBz-*t*.

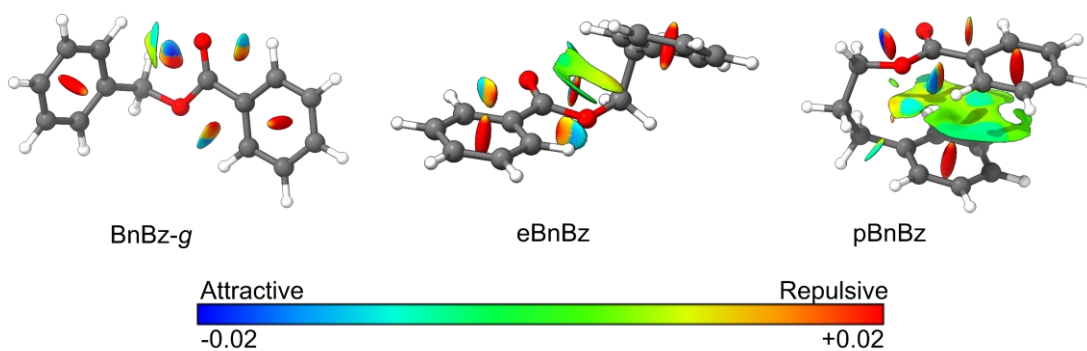


**Figure 5.8.** The NCI plots of the three optimized geometries of benzyl benzoate (BnBz), ethyl benzyl benzoate (eBnBz), and propyl benzyl benzoate (pBnBz).

### 5.3.5. BnBz Dimer

Once the assigned rotational transitions associated with BnBz-*g* and BnBz-*t* and their isotopologues were removed, the rotational transitions associated with the dimer were found. The dimer was studied using a similar procedure to the monomer and the preliminary findings are presented below.

#### 5.3.5.1. Rotational Assignment and Conformational Identification

A total of 128 unique dimer conformers were identified from the CREST search (Table C.5). They are labelled by the monomer subunits involved in the dimer, i.e., -*g* for *gauche* and -*t* for *trans*, and in order of energy, with 1 indicating the lowest energy conformer. The 128 dimer structures can be organized into four families, i.e.,  $g^-g^-$ ,  $g^-g^+$ , *tg*, and *tt*, which describe the geometries of the subunits (see Table C.5). Of the 128 conformers, 28 are in the  $g^-g^-$ , 36 in the  $g^-g^+$ , 45 in the *tg*, and 20 in the *tt* family. We further categorize the conformers according to the type of  $\pi$  interactions involved. For instance, the  $g^-g^-$  and  $g^-g^+$  families contain dimers with only PD  $\pi$ - $\pi$  stacking interactions and dimers with both T-shaped and PD  $\pi$ - $\pi$  interactions, which we call mixed interactions (see Figure 5.9). The *tt* family contains dimers with only PD  $\pi$ - $\pi$  stacking interactions, only T-shaped interactions, and only ester- $\pi$  interactions with different degrees of deviation of their monomer subunit structures from those in the isolated monomers (see Figure 5.10). The *tg* family has conformers with only PD  $\pi$ - $\pi$  stacking interactions, only T-shaped interactions, mixed interactions, and ester- $\pi$  interactions (see Figures 5.11 and 5.12). For the lowest energy conformer, the results of NCI and QTAIM analyses are shown in Figure 5.13, while intrinsic bond strength indices can be found in Figure 5.14.

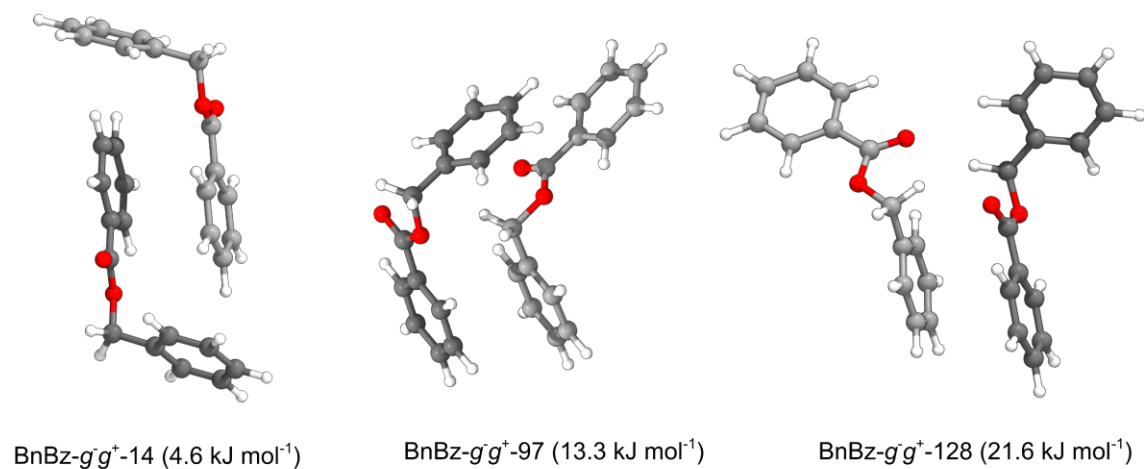


**Figure 5.9.** Examples of structure within the  $g^-g^+$  family.

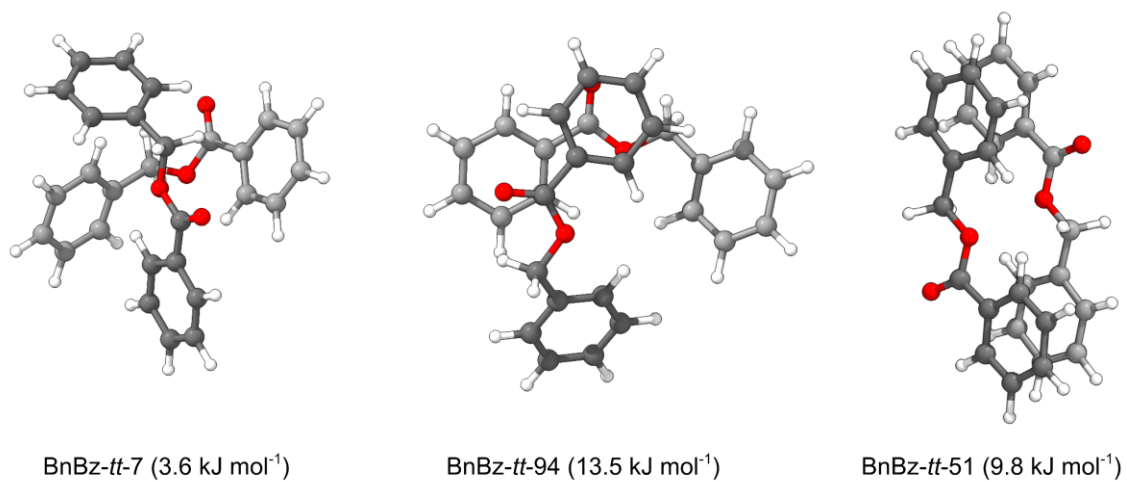


**Figure 5.10.** Examples of structure within the  $tt$  family.

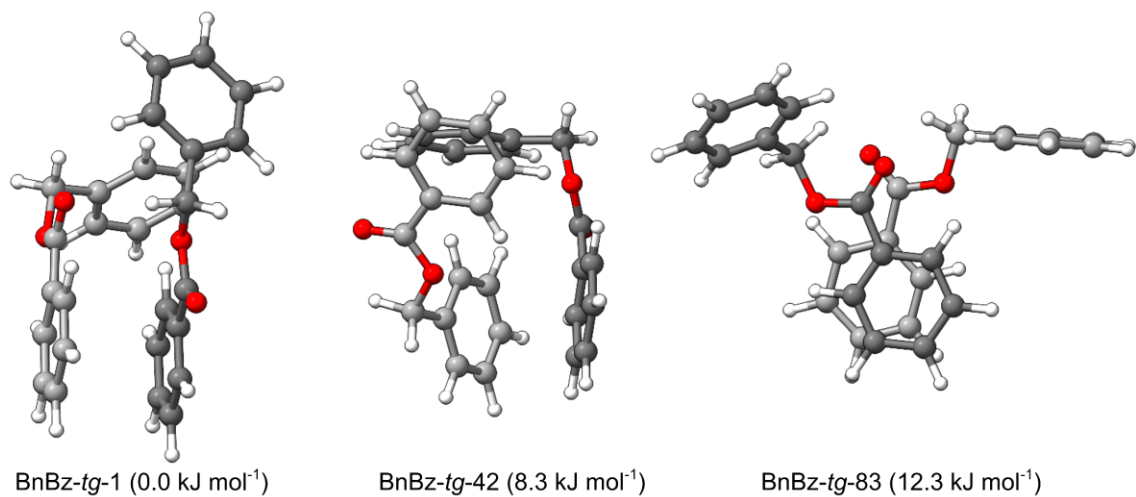


**Figure 5.11.** Examples of structure within the *tg* family with minimal distortion of the monomer subunits.

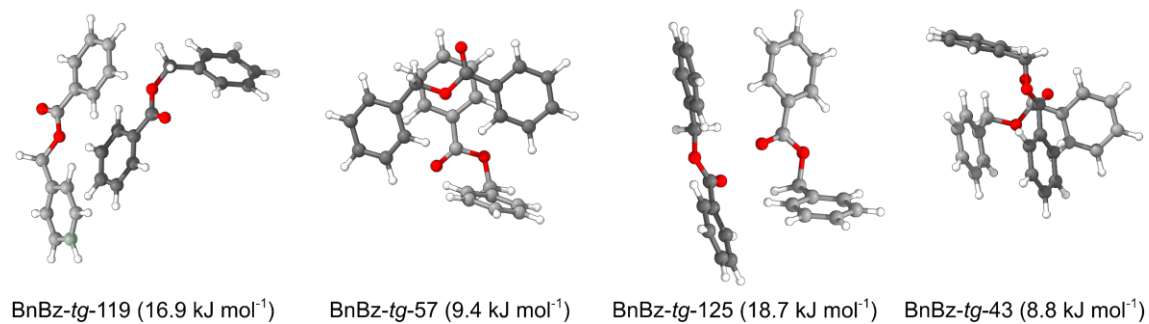


**Figure 5.12.** Examples of structure within the *tg* family with the trans subunit distorted from its monomer configuration.

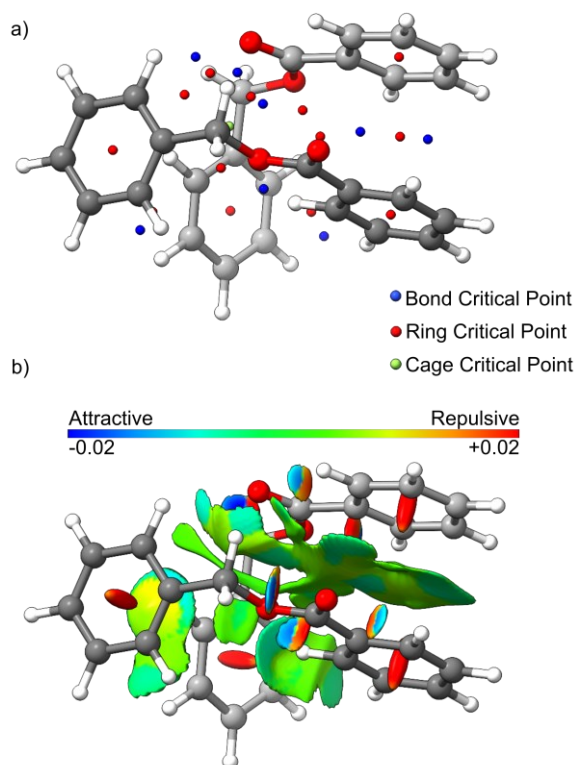


**Figure 5.13.** Results from a) a QTAIM analysis and b) an NCI analysis of the BnBz-*tg*-1 dimer.

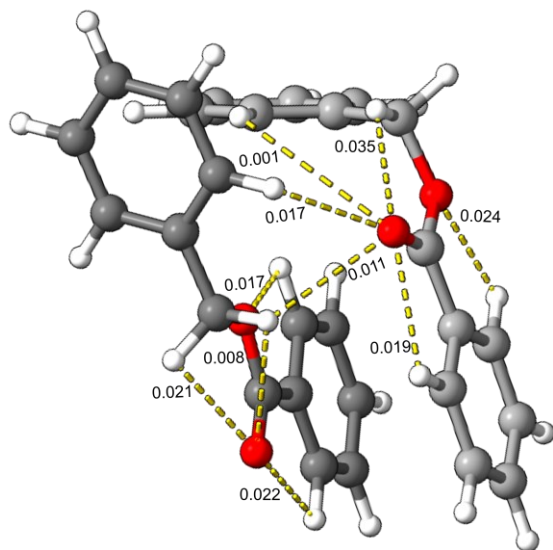


**Figure 5.14.** Intrinsic bond strength indices between atom pairs in the BnBz-*tg*-1 dimer.

Experimentally, one dimer candidate spectrum consisting only of b-type transitions could be assigned spectroscopically (Table 5.4). Experimental transition frequencies of the dimer are in Table C.6, together with the quantum number assignments. The assignment of the molecular carrier was difficult since there are 18 BnBz dimers predicted to be within 5 kJ mol<sup>-1</sup> of the global minimum structure (Table C.5). Of these 18 conformers, eight have rotational constants within 10% of the experimentally determined rotational constants. Out of those eight conformers, four have a  $\mu_b$  dipole moment component larger than  $\mu_a$  and  $\mu_c$ , in accord with experimental observations, and are possible candidates for the conformational assignment. The energies of the four candidates were recalculated at the DLPNO-CCSD(T)/cc-pVTZ level of theory to obtain a more accurate relative energy ordering (see Table 5.4) and aid in the conformational assignment.

**Table 5.5** Experimental spectroscopic parameters of the BnBz dimer and parameters of four candidate structures, calculated at the B3LYP-D3(BJ)/def2-TZVP level of theory with an energy correction at the CCSD(T)/cc-pVTZ level of theory.

	Experiment	BnBz- <i>tg</i> -1	BnBz- <i>tg</i> -2	BnBz- <i>g<sup>-</sup>g<sup>+</sup></i> -5	BnBz- <i>tg</i> -8
$\Delta E^a$ /kJ mol <sup>-1</sup>	-	0	0.5	3.2	3.9
$\Delta E^b$ /kJ mol <sup>-1</sup>	-	0	1.2	2.2	3.6
A /MHz	198.67868(12)	203.5	201.0	211.5	183.1
B	122.48892(14)	126.5	122.8	122.0	122.5
C	108.500959(64)	110.5	111.8	110.2	108.4
$ \mu_a ,  \mu_b ,  \mu_c $ /Debye	only <i>b</i> -type obs.	0.3,3.23,0.45	0.7,2.7,1.0	1.0,2.9,0.2	0.5,1.7,0.4
$\Delta_J$ /kHz	0.00544(17)	0.00283	0.00288	0.00253	0.00316
$\Delta_K$	0.03405(55)	0.00657	0.0170	0.01440	0.01054
$\Delta_{JK}$	-0.01174(70)	0.00579	-0.003318	-0.00366	-0.00327
$\delta_J$	0.000845(85)	-0.000131	-0.000130	0.000447	0.000744
$\delta_K$	-0.0109(15)	-0.01156	-0.008315	-0.005502	0.01206
N <sup>c</sup>	127	-	-	-	-
$\sigma^d$ /kHz	9.96	-	-	-	-

---

<sup>a</sup> Sum of electronic and zero-point energy relative to the lowest energy conformer with BSSE correction at the B3LYP-D3(BJ)\def2-TZVP level of theory.

<sup>b</sup> Sum of electronic energy, at the DLPNO-CCSD(T)/cc-pVTZ level of theory and zero-point energy, at the B3LYP-D3(BJ)\def2-TZVP level of theory, relative to the lowest energy conformer.

<sup>c</sup> Number of transitions used in the fit.

<sup>d</sup> Root-mean-square deviation of the fit.

The four low-energy conformers that are structural candidates for the assigned experimental spectrum, BnBz-*tg*-1, BnBz-*tg*-2, and BnBz-*g<sup>-</sup>g<sup>+</sup>*-5, and BnBz-*tg*-8 have both T-shaped and PD  $\pi$ - $\pi$  stacking interactions (see Figure 5.15). These conformers, and in fact in most of the dimers identified, have the phenyl group in the plane of the ester where its main role is forming a parallel displaced  $\pi$ - $\pi$  stacking interactions. Structures containing only PD  $\pi$ - $\pi$  stacking or only distorted T-shape arrangements were also identified and are at least 3.6 kJ mol<sup>-1</sup> higher in energy, while no dimer structure that contains only hydrogen bonding was identified. After recalculating the energies of the structural candidates at the DLPNO-CCSD(T)/cc-pVTZ level of theory it is clear that BnBz-*tg*-2, BnBz-*g<sup>-</sup>g<sup>+</sup>*-5 and BnBz-*tg*-8 are unlikely to be the experimentally assigned conformer because their high relative energy.

In BnBz-*tg*-1 the benzyl ring of the *gauche* monomer acts simultaneously as H-bond donor in a C-H $\cdots$   $\pi$  hydrogen bond to the (*trans*) phenyl ring and as H-bond acceptor in a  $\pi$   $\cdots$  H-C hydrogen bond involving a (*trans*) benzyl ring H-atom (see Figure 5.13). At the same time, the phenyl rings of the two monomers adopt a PD  $\pi$ - $\pi$  stacking arrangement so that a compact arrangement results. The centroid-to-centroid distances between the T-shaped geometries formed between the phenyl –benzyl ring and benzyl ring – benzyl ring are 4.8 Å and 4.9 Å, respectively, similar to the separation of 4.8 Å in the T-shaped benzene dimer.<sup>8</sup> The plane-to-plane distance between the PD  $\pi$ - $\pi$  stacked rings in BnBz-*tg*-1 is 3.4 Å, within the distance of  $\pi$ - $\pi$  stacked rings found in X-ray crystallography of 3.3 to 3.6 Å for benzene derivatives.<sup>46</sup>

### 5.3.5.2. Noncovalent Interactions in the BnBz Dimer

Adjustments of  $\tau_1$ ,  $\tau_2$ , and  $\tau_4$  in the BnBz monomers facilitate the formation of a blanket of dispersive noncovalent interaction between the aromatic rings of the dimer subunits while still allowing for stabilization through intramolecular hydrogen bonding in BnBz-*tg*-1. The NCI blanket of dispersive interactions in BnBz-*tg*-1 by PD stacking of the benzene subunits is similar to the blanket of interaction seen in the other aromatic dimers.<sup>12,47,48</sup> In BnBz-*tg*-1 however, the interaction blanket includes two distorted T-shape interactions that form pockets of dispersive interactions, Figure 5.13.

Intermolecular hydrogen bonding can occur through the carbonyl or bridging O-atoms and can further stabilize the dimer structure. In the BnBz-*tg*-1 conformer, carbonyl centric intermolecular hydrogen bonding is present to supplement the PD  $\pi$ - $\pi$  stacking and the two CH $\cdots$  $\pi$  T-shape interactions (see Figure 5.15). Critically, the BnBz-*tg*-1 conformer maximizes its intermolecular hydrogen bonds through the carbonyl of the *gauche* subunit and the hydrogens of the benzyl group and the methylene group of the *trans* subunit at the expense of its intramolecular interactions. This is in contrast to BnBz-*tg*-2 and BnBz-*g*<sup>-</sup>*g*<sup>+</sup>-5 which have one less intermolecular interaction but maintain the intramolecular hydrogen bond present in the *gauche* subunits of the monomer (see Figures 5.15 and 5.16). In BnBz-*tg*-8, the carbonyl groups point away from any interactions and BnBz-*tg*-8 depends on the bridging oxygen in the ester for additional stabilization to be 3.9 kJ mol<sup>-1</sup> higher in energy. The likely candidates for the structural BnBz dimer assignment, exhibit all PD  $\pi$ - $\pi$  stacking or T-shaped interactions or both in addition to other noncovalent interactions.

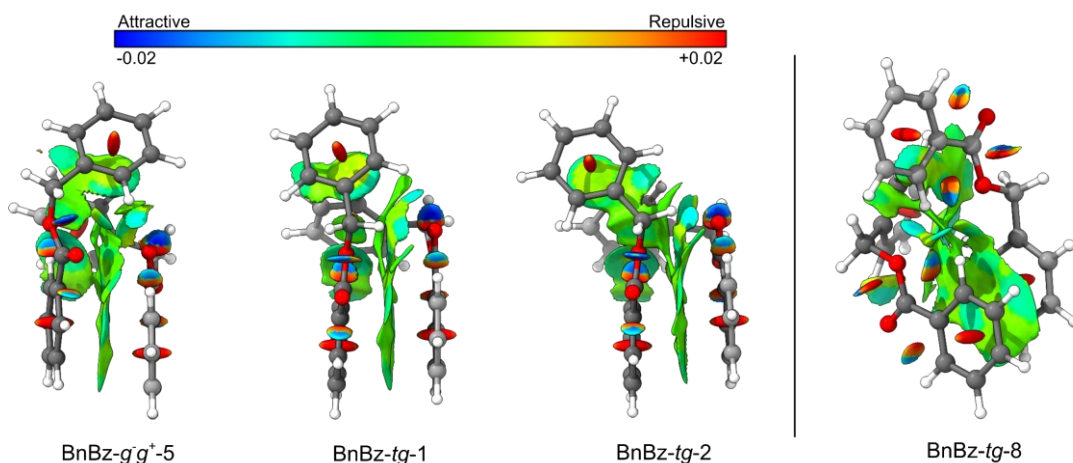


**Figure 5.15.** Visualization of results from NCI analyses of BnBz- $g^-g^+$ -5, BnBz-*tg*-1, BnBz-*tg*-2, BnBz-*tg*-8.

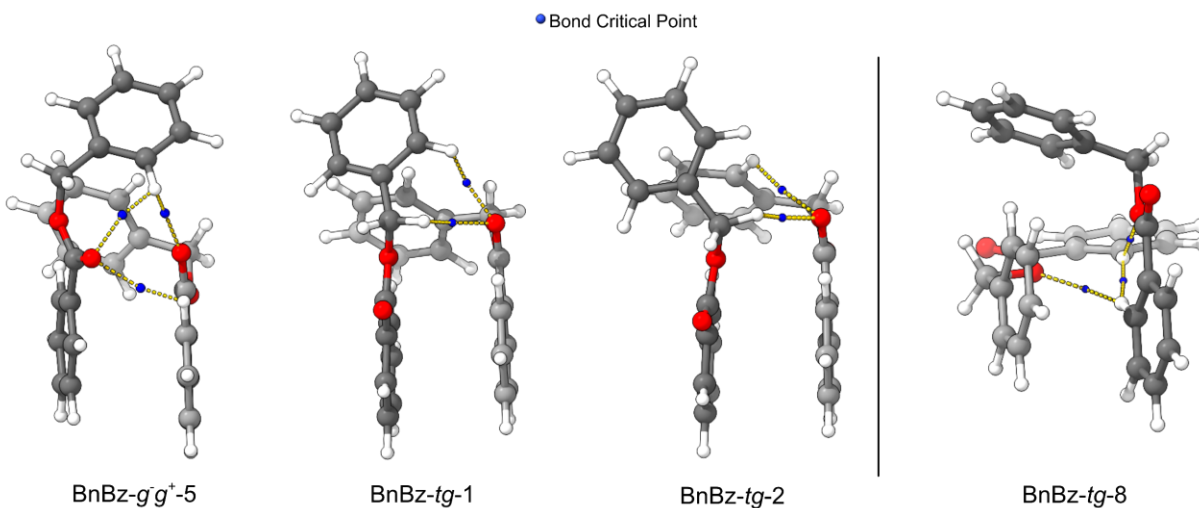


**Figure 5.16.** QTAIM results of BnBz- $g^-g^+$ -5, BnBz-*tg*-1, BnBz-*tg*-2, BnBz-*tg*-8 with the  $\pi$ - $\pi$  and  $\text{CH}\cdots\pi$  bond critical points, ring critical points, and cage critical points removed for clarity.

Apart from the T-shaped and  $\pi$ - $\pi$  interactions, auxiliary noncovalent interactions, non  $\pi$ - $\pi$  stacking and  $\text{C-H}\cdots\pi$  (T-shaped) interactions, exist between subunit-I and subunit-II in BnBz-*tg*-1, Figure 5.13. Out of all the auxiliary interactions formed between subunit-I and subunit-II, the intramolecular interactions between the carbonyl and the methylene hydrogen remain the strongest noncovalent interaction (see Figure 5.14). Interestingly the bond critical point between

the carbonyl of the ester and the ring hydrogen of the benzyl group, signifying a intramolecular hydrogen bond that's seen in the BnBz-*g* monomer, disappears in the dimer as consequence of the  $\tau_2$  and  $\tau_4$  adjustments during dimer formation, Figure 5.13. As mentioned above the lack of bond critical point does not necessarily mean a lack of interaction but, from the IBSI analysis (Figure 5.14) this is the case in this instance.

Utilizing symmetry adapted perturbation theory (SAPT), the binding energy can be decomposed into individual contributions from electrostatic, induction, dispersion, and electron exchange.<sup>49,50</sup> In BnBz-*tg*-1 it can be clearly seen that dispersion plays a significant role with 65% of the overall attractive interaction (see Table 5.5), similar to the diphenyl ether dimer dibenzofuran dimer, dibenzofuran dimer, fluorene dimer,<sup>47</sup> and 2-naphthalenethiol dimer.<sup>48</sup> In BnBz-*g*<sup>-</sup>*g*<sup>+</sup>-5, BnBz-*tg*-2, and BnBz-*tg*-8 the SAPT results show a similar dispersion contribution to the binding energy. In the case of BnBz-*tg*-1, the PD  $\pi$ - $\pi$  stacking, CH $\cdots$  $\pi$  interaction, and several intermolecular hydrogen bonds exist that add stability to the dimer because of the flexibility of the monomer subunits and availability of binding sites. The flexibility of the monomer allows for a more synergetic packing structure of the dimer instead of competition between two motifs in BnBz.

**Table 5.6.** SAPT2+/aug-cc-pVDZ results of the BnBz dimer, in of kJ mol<sup>-1</sup>, with negative values signifying attractive contributions to the overall energy and positive values repulsive contributions. Energies are in kJ mol<sup>-1</sup>.

	$E_{\text{binding}}^a$	$E_{\text{Exchange}}$	$E_{\text{Electrostatic}}$	$E_{\text{Induction}}$	$E_{\text{Dispersion}}$	$E_{\text{Total}}^c$
BnBz- <i>tg</i> -1	-65.0	98.6	-45.0 (27 %) <sup>b</sup>	-12.3 (7 %)	-109.6 (66 %)	-68.3
BnBz- <i>tg</i> -2	-63.1	91.5	-41.7 (26 %)	-10.6 (7 %)	-105.2 (67 %)	-66.0
BnBz- <i>g</i> <sup>-</sup> <i>g</i> <sup>+</sup> -5	-58.7	99.5	-41.5 (26 %)	-12.2 (8 %)	-107.6 (67 %)	-61.8
BnBz- <i>tg</i> -8	-57.6	97.2	-40.8 (25%)	-12.7 (8%)	-103.6 (64%)	-59.9

---

<sup>a</sup> Binding energy computed at the B3LYP-D3(BJ)/def2-TZVP level of theory with BSSE correction.

<sup>b</sup> Percent contribution to the attractive overall energy ( $E_{el}+E_{ind}+E_{disp}$ ).

<sup>c</sup> Binding energy obtained from SAPT(2+)/aug-cc-pVDZ.

## 5.4. Conclusion

The conformational landscape of BnBz was investigated using a combination of computational chemistry calculations and CP-FTMW spectroscopy. Four conformers of BnBz were identified theoretically following the CREST search and several 1D-PES scans along the four dihedral angles associated the  $\sigma$ -bonds in the molecule. Rotational spectra of the parent BnBz-*g* and BnBz-*t*, as well as those of the 14  $^{13}\text{C}$  of BnBz-*g* and two  $^{13}\text{C}$  of BnBz-*t* isotopologues were measured and assigned. The experimental data, together with the relative experimental line intensity variation of BnBz-*g* and BnBz-*t* allowed one to unambiguously establish that BnBz-*g* is the global minimum. The conformational conversion barrier from BnBz-*t* to BnBz-*g*, together with the aforementioned experimental intensity, provided the satisfactory explanation of the deviation in the observed and predicted conformational abundances. Furthermore, the intramolecular non-covalent interactions were analyzed using the QTAIM, NCI, and IBSI analyses, where the latter two provide very consistent pictures about the relative strength of different attractive interactions. between the carbonyl O and a methylene H by the NCI analysis has the highest IBSI value of 0.027. These analyses demonstrated that the intramolecular hydrogen bond between the carbonyl O and a methylene H, identified by both the NCI and IBSI as the strongest non-covalent interaction, plays the dominant role preferentially stabilize BnBz-*g* over BnBz-*t*. A dimer of BnBz was identified in the experimental spectrum and preliminary analysis of its conformation landscape and noncovalent interactions are presented. The experimental identification of the dimer which account for 32 heavy atoms using gas phase rotational spectroscopy accounts for one of the biggest dimer species identified experimentally.

Out of the 128 dimers found, one dimer was experimentally identified. Computationally, all the dimers identified had some form of  $\pi$ -interactions stabilizing their structure. Breaking down the energetic contribution found in the dimer, through SAPT, shows that dispersion accounts for 65% of the overall attractive interaction. The dimer has a plethora of noncovalent interaction present and may provide details about noncovalent interaction in large systems in the gas phase. The current study sheds light on the diverse factors which influence the structural outcomes of aromatic systems and also provides important structural input for future investigation into the potential role of BnBz in the formation of secondary organic aerosols.

## References

- (1) Ayinla, R. T.; Shiri, M.; Song, B.; Gangishetty, M.; Wang, K. The Pivotal Role of Non-Covalent Interactions in Single-Molecule Charge Transport. *Mater. Chem. Front.* **2023**, *7* (17), 3524–3542. <https://doi.org/10.1039/D3QM00210A>.
- (2) Carter-Fenk, K.; Liu, M.; Pujal, L.; Loipersberger, M.; Tsanai, M.; Vernon, R. M.; Forman-Kay, J. D.; Head-Gordon, M.; Heidar-Zadeh, F.; Head-Gordon, T. The Energetic Origins of Pi–Pi Contacts in Proteins. *J. Am. Chem. Soc.* **2023**, *145* (45), 24836–24851. <https://doi.org/10.1021/jacs.3c09198>.
- (3) Hong, Y.; Schlosser, F.; Kim, W.; Würthner, F.; Kim, D. Ultrafast Symmetry-Breaking Charge Separation in a Perylene Bisimide Dimer Enabled by Vibronic Coupling and Breakdown of Adiabaticity. *J. Am. Chem. Soc.* **2022**, *144* (34), 15539–15548. <https://doi.org/10.1021/jacs.2c03916>.
- (4) Gilissen, P. J.; White, P. B.; Berrocal, J. A.; Vanthuyne, N.; Rutjes, F. P. J. T.; Feringa, B. L.; Elemans, J. A. A. W.; Nolte, R. J. M. Molecular Motor-Functionalized Porphyrin Macrocycles. *Nat. Commun.* **2020**, *11* (1), 5291. <https://doi.org/10.1038/s41467-020-19123-y>.
- (5) Izadnia, S.; LaForge, A. C.; Stienkemeier, F.; Cheeseman, J. R.; Bloino, J.; Cheramy, J.; Jäger, W.; Xu, Y. Unusual Binary Aggregates of Perylene Bisimide Revealed by Their Electronic Transitions in Helium Nanodroplets and DFT Calculations. *Phys. Chem. Chem. Phys.* **2021**, *23* (25), 13862–13872. <https://doi.org/10.1039/D1CP01923F>.
- (6) Grimme, S. Do Special Noncovalent  $\pi$ – $\pi$  Stacking Interactions Really Exist? *Angew. Chem. Int. Ed.* **2008**, *47* (18), 3430–3434. <https://doi.org/10.1002/anie.200705157>.

- (7) Martinez, C. R.; Iverson, B. L. Rethinking the Term “Pi-Stacking.” *Chem. Sci.* **2012**, *3* (7), 2191–2201. <https://doi.org/10.1039/C2SC20045G>.
- (8) Arunan, E.; Gutowsky, H. S. The Rotational Spectrum, Structure and Dynamics of a Benzene Dimer. *J. Chem. Phys.* **1993**, *98* (5), 4294–4296. <https://doi.org/10.1063/1.465035>.
- (9) Schnell, M.; Erlekam, U.; Bunker, P. R.; von Helden, G.; Grabow, J.-U.; Meijer, G.; van der Avoird, A. Structure of the Benzene Dimer—Governed by Dynamics. *Angew. Chem. Int. Ed.* **2013**, *52* (19), 5180–5183. <https://doi.org/10.1002/anie.201300653>.
- (10) Podeszwa, R.; Bukowski, R.; Szalewicz, K. Potential Energy Surface for the Benzene Dimer and Perturbational Analysis of  $\Pi$ – $\pi$  Interactions. *J. Phys. Chem. A* **2006**, *110* (34), 10345–10354. <https://doi.org/10.1021/jp064095o>.
- (11) Seifert, N. A.; Steber, A. L.; Neill, J. L.; Pérez, C.; Zaleski, D. P.; Pate, B. H.; Lesarri, A. The Interplay of Hydrogen Bonding and Dispersion in Phenol Dimer and Trimer: Structures from Broadband Rotational Spectroscopy. *Phys. Chem. Chem. Phys.* **2013**, *15* (27), 11468–11477. <https://doi.org/10.1039/C3CP51725J>.
- (12) Seifert, N. A.; Hazrah, A. S.; Jäger, W. The 1-Naphthol Dimer and Its Surprising Preference for  $\pi$ – $\pi$  Stacking over Hydrogen Bonding. *J. Phys. Chem. Lett.* **2019**, *10* (11), 2836–2841. <https://doi.org/10.1021/acs.jpcclett.9b00646>.
- (13) Huber, F. K.; Kaiser, R.; Sauter, W.; Schiestl, F. P. Floral Scent Emission and Pollinator Attraction in Two Species of *Gymnadenia* (Orchidaceae). *Oecologia* **2005**, *142* (4), 564–575. <https://doi.org/10.1007/s00442-004-1750-9>.
- (14) Qin, X.-W.; Hao, C.-Y.; He, S.-Z.; Wu, G.; Tan, L.-H.; Xu, F.; Hu, R.-S. Volatile Organic Compound Emissions from Different Stages of *Cananga Odorata* Flower Development. *Molecules* **2014**, *19* (7), 8965–8980. <https://doi.org/10.3390/molecules19078965>.

- (15) Yang, J.-O.; Nakayama, N.; Toda, K.; Tebayashi, S.; Kim, C.-S. Structural Determination of Elicitors in *Sogatella Furcifera* (Horváth) That Induce Japonica Rice Plant Varieties (*Oryza Sativa* L.) to Produce an Ovicidal Substance against *S. Furcifera* Eggs. *Biosci. Biotechnol. Biochem.* **2014**, *78* (6), 937–942.  
<https://doi.org/10.1080/09168451.2014.917266>.
- (16) Pearson, M. A.; Miller, G. W. Benzyl Benzoate. In *Encyclopedia of Toxicology (Third Edition)*; Wexler, P., Ed.; Academic Press: Oxford, 2014; pp 433–434.  
<https://doi.org/10.1016/B978-0-12-386454-3.00103-2>.
- (17) Srivastava, D.; Vu, T. V.; Tong, S.; Shi, Z.; Harrison, R. M. Formation of Secondary Organic Aerosols from Anthropogenic Precursors in Laboratory Studies. *Npj Clim. Atmospheric Sci.* **2022**, *5* (1), 1–30. <https://doi.org/10.1038/s41612-022-00238-6>.
- (18) Pracht, P.; Grimme, S.; Bannwarth, C.; Bohle, F.; Ehlert, S.; Feldmann, G.; Gorges, J.; Müller, M.; Neudecker, T.; Plett, C.; Spicher, S.; Steinbach, P.; Wesolowski, P. A.; Zeller, F. CREST—A Program for the Exploration of Low-Energy Molecular Chemical Space. *J. Chem. Phys.* **2024**, *160* (11), 114110. <https://doi.org/10.1063/5.0197592>.
- (19) Xie, F.; Seifert, N. A.; Heger, M.; Thomas, J.; Jäger, W.; Xu, Y. The Rich Conformational Landscape of Perillyl Alcohol Revealed by Broadband Rotational Spectroscopy and Theoretical Modelling. *Phys. Chem. Chem. Phys.* **2019**, *21* (28), 15408–15416.  
<https://doi.org/10.1039/C9CP03028J>.
- (20) Xie, F.; Ng, X.; Seifert, N. A.; Thomas, J.; Jäger, W.; Xu, Y. Rotational Spectroscopy of Chiral Tetrahydro-2-Furoic Acid: Conformational Landscape, Conversion, and Abundances. *J. Chem. Phys.* **2018**, *149* (22), 224306. <https://doi.org/10.1063/1.5063683>.

- (21) Becke, A. D. A New Mixing of Hartree–Fock and Local Density-functional Theories. *J. Chem. Phys.* **1993**, *98* (2), 1372–1377. <https://doi.org/10.1063/1.464304>.
- (22) Grimme, S.; Ehrlich, S.; Goerigk, L. Effect of the Damping Function in Dispersion Corrected Density Functional Theory. *J. Comput. Chem.* **2011**, *32* (7), 1456–1465. <https://doi.org/10.1002/jcc.21759>.
- (23) Becke, A. D.; Johnson, E. R. A Density-Functional Model of the Dispersion Interaction. *J. Chem. Phys.* **2005**, *123* (15), 154101. <https://doi.org/10.1063/1.2065267>.
- (24) Frisch, M. J.; Trucks, G. W.; Schlegel, H. B.; Scuseria, G. E.; Robb, M. A.; Cheeseman, J. R.; Scalmani, G.; Barone, V.; Petersson, G. A.; Nakatsuji, H.; Li, X.; Caricato, M.; Marenich, A. V.; Bloino, J.; Janesko, B. G.; Gomperts, R.; Mennucci, B.; Hratchian, H. P.; Ortiz, J. V.; Izmaylov, A. F.; Sonnenberg, J. L.; Williams; Ding, F.; Lipparini, F.; Egidi, F.; Goings, J.; Peng, B.; Petrone, A.; Henderson, T.; Ranasinghe, D.; Zakrzewski, V. G.; Gao, J.; Rega, N.; Zheng, G.; Liang, W.; Hada, M.; Ehara, M.; Toyota, K.; Fukuda, R.; Hasegawa, J.; Ishida, M.; Nakajima, T.; Honda, Y.; Kitao, O.; Nakai, H.; Vreven, T.; Throssell, K.; Montgomery Jr., J. A.; Peralta, J. E.; Ogliaro, F.; Bearpark, M. J.; Heyd, J. J.; Brothers, E. N.; Kudin, K. N.; Staroverov, V. N.; Keith, T. A.; Kobayashi, R.; Normand, J.; Raghavachari, K.; Rendell, A. P.; Burant, J. C.; Iyengar, S. S.; Tomasi, J.; Cossi, M.; Millam, J. M.; Klene, M.; Adamo, C.; Cammi, R.; Ochterski, J. W.; Martin, R. L.; Morokuma, K.; Farkas, O.; Foresman, J. B.; Fox, D. J. Gaussian 16 Rev. C.01, 2016.
- (25) Bader, R. F. W. A Quantum Theory of Molecular Structure and Its Applications. *Chem. Rev.* **1991**, *91* (5), 893–928. <https://doi.org/10.1021/cr00005a013>.

- (26) Johnson, E. R.; Keinan, S.; Mori-Sánchez, P.; Contreras-García, J.; Cohen, A. J.; Yang, W. Revealing Noncovalent Interactions. *J. Am. Chem. Soc.* **2010**, *132* (18), 6498–6506. <https://doi.org/10.1021/ja100936w>.
- (27) Lu, T.; Chen, F. Multiwfn: A Multifunctional Wavefunction Analyzer. *J. Comput. Chem.* **2012**, *33* (5), 580–592. <https://doi.org/10.1002/jcc.22885>.
- (28) Klein, J.; Khartabil, H.; Boisson, J.-C.; Contreras-García, J.; Piquemal, J.-P.; Hénon, E. New Way for Probing Bond Strength. *J. Phys. Chem. A* **2020**, *124* (9), 1850–1860. <https://doi.org/10.1021/acs.jpca.9b09845>.
- (29) *IGMPlot: a program revealing non-covalent interactions*. <http://igmpplot.univ-reims.fr/> (accessed 2021-11-18).
- (30) Western, C. M. PGOPHER: A Program for Simulating Rotational, Vibrational and Electronic Spectra. *J. Quant. Spectrosc. Radiat. Transf.* **2017**, *186*, 221–242. <https://doi.org/10.1016/j.jqsrt.2016.04.010>.
- (31) Pickett, H. M. The Fitting and Prediction of Vibration-Rotation Spectra with Spin Interactions. *J. Mol. Spectrosc.* **1991**, *148* (2), 371–377. [https://doi.org/10.1016/0022-2852\(91\)90393-O](https://doi.org/10.1016/0022-2852(91)90393-O).
- (32) Xie, F.; Seifert, N. A.; Jäger, W.; Xu, Y. Conformational Panorama and Chirality Controlled Structure–Energy Relationship in a Chiral Carboxylic Acid Dimer. *Angew. Chem. Int. Ed.* **2020**, *59* (36), 15703–15710. <https://doi.org/10.1002/anie.202005685>.
- (33) Seifert, N. A.; Thomas, J.; Jäger, W.; Xu, Y. Rotational Spectra and Theoretical Study of Tetramers and Trimers of 2-Fluoroethanol: Dramatic Intermolecular Compensation for Intramolecular Instability. *Phys. Chem. Chem. Phys.* **2018**, *20* (43), 27630–27637. <https://doi.org/10.1039/C8CP05653F>.

- (34) Insausti, A.; Ma, J.; Yang, Q.; Xie, F.; Xu, Y. Rotational Spectroscopy of 2-Furoic Acid and Its Dimer: Conformational Distribution and Double Proton Tunneling. *ChemPhysChem* **2022**, *23* (12), e202200176. <https://doi.org/10.1002/cphc.202200176>.
- (35) Pérez, C.; Lobsiger, S.; Seifert, N. A.; Zaleski, D. P.; Temelso, B.; Shields, G. C.; Kisiel, Z.; Pate, B. H. Broadband Fourier Transform Rotational Spectroscopy for Structure Determination: The Water Heptamer. *Chem. Phys. Lett.* **2013**, *571*, 1–15. <https://doi.org/10.1016/j.cplett.2013.04.014>.
- (36) Carter-Fenk, K.; Herbert, J. M. Reinterpreting  $\pi$ -Stacking. *Phys. Chem. Chem. Phys.* **2020**, *22* (43), 24870–24886. <https://doi.org/10.1039/D0CP05039C>.
- (37) Ruoff, R. S.; Klots, T. D.; Emilsson, T.; Gutowsky, H. S. Relaxation of Conformers and Isomers in Seeded Supersonic Jets of Inert Gases. *J. Chem. Phys.* **1990**, *93* (5), 3142–3150. <https://doi.org/10.1063/1.458848>.
- (38) Ma, J.; Insausti, A.; Al-Jabiri, M. H.; Carlson, C. D.; Jäger, W.; Xu, Y. Unlocking a New Hydrogen-Bonding Marker: C–O Bond Shortening in Vicinal Diols Revealed by Rotational Spectroscopy. *J. Chem. Phys.* **2024**, *160* (15), 154304. <https://doi.org/10.1063/5.0203123>.
- (39) Lu, T.; Xie, F.; Seifert, N. A.; Jäger, W.; Xu, Y. Conformational Landscape and Intricate Conformational Relaxation Paths of 4,4,4-Trifluoro-1-Butanol: Rotational Spectroscopy and Quantum Chemical Calculations. *J. Mol. Struct.* **2020**, *1217*, 128359. <https://doi.org/10.1016/j.molstruc.2020.128359>.
- (40) Lu, T.; Xie, F.; Seifert, N. A.; Mejlej, R. H.; Jäger, W.; Xu, Y. Binary Conformers of a Flexible, Long-Chain Fluoroalcohol: Dispersion Controlled Selectivity and Relative Abundances in a Jet. *Phys. Chem. Chem. Phys.* **2024**, *26* (14), 10538–10545. <https://doi.org/10.1039/D4CP00401A>.

- (41) Kraitchman, J. Determination of Molecular Structure from Microwave Spectroscopic Data. *Am. J. Phys.* **1953**, *21* (1), 17–24. <https://doi.org/10.1119/1.1933338>.
- (42) Rudolph, H. D. Extending Kraitchman's Equations. *J. Mol. Spectrosc.* **1981**, *89* (2), 430–439. [https://doi.org/10.1016/0022-2852\(81\)90036-9](https://doi.org/10.1016/0022-2852(81)90036-9).
- (43) Lefebvre, C.; Khartabil, H.; Boisson, J.-C.; Contreras-García, J.; Piquemal, J.-P.; Hénon, E. The Independent Gradient Model: A New Approach for Probing Strong and Weak Interactions in Molecules from Wave Function Calculations. *Chem. Phys. Chem.* **2018**, *19* (6), 724–735. <https://doi.org/10.1002/cphc.201701325>.
- (44) Al-Jabiri, M. H.; Hazrah, A. S.; Jäger, W. Conformers of Vanillic Acid and Its Monohydrate: A Rotational Spectroscopic and Theoretical Study. *J. Phys. Chem. A* **2022**. <https://doi.org/10.1021/acs.jpca.2c05120>.
- (45) Hazrah, A. S.; Nanayakkara, S.; Seifert, N. A.; Kraka, E.; Jäger, W. Structural Study of 1- and 2-Naphthol: New Insights into the Non-Covalent H–H Interaction in Cis-1-Naphthol. *Phys. Chem. Chem. Phys.* **2022**, *24* (6), 3722–3732. <https://doi.org/10.1039/D1CP05632H>.
- (46) Lutz, P. B.; Bayse, C. A. Interpreting Geometric Preferences in  $\pi$ -Stacking Interactions through Molecular Orbital Analysis. *Int. J. Quantum Chem.* **2018**, *118* (7), e25513. <https://doi.org/10.1002/qua.25513>.
- (47) Fatima, M.; Steber, A. L.; Poblitzki, A.; Pérez, C.; Zinn, S.; Schnell, M. Rotational Signatures of Dispersive Stacking in the Formation of Aromatic Dimers. *Angew. Chem.* **2019**, *131* (10), 3140–3145. <https://doi.org/10.1002/ange.201812556>.
- (48) Saragi, R. T.; Calabrese, C.; Juanes, M.; Pinacho, R.; Rubio, J. E.; Pérez, C.; Lesarri, A.  $\pi$ -Stacking Isomerism in Polycyclic Aromatic Hydrocarbons: The 2-Naphthalenethiol Dimer. *J. Phys. Chem. Lett.* **2023**, *14* (1), 207–213. <https://doi.org/10.1021/acs.jpcllett.2c03299>.

- (49) Parker, T. M.; Burns, L. A.; Parrish, R. M.; Ryno, A. G.; Sherrill, C. D. Levels of Symmetry Adapted Perturbation Theory (SAPT). I. Efficiency and Performance for Interaction Energies. *J. Chem. Phys.* **2014**, *140* (9), 094106. <https://doi.org/10.1063/1.4867135>.
- (50) Jeziorski, B.; Moszynski, R.; Szalewicz, K. Perturbation Theory Approach to Intermolecular Potential Energy Surfaces of van Der Waals Complexes. *Chem. Rev.* **1994**, *94* (7), 1887–1930. <https://doi.org/10.1021/cr00031a008>.

# 6

## Instruments and Techniques to Probe Emissions from PVC Pyrolysis

### 6.1. Introduction

In this chapter, I outline how to study the emissions resulting from the thermal degradation of PVC as a stepping stone for studying waste burning. I summarize the necessary steps in generating PVC emissions, measure the resulting HCl emissions, and discuss how the aerosol particles that are also emitted can be classified and their properties measured. The results of these measurements are presented and discussed in Chapter 7. In Section 6.2, I discuss how PVC can be pyrolyzed to emit volatile organic compounds, particulate matter, and HCl. In Section 6.3, I discuss how an HCl trap can be constructed to measure gaseous HCl concentration using colorimetry. In Section 6.4, I discuss how aerosol particles can be classified by the amount of organic carbon and elemental carbon to better understand how they can interact with solar radiation. In Section 6.5, I discuss how aerosol instrumentation can be used to measure particle size distribution using a scanning mobility particle sizer and the ability to scatter and absorb solar radiation using a photoacoustic extinctions meter and an aethalometer. The overall experiment and how the different components interconnect can be seen in Figure 6.1.

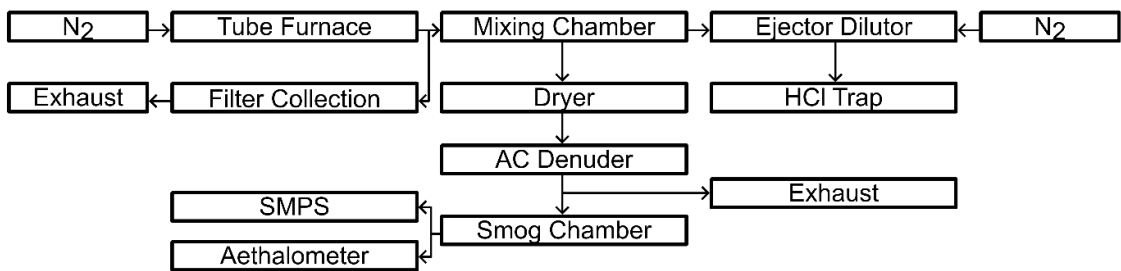


**Figure 6.1.** Schematic of experimental setup utilized in Chapter 7 to study the emissions resulting from PVC pyrolysis.

## 6.2. Thermal Degradation of PVC using a Tube Furnace

The thermal decomposition of PVC can be described by two stages characterized by temperature and emission dependence.<sup>1</sup> The initial stage, occurring at temperatures between 250°C to 350°C, involves dehydrochlorination, resulting in an initial weight loss attributed to HCl emissions.<sup>1</sup> This is followed by a second stage, extending from 350°C to 525°C, during which particulate matter and volatile organic compounds such as methane, toluene, and xylene are emitted.<sup>2</sup> A detailed study of the behaviour of PVC pyrolysis at different temperatures can lead to greater control of emissions from thermal PVC degradation.

For the controlled thermal degradation of PVC, I have constructed a tube furnace with precise environmental control, see Figure 6.2. The furnace holds a quartz tube with an inner diameter of 2.5 cm. Upstream of the quartz tube, a mass flow controller regulates the flow of carrier gas into the tube at a rate between 1000 and 5000 ccm. The carrier gas displaces air in the tube, creating an oxygen-free environment for PVC thermal degradation. The tube furnace contains a high-temperature ceramic fiber heater and a TEC-2400 temperature controller (Thermal Devices) with a K-type thermocouple. It offers temperature control within a range of 0°C to 1200°C.

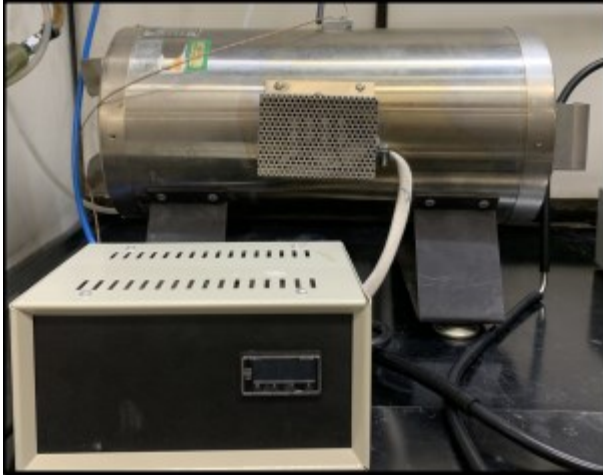


**Figure 6.2.** Custom built tube furnace utilized in Chapter 7 for the pyrolysis of PVC.

### **6.3. Thermal Optical Transmission Analysis for Classification of Aerosol particles**

After the tube furnace, a portion of the emissions is sampled and deposited onto a quartz fiber filter for classification of the emitted aerosol particles. One method to classify aerosol particles is to determine the amount of elemental carbon (EC) and organic carbon (OC) on an aerosol-laden filter.<sup>3</sup> The EC and OC content on the filter can be measured using a thermal optical transmission analyser. The thermal optical transmission analyzer operates by heating a filter sample in an oven, which permits control over the gas atmosphere and gas flow in the oven.<sup>3</sup> To initially measure the amount of OC present on the filter, the oven is heated to 870°C without oxygen, releasing any OC on the filter.<sup>3</sup> The emitted OC is then transported via a helium sheath flow to a catalytic chamber to be converted to CO<sub>2</sub> and then methane, which is quantified with a flame ionization detection system.<sup>3</sup> Once all the OC is removed, the oven is cooled to 500°C in preparation for the next heating cycle. The next heating cycle occurs in the presence of 2% oxygen in helium and the temperature is increased to 900°C, to oxidize the elemental carbon on the filter to CO/CO<sub>2</sub>.<sup>3</sup> The CO/CO<sub>2</sub> mixture is then transported into the catalytic chamber to be converted to methane and finally into the flame ionization detector.<sup>3</sup> The flame ionization

detector is calibrated for a known amount of methane, thus enabling the determination of the amounts of EC and OC in  $\mu\text{g cm}^{-2}$ .<sup>3</sup>

The OC on the filter when heated can pyrolyze, instead of volatilize, and form a char, an incomplete form of EC often called pyrolytic carbon (PC). The conversion of OC to PC adds an uncertainty to how much OC is measured during the first heating cycle. To monitor, and correct for, PC produced during the heating, laser transmittance is observed.<sup>3</sup> During the second heating cycle, if PC was produced during the first heating cycle, the transmittance is reduced, returning to normal levels when the PC has been released from the filter.<sup>3</sup> Emissions from the time period of decreased transmittance are then associated with PC. This time period is often called the split-time and differentiates the OC and EC emissions from the filter.

The thermal-optical transmission analysis in Chapter 7 was performed using a Sunset Laboratory Inc. analyzer. A 1.5 cm<sup>2</sup> sized punch is made from the original filter and inserted into the thermal optical transmission analyzer. The thermal optical transmission trace can be seen in Figure 6.3 with the preprogrammed steps to obtain an EC/OC mass signified by the black peaks in the bottom trace. The temperature and laser transmission can be seen as a function of time in the blue trace and red trace. The first peak is associated with the OC emission from the filter, and the second peak, not shown in Figure 6.3, is associated with the EC released from the filter. The peak in between the OC and EC peaks, not shown in the Figure 6.3, is the pyrolytic carbon peak. The final peak in Figure 6.3 is a known amount of CH<sub>4</sub> used for calibration. Downstream of the filter holder is a mass flow controller and a vacuum source to control the number of aerosols sampled by the filter.

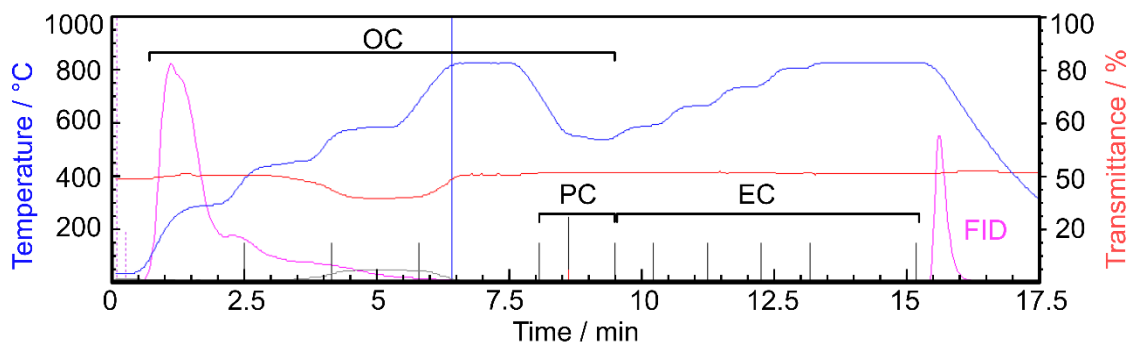


**Figure 6.3.** Thermogram of an EC/OC analysis of PVC. The blue and red traces are the temperature and transmittance respectively. The signal from the flame-ionization (FID) detector is shown in purple. Regions where peaks of organic carbon (OC), pyrolytic carbon (PC), and elemental carbon (EC) are shown. The last peak in the thermogram is a methane calibration peak.

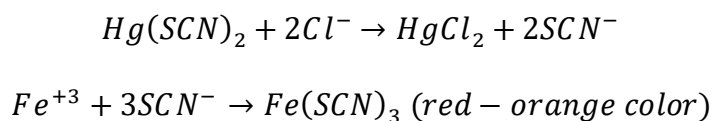
#### **6.4. Colorimetric Analysis for Determination of Hydrogen Chloride Concentration from PVC Pyrolysis**

Chlorine radicals in the atmosphere are known to influence the formation of SOA by oxidizing VOCs.<sup>4</sup> Source of chlorine radicals in the atmosphere include perchlorates, HCl, and particulate chloride.<sup>4</sup> An anthropogenic source of gaseous HCl and particulate chloride is open waste burning of PVC.<sup>5</sup> The first stage of the thermal degradation of PVC is dehydrochlorination at a temperature of 250°C, leading to the release of gaseous HCl.<sup>6</sup> At higher temperatures, aerosols are emitted, containing chloride and chlorinated benzenes.<sup>6</sup> To quantify the emitted hydrogen chloride and aqueous particulate chloride, I constructed a chloride trap similar to that by Heji et al.,<sup>7</sup> through which the pyrolyzed emissions are passed.

The chloride trap consists of three empty condensation vessels, in series, designed to capture any low-volatile species such as large oil mist particles emitted during the pyrolysis process. Following the condensation vessels are five bubblers, also in series, each containing 100 ml of 2M NaOH to trap the chloride in the aqueous phase. Finally, the last vessel is an empty

bubbler used to prevent the loss of solution from the bubbling process. In the experimental setup used in Chapter 7 there are multiple paths from the tube furnace to different instruments for characterization of the emissions (see Figure 6.1). The path to the photo-reaction “smog” chamber has little resistance and will therefore prevent pressure buildup so that the emissions do not bubble through the chloride trap. To circumvent this issue and force emission from the mixing chamber to the chloride trap, an injector-dilutor is used. The injector dilutor is a single-stage venturi pump (AVR038H) that builds up enough pressure to force the N<sub>2</sub> plus PVC pyrolysis emissions mixture to flow through the chloride trap.

The aqueous chloride from the emission is dissolved in the 2M NaOH solution and then neutralized to a pH of 7 using 3M sulfuric acid. To avoid possible interference from aerosol particles, the solution is then filtered. The chloride concentration is then measured using a colorimetric method (HACH Chloride TNT879 test kit).<sup>8</sup> The method functions by mixing the neutralized sample with a mercury thiocyanate ferric nitrate nonahydrate solution that turns orange in the presence of chloride ions. The onset of color occurs when chloride liberates thiocyanate from mercury thiocyanate to form ferric thiocyanate, an orange-colored compound, see reaction scheme 6.1. The higher the concentration of chloride present, the more ferric thiocyanate forms, and the darker the solution becomes. The absorbances between 400 nm and 500 nm is recorded using a JASCO, J-1500, CD spectrometer and a calibration curve with absorbances for known concentration is used to determine the exact concentration of chloride ions from the sample solution. The absorbance at 468 nm is used, as recommended by HACH method 10291,<sup>8</sup> to determine the concentration of chloride.



**Scheme 6.1.** The reaction of chloride ions to form a red-orange colored ferric thiocyanate compound.

## 6.5. Instruments to Probe Aerosol Properties

### 6.5.1. Photo-reaction “Smog” Chamber

The pyrolyzed emissions, not captured by the filter or HCl trap, can be sampled to assess their size distribution and their ability to scatter and absorb solar radiation. These properties are directly measured from the tube furnace, reflecting instantaneous emission characteristics. Conversely, the aging of aerosol properties is studied using a smog chamber, offering precise control over aerosol exposure. Before injection into the chamber, emissions undergo cleaning to remove H<sub>2</sub>O or VOCs, allowing systematic aging studies relative to VOC or oxidant exposure.

Our smog chamber comprises a 1.8 m<sup>3</sup> bag that consists of perfluoralkoxy (PFA) film and is surrounded by three sets of eight 32W black lights with peak emission at 350 nm. The Teflon bag is kept at atmospheric pressure, which is maintained by a pure air generator (Aadco 737). Fans inside the bag ensure that the contents are completely mixed and temperature and relative humidity sensors are used to monitor environmental conditions. The UV-transparent PFA film was chosen because we can form hydroxyl radicals through UV irradiation a naturally occurring atmospheric radical within the chamber. By being able to forms hydroxyl radicals, we can form secondary organic aerosol and a secondary organic coat and study aging due to the oxidation of VOC. Various instruments can sample from the chamber to evaluate aerosol properties, including size distributions and optical properties.

Loss of aerosol particles from the chamber, typical for small chambers like ours, can occur through dilution, diffusion to chamber walls, coagulation, and gravitational settling. Loss

due to diffusion and gravitational settling is size-dependent: particles smaller than 100 nm primarily undergo Brownian diffusion, while those larger than 500 nm preferentially settle gravitationally.<sup>9</sup> In the intermediate size range, minimal loss occurs to these processes.<sup>9</sup> Corrective measures, both size-dependent and size-independent, can minimize experimental uncertainties.<sup>9</sup> In Chapter 7, I use an empirical method to correct size independent and size dependent particles losses. The size independent method assumes that the loss in particles is a first order process where the rate of loss is the slope of the natural logarithm of the total concentration vs time plot.<sup>9</sup> The size dependent correction utilizes a similar approach however the plot is the natural logarithm of concentration at a particles size versus time.<sup>9</sup> Correcting for wall losses is crucial for aging studies to be able to attribute the evolution of the size distribution in the chamber as a result of an atmospheric process or as a consequence of the loss processes.

### **6.5.2. Scanning Mobility Particle Sizer**

Atmospheric aerosols naturally occur in a distribution of different sizes. The initial step in analyzing an aerosol size distribution is to classify the aerosol particles into size bins and then count how many are present in a given bin. In Chapter 7, to obtain a size distribution of pyrolyzed PVC, I use a scanning mobility particle sizer (SMPS 3936L76), which consists of two instruments: a differential mobility analyzer (DMA) that utilizes the electric mobility of charged aerosol particles to select a size, and a condensation particle counter (CPC) to counts those particles.

A DMA consists of two concentric cylindrical metal tubes with a laminar sheath flow of clean air between them. An electrostatic potential is applied to the central cylinder. Charged aerosol particles are introduced at the top of the DMA and experience an attractive electrostatic force towards the inner cylinder. The electrostatic force is opposed by an aerodynamic drag as

the particle travels through the sheath flow. If electrostatic force and drag are balanced for a certain particle size, these particles will leave the DMA through an exit port, to be counted in the CPC. A size distribution can be obtained by scanning the electrostatic potential through an appropriate range.<sup>10</sup> For this method of size selection, it is necessary to have aerosol particles with a known charge and be able to reproduce that charge on similarly sized particles.<sup>10</sup> The DMA I used is equipped with an aerosol neutralizer that can produce a well-characterized charge distribution. A radioactive source in the aerosol neutralizer is used to generate ions that collide with aerosol particles to produce a known Boltzmann charge distribution. The resulting charged particles are then injected into the classification region of the DMA. Typical aerosol particle sizes that a DMA can select range from 25 nm to 1000 nm.

The second instrument in an SMPS is a CPC that is used to count the number of particles classified by the DMA. In Chapter 7, I used a conductive cooling CPC in which aerosol particles pass through a heated region saturated with butanol.<sup>10</sup> The aerosol particles then enter a cooling region where the now supersaturated butanol condenses onto the particles.<sup>10</sup> The aerosol particles will grow to a size of about 12  $\mu\text{m}$  and can now be detected by optical means. The particles cross through a laser light beam and the scattered light is detected by a photodiode.<sup>10</sup> The particle number can then be extracted from the scattering signal.

### **6.5.3. Aethalometer**

The absorption of radiation by aerosol particles depends on the type of aerosol particle present. For example, brown carbon aerosols exhibit wavelength-dependent absorption, wherein the light-absorbing component within the aerosol particle shows stronger absorption in the ultraviolet region.<sup>11</sup> The wavelength-dependent absorption of an aerosol is often expressed as a power law

expression, Equation (6.4), where  $B_{abs}(\lambda)$  is the absorption coefficient at wavelength  $\lambda$ , and  $AAC$  is the absorption Ångström exponent.<sup>12</sup>

$$\frac{B_{abs}(\lambda_1)}{B_{abs}(\lambda_2)} = \left(\frac{\lambda_1}{\lambda_2}\right)^{-AAC} \quad (6.4)$$

The importance of this expression lies in its ability to differentiate between aerosol types using the  $AAC$  value. For instance, black carbon aerosols have an  $AAC$  of 1, while a value greater than 1 can be attributed to organic aerosols such as brown carbon aerosols.<sup>13</sup> The calculation of  $AAC$  requires the experimental determination of the absorption coefficient at a minimum of two wavelengths.

An aethalometer serves as a low-cost alternative that can be purchased as a handheld device and used in remote sensing contexts to obtain the  $AAC$ .<sup>14</sup> The aethalometer is a filter-based measurement device that traps aerosol particles on a filter which is then irradiated by several different wavelengths, so that the light attenuation by the particles can be measured.<sup>15</sup> For instance, in Chapter 7, a MA200 Aethlabs aethalometer is used that has light of five different wavelengths (370nm, 475nm, 528nm, 625nm, 880nm) to irradiate the aerosol-laden filter and obtain the absorption coefficient at these wavelengths.

The attenuation,  $ATN$ , measured by the aethalometer can be described by the Beer-Lambert law, Equation (6.5), where  $I_0$  and  $I$  represent the light intensity transmitted through a particle-free filter and the aerosol-filled filter.<sup>16</sup>

$$ATN = -100 \cdot \ln\left(\frac{I}{I_0}\right) \quad (6.5)$$

The change in attenuation,  $\Delta ATN$ , caused by the deposition of aerosols on a filter at a known flow rate (in mL min<sup>-1</sup>),  $Q$ , over a filter surface area (in mm),  $A$ , and time (in minutes),  $\Delta t$ , can then be utilized in Equation (6.6) to calculate the attenuation coefficient,  $b_{ATN}$ .<sup>14</sup>

$$b_{ATN} = \frac{A}{Q} \cdot \frac{\Delta ATN}{\Delta t} \quad (6.6)$$

The attenuation measured by the detector in the aethalometer is caused by several processes. The first cause of a decrease in attenuation is the scattering and absorption by the aerosol particles deposited on the filter.<sup>16</sup> The second cause is scattering of radiation by filter fibers, and the third cause is shadowing of the filter by multiple particles depositing on the same spot, causing the optical path length to decrease (often called the filter-loading effect).<sup>16</sup> To mitigate filter-loading effects, the DualSpot measurement technique can be applied.<sup>17</sup> This technique allows the simultaneous measurement of attenuation through a clean filter spot and an aerosol-laden spot.<sup>17</sup> Further corrections are necessary and applied through data processing algorithms to correct for artifacts caused by the filter, such as scatter by filter fibers.<sup>16</sup> These corrections are applied in the instrument software.

The aethalometer data output includes the raw uncorrected attenuation and a black carbon mass equivalence obtained by the computation of absorption. Thus, the absorption,  $B_{abs}(\lambda)$ , in units of  $\text{Mm}^{-1}$ , can be back-calculated using Equation (6.7)<sup>18</sup> to determine the  $AAC$ .

$$B_{abs}(\lambda) = \frac{C_{BC}(\lambda) \cdot MAE_{BC}(\lambda)}{f} \cdot 10^{-3} \quad (6.7)$$

In Equation (6.7),  $C_{BC}(\lambda)$  represents the equivalent black carbon mass (in  $\text{ng m}^{-3}$ ) reported by the aethalometer,  $MAE_{BC}(\lambda)$  stands for the mass-specific absorption cross-section ( $\text{m}^2 \text{g}^{-1}$ ) of black carbon, and,  $f$  denotes the calibration factor for filter loading and scattering by aerosols on the filter.<sup>18</sup> In Chapter 7, a calibration factor  $f = 1.3$  was used, as recommended by the manufacturer, and the  $MAE$  values were obtained from Li et al.<sup>18</sup>

## References

- (1) Marongiu, A.; Faravelli, T.; Bozzano, G.; Dente, M.; Ranzi, E. Thermal Degradation of Poly(Vinyl Chloride). *J. Anal. Appl. Pyrolysis* **2003**, *70* (2), 519–553.  
[https://doi.org/10.1016/S0165-2370\(03\)00024-X](https://doi.org/10.1016/S0165-2370(03)00024-X).
- (2) Aracil, I.; Font, R.; Conesa, J. A. Semivolatile and Volatile Compounds from the Pyrolysis and Combustion of Polyvinyl Chloride. *J. Anal. Appl. Pyrolysis* **2005**, *74* (1), 465–478.  
<https://doi.org/10.1016/j.jaap.2004.09.008>.
- (3) User's Manual for Organic and Elemental Carbon (OCEC) Laboratory Analyzer, Mode 5L, Sunset Laboratory Inc., Oregon, USA (2015)
- (4) Zhang, B.; Shen, H.; Yun, X.; Zhong, Q.; Henderson, B. H.; Wang, X.; Shi, L.; Gunthe, S. S.; Huey, L. G.; Tao, S.; Russell, A. G.; Liu, P. Global Emissions of Hydrogen Chloride and Particulate Chloride from Continental Sources. *Environ. Sci. Technol.* **2022**, *56* (7), 3894–3904. <https://doi.org/10.1021/acs.est.1c05634>.
- (5) Christian, T. J.; Yokelson, R. J.; Cárdenas, B.; Molina, L. T.; Engling, G.; Hsu, S.-C. Trace Gas and Particle Emissions from Domestic and Industrial Biofuel Use and Garbage Burning in Central Mexico. *Atmospheric Chem. Phys.* **2010**, *10* (2), 565–584.  
<https://doi.org/10.5194/acp-10-565-2010>.
- (6) Yu, J.; Sun, L.; Ma, C.; Qiao, Y.; Yao, H. Thermal Degradation of PVC: A Review. *Waste Manag.* **2016**, *48*, 300–314. <https://doi.org/10.1016/j.wasman.2015.11.041>.
- (7) Yu, H.; Qu, J.; Liu, Y.; Yun, H.; Li, X.; Zhou, C.; Jin, Y.; Zhang, C.; Dai, J.; Bi, X. Co-Pyrolysis of Biomass and Polyvinyl Chloride under Microwave Irradiation: Distribution of Chlorine. *Sci. Total Environ.* **2022**, *806*, 150903.  
<https://doi.org/10.1016/j.scitotenv.2021.150903>.

- (8) *Chloride TNTplus Vial Test (1.0-1,000 mg/L Cl), 24 Tests | Hach Canada - Overview.*  
<https://ca.hach.com/chloride-tntplus-vial-test-1-0-1-000-mg-l-cl-24-tests/product?id=54566921144> (accessed 2024-04-13).
- (9) Pierce, J. R.; Engelhart, G. J.; Hildebrandt, L.; Weitkamp, E. A.; Pathak, R. K.; Donahue, N. M.; Robinson, A. L.; Adams, P. J.; Pandis, S. N. Constraining Particle Evolution from Wall Losses, Coagulation, and Condensation-Evaporation in Smog-Chamber Experiments: Optimal Estimation Based on Size Distribution Measurements. *Aerosol Sci. Technol.* **2008**, *42* (12), 1001–1015. <https://doi.org/10.1080/02786820802389251>.
- (10) Kulkarni, P.; Baron, P. A.; Willeke, K. *Aerosol Measurement: Principles, Techniques, and Applications*; John Wiley & Sons, 2011.
- (11) Hems, R. F.; Schnitzler, E. G.; Liu-Kang, C.; Cappa, C. D.; Abbatt, J. P. D. Aging of Atmospheric Brown Carbon Aerosol. *ACS Earth Space Chem.* **2021**, *5* (4), 722–748. <https://doi.org/10.1021/acsearthspacechem.0c00346>.
- (12) Moosmüller, H.; Chakrabarty, R. K.; Arnott, W. P. Aerosol Light Absorption and Its Measurement: A Review. *J. Quant. Spectrosc. Radiat. Transf.* **2009**, *110* (11), 844–878. <https://doi.org/10.1016/j.jqsrt.2009.02.035>.
- (13) Liu, C.; Chung, C. E.; Yin, Y.; Schnaiter, M. The Absorption Ångström Exponent of Black Carbon: From Numerical Aspects. *Atmospheric Chem. Phys.* **2018**, *18* (9), 6259–6273. <https://doi.org/10.5194/acp-18-6259-2018>.
- (14) Zotter, P.; Herich, H.; Gysel, M.; El-Haddad, I.; Zhang, Y.; Močnik, G.; Hüglin, C.; Baltensperger, U.; Szidat, S.; Prévôt, A. S. H. Evaluation of the Absorption Ångström Exponents for Traffic and Wood Burning in the Aethalometer-Based Source

- Apportionment Using Radiocarbon Measurements of Ambient Aerosol. *Atmospheric Chem. Phys.* **2017**, *17* (6), 4229–4249. <https://doi.org/10.5194/acp-17-4229-2017>.
- (15) Cuesta-Mosquera, A.; Močnik, G.; Drinovec, L.; Müller, T.; Pfeifer, S.; Minguillón, M. C.; Briel, B.; Buckley, P.; Dudoitis, V.; Fernández-García, J.; Fernández-Amado, M.; Ferreira De Brito, J.; Riffault, V.; Flentje, H.; Heffernan, E.; Kalivitis, N.; Kalogridis, A.-C.; Keernik, H.; Marmureanu, L.; Luoma, K.; Marinoni, A.; Pikridas, M.; Schauer, G.; Serfozo, N.; Servomaa, H.; Titos, G.; Yus-Díez, J.; Zioła, N.; Wiedensohler, A. Intercomparison and Characterization of 23 Aethalometers under Laboratory and Ambient Air Conditions: Procedures and Unit-to-Unit Variabilities. *Atmospheric Meas. Tech.* **2021**, *14* (4), 3195–3216. <https://doi.org/10.5194/amt-14-3195-2021>.
- (16) Saturno, J.; Pöhlker, C.; Massabò, D.; Brito, J.; Carbone, S.; Cheng, Y.; Chi, X.; Ditas, F.; Hrabě de Angelis, I.; Morán-Zuloaga, D.; Pöhlker, M. L.; Rizzo, L. V.; Walter, D.; Wang, Q.; Artaxo, P.; Prati, P.; Andreae, M. O. Comparison of Different Aethalometer Correction Schemes and a Reference Multi-Wavelength Absorption Technique for Ambient Aerosol Data. *Atmospheric Meas. Tech.* **2017**, *10* (8), 2837–2850. <https://doi.org/10.5194/amt-10-2837-2017>.
- (17) Drinovec, L.; Močnik, G.; Zotter, P.; Prévôt, A. S. H.; Ruckstuhl, C.; Coz, E.; Rupakheti, M.; Sciare, J.; Müller, T.; Wiedensohler, A.; Hansen, A. D. A. The “Dual-Spot” Aethalometer: An Improved Measurement of Aerosol Black Carbon with Real-Time Loading Compensation. *Atmospheric Meas. Tech.* **2015**, *8* (5), 1965–1979. <https://doi.org/10.5194/amt-8-1965-2015>.

- (18) Li, C.; Windwer, E.; Fang, Z.; Nissenbaum, D.; Rudich, Y. Correcting Micro-Aethalometer Absorption Measurements for Brown Carbon Aerosol. *Sci. Total Environ.* **2021**, *777*, 146143. <https://doi.org/10.1016/j.scitotenv.2021.146143>.

# 7

## Analyzing Emissions of Pyrolyzed PVC: Measuring Hydrogen Chloride Emissions and Aerosol Properties

### 7.1. Introduction

An estimated 2000 Tg of waste is produced yearly<sup>1</sup> and will eventually need disposing of. The primary method of waste disposal is through landfills; however, incineration is an alternative.<sup>2</sup> The incineration process has the advantage of not only disposing of waste but also generating energy at a cost of resources.<sup>3,4</sup> In areas where waste disposal services are insufficient, open pit waste burning is a common practice.<sup>5</sup> In open pit waste burning, the fuel source is a mixture of different products, such as plastics and biomass, making the emissions complex. Globally, an estimate of 972 Tg of waste is burned every year, releasing toxic and hazardous emissions.<sup>5</sup> Emissions from waste burning include PM<sub>2.5</sub>, polychlorinated biphenyls (PCBs), and volatile organic compounds (VOCs).<sup>5</sup> Without knowing the precise waste mixture, the composition of emissions from waste burning is unknown. Interestingly, certain emissions can function as tracers for certain types of waste and provide insights into what is being burned. For instance, the majority of HCl emissions from open waste burning are from the thermal decomposition of polyvinyl chloride (PVC).<sup>1</sup>

Since the development of PVC, it has become a staple of manufacturing.<sup>6</sup> The popularity of PVC comes from its low cost of production and durability, allowing for mass production and incorporation into medical instruments, piping, and electronics, for example.<sup>7-9</sup> In 2018 alone, 44.3 million tons of PVC resin were produced globally, with a market demand of 59.1 billion USD of PVC products.<sup>10</sup> In the end, the millions of tons of PVC plastics produced will need disposing of.

The thermal decomposition of PVC occurs in two stages that are temperature dependent and can be characterized by their emissions.<sup>11</sup> The initial stage of thermal decomposition of pure PVC is dehydrochlorination between 250°C to 350°C, releasing hydrogen chloride gas.<sup>11</sup> The thermal stability of PVC is tied to its chlorine content<sup>12</sup> which can range from 56 % to 73 % by mass depending on the specific type of PVC.<sup>12</sup> The second stage of pure PVC decomposition is from 350°C to 525°C, releasing semi volatile organic acids<sup>13</sup> such as benzene and toluene derivatives<sup>3</sup> that can form particulate matter.<sup>13</sup> The emissions of PVC degradation are further complicated by the inclusion of additives and stabilizers such as barium and phthalate in the manufacturing process of PVC.<sup>2,9,14</sup> The inclusion of additives can influence PVC properties such as thermal stability and will influence the thermal degradation of the PVC plastics and therefore emissions.<sup>3</sup>

While incorporated into garbage, the thermal degradation of PVC overlaps with the thermal degradation of biomass.<sup>3</sup> This overlap in emissions increases the likelihood of emissions interacting, making the assessment of the combined emissions difficult. As such, I set out to study the emissions from the thermal degradation of PVC as a starting point to study the combined emission of PVC and biomass.

It is estimated that out of the 9 Tg of HCl anthropogenically emitted, 3.5 Tg is a result of open pit waste burning,<sup>5</sup> where the main contributor to the HCl emission is PVC.<sup>1</sup> The importance of HCl emissions from open waste burning is that HCl can act as a chloride source. For instance, once HCl is emitted from PVC thermal degradation, it can undergo photolysis and form chlorine radicals that may interact with, and deplete, atmospheric ozone or enhance aerosol hygroscopicity.<sup>15,16</sup> In a local context, toxicity from PVC thermal degradation emission is of concern during house fires that can produce toxic chlorinated VOCs and in particular dioxins.<sup>7</sup>

Another type of emission that has consequences for the environment is aerosol particles. The aerosol particle emissions from PVC pyrolysis are often ignored; however, they may present a risk to human health through exposure to aerosols particles loaded with benzene derivatives, for example.<sup>3</sup> Information about the size distribution of the emitted aerosol particles can be important in determining their health impacts. For instance, smaller aerosol particles such as PM<sub>2.5</sub> can penetrate more efficiently into the respiratory system and inject potentially toxic chemicals into our bodies when compared with larger particles.<sup>17</sup>

The aerosol from PVC-pyrolysis can also impact the local climate by absorbing and scattering solar radiation. This ability of aerosol from PVC pyrolysis to scatter and absorb solar radiation has not been quantified and, in comparison to emissions from wildfires, their impact may be small. However, co-pyrolysis of PVC with other waste may influence the evolution and composition of the produced aerosol particles and change their optical properties. As such, I studied size distribution and optical properties of aerosol particles emitted from PVC pyrolysis together with accompanying HCl emissions to provide a reference point for future studies of emissions from co-pyrolysis of biomass and PVC.

## 7.2. Experimental Methods

### 7.2.1. Generation and Sampling of Pyrolysis Emissions

The emissions from PVC pyrolysis were generated using a custom-built tube furnace. The tube furnace was constructed from a cylindrical ceramic fiber heater with an inner diameter of 2.5 cm and a temperature controller (Thermal Devices Inc) equipped with a K-type thermocouple. A quartz tube, fitted with adapters at both ends, was used as a pyrolysis vessel. Upstream of the tube furnace is a mechanical flow controller that regulates the flow of carrier gas into the pyrolysis tube.

A simplified version of the experimental setup can be seen in Figure 7.1. The PVC sample consisted of 5 mm by 8 mm pieces of PVC piping weighing 0.7 g. The PVC piping was purchased from Wolseley Plumbing, a local distributor of plumbing equipment, to mimic PVC waste that may be found in open waste burning of construction material. The PVC sample was first placed in the tube furnace, and the system was flushed with 3 slpm of N<sub>2</sub> for at least 10 minutes. The heating cycle of the tube furnace was then initiated only if the total aerosol particle number concentration within the system was less than 50 particles/cm<sup>3</sup>, which was measured after an activated charcoal (AC) denuder using a condensation particle counter (CPC 3776). The tube furnace was then set to heat at a rate of 50 °C min<sup>-1</sup> until a temperature of 350°C was reached. The emissions from the thermal degradation of PVC flowed through the experimental set-up shown in Figure 7.1. from the onset of the heating cycle until 40 minutes after the final temperature was reached. At this time the pyrolysis of the PVC sample was assumed to be completed.

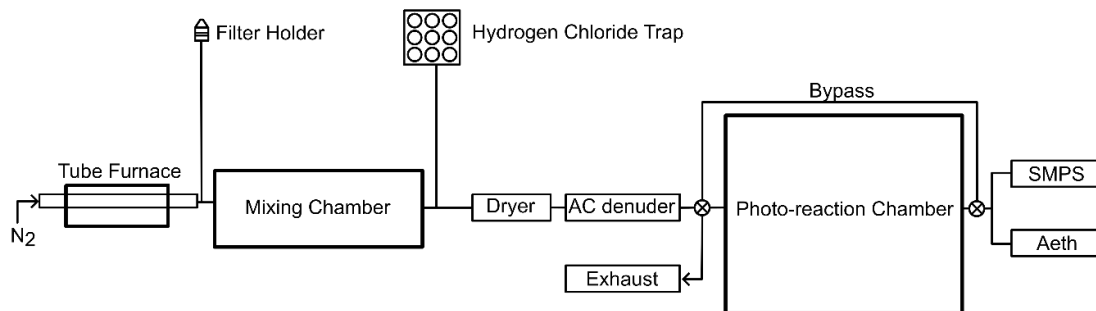


**Figure 7.1.** The overall experimental set up to study the emissions form pyrolysis of PVC piping.

Starting with the beginning of the heating cycle, a 0.7 slpm flow was sampled from the tube furnace to a filter holder where a quartz filter collected aerosol particles for thermal optical analysis. The filter was removed from the filter holder 3 minutes after a temperature of 350°C was reached. The remaining flow that exits the tube furnace was directed to a 5 L mixing chamber. After the mixing chamber, the emissions are split into two paths. In the first path the emissions underwent pre-treatment using a 25 cm long diffusion dryer containing calcium sulfate and a 100 cm long active charcoal (AC) denuder. The treatment of the emissions in this path was to prevent damage from HCl to the stainless steel instruments. The emissions were then injected into the photo-reaction “smog” chamber. The injection of particles into the smog chamber started with the beginning of the heating cycle. During the injection into the smog chamber, the total particle number concentration in the smog chamber was measured using a CPC for the duration of the injection. The injection continued during the entire pyrolysis time, i.e., for 40 min, consistent with the HCl trapping time. After the injection phase of the experiment, the aerosol size distribution within the smog chamber was measured using a scanning mobility particle sizer (SMPS 3936L76) composed of a CPC 3776 and a differential mobility analyzer (DMA) 3080 long. The samples within the chamber were then diluted with pure air until the mass

concentration of particles was approximately  $400 \text{ ug/m}^3$  and optical measurements with an MA200 aethalometer can begin. For some experiments, the smog chamber was bypassed and the size distribution of aerosol particles that are emitted were directly measured using the SMPS. The VOC content in the smog chamber after cleaning and during experiments was assessed using ultra-violet differential optical absorption (DOAS) spectroscopy. The DOAS light source, located at one end of the smog chamber, is a broadband deuterium lamp (Ocean Optics, D-2000-S) with emission output from 215-400 nm. The light beam is transported through an optical fibre to collimator lens, transmitted through the chamber to a collecting lens, and then transmitted to the detector (Ocean Optics, HR-2000+) through another optical fibre. A measured absorption spectrum is fitted to a ninth order polynomial to capture only broad background features without the molecular signals. This background is then subtracted from the original spectrum to yield the differential absorption spectrum that contains the molecular signals.<sup>18</sup> The concentration of the species of interest is then determined by fitting the differential absorption spectrum to a literature spectrum.

The second path after the mixing chamber leads to a hydrogen chloride trap. The chloride trap consists of nine 250 ml Erlenmeyer flasks that have been modified into bubblers, see Figure 7.2. The first three flasks are empty and trap any low volatility condensate. The next five contain 100 ml of 2 M NaOH to trap any gaseous HCl in the liquid phase as chloride. By the time the gas is bubbled into the last of the five flasks that contains NaOH, no gaseous HCl remained in the gas. This was verified by measuring the HCl concentration in the fifth flask which was kept as a precaution for experiments larger PVC samples. The last flask in the series is empty to prevent NaOH solution exiting the trap.



**Figure 7.2.** The HCl trap used to capture gaseous HCl by bubbling the emissions through 2M NaOH solution.

### 7.2.2. Emissions Characterization

The portion of the pyrolysis emissions that are sampled onto an 11.76 cm<sup>2</sup> quartz filter were analyzed using a thermal-optical transmission analyzer (Sunset Laboratory Inc) to measure the elemental carbon (EC) and organic carbon (OC) content. A 1.5 cm<sup>2</sup> punch of the aerosol-laden filter was placed into the analyzer oven where control of the temperature and gas is possible. The initial analysis of the filter measures the OC content of the filter by gradually ramping the heat inside the oven to 870°C in the absence of oxygen.<sup>19</sup> A helium carrier gas sweeps the OC emissions to a manganese dioxide chamber to be converted to CO<sub>2</sub> gas and then to a nickel catalyst chamber to be reduced to methane.<sup>19</sup> The OC that has been converted to methane is fed into a fire ionization detector (FID) calibrated for a known amount of methane.<sup>19</sup> Once all the OC has been analyzed, the oven temperature is cooled to 500°C. At 500°C, a 2% mixture of oxygen in He is fed into the oven, and the temperature is ramped up again.<sup>19</sup> During this stage, the EC is oxidized, and the emissions follow the same path as OC to be quantified.<sup>19</sup>

The emissions that are not sampled by the filter are transported to the mixing chamber. A portion of the emissions that exits the mixing chamber is pushed into the HCl trap using an Air-

Vac venturi pump (AVR038H). The captured HCl is measured using a HACH chloride TNT879 test kit<sup>20</sup> after being neutralized by 3M H<sub>2</sub>SO<sub>4</sub> and filtered to remove particulate matter. The test kits utilize a colorimetric reaction between chloride and mercury thiocyanate ferric nonahydrates solution to form a red-orange ferric thiocyanate compound.<sup>20</sup> The concentration of colored compound formed is proportional to the chloride concentration and the absorbance is measured using a Jasco-1500 spectrometer at 468 nm. Measured calibration curves with known concentrations of HCl between 10 to 1000 ppm are shown in Figure 7.3 and are used to convert an absorbance measurement to an HCl concentration.

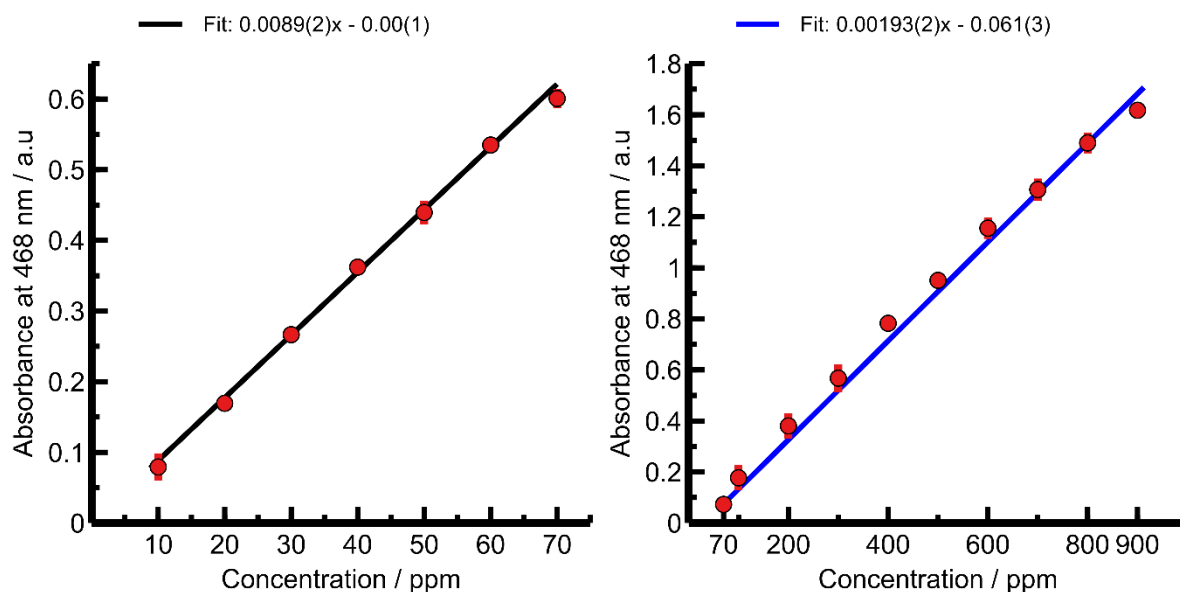


**Figure 7.3.** Colorimetric calibration curves for the determination of HCl concentration from the HCl trap. The error in the fit is one standard deviation of the last digit.

The remainder of the emissions that are not sampled for EC/OC or HCl are injected into the smog chamber. The smog chamber at the University of Alberta is composed of a 1.8 m<sup>3</sup> perfluoroalkoxy (PFA) film (Ingeniven) surrounded by three sets of eight 32 W black lights with peak emission at 350 nm. The photo-reaction chamber is equipped with a mixing fan and temperature and relative humidity sensors within the chamber. During continuous flow

experiments, a pure air generator (Aadco 737) supplies clean dry air to the chamber to maintain the volume of the PFA bag. The size distribution of the aerosol particles within the smog chamber was measured using an SMPS operating with a sheath flow of 1.7 L min<sup>-1</sup> and a sample flow of 0.3 L min<sup>-1</sup>.

The absorption wavelength dependence of emitted aerosol particles was measured using an MA200 aethalometer. The aethalometer is a filter-based absorption analyzer, operating at 370 nm, 475 nm, 528 nm, 625 nm, and 880 nm.<sup>21</sup> It is operated in Dualspot compensation mode to correct for the filter load effect, a decrease in optical path length over time. A sample flow rate of 100 mL min<sup>-1</sup> and an attenuation threshold of 100 to trigger PTFE filter advancement were used. The aethalometer outputs the black carbon equivalent ( $BC_{e,\lambda}$  in ng m<sup>-3</sup>) mass concentration at each wavelength which can be converted to an absorbance using Equation (1)<sup>21</sup> to determine the wavelength dependence of absorption ( $B_{abs}$ , in Mm<sup>-1</sup>).

$$B_{abs} = BC_{e,\lambda} \cdot MAE_{BC,\lambda} \cdot 10^{-3} \quad (1)$$

In Equation (1), MAE (in M<sup>2</sup> g<sup>-1</sup>) is the mass attenuation cross section of BC at the corresponding wavelength and is obtained from Li et al.<sup>21</sup>

### 7.3. Results and Discussion

The PVC sample used in this study is from PVC piping with additives that can influence its thermal degradation.<sup>3</sup> The choice of PVC piping is to mimic emissions from PVC that can be found in waste, such as construction waste. Since the temperature ranges for the two stages of thermal decomposition are not known for this specific PVC, a pyrolysis temperature that lies between the two stages of thermal decomposition of pure PVC<sup>3</sup> was chosen to potentially emit both HCl and aerosol particles. Assuming that aerosols are generated only during the second stage of thermal decomposition a CPC that directly samples from the tube furnace can be used to

determine an approximate transition temperature. The onset of aerosol emission from the thermal degradation of PVC piping in this study is approximately 290°C, signifying the end of the first stage of thermal decomposition. A thermogravimetric analysis of the PVC piping would be necessary to determine the exact temperature of each stage of the thermal degradation of the PVC piping. Without knowing the exact time and temperature of each stage, the aerosols and HCl emitted from our sample of PVC piping are sampled from the onset of heating.

### **7.3.1. HCl Emissions**

In the first stage of thermal decomposition of PVC, dehydrochlorination occurs, resulting in the formation of HCl along with trace amounts of chlorobenzene, benzyl chloride, and 1,1-dichloro-4-methyl-1,4-pentadiene.<sup>22</sup> During this stage, a weight loss of 61% of the total mass has been reported, associated with the release of HCl, while stage two accounts for an 8% decrease in mass.<sup>22</sup> In the current study, the percent mass emission yield is determined as the mass of the emissions divided by the original mass of PVC. The mass of emissions is the difference of the mass of PVC before ( $M_{PVC}$ ) and after pyrolysis ( $M_{char}$ ) see Table 7.1. A total weight loss of approximately 61%, as shown in Table 7.1, is observed. This weight loss accounts for both stage one and partially stage two of thermal decomposition because we observed aerosol particle emissions. The emission of HCl is temperature dependent and has been shown to increase with temperature.<sup>23</sup> In this study, only a single temperature of 350 °C was used. From the measured chloride concentrations in the HCl trap solutions, the total mass of HCl emitted was determined and the corresponding percent mass emission yields are given in Table 7.1. On average, the emissions from PVC pyrolysis at 350 °C are 25 % HCl. The difference between the 25 % HCl measured and the expected 50 – 60 % HCl, based on the chlorine content of pure PVC can be rationalized as follows. One possibility is that some of the HCl emitted is trapped in the bio-oil

that coats the pyrolysis tube. Another possibility is that a more significant amount of HCl gas is reacting with the additives and stabilizer in the PVC resulting in the formation of chloride residues.<sup>2</sup> Lastly, chlorinated aromatics may be forming that can nucleate to form aerosol particles that do not dissociate in NaOH solution. In future studies PVC pyrolysis must be probed at higher temperatures to determine HCl emissions as a function of temperature and heating rate. Further discussions on extending the temperature can be found in Section 7.5.

**Table 7.1** The mass of PVC pyrolyzed, emission yield ( $M_{PVC} - M_{char}$ )/ $M_{PVC}$ , and percent HCl in the emissions,  $M_{HCl}/(M_{PVC} - M_{char})$ .

Fuel	PVC Mass / g	Emission Yield / wt.%	HCl Yield / wt.%
PVC	0.7516	59	23
PVC	0.7328	65	25
PVC	0.7055	58	29
PVC	0.7223	60	24

### 7.3.2. Thermal Optical Analysis

The ratio of EC to OC of the PVC-derived aerosol can be seen in Table 7.2. The emitted aerosol from PVC pyrolysis is predominantly composed of organic compounds, as suggested by the low EC/OC ratio. Because the major component of the aerosol particles is organic carbon, the properties measured can be attributed to the low volatile and semi-volatile organic compounds that make up the aerosol particle.

The determined EC/OC ratio falls into the same range that was measured during garbage burning in landfills, which is between 0.434 and 0.035.<sup>1</sup> The garbage burned in these landfills contained mostly plastics as fuel, confirming that most of the emissions are low or semi volatile organic compounds. Comparatively, the EC/OC ratio measured for biomass burning ranges from 0 to 1, depending on the extent of combustion, and for vehicle exhaust, it ranges from 0.4 to 50.<sup>24</sup>

This suggests that the thermal-optical method cannot differentiate between plastic burning and biomass burning.

**Table 7.2.** Results from the thermal-optical analysis of PVC pyrolysis emissions.

	Pyrolysis 1	Pyrolysis 2	Pyrolysis 3	Pyrolysis 4
OC / mg	1.925	1.8289	1.3298	0.9856
EC / mg	0.1161	0.0648	0.0163	0.0002
EC/OC	0.06	0.04	0.01	0.00

### 7.3.3. Size Distribution

The aerosol particle size distributions that were directly measured from the mixing chamber are shown in Figure 7.4. for different pyrolysis times. The aerosol particle size distributions are unimodal. The total number concentration and mean aerosol particle mobility diameter of aerosol particles are in Figures 7.5a) and b), respectively, for three different experiments. Figure 7.5 illustrates how the emissions from the PVC pyrolysis change with pyrolysis time; the onset of heating defines measurement time = 0. The aerosols are first detected at 270 °C and reach a maximum total aerosol particle number concentration after reaching the target temperature of 350 °C. Interestingly, the initial increase in aerosol particle number concentration coincides with an increase in particle mean diameter. A possible explanation is that the pyrolysis of plastics is known to emit aerosols that agglomerate,<sup>26</sup> and at the highest concentration, larger agglomerates can form.

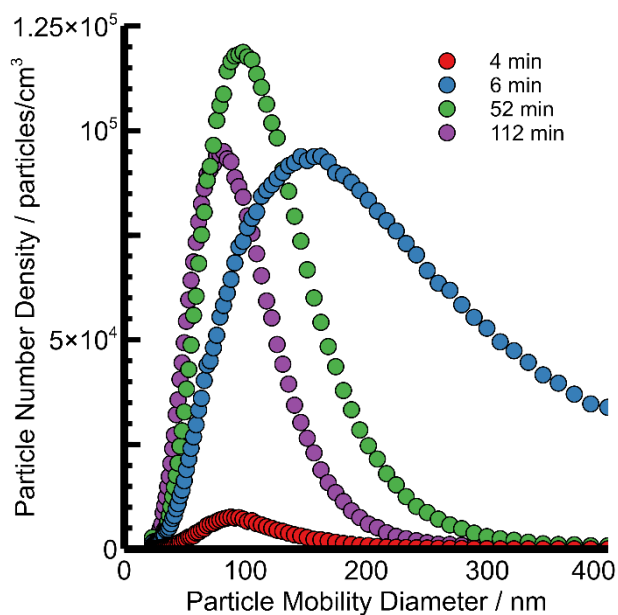


**Figure 7.4.** Measurements of size distribution of PVC pyrolyzed at 350°C at onset of heating. The SMPS scans takes 2 minutes per scan and the scans are labelled by the start time of the scan relative to the start of the tube furnace.

To investigate concentration-dependent agglomeration, the flow into the mixing chamber was decreased for 30 seconds, 11 minutes after the onset of heating (Exp 3 in Figure 7.5). Comparing Exp 1 and 2 to Exp 3 in Figure 7.5, the mean particle mobility diameter in Exp 3 is approximately 37 nm smaller. The initial rapid decrease in total particle number density and mean particle diameter is followed by a steady rate of decreasing emissions. The size changes consistently between experiments once the emission rate into the mixing chamber is the same.

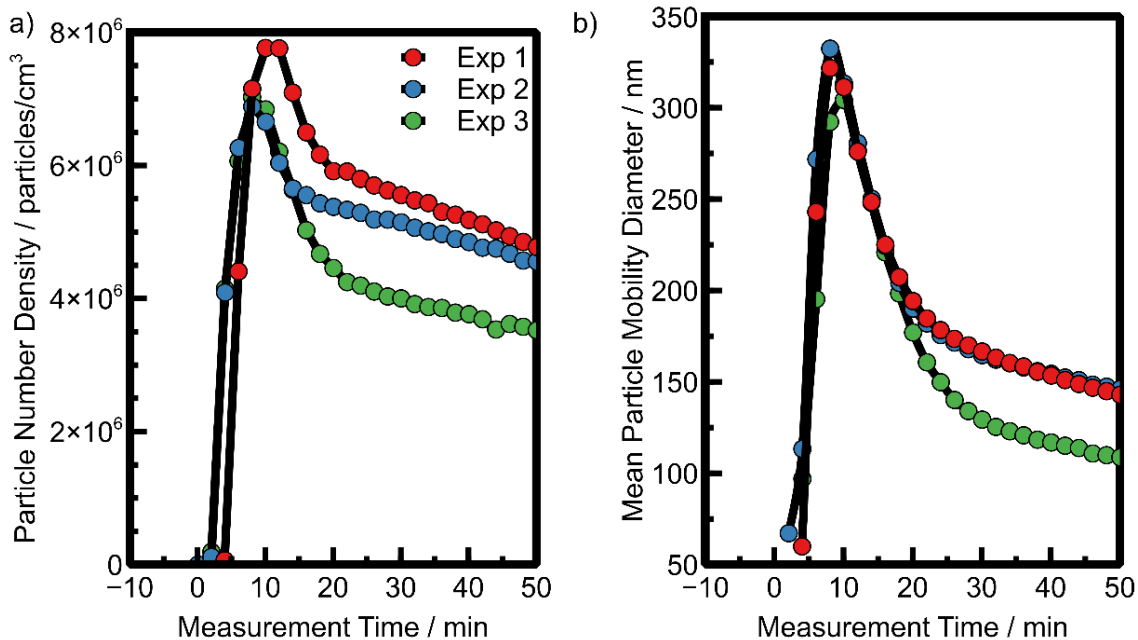


**Figure 7.5.** a) The total particle concentration emitted by the thermal degradation of PVC at 350°C as a function of pyrolysis time. b) The corresponding mean particle mobility diameter of the aerosol size distribution measured directly from the tube furnace. Experiments 1 and 2 were done under the same conditions; for experiment 3, the emissions flow was interrupted for 30 s, 11 min after onset of heating.

A different progression is observed when the aerosol particles are injected into the smog chamber. For these experiments aerosol injection into the smog chamber was done for the duration of the pyrolysis (40 minutes). Once the injection stopped, measurements with the SMPS began. These experiments were conducted with no radical source or radiation source. The evolution of the mean particle size for 1500 minutes under these conditions is shown in Figure 7.6. In the smog chamber several processes can occur, including agglomeration, condensation/evaporation, nucleation, and deposition at chamber walls that can result in changes in the observed aerosol particle size distribution.<sup>27</sup> In this study nucleation is suppressed by removing the VOCs in the emissions with an AC denuder and by not introducing a radical source to form semi-volatile species from any volatile organic species that remain. Additionally, from

the UV-DOAS measurements no benzene, toluene, and xylene compounds were detected. At the start of the measurements, the mean particle mobility diameter is about 200 nm and then increases to plateau at about 350 nm after 700 min. The increase could be a result of more efficient wall deposition of aerosol particles that are smaller than 100 nm and larger than 500 nm<sup>27</sup> resulting in a biased time evolution of the size distribution. The size-dependent loss of the aerosol particles inside the chamber can be seen in Figure 7.7, where the particle number concentration for four different aerosol particle sizes is plotted as function of time. Exponential functions can be fitted to the decays, and the coefficients in the exponential functions represent total rate constants (Figure 7.7) associated with the processes involved.

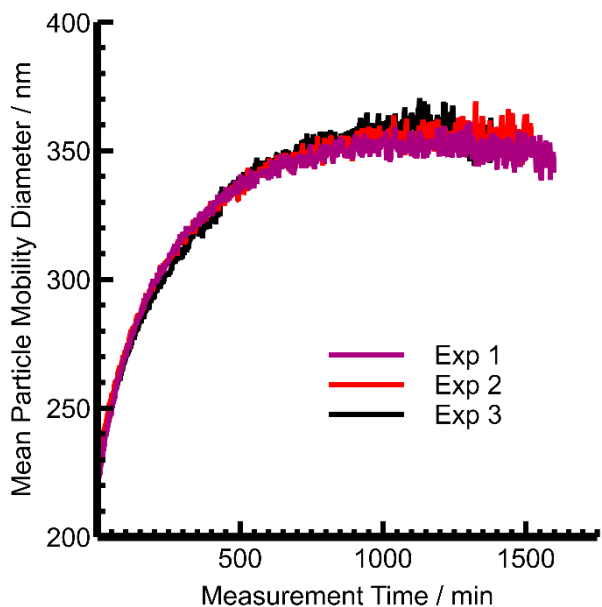


**Figure 7.6.** The change in the mean mobility diameter of aerosol particles in the smog chamber. Measurements began after injection of aerosol particles into the smog chamber ended (40 minutes).

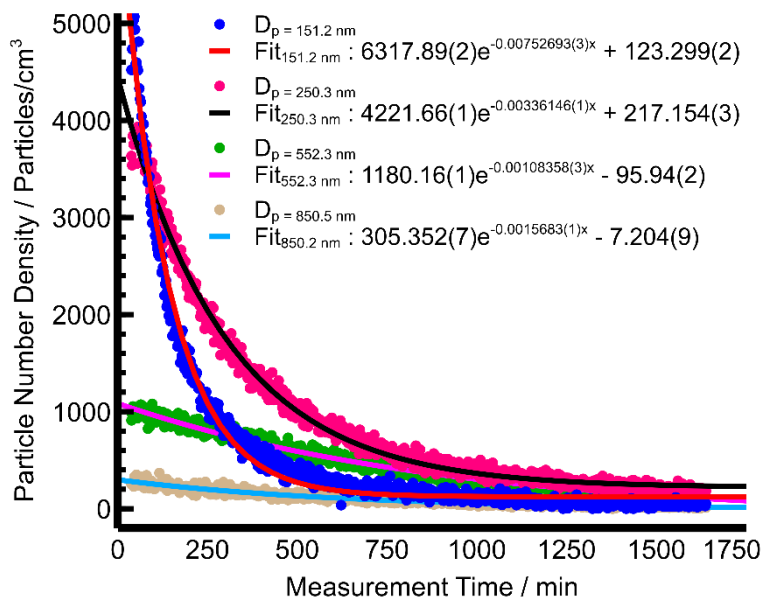


**Figure 7.7.** The number densities of particles with diameters ( $D_p$ ) of 151.2 nm, 250.3 nm, 552.3 nm, and 850.5 nm throughout experiment. The numbers in brackets are the errors in units of the last digit.

### 7.3.4. Optical Properties

Aerosols composition determines to a large degree the ability of an aerosol particles to scatter or absorb solar radiation. For example, aerosol particles composed of organic constituents preferentially absorb at lower wavelengths compared to black carbon (BC) rich aerosol particles which are produced during complete combustion.<sup>28</sup> In instances were different aerosols with different abilities to absorb solar radiation, such as BC aerosol and brown carbon (BrC) aerosol, coexist, absorption amplification at lower wavelengths can occur.<sup>29</sup> The particles emitted from the pyrolysis of PVC are primarily organic aerosols, suggesting that they will have wavelength dependent light absorption. If PVC is mixed with biomass during the burning process, the composition of the aerosol particles will change, which will alter their interactions with solar radiation. The absorption Ångstrom coefficient (AAC) is a unitless parameter that describes the wavelength dependence of absorption of an aerosol particle.<sup>30</sup> The AAC can be determined by

Equation (2) where  $B_{abs}$  is the wavelength dependent absorption in  $\text{Mm}^{-1}$ ,  $\lambda$  is the wavelength in nm, and  $B_0$  the wavelength independent absorption constant in  $\text{Mm}^{-1}$ .<sup>29</sup>

$$B_{abs}(\lambda) = B_0\lambda^{-AAC} \quad (2)$$

The wavelength dependence of the absorption of aerosol particles from PVC pyrolysis was measured with an aethalometer at several different wavelengths and the results are shown in Figure 7.8 for three different experiments. Also given in Figure 7.8 are the AACs that were obtained from fits to the experimental data. The obtained AAC values are reasonably consistent and range from 5.5 to 6.1. The AACs for aerosol particles from PVC pyrolysis are comparable to those of brown carbon aerosols, which are predominantly composed of organic compounds and have AAC values ranging from 2 to 11.<sup>31</sup> Black carbon-rich aerosols have an AAC of 1.<sup>31</sup>

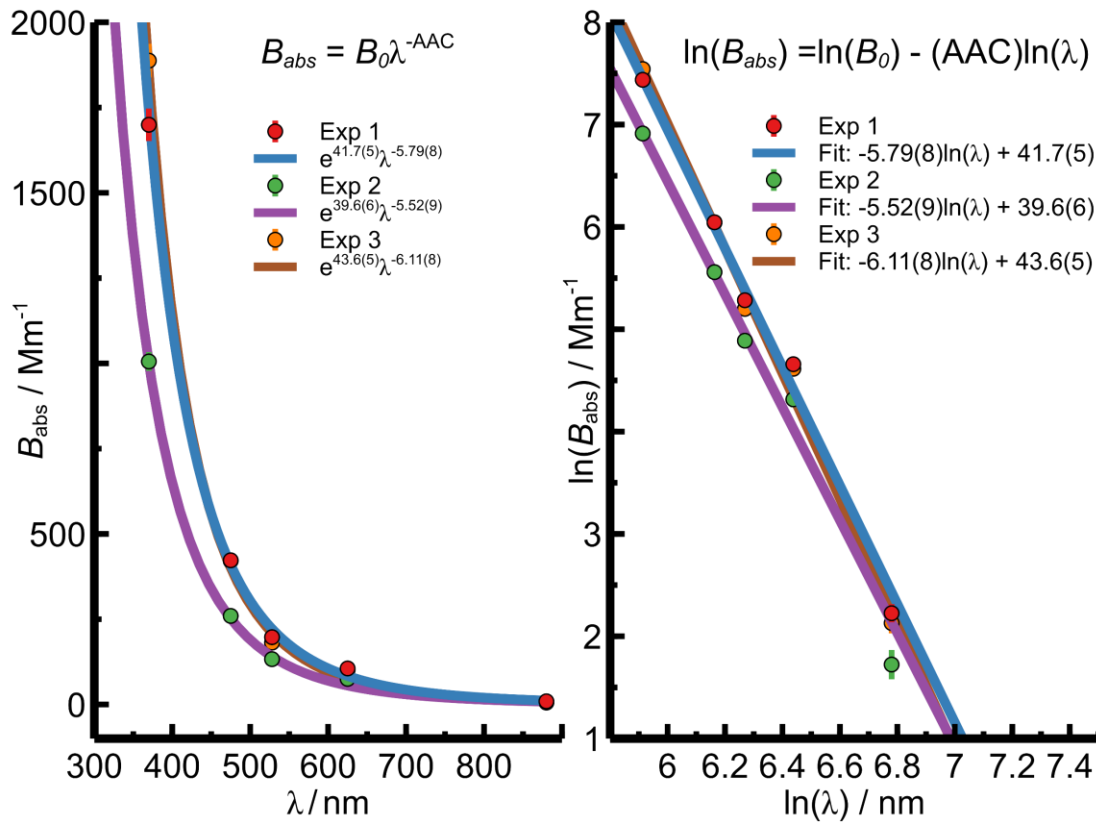


**Figure 7.8.** The absorption ( $B_{abs}$ ) of PVC pyrolyzed emission, in  $\text{Mm}^{-1}$ , at different wavelengths ( $\lambda$ ) in nm, is fit as a power law relationship to determine the absorption Ångstrom coefficients

(AAC), a unitless parameter. The errors of the fitted parameters are given in brackets in units of the last digit.

An alternative approach can be used to approximate the AAC using absorptions at two wavelengths through Equation (3)

$$AAC(\lambda_1, \lambda_2) = -\frac{\ln(B_{abs,\lambda_1}/B_{abs,\lambda_2})}{\ln(\lambda_1/\lambda_2)} \quad (3)$$

were  $B_{abs,\lambda_1}$  and  $B_{abs,\lambda_2}$  are the absorption coefficients, in  $Mm^{-1}$ , at  $\lambda_1$  and  $\lambda_2$ , in nm.<sup>29</sup> The results from the two wavelengths approach for 10 different wavelength combinations are given in Table 7.3. Depending on the wavelengths chosen, the AAC ranges from 3.5 to 7.2. The two approaches lead to slightly different ranges for the AAC values. However, both results confirm that the aerosol particles emitted by PVC pyrolysis are predominantly composed of organic compounds. These result suggest that if these aerosol particles can enhance the short wavelength absorption of BC aerosol particles, that may be co-emitted in open pit waste burning.

**Table 7.3.** The AAC calculated using the two-wavelength ( $\lambda_1, \lambda_2$ ) approximation (Equation (2)) for the different possible combinations of wavelengths.

	Exp 1	Exp 2	Exp 3	Average
AAC (370 nm, 475 nm)	5.4	6.0	5.6	5.7
AAC (370 nm, 528 nm)	5.7	6.6	6.1	6.1
AAC (370 nm, 625 nm)	4.9	5.6	5.3	5.3
AAC (370 nm, 880 nm)	6.0	6.2	6.0	6.1
AAC (475 nm, 528 nm)	6.3	8.0	7.2	7.2
AAC (475 nm, 625 nm)	4.5	5.2	5.1	4.9
AAC (475 nm, 880 nm)	6.2	6.3	6.2	6.2
AAC (528 nm, 625 nm)	3.4	3.5	3.7	3.5
AAC (528 nm, 880 nm)	6.2	6.0	6.0	6.1
AAC (625 nm, 880 nm)	7.6	7.3	7.1	7

#### **7.4. Future Studies**

Further characterization of the emission from PVC pyrolysis is needed at different pyrolysis temperatures and at different rates of pyrolysis. Both temperature and rate of pyrolysis are known to influence emissions<sup>23,32</sup> and their effects on PVC pyrolysis and PVC and biomass co-pyrolysis need to be studied for a more complete characterization of the emissions to better assess impacts on environment and health. As such, the temperature range should be extended to 250°C - 750°C to span the full biomass decomposition range.<sup>32</sup> Additionally, heating rates from 0.1 °C s<sup>-1</sup> to 200 °C s<sup>-1</sup> that span slow and fast pyrolysis processes<sup>32</sup> should be used to assess the production of different emission. At each temperature and pyrolysis rate the aerosols and HCl emission should be characterized.<sup>32</sup> Further experiments could probe heterogeneous reactions on the surface of the emitted aerosols that may release chlorine radicals from the particulate phase into the gas phase.<sup>33</sup> The chemical composition of aerosol particles from PVC pyrolysis could be probed by, for example, an aerosol mass spectrometer.

Beyond measurements of thermal decomposition stages and aerosol composition, studying the fate of the aerosol particles after being released into the atmosphere is of interest. During their residence time in the atmosphere, particles can age, that is, they can change composition and morphology. For example, For example, the aerosol particles can increase in size through condensation of a layer of SOA.

#### **7.5. Conclusions**

HCl and aerosol emissions from PVC pyrolysis at 350°C were measured. The pyrolysis of 0.7 g of PVC resulted in the conversion of 61 % of its initial mass into emissions. Of those emissions, 25 % was HCl. The emitted aerosol particles were classified by their OC and EC content and found to be composed primarily of organic compounds. The organic aerosol emitted by PVC

pyrolysis has a wavelength absorption dependence with an AAC ranging from 5.5 to 6.1. Aerosol particle size distributions were measured directly after pyrolysis and after injection into a smog chamber. Both size distributions were found to be unimodal within the size range of the SMPS. The mean particle mobility diameter when measured directly from the mixing chamber was initially ~ 340 nm and decreased with time to ~ 150 nm. This change is believed to be a result of concentration dependent agglomeration and further experiments are needed to probe how these aerosols grow after nucleation. An opposite trend is seen when sampling from the smog chamber where the mean particle mobility diameter is initially ~200 nm and increases to ~ 350 nm. This increase in mean particle mobility diameter is also thought to be a result of agglomeration. However, it is convoluted by loss processes to smog chamber walls and requires further investigation. The data obtained in this study is a first step towards studies of co-pyrolysis of PVC and biomass in the hopes to better assess the impact of open pit waste burning on health and environment.

## References

- (1) Christian, T. J.; Yokelson, R. J.; Cárdenas, B.; Molina, L. T.; Engling, G.; Hsu, S.-C. Trace Gas and Particle Emissions from Domestic and Industrial Biofuel Use and Garbage Burning in Central Mexico. *Atmospheric Chem. Phys.* **2010**, *10* (2), 565–584.  
<https://doi.org/10.5194/acp-10-565-2010>.
- (2) Kim, S. Pyrolysis Kinetics of Waste PVC Pipe. *Waste Manag.* **2001**, *21* (7), 609–616.  
[https://doi.org/10.1016/S0956-053X\(00\)00127-6](https://doi.org/10.1016/S0956-053X(00)00127-6).
- (3) Yu, J.; Sun, L.; Ma, C.; Qiao, Y.; Yao, H. Thermal Degradation of PVC: A Review. *Waste Manag.* **2016**, *48*, 300–314. <https://doi.org/10.1016/j.wasman.2015.11.041>.
- (4) Liu, Y.; Zhou, C.; Li, F.; Liu, H.; Yang, J. Stocks and Flows of Polyvinyl Chloride (PVC) in China: 1980-2050. *Resour. Conserv. Recycl.* **2020**, *154*, 104584.  
<https://doi.org/10.1016/j.resconrec.2019.104584>.
- (5) Wiedinmyer, C.; Yokelson, R. J.; Gullett, B. K. Global Emissions of Trace Gases, Particulate Matter, and Hazardous Air Pollutants from Open Burning of Domestic Waste. *Environ. Sci. Technol.* **2014**, *48* (16), 9523–9530. <https://doi.org/10.1021/es502250z>.
- (6) Braun, D. Poly(Vinyl Chloride) on the Way from the 19th Century to the 21st Century. *J. Polym. Sci. Part Polym. Chem.* **2004**, *42* (3), 578–586. <https://doi.org/10.1002/pola.10906>.
- (7) Zhang, M.; Buekens, A.; Jiang, X.; Li, X. Dioxins and Polyvinylchloride in Combustion and Fires. *Waste Manag. Res.* **2015**, *33* (7), 630–643.  
<https://doi.org/10.1177/0734242X15590651>.
- (8) Chong, N. S.; Abdulramoni, S.; Patterson, D.; Brown, H. Releases of Fire-Derived Contaminants from Polymer Pipes Made of Polyvinyl Chloride. *Toxics* **2019**, *7* (4), 57.  
<https://doi.org/10.3390/toxics7040057>.

- (9) Koerner, G. R.; Koerner, R. M. 7.3 - Polymeric Geomembrane Components in Landfill Liners. In *Solid Waste Landfilling*; Cossu, R., Stegmann, R., Eds.; Elsevier, 2018; pp 313–341. <https://doi.org/10.1016/B978-0-12-407721-8.00017-6>.
- (10) Alsabri, A.; Al-Ghamdi, S. G. Carbon Footprint and Embodied Energy of PVC, PE, and PP Piping: Perspective on Environmental Performance. *Energy Rep.* **2020**, *6*, 364–370. <https://doi.org/10.1016/j.egy.2020.11.173>.
- (11) Marongiu, A.; Faravelli, T.; Bozzano, G.; Dente, M.; Ranzi, E. Thermal Degradation of Poly(Vinyl Chloride). *J. Anal. Appl. Pyrolysis* **2003**, *70* (2), 519–553. [https://doi.org/10.1016/S0165-2370\(03\)00024-X](https://doi.org/10.1016/S0165-2370(03)00024-X).
- (12) Khan, S. M.; Gull, N.; Khan, R. U.; Butt, M. T. Z. Polyvinylchloride (PVC): Structure and Properties Relationship. In *Polyvinylchloride-based Blends: Preparation, Characterization and Applications*; P. M., V., Darie-Nita, R. N., Eds.; Springer International Publishing: Cham, 2022; pp 19–47. [https://doi.org/10.1007/978-3-030-78455-3\\_2](https://doi.org/10.1007/978-3-030-78455-3_2).
- (13) Aracil, I.; Font, R.; Conesa, J. A. Semivolatile and Volatile Compounds from the Pyrolysis and Combustion of Polyvinyl Chloride. *J. Anal. Appl. Pyrolysis* **2005**, *74* (1), 465–478. <https://doi.org/10.1016/j.jaap.2004.09.008>.
- (14) Zakharyan, E. M.; Petrukhina, N. N.; Maksimov, A. L. Pathways of Chemical Recycling of Polyvinyl Chloride: Part 1. *Russ. J. Appl. Chem.* **2020**, *93* (9), 1271–1313. <https://doi.org/10.1134/S1070427220090013>.
- (15) Li, J.; Zhang, N.; Wang, P.; Choi, M.; Ying, Q.; Guo, S.; Lu, K.; Qiu, X.; Wang, S.; Hu, M.; Zhang, Y.; Hu, J. Impacts of Chlorine Chemistry and Anthropogenic Emissions on Secondary Pollutants in the Yangtze River Delta Region. *Environ. Pollut.* **2021**, *287*, 117624. <https://doi.org/10.1016/j.envpol.2021.117624>.

- (16) Gunthe, S. S.; Liu, P.; Panda, U.; Raj, S. S.; Sharma, A.; Darbyshire, E.; Reyes-Villegas, E.; Allan, J.; Chen, Y.; Wang, X.; Song, S.; Pöhlker, M. L.; Shi, L.; Wang, Y.; Kommula, S. M.; Liu, T.; Ravikrishna, R.; McFiggans, G.; Mickley, L. J.; Martin, S. T.; Pöschl, U.; Andreae, M. O.; Coe, H. Enhanced Aerosol Particle Growth Sustained by High Continental Chlorine Emission in India. *Nat. Geosci.* **2021**, *14* (2), 77–84.  
<https://doi.org/10.1038/s41561-020-00677-x>.
- (17) Bernstein, J. A.; Alexis, N.; Barnes, C.; Bernstein, I. L.; Nel, A.; Peden, D.; Diaz-Sanchez, D.; Tarlo, S. M.; Williams, P. B.; Bernstein, J. A. Health Effects of Air Pollution. *J. Allergy Clin. Immunol.* **2004**, *114* (5), 1116–1123. <https://doi.org/10.1016/j.jaci.2004.08.030>.
- (18) Platt, U.; Stutz, J. Differential Absorption Spectroscopy. In *Differential Optical Absorption Spectroscopy: Principles and Applications*; Platt, U., Stutz, J., Eds.; Springer: Berlin, Heidelberg, 2008; pp 135–174. [https://doi.org/10.1007/978-3-540-75776-4\\_6](https://doi.org/10.1007/978-3-540-75776-4_6).
- (19) User's Manual for Organic and Elemental Carbon (OCEC) Laboratory Analyzer, Mode 5L, Sunset Laboratory Inc., Oregon, USA, 2015.
- (20) Chloride TNTplus Vial Test (1.0-1,000 mg/L Cl), 24 Tests | Hach Canada - Overview.  
<https://ca.hach.com/chloride-tntplus-vial-test-1-0-1-000-mg-l-cl-24-tests/product?id=54566921144> (accessed 2024-04-13).
- (21) Li, C.; Windwer, E.; Fang, Z.; Nissenbaum, D.; Rudich, Y. Correcting Micro-Aethalometer Absorption Measurements for Brown Carbon Aerosol. *Sci. Total Environ.* **2021**, *777*, 146143. <https://doi.org/10.1016/j.scitotenv.2021.146143>.
- (22) Zhou, J.; Liu, G.; Wang, S.; Zhang, H.; Xu, F. TG-FTIR and Py-GC/MS Study of the Pyrolysis Mechanism and Composition of Volatiles from Flash Pyrolysis of PVC. *J. Energy Inst.* **2020**, *93* (6), 2362–2370. <https://doi.org/10.1016/j.joei.2020.07.009>.

- (23) Yu, H.; Qu, J.; Liu, Y.; Yun, H.; Li, X.; Zhou, C.; Jin, Y.; Zhang, C.; Dai, J.; Bi, X. Co-Pyrolysis of Biomass and Polyvinyl Chloride under Microwave Irradiation: Distribution of Chlorine. *Sci. Total Environ.* **2022**, *806*, 150903.  
<https://doi.org/10.1016/j.scitotenv.2021.150903>.
- (24) Luo, Z.; Zhang, L.; Li, G.; Du, W.; Chen, Y.; Cheng, H.; Tao, S.; Shen, G. Evaluating Co-Emissions into Indoor and Outdoor Air of EC, OC, and BC from in-Home Biomass Burning. *Atmospheric Res.* **2021**, *248*, 105247.  
<https://doi.org/10.1016/j.atmosres.2020.105247>.
- (25) Shemwell, B. E.; Levendis, Y. A. Particulates Generated from Combustion of Polymers (Plastics). *J. Air Waste Manag. Assoc.* **2000**, *50* (1), 94–102.  
<https://doi.org/10.1080/10473289.2000.10463994>.
- (26) Pierce, J. R.; Engelhart, G. J.; Hildebrandt, L.; Weitkamp, E. A.; Pathak, R. K.; Donahue, N. M.; Robinson, A. L.; Adams, P. J.; Pandis, S. N. Constraining Particle Evolution from Wall Losses, Coagulation, and Condensation-Evaporation in Smog-Chamber Experiments: Optimal Estimation Based on Size Distribution Measurements. *Aerosol Sci. Technol.* **2008**, *42* (12), 1001–1015. <https://doi.org/10.1080/02786820802389251>.
- (27) Hems, R. F.; Schnitzler, E. G.; Liu-Kang, C.; Cappa, C. D.; Abbatt, J. P. D. Aging of Atmospheric Brown Carbon Aerosol. *ACS Earth Space Chem.* **2021**, *5* (4), 722–748.  
<https://doi.org/10.1021/acsearthspacechem.0c00346>.
- (28) Liu, C.; Chung, C. E.; Yin, Y.; Schnaiter, M. The Absorption Ångström Exponent of Black Carbon: From Numerical Aspects. *Atmospheric Chem. Phys.* **2018**, *18* (9), 6259–6273.  
<https://doi.org/10.5194/acp-18-6259-2018>.

- (29) Kim, J.-H.; Kim, S.-W.; Ogren, J. A.; Sheridan, P. J.; Yoon, S.-C.; Sharma, S.; Lin, N.-H. Multiple Scattering Correction Factor Estimation for Aethalometer Aerosol Absorption Coefficient Measurement. *Aerosol Sci. Technol.* **2019**, *53* (2), 160–171.  
<https://doi.org/10.1080/02786826.2018.1555368>.
- (30) Laskin, A.; Laskin, J.; Nizkorodov, S. A. Chemistry of Atmospheric Brown Carbon. *Chem. Rev.* **2015**, *115* (10), 4335–4382. <https://doi.org/10.1021/cr5006167>.
- (31) Maqsood, T.; Dai, J.; Zhang, Y.; Guang, M.; Li, B. Pyrolysis of Plastic Species: A Review of Resources and Products. *J. Anal. Appl. Pyrolysis* **2021**, *159*, 105295.  
<https://doi.org/10.1016/j.jaap.2021.105295>.
- (32) Yang, X.; Wang, T.; Xia, M.; Gao, X.; Li, Q.; Zhang, N.; Gao, Y.; Lee, S.; Wang, X.; Xue, L.; Yang, L.; Wang, W. Abundance and Origin of Fine Particulate Chloride in Continental China. *Sci. Total Environ.* **2018**, *624*, 1041–1051.  
<https://doi.org/10.1016/j.scitotenv.2017.12.205>.

# 8

## Conclusions

Alberta has endured a series of devastating wildfire seasons over the past decade. As I write this thesis, smoke once again shrouds the whole Alberta province and many parts of North America from wildfires currently raging near Fort McMurray and Grande Prairie. Polyvinyl chloride (PVC) plastic, widely used in construction and household items, releases toxic substances during fires, such as building fires. These severe and destructive events have partly inspired and motivated my thesis research. One primary focus of my thesis work is the (toxic) substances, including gaseous substances and aerosol particles, emitted by PVC pyrolysis in a laboratory environment. During the course of my research, I realized that to achieve a comprehensive evaluation of such complicated processes, many different pieces of information are needed. Consequently, I adopted a multi-pronged approach to investigate various aspects of PVC pyrolysis. In this thesis, I detail this approach, which includes examining structural and dynamics properties of several semi-volatile organic molecules and their non-covalently bonded complexes, as well as aerosol particle formation on different size scales. To achieve this, I employed a combination of distinctive experimental and theoretical methods. By integrating these diverse techniques, I aimed to gain a more complete understanding of the intricate processes involved in PVC pyrolysis.

I applied high resolution rotational spectroscopy to probe structural and dynamical properties of several semi-volatile organic compounds, including four substituted benzoic acids

(*para*-aminobenzoic acid, *para*-nitrobenzoic acid, *para*-chlorobenzoic acid, and *para*-hydroxybenzoic acid), vanillic acid, and benzyl benzoate, for the first time. These compounds may be released during PVC or biomass burning, or can be generated biogenically.<sup>1,2,3</sup> Additionally, I explored a first stage of secondary organic aerosol particle formation, which may involve the aggregation of semi-volatile organic compounds with water or themselves. In these investigations, I utilized a combination of jet-cooled Fourier transformation microwave spectroscopy and quantum chemical calculations. Very detailed and specific information regarding the conformational landscapes and large amplitude motions of these compounds and their non-covalently bonded complexes was obtained. The roles of intra- and intermolecular non-covalent interactions in preferentially stabilizing specific conformers were examined in considerable detail. The significant results, presented in Chapter 3 to 5, are outlined below.

To examine substances such as hydrogen chloride, semi-volatile organic compounds, and aerosol particles emitted during PVC pyrolysis, multiple sophisticated instruments are required. I have taken on the responsibility of setting up new laboratory components and integrating them with the existing smog chamber<sup>4,5</sup> specifically for this research activity. This involved configuring advanced equipment to ensure precise measurements, identifying essential spectroscopic instruments and chemical kits for specific characterization, and interpreting the data. My efforts in developing and refining the instrumentation are detailed in Chapter 6, while the key points are summarized below. The final result chapter of my thesis, Chapter 7, presents a series of experiments aimed at characterizing various substances emitted during PVC pyrolysis. These experiments include determining aerosol particle size distributions and examining their wavelength-dependent absorption under these conditions. The key and intriguing findings of these experiments are highlighted below.

In Chapter 3, the conformational preferences of four substituted benzoic acids: *para*-aminobenzoic acid, *para*-nitrobenzoic acid, *para*-chlorobenzoic acid, and *para*-hydroxybenzoic acid were investigated using chirped pulse Fourier transform microwave spectroscopy and quantum chemical calculations. I experimentally identified the lowest energy conformer of each acid which contain a planar carboxylic acid group in its *cis*-configuration in all cases. In the case of *para*-hydroxybenzoic acid, two *cis*-conformers were observed, related to different relative orientations between the OH and the COOH groups. Theoretically, the *trans*-conformers are approximately 23 kJ mol<sup>-1</sup> higher in energy than the global minimum *cis*-conformers, with the carboxylic acid group being out-of-plane with respect to the benzene ring. A comparative analysis of the electron density distribution of in these *trans*-conformers indicates that different degrees of out-of-plane excursion experienced by the carboxylic acid group is related to the electron donating or withdrawing nature of the *para*-substituents. From a nucleation perspective, these benzoic acid derivatives exhibit a similar carboxylic acid conformational preference as benzoic acid,<sup>6</sup> 3,5-difluorobenzoic acid,<sup>7</sup> *ortho*- and *para*-toluic acid,<sup>8,9</sup> whereas the functional groups substituted at the *para*-position may offer additional binding sites for intermolecular non-covalent interactions. Additionally, there is on-going interested in probing how the substitution in the *para* position of benzoic acid influences the double proton tunnelling in binary complexes of substituted benzoic acids.<sup>10</sup> *para*-chlorobenzoic acid may be a product of PVC pyrolysis and could be a component of the emitted aerosol particles.

In Chapter 4, I explored the conformational flexibility of vanillic acid and its monohydrate using electronic structure calculations and Fourier transform microwave spectroscopy. This study aims to shed light on the preferential binding of water in a highly functionalized benzoic acid derivative. Vanillic acid is a semi-volatile benzoic acid derivative

released during biomass burning.<sup>2</sup> Guided by quantum chemical calculations, two conformers of the monomer and monohydrate were identified experimentally. In the two lowest energy conformers of the monomer and the monohydrate, the carboxylic acid functional group adopts the *cis*-configuration, similar to my findings in Chapter 3. Additionally, the hydroxyl group and methoxy group form an intramolecular hydrogen bond that potentially limits their interaction with the first water molecule. The structure of the monohydrate has the carboxylic acid forming a five-membered ring with the water molecule through two hydrogen bonds. This bonding motif is similar to benzoic acid-water,<sup>6</sup> *p*- and *o*-toluic acid – water,<sup>11,12</sup> and oxalic acid-water.<sup>13</sup> Building upon the findings in Chapter 3, this study demonstrates that *ortho*-functional groups possess the potential to interact with each other, thereby limiting their involvement in the initial cluster formation. However, this does not necessarily imply their exclusion from cluster formation; rather, it presents a possibility that must be taken into account when seeking to comprehend the early stages of cluster formation.

In Chapter 5, I transitioned to a larger, volatile aromatic organic molecule, i.e., benzyl benzoate, and its non-covalently bonded dimer. Benzyl benzoate is an ester with terminal benzyl and phenyl groups, constituting a high molecular weight biogenically emitted semi-volatile organic compound.<sup>3</sup> This study uses benzyl benzoate as a proxy to understand how large semi-volatile aromatic compounds may aggregate. Benzyl benzoate is unique in that it is much more flexible than naphthalene and can exist in multiple low energy conformers. Experimentally, two conformers of the monomer were identified. Aided by quantum chemical calculations, I showed that CH $\cdots$ O hydrogen bonding interactions play a larger role in the structural preference than the interactions responsible for the  $\pi$ - $\pi$  stacking structural motif, i.e., dispersion forces and a reduction in Pauli exchange repulsion,

The situation changes drastically in the corresponding dimer, where dispersion interactions, which favor a parallel-displaced  $\pi$ - $\pi$  stacking structural motif, play a central role in stabilizing the preferred binary conformers. This preference for the  $\pi$ - $\pi$  stacking structural motif mirrors that observed in the 2-naphthalenethiol dimer<sup>14</sup> and the 1-naphol dimer.<sup>15</sup> Additionally, two C-H $\cdots$   $\pi$  interactions are present in the benzyl benzoate dimer. This study highlights the importance of the  $\pi$ - $\pi$  stacking structural motif for larger semi-volatile aromatic compounds in cluster formation.

In Chapter 6, I describe instruments used for my studies of emissions from PVC pyrolysis. This includes brief explanations of the operating principles of some of the commercial instruments I used, such as the scanning mobility particle sizer, which consists of a differential mobility analyzer and condensation particle counter, to study aerosol particle size distributions and an aethalometer to measure the wavelength dependence of aerosol particle absorption. The process of measuring the hydrogen chloride concentrations in the emissions is described in detail. The setup of the photo-reaction chamber, which I renovated and made operational again, is given as well as the details of the design and operational procedure for the tube furnace which I constructed for the PVC pyrolysis.

In Chapter 7, I describe my experimental studies of the emissions from PVC pyrolysis. A 61% loss of mass after 40 min PVC pyrolysis at 350°C is observed. The gaseous emissions from this process consist of a mixture of hydrogen chloride, volatile organic compounds, and aerosol particles.<sup>16</sup> Of those emissions an average of 25% is HCl. The aerosol particle emissions are predominantly composed of organic compounds that form concentration-dependent agglomerates. The emitted aerosol particles have a unimodal size distribution between 25 nm and 900 nm, with a mean size of approximately 150 nm. This is comparable to the accumulation

mode of biomass burning, which ranges in mean size between 100 nm and 150 nm.<sup>17</sup> The absorption Ångstrom coefficient, AAC, a measure of the wavelength dependence of absorption,<sup>18</sup> was determined to be between 5.8 and 6.1. This can be compared to an AAC of 1 for black carbon-rich aerosol particles emitted by biomass burning.<sup>19</sup> This suggests that the semi-volatile compounds that make up these aerosols preferentially absorb at lower wavelengths and, if deposited onto black carbon aerosols, may influence their impact on solar radiation.

Many of the studies outlined in this thesis are starting points for future studies, some of which have already begun. For instance, the studies on *para*-substituted benzoic acid derivative described in Chapter 3 have laid the groundwork for investigations on double proton tunneling in dimers of benzoic acid with the *para*-substituted species. In this study, how the *para*-substitution affects the barrier to double proton exchange in the heterodimers is being investigated. A collaboration with the Cvitaš group in Croatia is ongoing, and a graduate student, Mihael Eraković, has been visiting our laboratory to participate in measurements. We have already identified and analyzed the spectrum of the *para*-nitrobenzoic acid – benzoic acid dimer. From the observed tunneling splittings, a barrier was determined experimentally which we compared with the barrier determined from instanton calculations done by Mihael Eraković. Further work to measure the spectra of the *para*-chlorobenzoic acid – benzoic acid and the *para*-aminobenzoic acid – benzoic acid heterodimers is underway.

With the work on PVC pyrolysis described in Chapter 7, I have set up the laboratory instrumentation and established the experimental procedures necessary for the studies on co-pyrolysis of PVC with biomass. Those studies are important to better simulate the conditions in open pit waste burning and also those in house fires. Preliminary experiments on wood pyrolysis have already begun, together with a summer student, Mason D'Souza.

The aerosol particle analysis in Chapter 7 can still be made more comprehensive by, for example, including light absorption and scattering measurements with more sensitive instruments, such as a photo-acoustic extinctionsmeter (PAX). I have put a newly purchased PAX into operation in our laboratory and established the measurement protocols. Measurements of both absorption and scattering coefficients are important to better establish the effects of the aerosol particles on our climate in terms of their radiative forcing.

## References

- (1) Zhou, J.; Liu, G.; Wang, S.; Zhang, H.; Xu, F. TG-FTIR and Py-GC/MS Study of the Pyrolysis Mechanism and Composition of Volatiles from Flash Pyrolysis of PVC. *J. Energy Inst.* **2020**, *93* (6), 2362–2370. <https://doi.org/10.1016/j.joei.2020.07.009>.
- (2) Grieman, M. M.; Aydin, M.; McConnell, J. R.; Saltzman, E. S. Burning-Derived Vanillic Acid in an Arctic Ice Core from Tunu, Northeastern Greenland. *Clim. Past* **2018**, *14* (11), 1625–1637. <https://doi.org/10.5194/cp-14-1625-2018>.
- (3) Qi, Y.; Yuan, Y.-K.; Zhang, J.-W.; Du, Y.-S.; Fu, K.-C.; Cui, M.-J.; Du, S.-S. Contact Toxicity and Repellent Efficacy of *Kaempferia Rotunda* L. to Three Stored Product Insects and Synergistic Interactions between Two Major Compounds Benzyl Benzoate and Bornyl Acetate. *J. Essent. Oil Bear. Plants* **2023**, *26* (2), 343–355. <https://doi.org/10.1080/0972060X.2023.2185545>.
- (4) Parsons, M. T.; Sydoryk, I.; Lim, A.; McIntyre, T. J.; Tulip, J.; Jäger, W.; McDonald, K. Real-Time Monitoring of Benzene, Toluene, and p-Xylene in a Photoreaction Chamber with a Tunable Mid-Infrared Laser and Ultraviolet Differential Optical Absorption Spectroscopy. *Appl. Opt.* **2011**, *50* (4), A90-99. <https://doi.org/10.1364/AO.50.000A90>.
- (5) Schnitzler, E. G.; Dutt, A.; Charbonneau, A. M.; Olfert, J. S.; Jäger, W. Soot Aggregate Restructuring Due to Coatings of Secondary Organic Aerosol Derived from Aromatic Precursors. *Environ. Sci. Technol.* **2014**, *48* (24), 14309–14316. <https://doi.org/10.1021/es503699b>.
- (6) Schnitzler, E. G.; Jäger, W. The Benzoic Acid–Water Complex: A Potential Atmospheric Nucleation Precursor Studied Using Microwave Spectroscopy and Ab Initio Calculations. *Phys. Chem. Chem. Phys.* **2014**, *16* (6), 2305–2314. <https://doi.org/10.1039/C3CP54486A>.

- (7) Gracia, A.; Hong, J.; Arismendi, R.; Zhou, M.; Li, W.; Lin, W. Conformational Landscapes of Symmetrically Fluorine-Substituted Benzoic Acids I: Microwave Spectroscopic and Theoretical Studies on 3,5-Difluorobenzoic Acid. *J. Mol. Spectrosc.* **2023**, *397*, 111839. <https://doi.org/10.1016/j.jms.2023.111839>.
- (8) Schnitzler, E. G.; Zenchyzen, B. L. M.; Jäger, W. Rotational Spectroscopy of the Atmospheric Photo-Oxidation Product o-Toluic Acid and Its Monohydrate. *Phys. Chem. Chem. Phys.* **2015**, *18* (1), 448–457. <https://doi.org/10.1039/C5CP06073G>.
- (9) Schnitzler, E. G.; Seifert, N. A.; Kusuma, I.; Jäger, W. Rotational Spectroscopy of P-Toluic Acid and Its 1:1 Complex with Water. *J. Phys. Chem. A* **2017**, *121* (45), 8625–8631. <https://doi.org/10.1021/acs.jpca.7b08984>.
- (10) Al-Jabiri, M.H.; Insausti, A.; A.; Eraković, M.; Jäger, W.; Cvitaš, M. T. Double Proton Tunneling/Instanton Theory (Private Communication).
- (11) Schnitzler, E. G.; Zenchyzen, B. L. M.; Jäger, W. Rotational Spectroscopy of the Atmospheric Photo-Oxidation Product o-Toluic Acid and Its Monohydrate. *Phys. Chem. Chem. Phys.* **2015**, *18* (1), 448–457. <https://doi.org/10.1039/C5CP06073G>.
- (12) Schnitzler, E. G.; Seifert, N. A.; Kusuma, I.; Jäger, W. Rotational Spectroscopy of P-Toluic Acid and Its 1:1 Complex with Water. *J. Phys. Chem. A* **2017**, *121* (45), 8625–8631. <https://doi.org/10.1021/acs.jpca.7b08984>.
- (13) Schnitzler, E. G.; Badran, C.; Jäger, W. Contrasting Effects of Water on the Barriers to Decarboxylation of Two Oxalic Acid Monohydrates: A Combined Rotational Spectroscopic and Ab Initio Study. *J. Phys. Chem. Lett.* **2016**, *7* (7), 1143–1147. <https://doi.org/10.1021/acs.jpcclett.6b00278>.

- (14) Saragi, R. T.; Calabrese, C.; Juanes, M.; Pinacho, R.; Rubio, J. E.; Pérez, C.; Lesarri, A.  $\pi$ -Stacking Isomerism in Polycyclic Aromatic Hydrocarbons: The 2-Naphthalenethiol Dimer. *J. Phys. Chem. Lett.* **2023**, *14* (1), 207–213. <https://doi.org/10.1021/acs.jpcllett.2c03299>.
- (15) Seifert, N. A.; Hazrah, A. S.; Jäger, W. The 1-Naphthol Dimer and Its Surprising Preference for  $\pi$ - $\pi$  Stacking over Hydrogen Bonding. *J. Phys. Chem. Lett.* **2019**, *10* (11), 2836–2841. <https://doi.org/10.1021/acs.jpcllett.9b00646>.
- (16) Yu, J.; Sun, L.; Ma, C.; Qiao, Y.; Yao, H. Thermal Degradation of PVC: A Review. *Waste Manag.* **2016**, *48*, 300–314. <https://doi.org/10.1016/j.wasman.2015.11.041>.
- (17) Janhäll, S.; Andreae, M. O.; Pöschl, U. Biomass Burning Aerosol Emissions from Vegetation Fires: Particle Number and Mass Emission Factors and Size Distributions. *Atmospheric Chem. Phys.* **2010**, *10* (3), 1427–1439. <https://doi.org/10.5194/acp-10-1427-2010>.
- (18) Kim, J.-H.; Kim, S.-W.; Ogren, J. A.; Sheridan, P. J.; Yoon, S.-C.; Sharma, S.; Lin, N.-H. Multiple Scattering Correction Factor Estimation for Aethalometer Aerosol Absorption Coefficient Measurement. *Aerosol Sci. Technol.* **2019**, *53* (2), 160–171. <https://doi.org/10.1080/02786826.2018.1555368>.
- (19) Laskin, A.; Laskin, J.; Nizkorodov, S. A. Chemistry of Atmospheric Brown Carbon. *Chem. Rev.* **2015**, *115* (10), 4335–4382. <https://doi.org/10.1021/cr5006167>.

# Bibliography

- (1) Hinds, W. C. *Aerosol Technology: Properties, Behavior, and Measurement of Airborne Particles*; John Wiley & Sons, 1999.
- (2) Almetwally, A. A.; Bin-Jumah, M.; Allam, A. A. Ambient Air Pollution and Its Influence on Human Health and Welfare: An Overview. *Environ. Sci. Pollut. Res.* **2020**, *27* (20), 24815–24830. <https://doi.org/10.1007/s11356-020-09042-2>.
- (3) Li, J.; Carlson, B. E.; Yung, Y. L.; Lv, D.; Hansen, J.; Penner, J. E.; Liao, H.; Ramaswamy, V.; Kahn, R. A.; Zhang, P.; Dubovik, O.; Ding, A.; Lacis, A. A.; Zhang, L.; Dong, Y. Scattering and Absorbing Aerosols in the Climate System. *Nat. Rev. Earth Environ.* **2022**, *3* (6), 363–379. <https://doi.org/10.1038/s43017-022-00296-7>.
- (4) Bernstein, J. A.; Alexis, N.; Barnes, C.; Bernstein, I. L.; Nel, A.; Peden, D.; Diaz-Sanchez, D.; Tarlo, S. M.; Williams, P. B.; Bernstein, J. A. Health Effects of Air Pollution. *J. Allergy Clin. Immunol.* **2004**, *114* (5), 1116–1123. <https://doi.org/10.1016/j.jaci.2004.08.030>.
- (5) Kim, K.H.; Kabir, E.; Kabir, S. A Review on the Human Health Impact of Airborne Particulate Matter. *Environ. Int.* **2015**, *74*, 136–143. <https://doi.org/10.1016/j.envint.2014.10.005>.
- (6) Canada, E. and C. C. *About the Air Quality Health Index*. <https://www.canada.ca/en/environment-climate-change/services/air-quality-health-index/about.html> (accessed 2024-04-04).
- (7) Stieb, D. M.; Burnett, R. T.; Smith-Doiron, M.; Brion, O.; Shin, H. H.; Economou, V. A. New Multipollutant, No-Threshold Air Quality Health Index Based on Short-Term

- Associations Observed in Daily Time-Series Analyses. *J. Air Waste Manag. Assoc.* **2008**, *58* (3), 435–450. <https://doi.org/10.3155/1047-3289.58.3.435>.
- (8) *Methods for Measurement of Filterable PM10 and PM2.5 and Measurement of Condensable PM Emissions From Stationary Sources*. Federal Register. <https://www.federalregister.gov/documents/2010/12/21/2010-30847/methods-for-measurement-of-filterable-pm10-and-pm25-and-measurement-of-condensable-pm-emissions-from> (accessed 2024-03-20).
- (9) Park, M.; Joo, H. S.; Lee, K.; Jang, M.; Kim, S. D.; Kim, I.; Borlaza, L. J. S.; Lim, H.; Shin, H.; Chung, K. H.; Choi, Y.-H.; Park, S. G.; Bae, M.-S.; Lee, J.; Song, H.; Park, K. Differential Toxicities of Fine Particulate Matters from Various Sources. *Sci. Rep.* **2018**, *8* (1), 17007. <https://doi.org/10.1038/s41598-018-35398-0>.
- (10) Unga, F.; Choël, M.; Derimian, Y.; Deboudt, K.; Dubovik, O.; Goloub, P. Microscopic Observations of Core-Shell Particle Structure and Implications for Atmospheric Aerosol Remote Sensing. *J. Geophys. Res. Atmospheres* **2018**, *123* (24), 13,944–13,962. <https://doi.org/10.1029/2018JD028602>.
- (11) Kameda, T.; Azumi, E.; Fukushima, A.; Tang, N.; Matsuki, A.; Kamiya, Y.; Toriba, A.; Hayakawa, K. Mineral Dust Aerosols Promote the Formation of Toxic Nitropolycyclic Aromatic Compounds. *Sci. Rep.* **2016**, *6* (1), 24427. <https://doi.org/10.1038/srep24427>.
- (12) Saikawa, E.; Wu, Q.; Zhong, M.; Avramov, A.; Ram, K.; Stone, E. A.; Stockwell, C. E.; Jayarathne, T.; Panday, A. K.; Yokelson, R. J. Garbage Burning in South Asia: How Important Is It to Regional Air Quality? *Environ. Sci. Technol.* **2020**, *54* (16), 9928–9938. <https://doi.org/10.1021/acs.est.0c02830>.

- (13) Haywood, J.; Boucher, O. Estimates of the Direct and Indirect Radiative Forcing Due to Tropospheric Aerosols: A Review. *Rev. Geophys.* **2000**, *38* (4), 513–543.  
<https://doi.org/10.1029/1999RG000078>.
- (14) Brown, H.; Liu, X.; Pokhrel, R.; Murphy, S.; Lu, Z.; Saleh, R.; Mielonen, T.; Kokkola, H.; Bergman, T.; Myhre, G.; Skeie, R. B.; Watson-Paris, D.; Stier, P.; Johnson, B.; Bellouin, N.; Schulz, M.; Vakkari, V.; Beukes, J. P.; van Zyl, P. G.; Liu, S.; Chand, D. Biomass Burning Aerosols in Most Climate Models Are Too Absorbing. *Nat. Commun.* **2021**, *12* (1), 277. <https://doi.org/10.1038/s41467-020-20482-9>.
- (15) Friebel, F.; Lobo, P.; Neubauer, D.; Lohmann, U.; Drossaert van Dusseldorp, S.; Mühlhofer, E.; Mensah, A. A. Impact of Isolated Atmospheric Aging Processes on the Cloud Condensation Nuclei Activation of Soot Particles. *Atmospheric Chem. Phys.* **2019**, *19* (24), 15545–15567. <https://doi.org/10.5194/acp-19-15545-2019>.
- (16) Intergovernmental Panel on Climate Change. *Climate Change 2013 – The Physical Science Basis: Working Group I Contribution to the Fifth Assessment Report of the Intergovernmental Panel on Climate Change*; Cambridge University Press: Cambridge, 2014. <https://doi.org/10.1017/CBO9781107415324>.
- (17) Hems, R. F.; Schnitzler, E. G.; Liu-Kang, C.; Cappa, C. D.; Abbatt, J. P. D. Aging of Atmospheric Brown Carbon Aerosol. *ACS Earth Space Chem.* **2021**, *5* (4), 722–748.  
<https://doi.org/10.1021/acsearthspacechem.0c00346>.
- (18) Canada, E. and C. C. *Greenhouse gases and aerosols monitoring*.  
<https://www.canada.ca/en/environment-climate-change/services/climate-change/greenhouse-gases-aerosols-monitoring.html> (accessed 2024-03-20).

- (19) Riipinen, I.; Yli-Juuti, T.; Pierce, J. R.; Petäjä, T.; Worsnop, D. R.; Kulmala, M.; Donahue, N. M. The Contribution of Organics to Atmospheric Nanoparticle Growth. *Nat. Geosci.* **2012**, *5* (7), 453–458. <https://doi.org/10.1038/ngeo1499>.
- (20) Kulmala, M.; Kerminen, V.-M.; Petäjä, T.; Ding, A.; Wang, L. Atmospheric Gas-to-Particle Conversion: Why NPF Events Are Observed in Megacities? *Faraday Discuss.* **2017**, *200* (0), 271–288. <https://doi.org/10.1039/C6FD00257A>.
- (21) Lee, S.H.; Gordon, H.; Yu, H.; Lehtipalo, K.; Haley, R.; Li, Y.; Zhang, R. New Particle Formation in the Atmosphere: From Molecular Clusters to Global Climate. *J. Geophys. Res. Atmospheres* **2019**, *124* (13), 7098–7146. <https://doi.org/10.1029/2018JD029356>.
- (22) Zhang, R. Getting to the Critical Nucleus of Aerosol Formation. *Science* **2010**, *328* (5984), 1366–1367. <https://doi.org/10.1126/science.1189732>.
- (23) Zhang, R.; Khalizov, A.; Wang, L.; Hu, M.; Xu, W. Nucleation and Growth of Nanoparticles in the Atmosphere. *Chem. Rev.* **2012**, *112* (3), 1957–2011. <https://doi.org/10.1021/cr2001756>.
- (24) Tröstl, J.; Chuang, W. K.; Gordon, H.; Heinritzi, M.; Yan, C.; Molteni, U.; Ahlm, L.; Frege, C.; Bianchi, F.; Wagner, R.; Simon, M.; Lehtipalo, K.; Williamson, C.; Craven, J. S.; Duplissy, J.; Adamov, A.; Almeida, J.; Bernhammer, A.-K.; Breitenlechner, M.; Brilke, S.; Dias, A.; Ehrhart, S.; Flagan, R. C.; Franchin, A.; Fuchs, C.; Guida, R.; Gysel, M.; Hansel, A.; Hoyle, C. R.; Jokinen, T.; Junninen, H.; Kangasluoma, J.; Keskinen, H.; Kim, J.; Krapf, M.; Kürten, A.; Laaksonen, A.; Lawler, M.; Leiminger, M.; Mathot, S.; Möhler, O.; Nieminen, T.; Onnela, A.; Petäjä, T.; Piel, F. M.; Miettinen, P.; Rissanen, M. P.; Rondo, L.; Sarnela, N.; Schobesberger, S.; Sengupta, K.; Sipilä, M.; Smith, J. N.; Steiner, G.; Tomè, A.; Virtanen, A.; Wagner, A. C.; Weingartner, E.; Wimmer, D.; Winkler, P. M.; Ye, P.;

- Carslaw, K. S.; Curtius, J.; Dommen, J.; Kirkby, J.; Kulmala, M.; Riipinen, I.; Worsnop, D. R.; Donahue, N. M.; Baltensperger, U. The Role of Low-Volatility Organic Compounds in Initial Particle Growth in the Atmosphere. *Nature* **2016**, *533* (7604), 527–531.  
<https://doi.org/10.1038/nature18271>.
- (25) Zhang, R.; Suh, I.; Zhao, J.; Zhang, D.; Fortner, E. C.; Tie, X.; Molina, L. T.; Molina, M. J. Atmospheric New Particle Formation Enhanced by Organic Acids. *Science* **2004**, *304* (5676), 1487–1490. <https://doi.org/10.1126/science.1095139>.
- (26) Al-Jabiri, M. H.; Hazrah, A. S.; Insausti, A.; Xu, Y.; Jäger, W. Rotational Spectroscopic Studies of Para-Nitrobenzoic Acid, Para-Aminobenzoic Acid, Para-Chlorobenzoic Acid, and Para-Hydroxybenzoic Acid. *J. Mol. Spectrosc.* **2023**, *394*, 111790.  
<https://doi.org/10.1016/j.jms.2023.111790>.
- (27) Al-Jabiri, M. H.; Hazrah, A. S.; Jäger, W. Conformers of Vanillic Acid and Its Monohydrate: A Rotational Spectroscopic and Theoretical Study. *J. Phys. Chem. A* **2022**.  
<https://doi.org/10.1021/acs.jpca.2c05120>.
- (28) Knopf, D. A.; Alpert, P. A.; Wang, B. The Role of Organic Aerosol in Atmospheric Ice Nucleation: A Review. *ACS Earth Space Chem.* **2018**, *2* (3), 168–202.  
<https://doi.org/10.1021/acsearthspacechem.7b00120>.
- (29) Xu, Y.; Wijngaarden, J. V.; Jäger, W. Microwave Spectroscopy of Ternary and Quaternary van Der Waals Clusters. *Int. Rev. Phys. Chem.* **2005**, *24* (2), 301–338.  
<https://doi.org/10.1080/01442350500252039>.
- (30) Leopold, K. R. Hydrated Acid Clusters. *Annu. Rev. Phys. Chem.* **2011**, *62* (20), 327–349.  
<https://doi.org/10.1146/annurev-physchem-032210-103409>.

- (31) Park, G. B.; Field, R. W. Perspective: The First Ten Years of Broadband Chirped Pulse Fourier Transform Microwave Spectroscopy. *J. Chem. Phys.* **2016**, *144* (20), 200901. <https://doi.org/10.1063/1.4952762>.
- (32) Tang, J.; Xu, Y.; McKellar, A. R. W.; Jäger, W. Quantum Solvation of Carbonyl Sulfide with Helium Atoms. *Science* **2002**, *297* (5589), 2030–2033. <https://doi.org/10.1126/science.1073718>.
- (33) McKellar, A. R. W.; Xu, Y.; Jäger, W. Spectroscopic Exploration of Atomic Scale Superfluidity in Doped Helium Nanoclusters. *Phys. Rev. Lett.* **2006**, *97* (18), 183401. <https://doi.org/10.1103/PhysRevLett.97.183401>.
- (34) Song, X.; Xu, Y.; Roy, P.-N.; Jäger, W. Rotational Spectrum, Potential Energy Surface, and Bound States of the Weakly Bound Complex He–N<sub>2</sub>O. *J. Chem. Phys.* **2004**, *121* (24), 12308–12314. <https://doi.org/10.1063/1.1819875>.
- (35) King, A. K.; Howard, B. J. A Microwave Study of the Hetero-Chiral Dimer of Butan-2-ol. *Chem. Phys. Lett.* **2001**, *348* (3), 343–349. [https://doi.org/10.1016/S0009-2614\(01\)01121-6](https://doi.org/10.1016/S0009-2614(01)01121-6).
- (36) Borho, N.; Xu, Y. Rotational Spectrum of a Chiral  $\alpha$ -Hydroxyester: Conformation Stability and Internal Rotation Barrier Heights of Methyl Lactate. *Phys. Chem. Chem. Phys.* **2007**, *9* (11), 1324–1328. <https://doi.org/10.1039/B608561J>.
- (37) Thomas, J.; Sunahori, F. X.; Borho, N.; Xu, Y. Chirality Recognition in the Glycidol···Propylene Oxide Complex: A Rotational Spectroscopic Study. *Chem. – Eur. J.* **2011**, *17* (16), 4582–4587. <https://doi.org/10.1002/chem.201003536>.
- (38) Pate, B. H.; Evangelisti, L.; Caminati, W.; Xu, Y.; Thomas, J.; Patterson, D.; Perez, C.; Schnell, M. Chapter 17 - Quantitative Chiral Analysis by Molecular Rotational

- Spectroscopy. In *Chiral Analysis (Second Edition)*; Polavarapu, P. L., Ed.; Elsevier, 2018; pp 679–729. <https://doi.org/10.1016/B978-0-444-64027-7.00019-7>.
- (39) Huff, A. K.; Love, N.; Leopold, K. R. Microwave and Computational Study of Methanesulfonic Acid and Its Complex with Water. *J. Phys. Chem. A* **2023**, *127* (16), 3658–3667. <https://doi.org/10.1021/acs.jpca.3c01395>.
- (40) Fiacco, D. L.; Hunt, S. W.; Leopold, K. R. Microwave Investigation of Sulfuric Acid Monohydrate. *J. Am. Chem. Soc.* **2002**, *124* (16), 4504–4511. <https://doi.org/10.1021/ja012724w>.
- (41) Schnitzler, E. G.; Seifert, N. A.; Ghosh, S.; Thomas, J.; Xu, Y.; Jäger, W. Hydration of the Simplest  $\alpha$ -Keto Acid: A Rotational Spectroscopic and Ab Initio Study of the Pyruvic Acid–Water Complex. *Phys. Chem. Chem. Phys.* **2017**, *19* (6), 4440–4446. <https://doi.org/10.1039/C6CP08741H>.
- (42) Schnitzler, E. G.; Zenchyzen, B. L. M.; Jäger, W. Rotational Spectroscopy of the Atmospheric Photo-Oxidation Product o-Toluic Acid and Its Monohydrate. *Phys. Chem. Chem. Phys.* **2015**, *18* (1), 448–457. <https://doi.org/10.1039/C5CP06073G>.
- (43) Schnitzler, E. G.; Badran, C.; Jäger, W. Contrasting Effects of Water on the Barriers to Decarboxylation of Two Oxalic Acid Monohydrates: A Combined Rotational Spectroscopic and Ab Initio Study. *J. Phys. Chem. Lett.* **2016**, *7* (7), 1143–1147. <https://doi.org/10.1021/acs.jpcclett.6b00278>.
- (44) Ma, J.; Insausti, A.; Al-Jabiri, M. H.; Carlson, C. D.; Jäger, W.; Xu, Y. Unlocking a New Hydrogen-Bonding Marker: C–O Bond Shortening in Vicinal Diols Revealed by Rotational Spectroscopy. *J. Chem. Phys.* **2024**, *160* (15), 154304. <https://doi.org/10.1063/5.0203123>.

- (45) Xie, F.; Seifert, N. A.; Heger, M.; Thomas, J.; Jäger, W.; Xu, Y. The Rich Conformational Landscape of Perillyl Alcohol Revealed by Broadband Rotational Spectroscopy and Theoretical Modelling. *Phys. Chem. Chem. Phys.* **2019**, *21* (28), 15408–15416. <https://doi.org/10.1039/C9CP03028J>.
- (46) Wu, B.; Seifert, N. A.; Insausti, A.; Ma, J.; Oswald, S.; Jäger, W.; Xu, Y. 2,2,3,3,3-Pentafluoro-1-Propanol and Its Dimer: Structural Diversity, Conformational Conversion, and Tunnelling Motion. *Phys. Chem. Chem. Phys.* **2022**, *24* (24), 14975–14984. <https://doi.org/10.1039/D2CP01895K>.
- (47) Lu, T.; Xie, F.; Seifert, N. A.; Jäger, W.; Xu, Y. Conformational Landscape and Intricate Conformational Relaxation Paths of 4,4,4-Trifluoro-1-Butanol: Rotational Spectroscopy and Quantum Chemical Calculations. *J. Mol. Struct.* **2020**, *1217*, 128359. <https://doi.org/10.1016/j.molstruc.2020.128359>.
- (48) Lu, T.; Xie, F.; Seifert, N. A.; Mejlej, R. H.; Jäger, W.; Xu, Y. Binary Conformers of a Flexible, Long-Chain Fluoroalcohol: Dispersion Controlled Selectivity and Relative Abundances in a Jet. *Phys. Chem. Chem. Phys.* **2024**, *26* (14), 10538–10545. <https://doi.org/10.1039/D4CP00401A>.
- (49) Thomas, J.; Xu, Y. Chirality Synchronization in Trifluoroethanol Dimer Revisited: The Missing Heterochiral Dimer. *J. Phys. Chem. Lett.* **2014**, *5* (11), 1850–1855. <https://doi.org/10.1021/jz500718f>.
- (50) Thomas, J.; Seifert, N. A.; Jäger, W.; Xu, Y. A Direct Link from the Gas to the Condensed Phase: A Rotational Spectroscopic Study of 2,2,2-Trifluoroethanol Trimers. *Angew. Chem. Int. Ed.* **2017**, *56* (22), 6289–6293. <https://doi.org/10.1002/anie.201612161>.

- (51) Xu, Y.; Jäger, W. High Resolution Spectroscopy of Ne and Ar Containing Noble Gas Clusters. *J. Chem. Phys.* **1997**, *107* (13), 4788–4796. <https://doi.org/10.1063/1.474842>.
- (52) Hazrah, A. S.; Insausti, A.; Ma, J.; Al-Jabiri, M. H.; Jäger, W.; Xu, Y. Wetting vs Droplet Aggregation: A Broadband Rotational Spectroscopic Study of 3-Methylcatechol···Water Clusters. *Angew. Chem. Int. Ed.* **2023**, *62* (44), e202310610. <https://doi.org/10.1002/anie.202310610>.
- (53) Oswald, S.; Seifert, N. A.; Bohle, F.; Gawrilow, M.; Grimme, S.; Jäger, W.; Xu, Y.; Suhm, M. A. The Chiral Trimer and a Metastable Chiral Dimer of Achiral Hexafluoroisopropanol: A Multi-Messenger Study. *Angew. Chem. Int. Ed Engl.* **2019**, *58* (15), 5080–5084. <https://doi.org/10.1002/anie.201813881>.
- (54) Xie, F.; Fusè, M.; Hazrah, A. S.; Jäger, W.; Barone, V.; Xu, Y. Discovering the Elusive Global Minimum in a Ternary Chiral Cluster: Rotational Spectra of Propylene Oxide Trimer. *Angew. Chem. Int. Ed.* **2020**, *59* (50), 22427–22430. <https://doi.org/10.1002/anie.202010055>.
- (55) Neese, F.; Wennmohs, F.; Becker, U.; Riplinger, C. The ORCA Quantum Chemistry Program Package. *J. Chem. Phys.* **2020**, *152* (22), 224108. <https://doi.org/10.1063/5.0004608>.
- (56) Frisch, M. J.; Trucks, G. W.; Schlegel, H. B.; Scuseria, G. E.; Robb, M. A.; Cheeseman, J. R.; Scalmani, G.; Barone, V.; Petersson, G. A.; Nakatsuji, H.; Li, X.; Caricato, M.; Marenich, A. V.; Bloino, J.; Janesko, B. G.; Gomperts, R.; Mennucci, B.; Hratchian, H. P.; Ortiz, J. V.; Izmaylov, A. F.; Sonnenberg, J. L.; Williams; Ding, F.; Lipparini, F.; Egidi, F.; Goings, J.; Peng, B.; Petrone, A.; Henderson, T.; Ranasinghe, D.; Zakrzewski, V. G.; Gao, J.; Rega, N.; Zheng, G.; Liang, W.; Hada, M.; Ehara, M.; Toyota, K.; Fukuda, R.;

- Hasegawa, J.; Ishida, M.; Nakajima, T.; Honda, Y.; Kitao, O.; Nakai, H.; Vreven, T.; Throssell, K.; Montgomery Jr., J. A.; Peralta, J. E.; Ogliaro, F.; Bearpark, M. J.; Heyd, J. J.; Brothers, E. N.; Kudin, K. N.; Staroverov, V. N.; Keith, T. A.; Kobayashi, R.; Normand, J.; Raghavachari, K.; Rendell, A. P.; Burant, J. C.; Iyengar, S. S.; Tomasi, J.; Cossi, M.; Millam, J. M.; Klene, M.; Adamo, C.; Cammi, R.; Ochterski, J. W.; Martin, R. L.; Morokuma, K.; Farkas, O.; Foresman, J. B.; Fox, D. J. Gaussian 16 Rev. C.01, 2016.
- (57) Becke, A. D. A New Mixing of Hartree–Fock and Local Density-functional Theories. *J. Chem. Phys.* **1993**, *98* (2), 1372–1377. <https://doi.org/10.1063/1.464304>.
- (58) Grimme, S.; Antony, J.; Ehrlich, S.; Krieg, H. A Consistent and Accurate Ab Initio Parametrization of Density Functional Dispersion Correction (DFT-D) for the 94 Elements H–Pu. *J. Chem. Phys.* **2010**, *132* (15), 154104. <https://doi.org/10.1063/1.3382344>.
- (59) Becke, A. D.; Johnson, E. R. A Density-Functional Model of the Dispersion Interaction. *J. Chem. Phys.* **2005**, *123* (15), 154101. <https://doi.org/10.1063/1.2065267>.
- (60) Frisch, M. J.; Pople, J. A.; Binkley, J. S. Self-consistent Molecular Orbital Methods 25. Supplementary Functions for Gaussian Basis Sets. *J. Chem. Phys.* **1984**, *80* (7), 3265–3269. <https://doi.org/10.1063/1.447079>.
- (61) Schäfer, A.; Huber, C.; Ahlrichs, R. Fully Optimized Contracted Gaussian Basis Sets of Triple Zeta Valence Quality for Atoms Li to Kr. *J. Chem. Phys.* **1994**, *100* (8), 5829–5835. <https://doi.org/10.1063/1.467146>.
- (62) Ma, J.; Insausti, A.; Hazrah, A. S.; Xu, Y. Deciphering the Non-Covalent Interactions in the Furan···hexane Complex Using Rotational Spectroscopy and Theoretical Analyses. *J. Chem. Phys.* **2023**, *159* (13), 134302. <https://doi.org/10.1063/5.0166935>.

- (63) Wu, B.; Seifert, N. A.; Oswald, S.; Jäger, W.; Xu, Y. Rotational Spectrum and Molecular Structures of the Binary Aggregates of 1,1,1,3,3,3-Hexafluoro-2-Propanol with Ne and Ar. *J. Phys. Chem. A* **2021**, *125* (24), 5355–5364. <https://doi.org/10.1021/acs.jpca.1c03757>.
- (64) Insausti, A.; Ma, J.; Yang, Q.; Xie, F.; Xu, Y. Rotational Spectroscopy of 2-Furoic Acid and Its Dimer: Conformational Distribution and Double Proton Tunneling. *Chem. Phys. Chem.* **2022**, *23* (12), e202200176. <https://doi.org/10.1002/cphc.202200176>.
- (65) Wu, B.; Hazrah, A. S.; Seifert, N. A.; Oswald, S.; Jäger, W.; Xu, Y. Higher-Energy Hexafluoroisopropanol···Water Isomer and Its Large Amplitude Motions: Rotational Spectra and DFT Calculations. *J. Phys. Chem. A* **2021**, *125* (48), 10401–10409. <https://doi.org/10.1021/acs.jpca.1c09058>.
- (66) Carlson, C. D.; Hazrah, A. S.; Mason, D.; Yang, Q.; Seifert, N. A.; Xu, Y. Alternating 1-Phenyl-2,2,2-Trifluoroethanol Conformational Landscape With the Addition of One Water: Conformations and Large Amplitude Motions. *J. Phys. Chem. A* **2022**, *126* (40), 7250–7260. <https://doi.org/10.1021/acs.jpca.2c05803>.
- (67) Gall, J. T. A.; Thomas, J.; Xie, F.; Wang, Z.; Jäger, W.; Xu, Y. Rotational Spectroscopy of the Methyl Glycidate–Water Complex: Conformation and Water and Methyl Rotor Tunnelling Motions. *Phys. Chem. Chem. Phys.* **2017**, *19* (43), 29508–29515. <https://doi.org/10.1039/C7CP05464E>.
- (68) Pracht, P.; Bohle, F.; Grimme, S. Automated Exploration of the Low-Energy Chemical Space with Fast Quantum Chemical Methods. *Phys. Chem. Chem. Phys.* **2020**, *22* (14), 7169–7192. <https://doi.org/10.1039/C9CP06869D>.

- (69) Bannwarth, C.; Caldeweyher, E.; Ehlert, S.; Hansen, A.; Pracht, P.; Seibert, J.; Spicher, S.; Grimme, S. Extended Tight-Binding Quantum Chemistry Methods. *WIREs Comput. Mol. Sci.* **2021**, *11* (2), e1493. <https://doi.org/10.1002/wcms.1493>.
- (70) Wang, H.; Heger, M.; Al-Jabiri, M. H.; Xu, Y. Vibrational Spectroscopy of Homo- and Heterochiral Amino Acid Dimers: Conformational Landscapes. *Molecules* **2022**, *27* (1), 38. <https://doi.org/10.3390/molecules27010038>.
- (71) Seifert, N. A.; Hazrah, A. S.; Jäger, W. The 1-Naphthol Dimer and Its Surprising Preference for  $\pi$ - $\pi$  Stacking over Hydrogen Bonding. *J. Phys. Chem. Lett.* **2019**, *10* (11), 2836–2841. <https://doi.org/10.1021/acs.jpcclett.9b00646>.
- (72) Fatima, M.; Steber, A. L.; Poblitzki, A.; Pérez, C.; Zinn, S.; Schnell, M. Rotational Signatures of Dispersive Stacking in the Formation of Aromatic Dimers. *Angew. Chem.* **2019**, *131* (10), 3140–3145. <https://doi.org/10.1002/ange.201812556>.
- (73) Johnson, E. R.; Keinan, S.; Mori-Sánchez, P.; Contreras-García, J.; Cohen, A. J.; Yang, W. Revealing Noncovalent Interactions. *J. Am. Chem. Soc.* **2010**, *132* (18), 6498–6506. <https://doi.org/10.1021/ja100936w>.
- (74) Boys, S. F.; Bernardi, F. The Calculation of Small Molecular Interactions by the Differences of Separate Total Energies. Some Procedures with Reduced Errors. *Mol. Phys.* **1970**, *19* (4), 553–566. <https://doi.org/10.1080/00268977000101561>.
- (75) Parker, T. M.; Burns, L. A.; Parrish, R. M.; Ryno, A. G.; Sherrill, C. D. Levels of Symmetry Adapted Perturbation Theory (SAPT). I. Efficiency and Performance for Interaction Energies. *J. Chem. Phys.* **2014**, *140* (9), 094106. <https://doi.org/10.1063/1.4867135>.

- (76) Bader, R. F. W. A Quantum Theory of Molecular Structure and Its Applications. *Chem. Rev.* **1991**, *91* (5), 893–928. <https://doi.org/10.1021/cr00005a013>.
- (77) Matta, C. F.; Boyd, R. J. An Introduction to the Quantum Theory of Atoms in Molecules. In *The Quantum Theory of Atoms in Molecules*; John Wiley & Sons, Ltd, 2007; pp 1–34. <https://doi.org/10.1002/9783527610709.ch1>.
- (78) Koch, U.; Popelier, P. L. A. Characterization of C-H-O Hydrogen Bonds on the Basis of the Charge Density. *J. Phys. Chem.* **1995**, *99* (24), 9747–9754. <https://doi.org/10.1021/j100024a016>.
- (79) Mata, I.; Alkorta, I.; Espinosa, E.; Molins, E. Relationships between Interaction Energy, Intermolecular Distance and Electron Density Properties in Hydrogen Bonded Complexes under External Electric Fields. *Chem. Phys. Lett.* **2011**, *507* (1), 185–189. <https://doi.org/10.1016/j.cplett.2011.03.055>.
- (80) Lane, J. R.; Contreras-García, J.; Piquemal, J.-P.; Miller, B. J.; Kjaergaard, H. G. Are Bond Critical Points Really Critical for Hydrogen Bonding? *J. Chem. Theory Comput.* **2013**, *9* (8), 3263–3266. <https://doi.org/10.1021/ct400420r>.
- (81) Gordy, W.; Cook, R. L. *Microwave Molecular Spectra*; Wiley: New York, 1970.
- (82) Townes, C. H.; Schawlow, A. L. *Microwave Spectroscopy*; Courier Corporation, 2013.
- (83) Brown, G. G.; Dian, B. C.; Douglass, K. O.; Geyer, S. M.; Shipman, S. T.; Pate, B. H. A Broadband Fourier Transform Microwave Spectrometer Based on Chirped Pulse Excitation. *Rev. Sci. Instrum.* **2008**, *79* (5), 053103. <https://doi.org/10.1063/1.2919120>.
- (84) Seifert, N. A.; Thomas, J.; Jäger, W.; Xu, Y. Rotational Spectra and Theoretical Study of Tetramers and Trimers of 2-Fluoroethanol: Dramatic Intermolecular Compensation for

- Intramolecular Instability. *Phys. Chem. Chem. Phys.* **2018**, *20* (43), 27630–27637.  
<https://doi.org/10.1039/C8CP05653F>.
- (85) Carlson, C. D.; Seifert, N. A.; Heger, M.; Xie, F.; Thomas, J.; Xu, Y. Conformational Dynamics of 1-Phenyl-2,2,2-Trifluoroethanol by Rotational Spectroscopy and *Ab Initio* Calculations. *J. Mol. Spectrosc.* **2018**, *351*, 62–67.  
<https://doi.org/10.1016/j.jms.2018.07.006>.
- (86) Pérez, C.; Lobsiger, S.; Seifert, N. A.; Zaleski, D. P.; Temelso, B.; Shields, G. C.; Kisiel, Z.; Pate, B. H. Broadband Fourier Transform Rotational Spectroscopy for Structure Determination: The Water Heptamer. *Chem. Phys. Lett.* **2013**, *571*, 1–15.  
<https://doi.org/10.1016/j.cplett.2013.04.014>.
- (87) Xie, F.; Seifert, N. A.; Jäger, W.; Xu, Y. Conformational Panorama and Chirality Controlled Structure–Energy Relationship in a Chiral Carboxylic Acid Dimer. *Angew. Chem. Int. Ed.* **2020**, *59* (36), 15703–15710. <https://doi.org/10.1002/anie.202005685>.
- (88) Borho, N.; Xu, Y. Molecular Recognition in 1 : 1 Hydrogen-Bonded Complexes of Oxirane and Trans-2,3-Dimethyloxirane with Ethanol: A Rotational Spectroscopic and *Ab Initio* Study. *Phys. Chem. Chem. Phys.* **2007**, *9* (32), 4514–4520.  
<https://doi.org/10.1039/B705746F>.
- (89) Xie, F.; Ng, X.; Seifert, N. A.; Thomas, J.; Jäger, W.; Xu, Y. Rotational Spectroscopy of Chiral Tetrahydro-2-Furoic Acid: Conformational Landscape, Conversion, and Abundances. *J. Chem. Phys.* **2018**, *149* (22), 224306. <https://doi.org/10.1063/1.5063683>.
- (90) Del Olmo, A.; Calzada, J.; Nuñez, M. Benzoic Acid and Its Derivatives as Naturally Occurring Compounds in Foods and as Additives: Uses, Exposure, and Controversy. *Crit.*

*Rev. Food Sci. Nutr.* **2017**, *57* (14), 3084–3103.

<https://doi.org/10.1080/10408398.2015.1087964>.

- (91) Schnitzler, E. G.; Jäger, W. The Benzoic Acid–Water Complex: A Potential Atmospheric Nucleation Precursor Studied Using Microwave Spectroscopy and Ab Initio Calculations. *Phys. Chem. Chem. Phys.* **2014**, *16* (6), 2305–2314. <https://doi.org/10.1039/C3CP54486A>.
- (92) Ho, K. F.; Lee, S. C.; Ho, S. S. H.; Kawamura, K.; Tachibana, E.; Cheng, Y.; Zhu, T. Dicarboxylic Acids, Ketocarboxylic Acids,  $\alpha$ -Dicarbonyls, Fatty Acids, and Benzoic Acid in Urban Aerosols Collected during the 2006 Campaign of Air Quality Research in Beijing (CAREBeijing-2006). *J. Geophys. Res.* **2010**, *115* (D19), D19312. <https://doi.org/10.1029/2009JD013304>.
- (93) Duan, X.; Song, X.; Shi, R.; Wang, X.; Chen, S.; Zhao, S. A Theoretical Perspective on the Structure and Thermodynamics of Secondary Organic Aerosols from Toluene: Molecular Hierarchical Synergistic Effects. *Environ. Sci. Nano* **2022**, *9* (3), 1052–1063. <https://doi.org/10.1039/D1EN00959A>.
- (94) Chipley, J. R. Sodium Benzoate and Benzoic Acid. In *Antimicrobials in food*; CRC Press, 2020; pp 41–88.
- (95) Marwan, A. G.; Nagel, C. W. Quantitative Determination of Infinite Inhibition Concentrations of Antimicrobial Agents. *Appl. Environ. Microbiol.* **1986**, *51* (3), 559–561. <https://doi.org/10.1128/aem.51.3.559-561.1986>.
- (96) Marwan, A. G.; Nagel, C. W. Microbial Inhibitors of Cranberries. *J. Food Sci.* **1986**, *51* (4), 1009–1013. <https://doi.org/10.1111/j.1365-2621.1986.tb11220.x>.

- (97) Chaudhary, J.; Jain, A.; Manuja, R.; Sachdeva, S. A Comprehensive Review on Biological Activities of P-Hydroxy Benzoic Acid and Its Derivatives. *Int. J. Pharm. Sci. Rev. Res.* **2013**, *22*.
- (98) Clissold, S. P. Aspirin and Related Derivatives of Salicylic Acid. *Drugs* **1986**, *32* (4), 8–26. <https://doi.org/10.2165/00003495-198600324-00003>.
- (99) Pathak, M. A.; Fitzpatrick, T. B.; Frenk, E. Evaluation of Topical Agents That Prevent Sunburn — Superiority of Para-Aminobenzoic Acid and Its Ester in Ethyl Alcohol. *N. Engl. J. Med.* **1969**, *280* (26), 1459–1463. <https://doi.org/10.1056/NEJM196906262802607>.
- (100) Maki, T.; Takeda, K. Benzoic Acid and Derivatives. In *Ullmann's Encyclopedia of Industrial Chemistry*; John Wiley & Sons, Ltd, 2000. [https://doi.org/10.1002/14356007.a03\\_555](https://doi.org/10.1002/14356007.a03_555).
- (101) Pi, Y.; Schumacher, J.; Jekel, M. The Use of Para-Chlorobenzoic Acid (pCBA) as an Ozone/Hydroxyl Radical Probe Compound. *Ozone Sci. Eng.* **2005**, *27* (6), 431–436. <https://doi.org/10.1080/01919510500349309>.
- (102) Onda, M.; Asai, M.; Takise, K.; Kuwae, K.; Hayami, K.; Kuroe, A.; Mori, M.; Miyazaki, H.; Suzuki, N.; Yamaguchi, I. Microwave Spectrum of Benzoic Acid. *J. Mol. Struct.* **1999**, *482–483*, 301–303. [https://doi.org/10.1016/S0022-2860\(98\)00675-9](https://doi.org/10.1016/S0022-2860(98)00675-9).
- (103) Godfrey, P. D.; McNaughton, D. Structural Studies of Aromatic Carboxylic Acids via Computational Chemistry and Microwave Spectroscopy. *J. Chem. Phys.* **2013**, *138* (2), 024303. <https://doi.org/10.1063/1.4773347>.
- (104) Kim, Y.; Machida, K. Vibrational Spectra, Normal Vibrations and Infrared Intensities of Six Isotopic Benzoic Acids. *Spectrochim. Acta Part Mol. Spectrosc.* **1986**, *42* (8), 881–889. [https://doi.org/10.1016/0584-8539\(86\)80206-9](https://doi.org/10.1016/0584-8539(86)80206-9).

- (105) Baum, J. C.; McClure, D. S. The Ultraviolet Transitions of Benzoic Acid. 1. Interpretation of the Singlet Absorption Spectrum. *J. Am. Chem. Soc.* **1979**, *101* (9), 2335–2339. <https://doi.org/10.1021/ja00503a016>.
- (106) Cismesia, A. P.; Nicholls, G. R.; Polfer, N. C. Amine vs. Carboxylic Acid Protonation in Ortho-, Meta-, and Para-Aminobenzoic Acid: An IRMPD Spectroscopy Study. *J. Mol. Spectrosc.* **2017**, *332*, 79–85. <https://doi.org/10.1016/j.jms.2016.10.020>.
- (107) Borah, B.; Gomti Devi, Th. Vibrational Study on the Molecular Interaction of L-Proline and Para-Aminobenzoic Acid. *J. Mol. Struct.* **2020**, *1203*, 127396. <https://doi.org/10.1016/j.molstruc.2019.127396>.
- (108) Badilescu, S.; Ashrit, P. V.; Truong, V.-V.; Badilescu, I. I. Enhanced Infrared ATR Spectra of O-, m-, and p-Nitrobenzoic Acid with Ag Films. *Appl. Spectrosc.* **1989**, *43* (3), 549–552. <https://doi.org/10.1366/0003702894202850>.
- (109) Sundaraganesan, N.; Anand, B.; Meganathan, C.; Joshua, B. D. FT-IR, FT-Raman Spectra and Ab Initio HF, DFT Vibrational Analysis of p-Chlorobenzoic Acid. *Spectrochim. Acta. A. Mol. Biomol. Spectrosc.* **2008**, *69* (3), 871–879. <https://doi.org/10.1016/j.saa.2007.05.051>.
- (110) Steill, J. D.; Oomens, J. Gas-Phase Deprotonation of p-Hydroxybenzoic Acid Investigated by IR Spectroscopy: Solution-Phase Structure Is Retained upon ESI. *J. Am. Chem. Soc.* **2009**, *131* (38), 13570–13571. <https://doi.org/10.1021/ja903877v>.
- (111) Eraković, M.; Vaillant, C. L.; Cvitaš, M. T. Instanton Theory of Ground-State Tunneling Splittings with General Paths. *J. Chem. Phys.* **2020**, *152* (8), 084111. <https://doi.org/10.1063/1.5145278>.

- (112) Mil'nikov, G. V.; Nakamura, H. Practical Implementation of the Instanton Theory for the Ground-State Tunneling Splitting. *J. Chem. Phys.* **2001**, *115* (15), 6881–6897.  
<https://doi.org/10.1063/1.1406532>.
- (113) Grimme, S.; Ehrlich, S.; Goerigk, L. Effect of the Damping Function in Dispersion Corrected Density Functional Theory. *J. Comput. Chem.* **2011**, *32* (7), 1456–1465.  
<https://doi.org/10.1002/jcc.21759>.
- (114) Pritchard, B. P.; Altarawy, D.; Didier, B.; Gibson, T. D.; Windus, T. L. New Basis Set Exchange: An Open, Up-to-Date Resource for the Molecular Sciences Community. *J. Chem. Inf. Model.* **2019**, *59* (11), 4814–4820. <https://doi.org/10.1021/acs.jcim.9b00725>.
- (115) Ásgeirsson, V.; Birgisson, B. O.; Bjornsson, R.; Becker, U.; Neese, F.; Riplinger, C.; Jónsson, H. Nudged Elastic Band Method for Molecular Reactions Using Energy-Weighted Springs Combined with Eigenvector Following. *J. Chem. Theory Comput.* **2021**, *17* (8), 4929–4945. <https://doi.org/10.1021/acs.jctc.1c00462>.
- (116) Lu, T.; Chen, F. Multiwfn: A Multifunctional Wavefunction Analyzer. *J. Comput. Chem.* **2012**, *33* (5), 580–592. <https://doi.org/10.1002/jcc.22885>.
- (117) Matito, E.; Poater, J.; Solà, M.; Duran, M.; Salvador, P. Comparison of the AIM Delocalization Index and the Mayer and Fuzzy Atom Bond Orders. *J. Phys. Chem. A* **2005**, *109* (43), 9904–9910. <https://doi.org/10.1021/jp0538464>.
- (118) Western, C. M. PGOPHER: A Program for Simulating Rotational, Vibrational and Electronic Spectra. *J. Quant. Spectrosc. Radiat. Transf.* **2017**, *186*, 221–242.  
<https://doi.org/10.1016/j.jqsrt.2016.04.010>.

- (119) Pickett, H. M. The Fitting and Prediction of Vibration-Rotation Spectra with Spin Interactions. *J. Mol. Spectrosc.* **1991**, *148* (2), 371–377. [https://doi.org/10.1016/0022-2852\(91\)90393-O](https://doi.org/10.1016/0022-2852(91)90393-O).
- (120) Schnitzler, E. G.; Seifert, N. A.; Kusuma, I.; Jäger, W. Rotational Spectroscopy of P-Toluic Acid and Its 1:1 Complex with Water. *J. Phys. Chem. A* **2017**, *121* (45), 8625–8631. <https://doi.org/10.1021/acs.jpca.7b08984>.
- (121) Perera, A. S.; Cheramy, J.; Poopari, M. R.; Xu, Y. Aggregation of Lactic Acid in Cold Rare-Gas Matrices and the Link to Solution: A Matrix Isolation-Vibrational Circular Dichroism Study. *Phys. Chem. Chem. Phys.* **2019**, *21* (7), 3574–3584. <https://doi.org/10.1039/C8CP04748K>.
- (122) Macario, A.; Blanco, S.; Thomas, J.; Xu, Y.; López, J. C. Competition Between Intra- and Intermolecular Hydrogen Bonding: O-Anisic Acid···Formic Acid Heterodimer. *Chem. Eur. J.* **2019**, *25* (53), 12325–12331. <https://doi.org/10.1002/chem.201902086>.
- (123) Lesarri, A.; Mata, S.; Cocinero, E. J.; Blanco, S.; López, J. C.; Alonso, J. L. The Structure of Neutral Proline. *Angew. Chem. Int. Ed.* **2002**, *41* (24), 4673–4676. <https://doi.org/10.1002/anie.200290012>.
- (124) León, I.; Alonso, E. R.; Mata, S.; Cabezas, C.; Alonso, J. L. Unveiling the Neutral Forms of Glutamine. *Angew. Chem.* **2019**, *131* (45), 16148–16153. <https://doi.org/10.1002/ange.201907222>.
- (125) Ruoff, R. S.; Klots, T. D.; Emilsson, T.; Gutowsky, H. S. Relaxation of Conformers and Isomers in Seeded Supersonic Jets of Inert Gases. *J. Chem. Phys.* **1990**, *93* (5), 3142–3150. <https://doi.org/10.1063/1.458848>.

- (126) Watson, J. K. G. In *Vibrational spectra and structure*; Durig, J. R., Ed.; Elsevier: Amsterdam, 1977; Vol. 6, p 1.
- (127) Lister, D. G.; Tyler, J. K.; Høg, J. H.; Larsen, N. W. The Microwave Spectrum, Structure and Dipole Moment of Aniline. *J. Mol. Struct.* **1974**, *23* (2), 253–264.  
[https://doi.org/10.1016/0022-2860\(74\)85039-8](https://doi.org/10.1016/0022-2860(74)85039-8).
- (128) Ye, E.; Chandrasekaran, K.; Bettens, R. P. A. Millimeter Wave Measurement and Assignment of the Rotational Spectrum of Aniline. *J. Mol. Spectrosc.* **2005**, *229* (1), 54–56.  
<https://doi.org/10.1016/j.jms.2004.08.011>.
- (129) Bird, R. G.; Neill, J. L.; Alstadt, V. J.; Young, J. W.; Pate, B. H.; Pratt, D. W. Ground State  $^{14}\text{N}$  Quadrupole Couplings in the Microwave Spectra of N,N-Dimethylaniline and 4,4'-Dimethylaminobenzonitrile. *J. Phys. Chem. A* **2011**, *115* (34), 9392–9398.  
<https://doi.org/10.1021/jp111075r>.
- (130) Betz, T.; Zinn, S.; Graneek, J. B.; Schnell, M. Nuclear Quadrupole Coupling Constants of Two Chemically Distinct Nitrogen Atoms in 4-Aminobenzonitrile. *J. Phys. Chem. A* **2014**, *118* (28), 5164–5169. <https://doi.org/10.1021/jp410964w>.
- (131) Insausti, A.; Calabrese, C.; Parra, M.; Usabiaga, I.; Vallejo-López, M.; Écija, P.; Basterretxea, F. J.; Grabow, J.-U.; Caminati, W.; Lesarri, A.; Cocinero, E. J. Conformational Impact of Aliphatic Side Chains in Local Anaesthetics: Benzocaine, Butamben and Isobutamben. *Chem. Commun.* **2020**, *56* (45), 6094–6097.  
<https://doi.org/10.1039/D0CC00760A>.
- (132) Høg, J. H.; Nygaard, L.; Ole Sørensen, G. Microwave Spectrum and Planarity of Nitrobenzene. *J. Mol. Struct.* **1971**, *7* (1), 111–121. [https://doi.org/10.1016/0022-2860\(71\)90012-3](https://doi.org/10.1016/0022-2860(71)90012-3).

- (133) Omelchenko, I. V.; Shishkin, O. V.; Gorb, L.; Hill, F. C.; Leszczynski, J. Properties, Aromaticity, and Substituents Effects in Poly Nitro- and Amino-Substituted Benzenes. *Struct. Chem.* **2012**, *23* (5), 1585–1597. <https://doi.org/10.1007/s11224-012-9971-8>.
- (134) Heineking, N.; Dreizler, H. Nitrogen Quadrupole Coupling Constants of Nitrobenzene and O-Nitrophenol. *Berichte Bunsenges. Für Phys. Chem.* **1993**, *97* (5), 663–665. <https://doi.org/10.1002/bbpc.19930970504>.
- (135) Graneek, J. B.; Pérez, C.; Schnell, M. Structural Determination and Population Transfer of 4-Nitroanisole by Broadband Microwave Spectroscopy and Tailored Microwave Pulses. *J. Chem. Phys.* **2017**, *147* (15), 154306. <https://doi.org/10.1063/1.4991902>.
- (136) Roucou, A.; Kleiner, I.; Goubet, M.; Bteich, S.; Mouret, G.; Bocquet, R.; Hindle, F.; Meerts, W. L.; Cuisset, A. Towards the Detection of Explosive Taggants: Microwave and Millimetre-Wave Gas-Phase Spectroscopies of 3-Nitrotoluene. *Chem. Phys. Chem.* **2018**, *19* (9), 1056–1067. <https://doi.org/10.1002/cphc.201701266>.
- (137) Baweja, S.; Antonelli, E.; Hussain, S.; Fernández-Ramos, A.; Kleiner, I.; Nguyen, H. V. L.; Sanz, M. E. Revealing Internal Rotation and <sup>14</sup>N Nuclear Quadrupole Coupling in the Atmospheric Pollutant 4-Methyl-2-Nitrophenol: Interplay of Microwave Spectroscopy and Quantum Chemical Calculations. *Molecules* **2023**, *28* (5), 2153. <https://doi.org/10.3390/molecules28052153>.
- (138) Schwabe, T.; Grimme, S. Double-Hybrid Density Functionals with Long-Range Dispersion Corrections: Higher Accuracy and Extended Applicability. *Phys. Chem. Chem. Phys.* **2007**, *9* (26), 3397–3406. <https://doi.org/10.1039/B704725H>.

- (139) Yang, Y.; Krin, A.; Cai, X.; Poopari, M. R.; Zhang, Y.; Cheeseman, J. R.; Xu, Y. Conformations of Steroid Hormones: Infrared and Vibrational Circular Dichroism Spectroscopy. *Molecules* **2023**, *28* (2), 771. <https://doi.org/10.3390/molecules28020771>.
- (140) Dorosh, O.; Białkowska-Jaworska, E.; Kisiel, Z.; Pszczółkowski, L. New Measurements and Global Analysis of Rotational Spectra of Cl-, Br-, and I-Benzene: Spectroscopic Constants and Electric Dipole Moments. *J. Mol. Spectrosc.* **2007**, *246* (2), 228–232. <https://doi.org/10.1016/j.jms.2007.09.010>.
- (141) Hansch, Corwin.; Leo, A.; Taft, R. W. A Survey of Hammett Substituent Constants and Resonance and Field Parameters. *Chem. Rev.* **1991**, *91* (2), 165–195. <https://doi.org/10.1021/cr00002a004>.
- (142) Hammett, L. P. The Effect of Structure upon the Reactions of Organic Compounds. Benzene Derivatives. *J. Am. Chem. Soc.* **1937**, *59* (1), 96–103. <https://doi.org/10.1021/ja01280a022>.
- (143) Sayyed, F. B.; Suresh, C. H. Quantification of Substituent Effects Using Molecular Electrostatic Potentials: Additive Nature and Proximity Effects. *New J. Chem.* **2009**, *33* (12), 2465–2471. <https://doi.org/10.1039/B9NJ00333A>.
- (144) Wang, X.; Liu, Z.; Yan, X.; Lu, T.; Zheng, W.; Xiong, W. Bonding Character, Electron Delocalization, and Aromaticity of Cyclo[18]Carbon (C18) Precursors, C18-(CO)<sub>n</sub> (N=6, 4, and 2): Focusing on the Effect of Carbonyl (-CO) Groups. *Chem. Eur. J.* **2022**, *28* (7), e202103815. <https://doi.org/10.1002/chem.202103815>.
- (145) Hanes, C. C.; Wang, X.; Jain, P.; Parisien, M.-A.; Little, J. M.; Flannigan, M. D. Fire-Regime Changes in Canada over the Last Half Century. *Can. J. For. Res.* **2019**, *49* (3), 256–269. <https://doi.org/10.1139/cjfr-2018-0293>.

- (146) Andreae, M. O.; Andreae, T. W.; Annegarn, H.; Beer, J.; Cachier, H.; Le Canut, P.; Elbert, W.; Maenhaut, W.; Salma, I.; Wienhold, F. G.; Zenker, T. Airborne Studies of Aerosol Emissions from Savanna Fires in Southern Africa: 2. Aerosol Chemical Composition. *J. Geophys. Res. Atmospheres* **1998**, *103* (D24), 32119–32128.  
<https://doi.org/10.1029/98JD02280>.
- (147) Simoneit, B. R. T. Biomass Burning — a Review of Organic Tracers for Smoke from Incomplete Combustion. *Appl. Geochem.* **2002**, *17* (3), 129–162.  
[https://doi.org/10.1016/S0883-2927\(01\)00061-0](https://doi.org/10.1016/S0883-2927(01)00061-0).
- (148) McClure, C. D.; Jaffe, D. A. US Particulate Matter Air Quality Improves except in Wildfire-Prone Areas. *Proc. Natl. Acad. Sci.* **2018**, *115* (31), 7901–7906.  
<https://doi.org/10.1073/pnas.1804353115>.
- (149) Fuzzi, S.; Baltensperger, U.; Carslaw, K.; Decesari, S.; Denier van der Gon, H.; Facchini, M. C.; Fowler, D.; Koren, I.; Langford, B.; Lohmann, U.; Nemitz, E.; Pandis, S.; Riipinen, I.; Rudich, Y.; Schaap, M.; Slowik, J. G.; Spracklen, D. V.; Vignati, E.; Wild, M.; Williams, M.; Gilardoni, S. Particulate Matter, Air Quality and Climate: Lessons Learned and Future Needs. *Atmospheric Chem. Phys.* **2015**, *15* (14), 8217–8299.  
<https://doi.org/10.5194/acp-15-8217-2015>.
- (150) Pettersen, R. C. The Chemical Composition of Wood. In *The Chemistry of Solid Wood*; Advances in Chemistry; American Chemical Society, 1984; Vol. 207, pp 57–126.  
<https://doi.org/10.1021/ba-1984-0207.ch002>.
- (151) Wan, X.; Kawamura, K.; Ram, K.; Kang, S.; Loewen, M.; Gao, S.; Wu, G.; Fu, P.; Zhang, Y.; Bhattarai, H.; Cong, Z. Aromatic Acids as Biomass-Burning Tracers in

- Atmospheric Aerosols and Ice Cores: A Review. *Environ. Pollut.* **2019**, *247*, 216–228.  
<https://doi.org/10.1016/j.envpol.2019.01.028>.
- (152) Bin Abas, M. R.; Simoneit, B. R. T.; Elias, V.; Cabral, J. A.; Cardoso, J. N. Composition of Higher Molecular Weight Organic Matter in Smoke Aerosol from Biomass Combustion in Amazonia. *Chemosphere* **1995**, *30* (5), 995–1015. [https://doi.org/10.1016/0045-6535\(94\)00442-W](https://doi.org/10.1016/0045-6535(94)00442-W).
- (153) Service, B. W. *Wildfire Season Summary - Province of British Columbia*.  
<https://www2.gov.bc.ca/gov/content/safety/wildfire-status/about-bcws/wildfire-history/wildfire-season-summary> (accessed 2021-09-28).
- (154) Grieman, M. M.; Aydin, M.; McConnell, J. R.; Saltzman, E. S. Burning-Derived Vanillic Acid in an Arctic Ice Core from Tunu, Northeastern Greenland. *Clim. Past* **2018**, *14* (11), 1625–1637. <https://doi.org/10.5194/cp-14-1625-2018>.
- (155) Liu, C.; Zeng, C. Heterogeneous Kinetics of Methoxyphenols in the OH-Initiated Reactions under Different Experimental Conditions. *Chemosphere* **2018**, *209*, 560–567.  
<https://doi.org/10.1016/j.chemosphere.2018.06.131>.
- (156) Donahue, N. M.; Chuang, W.; Epstein, S. A.; Kroll, J. H.; Worsnop, D. R.; Robinson, A. L.; Adams, P. J.; Pandis, S. N. Why Do Organic Aerosols Exist? Understanding Aerosol Lifetimes Using the Two-Dimensional Volatility Basis Set. *Environ. Chem.* **2013**, *10* (3), 151–157. <https://doi.org/10.1071/EN13022>.
- (157) Cabrera-Perez, D.; Taraborrelli, D.; Sander, R.; Pozzer, A. Global Atmospheric Budget of Simple Monocyclic Aromatic Compounds. *Atmospheric Chem. Phys.* **2016**, *16* (11), 6931–6947. <https://doi.org/10.5194/acp-16-6931-2016>.

- (158) Yan, J.; Wang, X.; Gong, P.; Wang, C.; Cong, Z. Review of Brown Carbon Aerosols: Recent Progress and Perspectives. *Sci. Total Environ.* **2018**, *634*, 1475–1485. <https://doi.org/10.1016/j.scitotenv.2018.04.083>.
- (159) Godfrey, P. D.; Mirabella, M. J.; Brown, R. D. Structural Studies of Higher Energy Conformers by Millimeter-Wave Spectroscopy: Oxalic Acid. *J. Phys. Chem. A* **2000**, *104* (2), 258–264. <https://doi.org/10.1021/jp992499t>.
- (160) Cortijo, V.; Alonso, E. R.; Mata, S.; Alonso, J. L. Conformational Map of Phenolic Acids. *J. Phys. Chem. A* **2018**, *122* (2), 646–651. <https://doi.org/10.1021/acs.jpca.7b08882>.
- (161) Weigend, F.; Ahlrichs, R. Balanced Basis Sets of Split Valence, Triple Zeta Valence and Quadruple Zeta Valence Quality for H to Rn: Design and Assessment of Accuracy. *Phys. Chem. Chem. Phys.* **2005**, *7* (18), 3297–3305. <https://doi.org/10.1039/B508541A>.
- (162) Kendall, R. A.; Dunning, T. H.; Harrison, R. J. Electron Affinities of the First-row Atoms Revisited. Systematic Basis Sets and Wave Functions. *J. Chem. Phys.* **1992**, *96* (9), 6796–6806. <https://doi.org/10.1063/1.462569>.
- (163) Peng, C.; Bernhard Schlegel, H. Combining Synchronous Transit and Quasi-Newton Methods to Find Transition States. *Isr. J. Chem.* **1993**, *33* (4), 449–454. <https://doi.org/10.1002/ijch.199300051>.
- (164) Lefebvre, C.; Rubez, G.; Khartabil, H.; Boisson, J.-C.; Contreras-García, J.; Hénon, E. Accurately Extracting the Signature of Intermolecular Interactions Present in the NCI Plot of the Reduced Density Gradient versus Electron Density. *Phys. Chem. Chem. Phys.* **2017**, *19* (27), 17928–17936. <https://doi.org/10.1039/C7CP02110K>.
- (165) Lefebvre, C.; Khartabil, H.; Boisson, J.-C.; Contreras-García, J.; Piquemal, J.-P.; Hénon, E. The Independent Gradient Model: A New Approach for Probing Strong and Weak

- Interactions in Molecules from Wave Function Calculations. *Chem. Phys. Chem.* **2018**, *19* (6), 724–735. <https://doi.org/10.1002/cphc.201701325>.
- (166) Ponce-Vargas, M.; Lefebvre, C.; Boisson, J.-C.; Hénon, E. Atomic Decomposition Scheme of Noncovalent Interactions Applied to Host–Guest Assemblies. *J. Chem. Inf. Model.* **2020**, *60* (1), 268–278. <https://doi.org/10.1021/acs.jcim.9b01016>.
- (167) Klein, J.; Khartabil, H.; Boisson, J.-C.; Contreras-García, J.; Piquemal, J.-P.; Hénon, E. New Way for Probing Bond Strength. *J. Phys. Chem. A* **2020**, *124* (9), 1850–1860. <https://doi.org/10.1021/acs.jpca.9b09845>.
- (168) *IGMPlot: a program revealing non-covalent interactions*. <http://igmpplot.univ-reims.fr/> (accessed 2024-05-12).
- (169) Cocinero, E. J.; Lesarri, A.; Écija, P.; Grabow, J.-U.; Fernández, J. A.; Castaño, F. Conformational Equilibria in Vanillin and Ethylvanillin. *Phys. Chem. Chem. Phys.* **2010**, *12* (39), 12486–12493. <https://doi.org/10.1039/C0CP00585A>.
- (170) Miller, B. J.; Lane, J. R.; Kjaergaard, H. G. Intramolecular OH $\cdots\pi$  Interactions in Alkenols and Alkynols. *Phys. Chem. Chem. Phys.* **2011**, *13* (31), 14183–14193. <https://doi.org/10.1039/C1CP21190K>.
- (171) Cocinero, E. J.; Basterretxea, F. J.; Écija, P.; Lesarri, A.; Fernández, J. A.; Castaño, F. Conformational Behaviour, Hydrogen Bond Competition and Intramolecular Dynamics in Vanillin Derivatives: Acetovanillone and 6-Hydroxy-3-Methoxyacetophenone. *Phys. Chem. Chem. Phys.* **2011**, *13* (29), 13310–13318. <https://doi.org/10.1039/C0CP02418J>.
- (172) Cocinero, E. J.; Lesarri, A.; Écija, P.; Basterretxea, F.; Fernández, J. A.; Castaño, F. Competing Hydrogen Bonding in Methoxyphenols: The Rotational Spectrum of o-Vanillin. *J. Mol. Spectrosc.* **2011**, *267* (1), 112–117. <https://doi.org/10.1016/j.jms.2011.02.009>.

- (173) Ouyang, B.; Howard, B. J. High-Resolution Microwave Spectroscopic and Ab Initio Studies of Propanoic Acid and Its Hydrates. *J. Phys. Chem. A* **2008**, *112* (36), 8208–8214.
- (174) Fernández-Ramos, A.; Ellingson, B. A.; Meana-Pañeda, R.; Marques, J.; Truhlar, D. G. Symmetry Numbers and Chemical Reaction Rates. *Theor. Chem. Acc.* **2007**, *118* (4), 813–826.
- (175) *EAS Weather Station | Earth and Atmospheric Sciences*. <https://www.ualberta.ca/earth-sciences/facilities/weather.html> (accessed 2022-03-08).
- (176) Messer, J. K.; De Lucia, F. C.; Helminger, P. The Pure Rotational Spectrum of Water Vapor—a Millimeter, Submillimeter, and Far Infrared Analysis. *Int. J. Infrared Millim. Waves* **1983**, *4* (4), 505–539.
- (177) Organization, W. M. *Guide to Instruments and Methods of Observation*; WMO Geneva, 2018; Vol. 1.
- (178) G. Schnitzler, E.; Jäger, W. The Benzoic Acid–Water Complex: A Potential Atmospheric Nucleation Precursor Studied Using Microwave Spectroscopy and Ab Initio Calculations. *Phys. Chem. Chem. Phys.* **2014**, *16* (6), 2305–2314. <https://doi.org/10.1039/C3CP54486A>.
- (179) Ayinla, R. T.; Shiri, M.; Song, B.; Gangishetty, M.; Wang, K. The Pivotal Role of Non-Covalent Interactions in Single-Molecule Charge Transport. *Mater. Chem. Front.* **2023**, *7* (17), 3524–3542. <https://doi.org/10.1039/D3QM00210A>.
- (180) Carter-Fenk, K.; Liu, M.; Pujal, L.; Loipersberger, M.; Tsanai, M.; Vernon, R. M.; Forman-Kay, J. D.; Head-Gordon, M.; Heidar-Zadeh, F.; Head-Gordon, T. The Energetic Origins of Pi–Pi Contacts in Proteins. *J. Am. Chem. Soc.* **2023**, *145* (45), 24836–24851. <https://doi.org/10.1021/jacs.3c09198>.

- (181) Hong, Y.; Schlosser, F.; Kim, W.; Würthner, F.; Kim, D. Ultrafast Symmetry-Breaking Charge Separation in a Perylene Bisimide Dimer Enabled by Vibronic Coupling and Breakdown of Adiabaticity. *J. Am. Chem. Soc.* **2022**, *144* (34), 15539–15548. <https://doi.org/10.1021/jacs.2c03916>.
- (182) Gilissen, P. J.; White, P. B.; Berrocal, J. A.; Vanthuyne, N.; Rutjes, F. P. J. T.; Feringa, B. L.; Elemans, J. A. A. W.; Nolte, R. J. M. Molecular Motor-Functionalized Porphyrin Macrocycles. *Nat. Commun.* **2020**, *11* (1), 5291. <https://doi.org/10.1038/s41467-020-19123-y>.
- (183) Izadnia, S.; LaForge, A. C.; Stienkemeier, F.; Cheeseman, J. R.; Bloino, J.; Cheramy, J.; Jäger, W.; Xu, Y. Unusual Binary Aggregates of Perylene Bisimide Revealed by Their Electronic Transitions in Helium Nanodroplets and DFT Calculations. *Phys. Chem. Chem. Phys.* **2021**, *23* (25), 13862–13872. <https://doi.org/10.1039/D1CP01923F>.
- (184) Grimme, S. Do Special Noncovalent  $\pi$ – $\pi$  Stacking Interactions Really Exist? *Angew. Chem. Int. Ed.* **2008**, *47* (18), 3430–3434. <https://doi.org/10.1002/anie.200705157>.
- (185) Martinez, C. R.; Iverson, B. L. Rethinking the Term “Pi-Stacking.” *Chem. Sci.* **2012**, *3* (7), 2191–2201. <https://doi.org/10.1039/C2SC20045G>.
- (186) Arunan, E.; Gutowsky, H. S. The Rotational Spectrum, Structure and Dynamics of a Benzene Dimer. *J. Chem. Phys.* **1993**, *98* (5), 4294–4296. <https://doi.org/10.1063/1.465035>.
- (187) Schnell, M.; Erlekam, U.; Bunker, P. R.; von Helden, G.; Grabow, J.-U.; Meijer, G.; van der Avoird, A. Structure of the Benzene Dimer—Governed by Dynamics. *Angew. Chem. Int. Ed.* **2013**, *52* (19), 5180–5183. <https://doi.org/10.1002/anie.201300653>.

- (188) Podeszwa, R.; Bukowski, R.; Szalewicz, K. Potential Energy Surface for the Benzene Dimer and Perturbational Analysis of  $\Pi$ - $\pi$  Interactions. *J. Phys. Chem. A* **2006**, *110* (34), 10345–10354. <https://doi.org/10.1021/jp064095o>.
- (189) Seifert, N. A.; Steber, A. L.; Neill, J. L.; Pérez, C.; Zaleski, D. P.; Pate, B. H.; Lesarri, A. The Interplay of Hydrogen Bonding and Dispersion in Phenol Dimer and Trimer: Structures from Broadband Rotational Spectroscopy. *Phys. Chem. Chem. Phys.* **2013**, *15* (27), 11468–11477. <https://doi.org/10.1039/C3CP51725J>.
- (190) Huber, F. K.; Kaiser, R.; Sauter, W.; Schiestl, F. P. Floral Scent Emission and Pollinator Attraction in Two Species of *Gymnadenia* (Orchidaceae). *Oecologia* **2005**, *142* (4), 564–575. <https://doi.org/10.1007/s00442-004-1750-9>.
- (191) Qin, X.-W.; Hao, C.-Y.; He, S.-Z.; Wu, G.; Tan, L.-H.; Xu, F.; Hu, R.-S. Volatile Organic Compound Emissions from Different Stages of *Cananga Odorata* Flower Development. *Molecules* **2014**, *19* (7), 8965–8980. <https://doi.org/10.3390/molecules19078965>.
- (192) Yang, J.-O.; Nakayama, N.; Toda, K.; Tebayashi, S.; Kim, C.-S. Structural Determination of Elicitors in *Sogatella Furcifera* (Horváth) That Induce Japonica Rice Plant Varieties (*Oryza Sativa* L.) to Produce an Ovicidal Substance against *S. Furcifera* Eggs. *Biosci. Biotechnol. Biochem.* **2014**, *78* (6), 937–942. <https://doi.org/10.1080/09168451.2014.917266>.
- (193) Pearson, M. A.; Miller, G. W. Benzyl Benzoate. In *Encyclopedia of Toxicology (Third Edition)*; Wexler, P., Ed.; Academic Press: Oxford, 2014; pp 433–434. <https://doi.org/10.1016/B978-0-12-386454-3.00103-2>.

- (194) Srivastava, D.; Vu, T. V.; Tong, S.; Shi, Z.; Harrison, R. M. Formation of Secondary Organic Aerosols from Anthropogenic Precursors in Laboratory Studies. *Npj Clim. Atmospheric Sci.* **2022**, *5* (1), 1–30. <https://doi.org/10.1038/s41612-022-00238-6>.
- (195) Pracht, P.; Grimme, S.; Bannwarth, C.; Bohle, F.; Ehlert, S.; Feldmann, G.; Gorges, J.; Müller, M.; Neudecker, T.; Plett, C.; Spicher, S.; Steinbach, P.; Wesolowski, P. A.; Zeller, F. CREST—A Program for the Exploration of Low-Energy Molecular Chemical Space. *J. Chem. Phys.* **2024**, *160* (11), 114110. <https://doi.org/10.1063/5.0197592>.
- (196) Carter-Fenk, K.; Herbert, J. M. Reinterpreting  $\pi$ -Stacking. *Phys. Chem. Chem. Phys.* **2020**, *22* (43), 24870–24886. <https://doi.org/10.1039/D0CP05039C>.
- (197) Kraitchman, J. Determination of Molecular Structure from Microwave Spectroscopic Data. *Am. J. Phys.* **1953**, *21* (1), 17–24. <https://doi.org/10.1119/1.1933338>.
- (198) Rudolph, H. D. Extending Kraitchman's Equations. *J. Mol. Spectrosc.* **1981**, *89* (2), 430–439. [https://doi.org/10.1016/0022-2852\(81\)90036-9](https://doi.org/10.1016/0022-2852(81)90036-9).
- (199) Hazrah, A. S.; Nanayakkara, S.; Seifert, N. A.; Kraka, E.; Jäger, W. Structural Study of 1- and 2-Naphthol: New Insights into the Non-Covalent H–H Interaction in Cis-1-Naphthol. *Phys. Chem. Chem. Phys.* **2022**, *24* (6), 3722–3732. <https://doi.org/10.1039/D1CP05632H>.
- (200) Lutz, P. B.; Bayse, C. A. Interpreting Geometric Preferences in  $\pi$ -Stacking Interactions through Molecular Orbital Analysis. *Int. J. Quantum Chem.* **2018**, *118* (7), e25513. <https://doi.org/10.1002/qua.25513>.
- (201) Saragi, R. T.; Calabrese, C.; Juanes, M.; Pinacho, R.; Rubio, J. E.; Pérez, C.; Lesarri, A.  $\pi$ -Stacking Isomerism in Polycyclic Aromatic Hydrocarbons: The 2-Naphthalenethiol Dimer. *J. Phys. Chem. Lett.* **2023**, *14* (1), 207–213. <https://doi.org/10.1021/acs.jpcllett.2c03299>.

- (202) Jeziorski, B.; Moszynski, R.; Szalewicz, K. Perturbation Theory Approach to Intermolecular Potential Energy Surfaces of van Der Waals Complexes. *Chem. Rev.* **1994**, *94* (7), 1887–1930. <https://doi.org/10.1021/cr00031a008>.
- (203) Marongiu, A.; Faravelli, T.; Bozzano, G.; Dente, M.; Ranzi, E. Thermal Degradation of Poly(Vinyl Chloride). *J. Anal. Appl. Pyrolysis* **2003**, *70* (2), 519–553. [https://doi.org/10.1016/S0165-2370\(03\)00024-X](https://doi.org/10.1016/S0165-2370(03)00024-X).
- (204) Aracil, I.; Font, R.; Conesa, J. A. Semivolatile and Volatile Compounds from the Pyrolysis and Combustion of Polyvinyl Chloride. *J. Anal. Appl. Pyrolysis* **2005**, *74* (1), 465–478. <https://doi.org/10.1016/j.jaap.2004.09.008>.
- (205) Zhang, B.; Shen, H.; Yun, X.; Zhong, Q.; Henderson, B. H.; Wang, X.; Shi, L.; Gunthe, S. S.; Huey, L. G.; Tao, S.; Russell, A. G.; Liu, P. Global Emissions of Hydrogen Chloride and Particulate Chloride from Continental Sources. *Environ. Sci. Technol.* **2022**, *56* (7), 3894–3904. <https://doi.org/10.1021/acs.est.1c05634>.
- (206) Christian, T. J.; Yokelson, R. J.; Cárdenas, B.; Molina, L. T.; Engling, G.; Hsu, S.-C. Trace Gas and Particle Emissions from Domestic and Industrial Biofuel Use and Garbage Burning in Central Mexico. *Atmospheric Chem. Phys.* **2010**, *10* (2), 565–584. <https://doi.org/10.5194/acp-10-565-2010>.
- (207) Yu, J.; Sun, L.; Ma, C.; Qiao, Y.; Yao, H. Thermal Degradation of PVC: A Review. *Waste Manag.* **2016**, *48*, 300–314. <https://doi.org/10.1016/j.wasman.2015.11.041>.
- (208) Yu, H.; Qu, J.; Liu, Y.; Yun, H.; Li, X.; Zhou, C.; Jin, Y.; Zhang, C.; Dai, J.; Bi, X. Co-Pyrolysis of Biomass and Polyvinyl Chloride under Microwave Irradiation: Distribution of Chlorine. *Sci. Total Environ.* **2022**, *806*, 150903. <https://doi.org/10.1016/j.scitotenv.2021.150903>.

- (209) Chloride TNTplus Vial Test (1.0-1,000 mg/L Cl), 24 Tests | Hach Canada - Overview.  
<https://ca.hach.com/chloride-tntplus-vial-test-1-0-1-000-mg-l-cl-24-tests/product?id=54566921144> (accessed 2024-04-13).
- (210) Pierce, J. R.; Engelhart, G. J.; Hildebrandt, L.; Weitkamp, E. A.; Pathak, R. K.; Donahue, N. M.; Robinson, A. L.; Adams, P. J.; Pandis, S. N. Constraining Particle Evolution from Wall Losses, Coagulation, and Condensation-Evaporation in Smog-Chamber Experiments: Optimal Estimation Based on Size Distribution Measurements. *Aerosol Sci. Technol.* **2008**, *42* (12), 1001–1015. <https://doi.org/10.1080/02786820802389251>.
- (211) Kulkarni, P.; Baron, P. A.; Willeke, K. *Aerosol Measurement: Principles, Techniques, and Applications*; John Wiley & Sons, 2011.
- (212) Moosmüller, H.; Chakrabarty, R. K.; Arnott, W. P. Aerosol Light Absorption and Its Measurement: A Review. *J. Quant. Spectrosc. Radiat. Transf.* **2009**, *110* (11), 844–878. <https://doi.org/10.1016/j.jqsrt.2009.02.035>.
- (213) Liu, C.; Chung, C. E.; Yin, Y.; Schnaiter, M. The Absorption Ångström Exponent of Black Carbon: From Numerical Aspects. *Atmospheric Chem. Phys.* **2018**, *18* (9), 6259–6273. <https://doi.org/10.5194/acp-18-6259-2018>.
- (214) Zotter, P.; Herich, H.; Gysel, M.; El-Haddad, I.; Zhang, Y.; Močnik, G.; Hüglin, C.; Baltensperger, U.; Szidat, S.; Prévôt, A. S. H. Evaluation of the Absorption Ångström Exponents for Traffic and Wood Burning in the Aethalometer-Based Source Apportionment Using Radiocarbon Measurements of Ambient Aerosol. *Atmospheric Chem. Phys.* **2017**, *17* (6), 4229–4249. <https://doi.org/10.5194/acp-17-4229-2017>.
- (215) Cuesta-Mosquera, A.; Močnik, G.; Drinovec, L.; Müller, T.; Pfeifer, S.; Minguillón, M. C.; Briel, B.; Buckley, P.; Dudoitis, V.; Fernández-García, J.; Fernández-Amado, M.;

- Ferreira De Brito, J.; Riffault, V.; Flentje, H.; Heffernan, E.; Kalivitis, N.; Kalogridis, A.-C.; Keernik, H.; Marmureanu, L.; Luoma, K.; Marinoni, A.; Pikridas, M.; Schauer, G.; Serfozo, N.; Servomaa, H.; Titos, G.; Yus-Díez, J.; Zioła, N.; Wiedensohler, A. Intercomparison and Characterization of 23 Aethalometers under Laboratory and Ambient Air Conditions: Procedures and Unit-to-Unit Variabilities. *Atmospheric Meas. Tech.* **2021**, *14* (4), 3195–3216. <https://doi.org/10.5194/amt-14-3195-2021>.
- (216) Saturno, J.; Pöhlker, C.; Massabò, D.; Brito, J.; Carbone, S.; Cheng, Y.; Chi, X.; Ditas, F.; Hrabě de Angelis, I.; Morán-Zuloaga, D.; Pöhlker, M. L.; Rizzo, L. V.; Walter, D.; Wang, Q.; Artaxo, P.; Prati, P.; Andreae, M. O. Comparison of Different Aethalometer Correction Schemes and a Reference Multi-Wavelength Absorption Technique for Ambient Aerosol Data. *Atmospheric Meas. Tech.* **2017**, *10* (8), 2837–2850. <https://doi.org/10.5194/amt-10-2837-2017>.
- (217) Drinovec, L.; Močnik, G.; Zotter, P.; Prévôt, A. S. H.; Ruckstuhl, C.; Coz, E.; Rupakheti, M.; Sciare, J.; Müller, T.; Wiedensohler, A.; Hansen, A. D. A. The “Dual-Spot” Aethalometer: An Improved Measurement of Aerosol Black Carbon with Real-Time Loading Compensation. *Atmospheric Meas. Tech.* **2015**, *8* (5), 1965–1979. <https://doi.org/10.5194/amt-8-1965-2015>.
- (218) Li, C.; Windwer, E.; Fang, Z.; Nissenbaum, D.; Rudich, Y. Correcting Micro-Aethalometer Absorption Measurements for Brown Carbon Aerosol. *Sci. Total Environ.* **2021**, *777*, 146143. <https://doi.org/10.1016/j.scitotenv.2021.146143>.
- (219) Kim, S. Pyrolysis Kinetics of Waste PVC Pipe. *Waste Manag.* **2001**, *21* (7), 609–616. [https://doi.org/10.1016/S0956-053X\(00\)00127-6](https://doi.org/10.1016/S0956-053X(00)00127-6).

- (220) Liu, Y.; Zhou, C.; Li, F.; Liu, H.; Yang, J. Stocks and Flows of Polyvinyl Chloride (PVC) in China: 1980-2050. *Resour. Conserv. Recycl.* **2020**, *154*, 104584.  
<https://doi.org/10.1016/j.resconrec.2019.104584>.
- (221) Wiedinmyer, C.; Yokelson, R. J.; Gullett, B. K. Global Emissions of Trace Gases, Particulate Matter, and Hazardous Air Pollutants from Open Burning of Domestic Waste. *Environ. Sci. Technol.* **2014**, *48* (16), 9523–9530. <https://doi.org/10.1021/es502250z>.
- (222) Braun, D. Poly(Vinyl Chloride) on the Way from the 19th Century to the 21st Century. *J. Polym. Sci. Part Polym. Chem.* **2004**, *42* (3), 578–586. <https://doi.org/10.1002/pola.10906>.
- (223) Zhang, M.; Buekens, A.; Jiang, X.; Li, X. Dioxins and Polyvinylchloride in Combustion and Fires. *Waste Manag. Res.* **2015**, *33* (7), 630–643.  
<https://doi.org/10.1177/0734242X15590651>.
- (224) Chong, N. S.; Abdulramoni, S.; Patterson, D.; Brown, H. Releases of Fire-Derived Contaminants from Polymer Pipes Made of Polyvinyl Chloride. *Toxics* **2019**, *7* (4), 57.  
<https://doi.org/10.3390/toxics7040057>.
- (225) Koerner, G. R.; Koerner, R. M. 7.3 - Polymeric Geomembrane Components in Landfill Liners. In *Solid Waste Landfilling*; Cossu, R., Stegmann, R., Eds.; Elsevier, 2018; pp 313–341. <https://doi.org/10.1016/B978-0-12-407721-8.00017-6>.
- (226) Alsabri, A.; Al-Ghamdi, S. G. Carbon Footprint and Embodied Energy of PVC, PE, and PP Piping: Perspective on Environmental Performance. *Energy Rep.* **2020**, *6*, 364–370.  
<https://doi.org/10.1016/j.egy.2020.11.173>.
- (227) Khan, S. M.; Gull, N.; Khan, R. U.; Butt, M. T. Z. Polyvinylchloride (PVC): Structure and Properties Relationship. In: *Polyvinylchloride-based Blends: Preparation, Characterization and Applications*; P. M., V., Darie-Nita, R. N., Eds.; Springer

International Publishing: Cham., **2022**, 19–47. [https://doi.org/10.1007/978-3-030-78455-3\\_2](https://doi.org/10.1007/978-3-030-78455-3_2).

- (228) Zakharyan, E. M.; Petrukhnina, N. N.; Maksimov, A. L. Pathways of Chemical Recycling of Polyvinyl Chloride: Part 1. *Russ. J. Appl. Chem.* **2020**, *93* (9), 1271–1313. <https://doi.org/10.1134/S1070427220090013>.
- (229) Li, J.; Zhang, N.; Wang, P.; Choi, M.; Ying, Q.; Guo, S.; Lu, K.; Qiu, X.; Wang, S.; Hu, M.; Zhang, Y.; Hu, J. Impacts of Chlorine Chemistry and Anthropogenic Emissions on Secondary Pollutants in the Yangtze River Delta Region. *Environ. Pollut.* **2021**, *287*, 117624. <https://doi.org/10.1016/j.envpol.2021.117624>.
- (230) Gunthe, S. S.; Liu, P.; Panda, U.; Raj, S. S.; Sharma, A.; Darbyshire, E.; Reyes-Villegas, E.; Allan, J.; Chen, Y.; Wang, X.; Song, S.; Pöhlker, M. L.; Shi, L.; Wang, Y.; Kommula, S. M.; Liu, T.; Ravikrishna, R.; McFiggans, G.; Mickleby, L. J.; Martin, S. T.; Pöschl, U.; Andreae, M. O.; Coe, H. Enhanced Aerosol Particle Growth Sustained by High Continental Chlorine Emission in India. *Nat. Geosci.* **2021**, *14* (2), 77–84. <https://doi.org/10.1038/s41561-020-00677-x>.
- (231) Platt, U.; Stutz, J. Differential Absorption Spectroscopy. In *Differential Optical Absorption Spectroscopy: Principles and Applications*; Platt, U., Stutz, J., Eds.; Springer: Berlin, Heidelberg, 2008; pp 135–174. [https://doi.org/10.1007/978-3-540-75776-4\\_6](https://doi.org/10.1007/978-3-540-75776-4_6).
- (232) Zhou, J.; Liu, G.; Wang, S.; Zhang, H.; Xu, F. TG-FTIR and Py-GC/MS Study of the Pyrolysis Mechanism and Composition of Volatiles from Flash Pyrolysis of PVC. *J. Energy Inst.* **2020**, *93* (6), 2362–2370. <https://doi.org/10.1016/j.joei.2020.07.009>.
- (233) Luo, Z.; Zhang, L.; Li, G.; Du, W.; Chen, Y.; Cheng, H.; Tao, S.; Shen, G. Evaluating Co-Emissions into Indoor and Outdoor Air of EC, OC, and BC from in-Home Biomass

- Burning. *Atmospheric Res.* **2021**, *248*, 105247.  
<https://doi.org/10.1016/j.atmosres.2020.105247>.
- (234) Shemwell, B. E.; Levendis, Y. A. Particulates Generated from Combustion of Polymers (Plastics). *J. Air Waste Manag. Assoc.* **2000**, *50* (1), 94–102.  
<https://doi.org/10.1080/10473289.2000.10463994>.
- (235) Kim, J.-H.; Kim, S.-W.; Ogren, J. A.; Sheridan, P. J.; Yoon, S.-C.; Sharma, S.; Lin, N.-H. Multiple Scattering Correction Factor Estimation for Aethalometer Aerosol Absorption Coefficient Measurement. *Aerosol Sci. Technol.* **2019**, *53* (2), 160–171.  
<https://doi.org/10.1080/02786826.2018.1555368>.
- (236) Laskin, A.; Laskin, J.; Nizkorodov, S. A. Chemistry of Atmospheric Brown Carbon. *Chem. Rev.* **2015**, *115* (10), 4335–4382. <https://doi.org/10.1021/cr5006167>.
- (237) Maqsood, T.; Dai, J.; Zhang, Y.; Guang, M.; Li, B. Pyrolysis of Plastic Species: A Review of Resources and Products. *J. Anal. Appl. Pyrolysis* **2021**, *159*, 105295.  
<https://doi.org/10.1016/j.jaap.2021.105295>.
- (238) Yang, X.; Wang, T.; Xia, M.; Gao, X.; Li, Q.; Zhang, N.; Gao, Y.; Lee, S.; Wang, X.; Xue, L.; Yang, L.; Wang, W. Abundance and Origin of Fine Particulate Chloride in Continental China. *Sci. Total Environ.* **2018**, *624*, 1041–1051.  
<https://doi.org/10.1016/j.scitotenv.2017.12.205>.
- (239) Qi, Y.; Yuan, Y.-K.; Zhang, J.-W.; Du, Y.-S.; Fu, K.-C.; Cui, M.-J.; Du, S.-S. Contact Toxicity and Repellent Efficacy of *Kaempferia Rotunda* L. to Three Stored Product Insects and Synergistic Interactions between Two Major Compounds Benzyl Benzoate and Bornyl Acetate. *J. Essent. Oil Bear. Plants* **2023**, *26* (2), 343–355.  
<https://doi.org/10.1080/0972060X.2023.2185545>.

- (240) Parsons, M. T.; Sydoryk, I.; Lim, A.; McIntyre, T. J.; Tulip, J.; Jäger, W.; McDonald, K. Real-Time Monitoring of Benzene, Toluene, and p-Xylene in a Photoreaction Chamber with a Tunable Mid-Infrared Laser and Ultraviolet Differential Optical Absorption Spectroscopy. *Appl. Opt.* **2011**, *50* (4), A90-99. <https://doi.org/10.1364/AO.50.000A90>.
- (241) Schnitzler, E. G.; Dutt, A.; Charbonneau, A. M.; Olfert, J. S.; Jäger, W. Soot Aggregate Restructuring Due to Coatings of Secondary Organic Aerosol Derived from Aromatic Precursors. *Environ. Sci. Technol.* **2014**, *48* (24), 14309–14316. <https://doi.org/10.1021/es503699b>.
- (242) Gracia, A.; Hong, J.; Arismendi, R.; Zhou, M.; Li, W.; Lin, W. Conformational Landscapes of Symmetrically Fluorine-Substituted Benzoic Acids I: Microwave Spectroscopic and Theoretical Studies on 3,5-Difluorobenzoic Acid. *J. Mol. Spectrosc.* **2023**, *397*, 111839. <https://doi.org/10.1016/j.jms.2023.111839>.
- (243) Al-Jabiri, M. H.; Insausti, A.; Eraković, M.; Jäger, W.; Cvitaš, M. T. Double Proton Tunneling/Instanton Theory (Private Communication).
- (244) Janhäll, S.; Andreae, M. O.; Pöschl, U. Biomass Burning Aerosol Emissions from Vegetation Fires: Particle Number and Mass Emission Factors and Size Distributions. *Atmospheric Chem. Phys.* **2010**, *10* (3), 1427–1439. <https://doi.org/10.5194/acp-10-1427-2010>.

# Appendix A

## Supplementary Information for Chapter 3

Rotational Spectroscopic Studies of *para*-Nitrobenzoic acid, *para*-Aminobenzoic acid, *para*-Chlorobenzoic acid, and *para*-Hydroxybenzoic acid

### Contents:

1. **Assigned Rotational Transitions of the *p*-aminoBA Monomer**
  - a. **Table A.1.** List of Assigned Rotational Transitions of *p*-aminoB
2. **Assigned Rotational Transitions of the *p*-nitroBA Monomer**
  - a. **Table A.2.** List of Assigned Rotational Transitions of *p*-nitroBA
3. **Assigned Rotational Transitions of the *p*-chloroBA**
  - a. **Table A.3.** Assigned transitions of the *p*-<sup>35</sup>chloroBA monomer
  - b. **Table A.4.** Assigned transitions of the *p*-<sup>37</sup>chloroBA monomer
4. **Assigned Rotational Transition of the conformers of *p*-hydroxyBA**
  - a. **Table A.5.** Assigned transitions of the *p*-hydroxyBA-I monomer
  - b. **Table A.6.** Assigned transitions of the *p*-hydroxyBA-II monomer

**Table A.1.** Assigned transitions of the *cis-p*-aminoBA monomer.

J'	Ka'	Kc'	F'	-	J''	Ka''	Kc''	F''	$\nu^a$ / MHz	$\nu^b$ / MHz
2	1	2	1	-	1	1	1	1	2765.0546	0.0020
2	1	2	3	-	1	1	1	2	2766.3849	0.0032
2	1	2	2	-	1	1	1	1	2767.2036	0.0002
2	1	2	2	-	1	1	1	2	2767.7637	-0.0006
2	0	2	1	-	1	0	1	1	2896.3333	0.0005
2	0	2	3	-	1	0	1	2	2897.5292	0.0097
2	0	2	1	-	1	0	1	0	2898.1540	-0.0014
2	0	2	2	-	1	0	1	2	2898.3436	0.0004
2	1	1	1	-	1	1	0	0	3035.7329	0.0035
2	1	1	2	-	1	1	0	2	3036.7290	0.0001
2	1	1	3	-	1	1	0	2	3037.3303	0.0000
2	1	1	2	-	1	1	0	1	3038.0208	0.0013
2	1	1	1	-	1	1	0	1	3038.9586	0.0024
1	1	0	1	-	1	0	1	1	3174.3559	-0.0019
1	1	0	1	-	1	0	1	2	3175.0861	-0.0008
1	1	0	2	-	1	0	1	1	3175.6498	0.0014
1	1	0	2	-	1	0	1	2	3176.3768	-0.0006
1	1	0	0	-	1	0	1	1	3177.5844	-0.0002
2	1	1	2	-	2	0	2	2	3314.7698	0.0067
2	1	1	3	-	2	0	2	2	3315.3623	-0.0022
2	1	1	2	-	2	0	2	3	3315.5954	0.0084
2	1	1	3	-	2	0	2	3	3316.1901	0.0017
2	1	1	1	-	2	0	2	1	3316.9839	0.0028
3	1	2	3	-	3	0	3	3	3532.8424	0.0060
3	1	2	3	-	3	0	3	4	3533.7523	-0.0044
3	1	2	4	-	3	0	3	4	3534.1689	0.0051
3	1	2	2	-	3	0	3	2	3534.6316	0.0027
7	1	6	7	-	7	1	7	7	3771.0603	-0.0085
7	1	6	6	-	7	1	7	6	3773.5368	0.0107
4	1	3	4	-	4	0	4	4	3838.4877	0.0014
4	1	3	4	-	4	0	4	5	3839.5172	0.0008
4	1	3	5	-	4	0	4	5	3839.8286	0.0013
4	1	3	3	-	4	0	4	3	3840.1737	0.0012
3	1	3	2	-	2	1	2	2	4145.1077	0.0004
3	1	3	4	-	2	1	2	3	4147.0663	-0.0011
3	1	3	3	-	2	1	2	3	4148.7160	-0.0014
5	1	4	5	-	5	0	5	5	4243.7226	0.0016
5	1	4	6	-	5	0	5	6	4245.1191	-0.0005
5	1	4	4	-	5	0	5	4	4245.4052	0.0004
3	0	3	2	-	2	0	2	2	4334.1513	-0.0023
3	0	3	4	-	2	0	2	3	4335.3125	0.0130

3	0	3	3	-	2	0	2	3	4336.2177	-0.0020
3	2	2	2	-	2	2	1	1	4352.3969	-0.0007
3	2	2	4	-	2	2	1	3	4352.8316	0.0000
3	2	2	3	-	2	2	1	2	4353.6120	-0.0008
3	2	1	2	-	2	2	0	1	4370.0939	0.0045
3	2	1	4	-	2	2	0	3	4370.5057	-0.0024
3	2	1	3	-	2	2	0	2	4371.2217	-0.0004
1	1	1	0	-	0	0	0	1	4490.6970	-0.0016
1	1	1	2	-	0	0	0	1	4491.5404	-0.0003
1	1	1	1	-	0	0	0	1	4492.0992	-0.0025
3	1	2	3	-	2	1	1	3	4552.8678	0.0000
3	1	2	2	-	2	1	1	1	4553.0808	-0.0019
3	1	2	4	-	2	1	1	3	4553.2731	-0.0018
3	1	2	3	-	2	1	1	2	4553.4673	-0.0019
3	1	2	2	-	2	1	1	2	4554.0128	-0.0067
6	1	5	6	-	6	0	6	6	4761.7732	0.0036
6	1	5	7	-	6	0	6	7	4763.2491	0.0016
6	1	5	5	-	6	0	6	5	4763.5004	0.0032
7	1	6	7	-	7	0	7	7	5405.3341	-0.0025
7	1	6	8	-	7	0	7	8	5406.8985	-0.0030
7	1	6	6	-	7	0	7	6	5407.1268	-0.0006
4	1	4	3	-	3	1	3	3	5522.4335	-0.0013
4	1	4	5	-	3	1	3	4	5524.5436	-0.0018
4	1	4	3	-	3	1	3	2	5524.6724	0.0100
4	1	4	4	-	3	1	3	4	5526.3329	-0.0033
4	0	4	3	-	3	0	3	3	5758.8311	-0.0029
4	0	4	4	-	3	0	3	3	5760.1318	0.0028
4	0	4	4	-	3	0	3	4	5761.0461	-0.0031
4	2	3	4	-	3	2	2	3	5800.8115	-0.0055
2	1	2	1	-	1	0	1	1	5805.5428	-0.0020
2	1	2	3	-	1	0	1	2	5807.0423	0.0002
2	1	2	1	-	1	0	1	0	5807.3676	0.0001
2	1	2	2	-	1	0	1	1	5807.6935	-0.0022
2	1	2	2	-	1	0	1	2	5808.4258	0.0009
4	3	2	3	-	3	3	1	2	5812.1424	0.0012
4	3	2	5	-	3	3	1	4	5812.4151	-0.0017
4	3	1	3	-	3	3	0	2	5812.6857	0.0017
4	3	2	4	-	3	3	1	3	5813.1206	0.0017
4	3	1	4	-	3	3	0	3	5813.6560	-0.0029
4	1	3	4	-	3	1	2	4	6065.3671	-0.0046
4	1	3	3	-	3	1	2	3	6066.1663	-0.0039

<sup>a</sup> Experimental transition frequency.

<sup>b</sup> Experimental transition frequency – Theoretical transition frequency.

**Table A.2.** Assigned transitions of the *cis-p*-nitroBA monomer.

J'	Ka'	Kc'	F'	-	J'	Ka''	Kc''	F''	$\nu^a$ / MHz	$\nu^b$ / MHz
3	1	3	3	-	2	1	2	3	2551.4090	0.0034
3	1	3	2	-	2	1	2	2	2552.1310	-0.0016
1	1	0	1	-	1	0	1	0	2577.5650	0.0030
1	1	0	2	-	1	0	1	2	2577.8190	-0.0002
1	1	0	1	-	1	0	1	1	2578.3800	-0.0015
3	0	3	4	-	2	0	2	3	2644.3560	0.0023
3	0	3	2	-	2	0	2	2	2644.8400	0.0041
3	2	2	3	-	2	2	1	2	2648.9710	0.0044
3	2	2	4	-	2	2	1	3	2649.3210	0.0033
3	2	2	2	-	2	2	1	1	2649.5140	0.0011
3	2	1	3	-	2	2	0	2	2653.8730	0.0045
3	2	1	4	-	2	2	0	3	2654.2210	0.0043
3	2	1	2	-	2	2	0	1	2654.4140	0.0028
3	1	2	4	-	2	1	1	3	2745.2400	-0.008
4	1	3	5	-	4	0	4	5	2883.2370	0.0105
4	1	3	4	-	4	0	4	4	2883.3730	0.0031
9	1	8	10	-	9	1	9	10	2889.2380	0.004
9	1	8	9	-	9	1	9	9	2889.3910	-0.0091
5	1	4	5	-	5	0	5	5	3063.4870	0.0063
6	0	6	7	-	5	1	5	6	3159.8220	0.0055
6	1	5	7	-	6	0	6	7	3289.0540	-0.0059
6	1	5	6	-	6	0	6	6	3289.1890	0.0042
1	1	1	0	-	0	0	0	1	3396.3250	-0.0091
4	1	4	4	-	3	1	3	4	3400.5290	0.0047
4	1	4	3	-	3	1	3	3	3401.3760	-0.0015
4	0	4	4	-	3	0	3	4	3519.7220	0.0043
4	0	4	5	-	3	0	3	4	3520.0970	-0.0019
4	0	4	3	-	3	0	3	3	3520.5710	0.0051
4	2	3	4	-	3	2	2	3	3531.2610	0.0044
4	2	3	5	-	3	2	2	4	3531.4000	-0.0061
4	2	2	4	-	3	2	1	3	3543.4930	0.0036
4	2	2	5	-	3	2	1	4	3543.6320	-0.0028
7	1	6	8	-	7	0	7	8	3565.0280	-0.0052
7	1	6	7	-	7	0	7	7	3565.1620	0.005
4	1	3	4	-	3	1	2	4	3658.6120	0.0044
4	1	3	3	-	3	1	2	3	3659.1080	0.0061
8	1	7	9	-	8	0	8	9	3896.0970	-0.0042
8	1	7	8	-	8	0	8	8	3896.2340	0.0077
7	0	7	8	-	6	1	6	7	4178.5760	-0.0025
11	1	10	12	-	11	1	11	12	4214.0370	-0.0047
11	1	10	11	-	11	1	11	11	4214.2100	0.0034

2	1	2	1	-	1	0	1	1	4215.5340	-0.0006
5	1	5	5	-	4	1	4	5	4248.5220	0.0054
5	1	5	4	-	4	1	4	4	4249.4270	0.0008
9	1	8	10	-	9	0	9	10	4286.8210	-0.0034
9	1	8	9	-	9	0	9	9	4286.960	0.008
5	0	5	5	-	4	0	4	5	4390.6380	0.0036
5	0	5	6	-	4	0	4	5	4391.0230	-0.0033
5	0	5	4	-	4	0	4	4	4391.4920	0.0046
5	2	4	5	-	4	2	3	5	4412.4630	-0.0083
5	2	4	6	-	4	2	3	5	4412.6960	-0.0034
5	4	1	5	-	4	4	0	4	4417.9080	0.0017
5	3	3	5	-	4	3	2	4	4419.3430	0.0037
5	2	3	6	-	4	2	2	5	4437.0750	-0.0021
5	1	4	5	-	4	1	3	5	4570.8890	0.0004
5	1	4	6	-	4	1	3	5	4571.1460	-0.0043
5	1	4	4	-	4	1	3	4	4571.4460	0.0045
10	1	9	11	-	10	0	10	11	4741.0000	0.0004
10	1	9	10	-	10	0	10	10	4741.1380	0.0076
2	2	1	1	-	3	1	2	2	4794.6120	-0.0049
2	2	1	3	-	3	1	2	4	4794.8730	-0.0074
2	2	1	2	-	3	1	2	3	4795.4230	-0.0038
3	1	3	3	-	2	0	2	3	5001.5170	0.0022
3	1	3	4	-	2	0	2	3	5001.8660	-0.0011
3	1	3	2	-	2	0	2	2	5002.3460	0.0025
6	1	6	6	-	5	1	5	6	5095.1360	0.0045
6	1	6	7	-	5	1	5	6	5095.5640	-0.0092
6	1	6	5	-	5	1	5	5	5096.0720	-0.0004
8	0	8	9	-	7	1	7	8	5203.1670	-0.007
6	0	6	6	-	5	0	5	6	5255.6690	0.0026
6	0	6	7	-	5	0	5	6	5256.0630	-0.0055
11	1	10	11	-	11	0	11	11	5261.3000	0.0060
6	1	5	7	-	5	1	4	6	5481.7750	-0.0029
12	1	11	13	-	12	0	12	13	5848.1430	-0.0093
12	1	11	12	-	12	0	12	12	5848.2870	-0.0022
7	1	7	8	-	6	1	6	7	5940.6070	-0.0078

<sup>a</sup> Experimental transition frequency.

<sup>b</sup> Experimental transition frequency – Theoretical transition frequency.

**Table A.3.** Assigned transitions of the *cis-p*-<sup>35</sup>chloroBA monomer.

J'	Ka'	Kc'	F'	-	J''	Ka''	Kc''	F''	$\nu^a$ / MHz	$\nu^b$ / MHz
5	2	4	4	-	6	1	5	5	3062.3992	0.0016
5	2	4	7	-	6	1	5	8	3063.4517	-0.0002
5	2	4	5	-	6	1	5	6	3069.0329	-0.0025
5	2	4	6	-	6	1	5	7	3070.1487	-0.0033
1	1	0	1	-	1	0	1	1	3349.5258	0.0035
6	0	6	6	-	5	1	5	5	3350.9805	0.0071
6	0	6	7	-	5	1	5	6	3351.0846	-0.0007
6	0	6	5	-	5	1	5	4	3353.4065	-0.0066
6	0	6	8	-	5	1	5	7	3353.5533	0.0052
1	1	0	2	-	1	0	1	1	3364.1034	0.0039
1	1	0	3	-	1	0	1	3	3370.3789	0.0025
1	1	0	2	-	1	0	1	3	3378.4489	0.0012
1	1	0	1	-	1	0	1	2	3381.6991	0.0045
1	1	0	3	-	1	0	1	2	3388.1979	-0.0026
1	1	0	2	-	1	0	1	2	3396.2724	0.0005
2	1	1	2	-	2	0	2	1	3428.3789	0.0014
2	1	1	3	-	2	0	2	4	3434.1667	-0.0009
2	1	1	1	-	2	0	2	1	3438.2188	0.0042
2	1	1	3	-	2	0	2	2	3439.1167	-0.0055
2	1	1	4	-	2	0	2	4	3443.8654	0.0032
2	1	1	2	-	2	0	2	2	3446.117	0.001
2	1	1	3	-	2	0	2	3	3451.993	0.0033
2	1	1	1	-	2	0	2	2	3455.9565	0.0034
2	1	1	2	-	2	0	2	3	3458.9864	0.003
2	1	1	4	-	2	0	2	3	3461.6886	0.0044
3	1	2	3	-	3	0	3	2	3536.9929	0.0017
3	1	2	4	-	3	0	3	5	3538.6915	0.002
3	1	2	4	-	3	0	3	3	3548.1008	0.0019
3	1	2	2	-	3	0	3	2	3551.2425	0.0008
3	1	2	5	-	3	0	3	5	3552.8802	0.0009
3	1	2	3	-	3	0	3	3	3554.7659	0.0015
3	1	2	4	-	3	0	3	4	3556.4912	0.0026
3	1	2	3	-	3	0	3	4	3563.1608	0.0067
3	1	2	2	-	3	0	3	3	3569.0155	0.0007
3	1	2	5	-	3	0	3	4	3570.6799	0.0016
4	1	3	4	-	4	0	4	3	3684.4343	-0.0007
4	1	3	5	-	4	0	4	6	3685.0674	-0.0032
4	1	3	5	-	4	0	4	4	3696.5446	-0.0002
4	1	3	3	-	4	0	4	3	3700.4455	-0.0015
4	1	3	6	-	4	0	4	6	3701.0505	-0.0023
4	1	3	4	-	4	0	4	4	3702.1838	-0.0021

4	1	3	5	-	4	0	4	5	3702.8311	-0.0019
4	1	3	4	-	4	0	4	5	3708.4711	-0.0031
4	1	3	3	-	4	0	4	4	3718.1963	-0.0016
4	1	3	6	-	4	0	4	5	3718.8201	0.0048
5	1	4	5	-	5	0	5	4	3874.7511	0.0033
5	1	4	6	-	5	0	5	7	3874.9913	-0.0028
5	1	4	6	-	5	0	5	5	3887.6611	-0.004
5	1	4	4	-	5	0	5	4	3891.6342	-0.0006
5	1	4	7	-	5	0	5	7	3891.8645	0.0002
5	1	4	5	-	5	0	5	5	3892.4559	0.0001
5	1	4	6	-	5	0	5	6	3892.7092	0.0007
5	1	4	5	-	5	0	5	6	3897.4994	0.0003
5	1	4	4	-	5	0	5	5	3909.3394	-0.0034
5	1	4	7	-	5	0	5	6	3909.5815	0.0029
6	1	5	7	-	6	0	6	6	4125.3288	0.0066
6	1	5	8	-	6	0	6	8	4129.2457	-0.0007
6	1	5	6	-	6	0	6	7	4133.6675	-0.0004
6	1	5	5	-	6	0	6	6	4146.8343	-0.0011
4	2	3	3	-	5	1	4	4	4302.1065	-0.0044
4	2	3	6	-	5	1	4	7	4304.3081	-0.0050
4	2	3	4	-	5	1	4	5	4311.7854	-0.0053
4	2	3	5	-	5	1	4	6	4314.0949	-0.0048
1	1	1	1	-	0	0	0	2	4336.3506	0.0029
1	1	1	3	-	0	0	0	2	4344.1772	0.0032
1	1	1	2	-	0	0	0	2	4353.938	0.0034
7	1	6	8	-	7	0	7	7	4413.9254	-0.0002
7	1	6	6	-	7	0	7	6	4417.4884	0.0041
7	1	6	9	-	7	0	7	9	4417.5972	0.0055
7	1	6	7	-	7	0	7	8	4421.135	0.0012
7	0	7	7	-	6	1	6	6	4548.2469	-0.0035
7	0	7	8	-	6	1	6	7	4548.4096	0.0000
7	0	7	9	-	6	1	6	8	4550.2954	-0.0085
10	3	8	9	-	11	2	9	10	4705.8955	0.0059
10	3	8	12	-	11	2	9	13	4706.136	0.0075
10	3	8	10	-	11	2	9	11	4709.0787	0.0022
10	3	8	11	-	11	2	9	12	4709.3394	0.0072
2	1	2	2	-	1	0	1	1	5298.8321	-0.0013
2	1	2	1	-	1	0	1	1	5306.9853	0.0013
2	1	2	3	-	1	0	1	3	5307.3587	-0.0027
2	1	2	3	-	1	0	1	2	5325.1883	0.0026
2	1	2	2	-	1	0	1	2	5331.007	0.0013
2	1	2	1	-	1	0	1	2	5339.1546	-0.0016
3	2	2	2	-	4	1	3	3	5506.6012	0.0017
3	2	2	5	-	4	1	3	6	5512.1127	-0.0028
3	2	2	3	-	4	1	3	4	5522.4756	-0.0089

3	2	2	4	-	4	1	3	5	5528.1768	-0.0074
10	1	9	12	-	10	0	10	12	5635.0254	0.0046
8	0	8	8	-	7	1	7	7	5756.3709	-0.0011
8	0	8	9	-	7	1	7	8	5756.4841	-0.0119
8	0	8	7	-	7	1	7	6	5757.8687	-0.0064
8	0	8	10	-	7	1	7	9	5758.0058	-0.0041
9	3	7	8	-	10	2	8	9	5908.1630	-0.0040
9	3	7	11	-	10	2	8	12	5908.5045	-0.0022
9	3	7	9	-	10	2	8	10	5911.9340	-0.0062
9	3	7	10	-	10	2	8	11	5912.3018	-0.0008
3	1	3	4	-	2	0	2	4	6239.3816	0.0051
3	1	3	2	-	2	0	2	1	6245.0626	0.0024
3	1	3	3	-	2	0	2	2	6250.2282	0.00300
3	1	3	5	-	2	0	2	4	6251.8890	0.0047
3	1	3	4	-	2	0	2	3	6257.2019	0.0034
3	1	3	2	-	2	0	2	2	6262.8060	0.0072
3	1	3	3	-	2	0	2	3	6263.0933	0.0007

<sup>a</sup> Experimental transition frequency.

<sup>b</sup> Experimental transition frequency – Theoretical transition frequency.

**Table A.4.** Assigned transitions of the *cis-p*-<sup>37</sup>chlorBA monomer.

J'	Ka'	Kc'	F'	-	J''	Ka''	Kc''	F''	$\nu^a$ / MHz	$\nu^b$ / MHz
5	2	4	4	-	6	1	5	5	3271.7494	0.0051
5	2	4	7	-	6	1	5	8	3272.5778	-0.0029
5	2	4	5	-	6	1	5	6	3276.9815	-0.0013
5	2	4	6	-	6	1	5	7	3277.8564	-0.0026
1	1	0	2	-	1	0	1	1	3376.7963	0.0057
1	1	0	1	-	1	0	1	2	3390.6565	-0.0007
1	1	0	3	-	1	0	1	2	3395.7824	0.0005
1	1	0	2	-	1	0	1	2	3402.1508	0.0018
2	1	1	1	-	2	0	2	1	3446.9154	0.0009
2	1	1	3	-	2	0	2	2	3447.6629	0.0018
2	1	1	4	-	2	0	2	4	3451.3896	0.0038
2	1	1	2	-	2	0	2	2	3453.1737	0.0026
2	1	1	3	-	2	0	2	3	3457.7859	-0.0003
2	1	1	3	-	2	0	2	3	3457.7861	-0.0001
2	1	1	1	-	2	0	2	2	3460.9115	-0.0029
2	1	1	2	-	2	0	2	3	3463.2987	0.0024
3	1	2	4	-	3	0	3	5	3543.9722	-0.0071
3	1	2	2	-	3	0	3	2	3553.8744	0.0014
3	1	2	5	-	3	0	3	5	3555.1741	0.0037

3	1	2	3	-	3	0	3	3	3556.6622	0.0002
3	1	2	4	-	3	0	3	4	3558.0157	0.0012
3	1	2	2	-	3	0	3	3	3567.8876	-0.0039
3	1	2	5	-	3	0	3	4	3569.2116	0.0060
4	1	3	4	-	4	0	4	3	3683.1238	-0.0032
4	1	3	5	-	4	0	4	6	3683.628	0.0008
4	1	3	5	-	4	0	4	4	3692.685	0.0001
4	1	3	3	-	4	0	4	3	3695.748	0.0000
4	1	3	6	-	4	0	4	6	3696.2291	0.0000
4	1	3	4	-	4	0	4	4	3697.126	-0.0012
4	1	3	5	-	4	0	4	5	3697.6351	0.0005
4	1	3	3	-	4	0	4	4	3709.7388	-0.0093
4	1	3	6	-	4	0	4	5	3710.2349	-0.0016
5	1	4	4	-	5	0	5	4	3877.5118	0.0018
5	1	4	7	-	5	0	5	7	3877.6941	0.0007
5	1	4	6	-	5	0	5	6	3878.3635	0.0000
5	1	4	5	-	5	0	5	6	3882.1406	0.0048
1	1	1	1	-	0	0	0	2	4328.1242	-0.0099
1	1	1	3	-	0	0	0	2	4334.3049	0.0036
1	1	1	3	-	0	0	0	2	4334.3055	0.0042
1	1	1	2	-	0	0	0	2	4341.9983	0.0023
7	0	7	9	-	6	1	6	8	4351.0360	-0.0086
4	2	3	3	-	5	1	4	4	4479.5857	0.0043
4	2	3	6	-	5	1	4	7	4481.3261	0.0000
4	2	3	4	-	5	1	4	5	4487.2200	-0.0019
9	1	8	11	-	9	0	9	11	5084.9399	0.0015
2	1	2	2	-	1	0	1	1	5271.7881	-0.0008
2	1	2	1	-	1	0	1	1	5278.2078	0.0013
2	1	2	3	-	1	0	1	3	5278.5108	0.0026
2	1	2	4	-	1	0	1	3	5284.8354	0.0016
2	1	2	3	-	1	0	1	2	5292.5681	0.0032
2	1	2	2	-	1	0	1	2	5297.1465	-0.0007
3	2	2	5	-	4	1	3	6	5658.5016	-0.0084
3	1	3	2	-	2	0	2	1	6196.8886	0.0010
3	1	3	3	-	2	0	2	2	6200.9798	0.0021
3	1	3	5	-	2	0	2	4	6202.2805	0.0039
3	1	3	4	-	2	0	2	3	6206.4607	-0.0009
4	1	4	3	-	3	0	3	2	7085.4413	-0.0012
4	1	4	5	-	3	0	3	4	7090.7741	-0.0036

<sup>a</sup> Experimental transition frequency.

<sup>b</sup> Experimental transition frequency – Theoretical transition frequency.

**Table A.5.** Assigned transitions of the *cis-p*-hydroxyBA-I monomer.

J'	Ka'	Kc'	-	J''	Ka''	Kc''	$\nu^a$ / MHz	$\nu^b$ / MHz
2	1	2	-	1	1	1	2762.3180	0.0028
3	1	3	-	2	1	2	4140.7980	0.0005
3	1	2	-	2	1	1	4544.6020	0.0009
2	0	2	-	1	0	1	2892.5980	0.0009
2	1	1	-	1	1	0	3031.5780	0.0018
3	0	3	-	2	0	2	4328.0580	0.0038
3	2	2	-	2	2	1	4345.4200	0.0015
3	2	1	-	2	2	0	4362.7900	0.0071
4	1	4	-	3	1	3	5516.1910	0.0001
4	0	4	-	3	0	3	5750.6800	0.0037
4	2	3	-	3	2	2	5790.5070	-0.0012
4	3	1	-	3	3	0	5802.8560	-0.0017
4	2	2	-	3	2	1	5833.7140	-0.0078
4	1	3	-	3	1	2	6054.1850	-0.0011
5	1	5	-	4	1	4	6887.6630	-0.0009
5	0	5	-	4	0	4	7156.7300	-0.0032
7	1	6	-	7	1	7	3751.3320	0.0018
8	1	7	-	8	1	8	4806.5710	-0.0032
6	1	5	-	6	1	6	2819.8910	0.0031

<sup>a</sup> Experimental transition frequency.<sup>b</sup> Experimental transition frequency – Theoretical transition frequency.**Table A.6.** Assigned transitions of the *cis-p*-hydroxyBA-II monomer.

J'	Ka'	Kc'	-	J''	Ka''	Kc''	$\nu^a$ / MHz	$\nu^b$ / MHz
7	1	6	-	6	2	5	2547.3480	-0.0092
2	1	2	-	1	1	1	2762.1080	0.0013
2	0	2	-	1	0	1	2892.3690	0.0038
3	2	2	-	4	1	3	2921.8170	-0.0046
4	0	4	-	3	1	3	3009.5060	0.0021
2	1	1	-	1	1	0	3031.3190	0.0028
1	1	0	-	1	0	1	3192.8220	0.0044
2	1	1	-	2	0	2	3331.7720	0.0035
7	3	5	-	8	2	6	3378.2340	-0.0029
3	1	2	-	3	0	3	3548.2740	0.0053
7	1	6	-	7	1	7	3750.6290	0.0017
4	1	3	-	4	0	4	3851.7120	0.0038

3	1	3	-	2	1	2	4140.4880	0.0019
5	1	4	-	5	0	5	4253.8540	0.0032
3	0	3	-	2	0	2	4327.7140	0.0015
3	2	2	-	2	2	1	4345.0700	0.0029
3	2	1	-	2	2	0	4362.4240	0.0022
8	1	7	-	7	2	6	4469.6640	-0.0087
1	1	1	-	0	0	0	4506.5710	0.0025
3	1	2	-	2	1	1	4544.2160	0.0033
2	2	1	-	3	1	2	4630.4200	-0.0057
5	0	5	-	4	1	4	4649.9210	0.0011
6	1	5	-	6	0	6	4767.7460	0.0076
8	1	7	-	8	1	8	4805.6790	-0.0066
6	3	4	-	7	2	5	5074.6830	-0.0033
7	1	6	-	7	0	7	5405.9730	0.0023
2	2	0	-	3	1	3	5442.3090	-0.0037
4	1	4	-	3	1	3	5515.7770	-0.0014
4	0	4	-	3	0	3	5750.2320	0.0002
4	2	3	-	3	2	2	5790.0420	0.0004
4	3	2	-	3	3	1	5801.8550	-0.0028
2	1	2	-	1	0	1	5820.3210	0.0015
4	2	2	-	3	2	1	5833.2320	0.0008
4	1	3	-	3	1	2	6053.6730	0.0018
8	1	7	-	8	0	8	6178.5000	0.0013
6	0	6	-	5	1	5	6305.5510	-0.0028

<sup>a</sup> Experimental transition frequency.

<sup>b</sup> Experimental transition frequency – Theoretical transition frequency.

# Appendix B

## Supplementary Information for Chapter 4

Conformers of Vanillic acid and Its Monohydrate: A Rotational Spectroscopic and Theoretical Study

### Contents:

1. **Assigned Rotational Transitions of the VA Monomer and Monohydrate**
  - a. **Table B.1.** List of Assigned Rotational Transitions of VA-I monomer
  - b. **Table B.2.** List of Assigned Rotational Transitions of VA-II monomer
  - c. **Table B.3.** List of Assigned Rotational Transitions of VA-I-W monohydrate
  - d. **Table B.4.** List of Assigned Rotational Transitions of VA-II-W monohydrate

**Table B.1.** List of the assigned rotational transitions of the VA-I monomer.

J'	Ka'	Kc'	-	J''	Ka''	Kc''	$\nu^a$ / MHz	$\nu^b$ / MHz
2	0	2	-	1	0	1	2186.582	0.008
4	1	3	-	4	0	4	2231.231	0.001
2	1	1	-	1	1	0	2396.814	-0.004
3	0	3	-	2	1	2	2443.336	0.005
4	2	2	-	4	1	3	2565.160	-0.001
5	2	3	-	5	1	4	2579.051	0.002
3	2	1	-	3	1	2	2673.298	0.002
6	2	4	-	6	1	5	2765.778	0.003
2	2	0	-	2	1	1	2838.009	-0.005
2	1	2	-	1	0	1	2963.772	-0.003
5	1	4	-	5	0	5	2964.886	-0.004
3	1	3	-	2	1	2	3024.463	-0.001
7	2	5	-	7	1	6	3161.466	0.000
3	0	3	-	2	0	2	3220.532	0.000
3	2	2	-	2	2	1	3317.156	0.001
3	2	1	-	2	2	0	3413.775	-0.004
3	1	2	-	2	1	1	3578.491	-0.007
4	0	4	-	3	1	3	3616.060	0.001
5	1	4	-	4	2	3	3642.164	0.002
3	2	2	-	3	1	3	3661.985	0.003
8	2	6	-	8	1	7	3784.998	-0.002
3	1	3	-	2	0	2	3801.653	-0.012
6	1	5	-	6	0	6	3865.968	-0.001
9	3	6	-	9	2	7	3893.549	-0.003
8	3	5	-	8	2	6	3907.071	-0.002
4	1	4	-	3	1	3	4008.086	0.002
4	2	3	-	4	1	4	4057.343	-0.002
7	3	4	-	7	2	5	4089.885	-0.003
4	0	4	-	3	0	3	4197.193	0.001
6	3	3	-	6	2	4	4368.335	0.004
4	2	3	-	3	2	2	4403.439	-0.008
4	3	2	-	3	3	1	4466.900	0.001
4	3	1	-	3	3	0	4479.388	-0.001
5	2	4	-	5	1	5	4554.763	0.000
4	1	4	-	3	0	3	4589.212	-0.006
4	2	2	-	3	2	1	4628.989	0.010
5	3	2	-	5	2	3	4660.301	-0.002
5	0	5	-	4	1	4	4734.622	0.004

4	1	3	-	3	1	2	4737.115	0.001
7	1	6	-	7	0	7	4876.822	0.001
4	3	1	-	4	2	2	4897.682	0.003
5	1	5	-	4	1	4	4976.003	0.001
3	3	0	-	3	2	1	5047.271	0.002
6	1	5	-	5	2	4	5102.367	0.002
5	0	5	-	4	0	4	5126.642	-0.001
6	2	5	-	6	1	6	5149.059	0.001
3	3	1	-	3	2	2	5166.649	-0.001
2	2	1	-	1	1	0	5209.982	0.014
4	3	2	-	4	2	3	5230.101	-0.001
5	3	3	-	5	2	4	5350.905	-0.002
5	1	5	-	4	0	4	5368.027	0.000
2	2	0	-	1	1	1	5420.210	-0.002
5	2	4	-	4	2	3	5473.421	0.001
6	3	4	-	6	2	5	5547.416	0.004
5	4	2	-	4	4	1	5583.753	0.002
5	4	1	-	4	4	0	5584.925	0.000
5	3	3	-	4	3	2	5594.228	0.002
6	0	6	-	5	1	5	5791.144	-0.016
7	3	5	-	7	2	6	5834.386	-0.003
5	1	4	-	4	1	3	5860.303	0.000
5	2	3	-	4	2	2	5874.191	0.000
6	1	6	-	5	1	5	5929.510	0.001
6	0	6	-	5	0	5	6032.549	0.004
3	2	2	-	2	1	1	6130.306	0.001
6	1	6	-	5	0	5	6170.897	0.004

<sup>a</sup> Experimental transitions frequency.

<sup>b</sup> Experimental transition frequency – theoretical transition frequency

**Table B.2.** List of the assigned transitions of the VA-II monomer.

J'	Ka'	Kc'	-	J''	Ka''	Kc''	$\nu^a$ / MHz	$\nu^b$ / MHz
1	1	1	-	0	0	0	2027.874	-0.003
2	1	2	-	1	1	1	2037.109	-0.008
2	0	2	-	1	0	1	2200.382	0.001
4	1	3	-	4	0	4	2249.344	-0.001
4	1	3	-	3	2	2	2296.613	0.004
3	0	3	-	2	1	2	2486.215	0.003
4	2	2	-	4	1	3	2505.864	0.003
5	2	3	-	5	1	4	2536.557	0.001
3	2	1	-	3	1	2	2606.077	0.006

6	2	4	-	5	3	3	2719.667	0.013
6	2	4	-	6	1	5	2749.568	0.005
2	2	0	-	2	1	1	2769.757	0.006
2	1	2	-	1	0	1	2951.499	0.003
5	1	4	-	5	0	5	3005.624	-0.001
3	1	3	-	2	1	2	3040.061	-0.001
7	2	5	-	7	1	6	3180.741	-0.001
3	0	3	-	2	0	2	3237.330	0.003
2	2	1	-	2	1	2	3312.771	-0.003
3	2	2	-	2	2	1	3340.496	0.002
3	2	1	-	2	2	0	3443.654	-0.007
3	1	2	-	2	1	1	3607.344	0.003
3	2	2	-	3	1	3	3613.212	0.006
4	0	4	-	3	1	3	3660.467	-0.003
5	1	4	-	4	2	3	3763.491	0.001
3	1	3	-	2	0	2	3791.179	0.002
8	3	5	-	8	2	6	3807.052	-0.005
9	3	6	-	9	2	7	3834.064	-0.002
8	2	6	-	8	1	7	3846.028	-0.005
6	1	5	-	6	0	6	3927.675	-0.003
7	3	4	-	7	2	5	3965.381	0.003
4	2	3	-	4	1	4	4019.050	0.006
4	1	4	-	3	1	3	4027.351	0.000
10	3	7	-	10	2	8	4097.775	0.000
4	0	4	-	3	0	3	4214.320	-0.001
6	3	3	-	6	2	4	4235.187	-0.002
7	2	5	-	6	3	4	4361.039	0.002
4	2	3	-	3	2	2	4433.182	-0.007
4	3	2	-	3	3	1	4500.879	0.007
4	3	1	-	3	3	0	4514.844	0.001
5	2	4	-	5	1	5	4529.286	0.001
5	3	2	-	5	2	3	4530.590	0.003
4	1	4	-	3	0	3	4581.199	-0.002
4	2	2	-	3	2	1	4672.687	0.000
9	2	7	-	9	1	8	4727.789	0.003
4	1	3	-	3	1	2	4772.898	0.001
5	0	5	-	4	1	4	4776.914	0.004
3	3	0	-	3	2	1	4934.784	0.007
7	1	6	-	7	0	7	4952.472	-0.001
5	1	5	-	4	1	4	4998.207	0.005
3	3	1	-	3	2	2	5062.197	-0.004
4	3	2	-	4	2	3	5129.879	-0.004
6	2	5	-	6	1	6	5137.918	-0.002

5	0	5	-	4	0	4	5143.786	-0.004
2	2	1	-	1	1	0	5160.010	-0.002
6	1	5	-	5	2	4	5228.436	0.000
5	3	3	-	5	2	4	5258.346	0.001
5	1	5	-	4	0	4	5365.082	-0.001
2	2	0	-	1	1	1	5376.511	0.004
6	3	4	-	6	2	5	5466.533	-0.003
5	2	4	-	4	2	3	5508.440	-0.003
10	4	6	-	10	3	7	5526.707	-0.002
5	4	2	-	4	4	1	5626.528	-0.001
5	4	1	-	4	4	0	5627.903	0.000
5	3	3	-	4	3	2	5636.880	-0.025
5	3	2	-	4	3	1	5684.415	-0.005
7	3	5	-	7	2	6	5769.300	0.001
10	2	8	-	10	1	9	5770.303	-0.001
6	0	6	-	5	1	5	5830.039	-0.003
7	2	6	-	7	1	7	5833.670	-0.004
5	1	4	-	4	1	3	5900.072	0.002
5	2	3	-	4	2	2	5930.766	0.000
9	4	5	-	9	3	6	5936.475	0.006
6	1	6	-	5	1	5	5954.195	-0.005
8	1	7	-	8	0	8	6012.003	-0.001
6	0	6	-	5	0	5	6051.337	0.002
8	2	6	-	7	3	5	6055.349	0.004
3	2	2	-	2	1	1	6083.628	-0.001
6	1	6	-	5	0	5	6175.494	0.002
8	4	4	-	8	3	5	6325.956	0.002
6	2	5	-	5	2	4	6562.836	0.001
8	2	7	-	8	1	8	6601.329	0.002
7	4	3	-	7	3	4	6632.307	0.001
7	1	6	-	6	2	5	6646.827	-0.004
9	3	7	-	9	2	8	6687.008	0.002
6	4	3	-	5	4	2	6769.590	0.000
6	3	4	-	5	3	3	6771.024	-0.002
6	4	2	-	5	4	1	6775.683	0.006
3	2	1	-	2	1	2	6783.050	-0.001
7	0	7	-	6	1	6	6832.278	0.000
6	4	2	-	6	3	3	6835.525	-0.004
6	3	3	-	5	3	2	6891.005	0.008
7	1	7	-	6	1	6	6898.393	0.002
4	2	3	-	3	1	2	6909.480	0.003
5	4	1	-	5	3	2	6950.851	0.003
7	0	7	-	6	0	6	6956.435	0.000

6	1	5	-	5	1	4	6973.383	-0.005
<sup>a</sup> Experimental transitions frequency								
<sup>b</sup> Experimental transition frequency – theoretical transition frequency								

**Table B.3.** List of the assigned transitions of the VA-I-W monohydrate.

J'	Ka'	Kc'	-	J''	Ka''	Kc''	$\nu^a$ / MHz	$\nu^b$ / MHz
7	2	5	-	7	1	6	2922.176	-0.003
8	2	6	-	8	1	7	2929.462	0.000
6	2	4	-	6	1	5	2971.124	-0.001
9	2	7	-	9	1	8	3006.576	-0.005
3	1	3	-	2	0	2	3045.689	-0.001
5	2	3	-	5	1	4	3059.985	0.001
8	1	7	-	8	0	8	3123.820	-0.003
10	2	8	-	10	1	9	3164.627	0.021
4	2	2	-	4	1	3	3170.515	-0.005
3	2	1	-	3	1	2	3284.359	0.005
6	0	6	-	5	1	5	3418.989	0.006
4	1	4	-	3	0	3	3600.240	0.010
2	2	1	-	2	1	2	3619.983	-0.002
9	1	8	-	9	0	9	3698.028	-0.002
5	1	4	-	4	1	3	3707.187	0.034
3	2	2	-	3	1	3	3741.990	-0.002
4	2	3	-	4	1	4	3905.950	-0.007
5	2	4	-	5	1	5	4112.619	0.001
5	1	5	-	4	0	4	4130.095	0.001
7	0	7	-	6	1	6	4192.595	0.002
10	1	9	-	10	0	10	4334.875	0.011
6	2	5	-	6	1	6	4362.490	0.006
6	1	6	-	5	0	5	4645.860	0.003
7	2	6	-	7	1	7	4655.610	-0.007
2	2	1	-	1	1	0	4871.510	0.007
8	0	8	-	7	1	7	4944.351	0.001
2	2	0	-	1	1	1	4955.260	-0.002
7	3	5	-	6	3	4	4964.261	0.013
8	2	7	-	8	1	8	4991.450	-0.001
11	1	10	-	11	0	11	5017.730	-0.010
7	1	7	-	6	0	6	5158.841	-0.004
9	3	6	-	9	2	7	5167.767	-0.004
10	1	9	-	9	2	8	5342.320	-0.011
8	3	5	-	8	2	6	5358.210	0.005
8	0	8	-	7	0	7	5365.083	-0.046
9	2	8	-	9	1	9	5368.659	-0.004
3	2	2	-	2	1	1	5497.265	0.003

7	3	4	-	7	2	5	5520.570	-0.002
6	3	3	-	6	2	4	5646.338	0.001
9	0	9	-	8	1	8	5671.850	0.001
8	1	8	-	7	0	7	5679.050	0.000
5	3	2	-	5	2	3	5733.993	0.001
3	2	1	-	2	1	2	5756.624	0.003
4	3	1	-	4	2	2	5787.989	-0.003
3	3	1	-	3	2	2	5836.575	-0.013
4	3	2	-	4	2	3	5847.533	-0.004
5	3	3	-	5	2	4	5869.283	-0.004
6	3	4	-	6	2	5	5906.533	-0.001
7	3	5	-	7	2	6	5964.281	0.004
8	3	6	-	8	2	7	6047.550	0.009
4	2	3	-	3	1	2	6082.625	0.002
9	3	7	-	9	2	8	6161.100	0.004
9	1	9	-	8	0	8	6213.338	0.010
10	0	10	-	9	1	9	6376.129	0.000

<sup>a</sup> Experimental transitions frequency.

<sup>b</sup> Experimental transition frequency – theoretical transition frequency

**Table B.4.** List of the assigned transitions of the VA-II-W monohydrate.

J'	Ka'	Kc'	-	J''	Ka''	Kc''	$\nu^a$ / MHz	$\nu^b$ / MHz
3	1	3	-	2	0	2	3032.383	-0.001
4	2	2	-	4	1	3	3100.284	0.008
3	2	1	-	3	1	2	3215.012	-0.005
6	0	6	-	5	1	5	3468.485	0.009
4	1	4	-	3	0	3	3588.173	-0.001
3	2	2	-	3	1	3	3683.733	-0.003
9	1	8	-	9	0	9	3759.074	0.005
4	2	3	-	4	1	4	3852.202	-0.008
5	2	4	-	5	1	5	4064.598	0.004
5	1	5	-	4	0	4	4119.335	-0.002
7	0	7	-	6	1	6	4242.800	-0.003
6	2	5	-	6	1	6	4321.373	-0.007
7	2	6	-	7	1	7	4622.560	0.001
11	3	8	-	11	2	9	4632.535	0.007
6	1	6	-	5	0	5	4637.110	0.003
2	2	1	-	1	1	0	4815.360	0.003
2	2	0	-	1	1	1	4901.513	0.004
8	2	7	-	8	1	8	4967.420	0.002
8	0	8	-	7	1	7	4993.902	0.002
9	3	6	-	9	2	7	5029.954	0.005
7	2	5	-	6	2	4	5149.757	-0.014
7	1	7	-	6	0	6	5153.310	-0.005
8	3	5	-	8	2	6	5225.180	0.006
7	3	4	-	7	2	5	5394.034	-0.011
3	2	2	-	2	1	1	5443.833	0.001
6	3	3	-	6	2	4	5526.300	-0.009
5	3	2	-	5	2	3	5619.260	0.002
4	3	1	-	4	2	2	5676.856	0.011
8	1	8	-	7	0	7	5678.093	0.002
3	2	1	-	2	1	2	5710.958	0.003
9	0	9	-	8	1	8	5719.988	0.005
4	3	2	-	4	2	3	5740.625	-0.002
5	3	3	-	5	2	4	5763.896	-0.008

<sup>a</sup> Experimental transitions frequency.<sup>b</sup> Experimental transition frequency – theoretical transition frequency

# Appendix C

## Supplementary Information for Chapter 5

Shapes of Benzyl Benzoate: A Rotational Spectroscopic and Computational Study

### Contents:

5. **Point C.1. Keywords used in Gaussian16 Calculation**
6. **List of assigned rotational transitions of BnBz-g and its Isotopologues**
  - a. **Table C.1.1.** List of assigned rotational transitions of BnBz-g
  - a. **Table C.1.2.** List of assigned rotational transitions of BnBz-g  $^{13}\text{C}1$
  - b. **Table C.1.3.** List of assigned rotational transitions of BnBz-g  $^{13}\text{C}2$
  - c. **Table C.1.4.** List of assigned rotational transitions of BnBz-g  $^{13}\text{C}3$
  - d. **Table C.1.5.** List of assigned rotational transitions of BnBz-g  $^{13}\text{C}4$
  - e. **Table C.1.6.** List of assigned rotational transitions of BnBz-g  $^{13}\text{C}5$
  - f. **Table C.1.7.** List of assigned rotational transitions of BnBz-g  $^{13}\text{C}6$
  - g. **Table C.1.8.** List of assigned rotational transitions of BnBz-g  $^{13}\text{C}7$
  - h. **Table C.1.9.** List of assigned rotational transitions of BnBz-g  $^{13}\text{C}8$
  - i. **Table C.1.10.** List of assigned rotational transitions of BnBz-g  $^{13}\text{C}9$
  - j. **Table C.1.11.** List of assigned rotational transitions of BnBz-g  $^{13}\text{C}10$
  - k. **Table C.1.12.** List of assigned rotational transitions of BnBz-g  $^{13}\text{C}11$
  - l. **Table C.1.13.** List of assigned rotational transitions of BnBz-g  $^{13}\text{C}12$
  - m. **Table C.1.14.** List of assigned rotational transitions of BnBz-g  $^{13}\text{C}13$
  - a. **Table C.1.15.** List of assigned rotational transitions of BnBz-g  $^{13}\text{C}14$
7. **List of Assigned Rotational Transitions of BnBz-t and its Isotopologues**
  - a. **Table C.2.1.** List of assigned rotational transitions of BnBz-t
  - b. **Table C.2.2.** List of assigned rotational transitions of BnBz-t  $^{13}\text{C}1$
  - c. **Table C.2.3.** List of assigned rotational transitions of BnBz-t  $^{13}\text{C}2$
8. **Cartesian Coordinates Obtained from Kraitchman's Substitution Equation**
  - a. **Table C.3.** Cartesian Coordinates of 14 in BnBz-g obtained through Kraitchman's substitution equation
  - b. **Table C.4.** Cartesian Coordinates of 4 in BnBz-t obtained through Kraitchman's substitution equation
9. **Computationally Identified Dimers**
  - a. **Table C.5.** List of computationally identified BnBz dimers
10. **List of Assigned Rotational Transition of the BnBz Dimer**
  - a. **Table C.6.** List of assigned rotational transitions of the BnBz dimer

**Point C.1.** Keywords used in Gaussian16 Calculation

- Opt
- freq=Vibro
- b3lyp/def2TZVP
- empiricaldispersion=gd3bj
- output=pickett

**Table C.1.1.** Assigned rotational transitions of the BnBz-g monomer.

J'	K <sub>a</sub> '	K <sub>c</sub> '	-	J''	K <sub>a</sub> ''	K <sub>c</sub> ''	$\nu_{Exp}$ /MHz	$\Delta\nu^a$ /MHz
5	0	5	-	4	1	4	1553.1846	0.0014
10	1	10	-	9	2	7	1789.4182	0.0018
2	1	2	-	1	0	1	1974.6393	-0.0005
4	0	4	-	3	0	3	1999.6954	0.0021
4	1	3	-	3	1	2	2016.7869	0.015
14	2	13	-	13	3	10	2039.8955	-0.0038
6	0	6	-	5	1	5	2072.4327	-0.0015
11	1	11	-	10	2	8	2233.6358	0.0013
10	1	9	-	9	2	8	2264.4663	-0.0013
12	5	7	-	13	4	10	2379.358	-0.0174
12	5	8	-	13	4	9	2379.358	-0.0007
8	4	5	-	9	3	6	2406.7512	0.0003
8	4	4	-	9	3	7	2406.9447	0.0009
4	3	2	-	5	2	3	2433.1674	-0.0002
4	3	1	-	5	2	4	2435.0143	0.0014
3	1	3	-	2	0	2	2462.2226	-0.0004
22	2	20	-	22	1	21	2477.8771	0.0008
5	1	5	-	4	1	4	2479.2175	-0.0044
23	2	21	-	23	1	22	2482.5694	0.0044
20	2	18	-	20	1	19	2487.6062	-0.01
24	2	22	-	24	1	23	2494.2833	-0.0075
5	0	5	-	4	0	4	2499.2197	0.0035
5	2	4	-	4	2	3	2500.1484	-0.0105
19	2	17	-	19	1	18	2500.9595	0.0031
5	2	3	-	4	2	2	2501.2091	-0.0033
18	2	16	-	18	1	17	2519.1536	-0.004
5	1	4	-	4	1	3	2520.86	0.0006
15	2	14	-	14	3	11	2531.5237	0.0029
17	2	15	-	17	1	16	2541.5893	-0.0008
16	2	14	-	16	1	15	2567.5955	-0.0012

7	0	7	-	6	1	6	2594.9278	-0.0027
15	2	13	-	15	1	14	2596.502	0.0013
14	2	12	-	14	1	13	2627.6151	0.0005
15	2	13	-	14	3	12	2656.1856	-0.0029
13	2	11	-	13	1	12	2660.2513	0.0012
12	1	12	-	11	2	9	2670.5368	-0.0004
12	2	10	-	12	1	11	2693.7273	-0.0005
11	2	9	-	11	1	10	2727.3869	-0.0009
10	2	8	-	10	1	9	2760.597	-0.0011
9	2	7	-	9	1	8	2792.7628	0.0000
11	1	10	-	10	2	9	2808.6572	0.0000
8	2	6	-	8	1	7	2823.3265	-0.0021
7	2	5	-	7	1	6	2851.7912	0.0008
15	6	9	-	16	5	12	2852.4605	0.0013
15	6	10	-	16	5	11	2852.4605	0.0021
6	2	4	-	6	1	5	2877.6948	0.0004
11	5	7	-	12	4	8	2879.9971	0.0012
11	5	6	-	12	4	9	2879.9971	-0.0075
5	2	3	-	5	1	4	2900.6429	0.0014
7	4	4	-	8	3	5	2907.3181	-0.0059
7	4	3	-	8	3	6	2907.4254	0.005
4	2	2	-	4	1	3	2920.2881	-0.0003
3	3	1	-	4	2	2	2934.0439	0.0004
3	3	0	-	4	2	3	2934.834	-0.0001
3	2	1	-	3	1	2	2936.349	-0.0001
4	1	4	-	3	0	3	2945.7265	0.0001
2	2	0	-	2	1	1	2948.5936	-0.0010
2	2	1	-	2	1	2	2973.5257	-0.0005
3	2	2	-	3	1	3	2986.0544	0.0001
6	0	6	-	5	0	5	2998.4728	-0.0002
6	3	4	-	5	3	3	3000.625	0.0079
6	3	3	-	5	3	2	3000.625	-0.0036
6	2	4	-	5	2	3	3001.9255	-0.0028
4	2	3	-	4	1	4	3002.7786	0.0001
16	2	15	-	15	3	12	3021.1977	0.0019
5	2	4	-	5	1	5	3023.7149	-0.0006
6	1	5	-	5	1	4	3024.8742	-0.0012
6	2	5	-	6	1	6	3048.8848	-0.0007
7	2	6	-	7	1	7	3078.3115	-0.0001
13	1	13	-	12	2	10	3099.5661	0.0004
8	2	7	-	8	1	8	3112.0166	-0.0023
8	0	8	-	7	1	7	3120.3822	-0.0016
9	2	8	-	9	1	9	3150.0339	-0.0006

16	2	14	-	15	3	13	3180.8812	-0.0019
10	2	9	-	10	1	10	3192.3818	-0.0043
11	2	10	-	11	1	11	3239.0997	-0.0018
12	2	11	-	12	1	12	3290.2083	0.0005
13	2	12	-	13	1	13	3345.731	0.0006
14	6	9	-	15	5	10	3353.0434	0.0003
14	6	8	-	15	5	11	3353.0434	0.0000
12	1	11	-	11	2	10	3356.5347	-0.0015
10	5	5	-	11	4	8	3380.5146	-0.0031
10	5	6	-	11	4	7	3380.5146	0.0012
14	2	13	-	14	1	14	3405.6913	-0.0003
5	1	5	-	4	0	4	3425.2552	0.0002
15	2	14	-	15	1	15	3470.1108	0.0002
7	1	7	-	6	1	6	3470.5293	-0.0005
7	0	7	-	6	0	6	3497.4121	0.0000
7	2	6	-	6	2	5	3499.9536	-0.0022
7	3	5	-	6	3	4	3500.8307	0.0284
7	3	4	-	6	3	3	3500.8307	0.0021
7	2	5	-	6	2	4	3502.8987	-0.0018
17	2	16	-	16	3	13	3508.624	-0.0026
14	1	14	-	13	2	11	3520.1408	0.0013
7	1	6	-	6	1	5	3528.8038	-0.0007
16	2	15	-	16	1	16	3539.0048	0.0033
21	3	19	-	20	4	16	3610.2678	0.0000
17	2	16	-	17	1	17	3612.3744	0.0015
9	0	9	-	8	1	8	3648.4685	-0.0016
18	2	17	-	18	1	18	3690.2287	0.0015
17	2	15	-	16	3	14	3709.9544	0.0022
19	2	18	-	19	1	19	3772.5644	0.0053
13	6	7	-	14	5	10	3853.533	-0.0038
13	6	8	-	14	5	9	3853.533	-0.0036
20	2	19	-	20	1	20	3859.3505	-0.005
9	5	5	-	10	4	6	3880.9285	-0.0007
9	5	4	-	10	4	7	3880.9285	-0.0027
6	1	6	-	5	0	5	3900.9543	-0.0003
13	1	12	-	12	2	11	3908.0074	-0.0048
15	1	15	-	14	2	12	3931.6677	0.0011
21	2	20	-	21	1	21	3950.5934	-0.0009
2	2	1	-	1	1	0	3956.9837	0.0000
2	2	0	-	1	1	1	3965.3657	0.0012
8	1	8	-	7	1	7	3966.0514	-0.0003
18	2	17	-	17	3	14	3993.491	0.0024
8	0	8	-	7	0	7	3995.9808	-0.0023

8	2	7	-	7	2	6	3999.7574	-0.0017
8	4	5	-	7	4	4	4000.8035	-0.0009
8	4	4	-	7	4	3	4000.8035	-0.0011
8	3	6	-	7	3	5	4001.0539	0.0312
8	3	5	-	7	3	4	4001.0539	-0.0213
8	2	6	-	7	2	5	4004.1668	-0.002
8	1	7	-	7	1	6	4032.63	-0.0005
22	2	21	-	22	1	22	4046.2527	0.0084
22	3	20	-	21	4	17	4112.1649	-0.0050
23	2	22	-	23	1	23	4146.2622	-0.0018
10	0	10	-	9	1	9	4178.8321	-0.0005
18	2	16	-	17	3	15	4243.7187	-0.0018
24	2	23	-	24	1	24	4250.5971	-0.0054
12	6	7	-	13	5	8	4353.9474	-0.0027
12	6	6	-	13	5	9	4353.9474	-0.0028
7	1	7	-	6	0	6	4373.0105	-0.0009
8	5	3	-	9	4	6	4381.2583	-0.0026
8	5	4	-	9	4	5	4381.2583	-0.0017
26	3	23	-	26	2	24	4399.2741	0.0028
4	4	1	-	5	3	2	4408.2662	0.0035
4	4	0	-	5	3	3	4408.2662	-0.0023
3	2	2	-	2	1	1	4448.7127	-0.0007
25	3	22	-	25	2	23	4456.5967	-0.0011
9	1	9	-	8	1	8	4461.4772	0.0065
14	1	13	-	13	2	12	4462.9787	-0.0008
3	2	1	-	2	1	2	4473.9606	-0.0006
19	2	18	-	18	3	15	4475.4313	0.0031
9	0	9	-	8	0	8	4494.1381	-0.0001
9	2	8	-	8	2	7	4499.4857	-0.0005
9	4	6	-	8	4	5	4500.9738	-0.0018
9	4	5	-	8	4	4	4500.9738	-0.0024
9	3	7	-	8	3	6	4501.2819	0.0005
9	3	6	-	8	3	5	4501.3768	-0.0008
9	2	7	-	8	2	6	4505.7721	0.0012
24	3	21	-	24	2	22	4511.7108	0.0004
9	1	8	-	8	1	7	4536.3347	-0.002
23	3	20	-	23	2	21	4564.0897	0.0004
22	3	19	-	22	2	20	4613.2978	-0.0002
21	3	18	-	21	2	19	4658.9803	-0.0086
20	3	17	-	20	2	18	4700.9071	0.0001
11	0	11	-	10	1	10	4711.0873	0.0026
17	1	17	-	16	2	14	4725.2269	-0.0001
19	3	16	-	19	2	17	4738.8891	-0.0016

18	3	15	-	18	2	16	4772.8715	0.0004
19	2	17	-	18	3	16	4782.4744	0.0041
17	3	14	-	17	2	15	4802.8717	0.0058
16	3	13	-	16	2	14	4828.9742	0.0009
8	1	8	-	7	0	7	4841.6498	-0.0013
15	3	12	-	15	2	13	4851.361	-0.0001
11	6	5	-	12	5	8	4854.2933	-0.0009
11	6	6	-	12	5	7	4854.2933	-0.0009
14	3	11	-	14	2	12	4870.2562	-0.0002
7	5	2	-	8	4	5	4881.5206	-0.0006
7	5	3	-	8	4	4	4881.5206	-0.0002
13	3	10	-	13	2	11	4885.9324	0.0006
12	3	9	-	12	2	10	4898.6927	0.0000
11	3	8	-	11	2	9	4908.865	-0.0001
10	3	7	-	10	2	8	4916.7839	0.001
9	3	6	-	9	2	7	4922.7782	0.0001
8	3	5	-	8	2	6	4927.1704	-0.0007
7	3	4	-	7	2	5	4930.2647	-0.0001
6	3	3	-	6	2	4	4932.3364	-0.0004
5	3	2	-	5	2	3	4933.6362	-0.0004
4	3	1	-	4	2	2	4934.3813	-0.0001
3	3	1	-	3	2	1	4934.7544	-0.0002
3	3	1	-	3	2	2	4935.0197	0.0015
4	3	2	-	4	2	3	4935.1695	-0.0009
5	3	3	-	5	2	4	4935.4748	0.0001
6	3	4	-	6	2	5	4936.0048	-0.0008
4	2	3	-	3	1	2	4936.2697	-0.0002
7	3	5	-	7	2	6	4936.8518	-0.0001
8	3	6	-	8	2	7	4938.1149	-0.0006
9	3	7	-	9	2	8	4939.911	0.0003
10	3	8	-	10	2	9	4942.3651	0.0015
11	3	9	-	11	2	10	4945.6121	0.0013
12	3	10	-	12	2	11	4949.8019	0.0025
13	3	11	-	13	2	12	4955.0841	-0.0006
10	1	10	-	9	1	9	4956.774	-0.0021
14	3	12	-	14	2	13	4961.6309	0.0009
15	3	13	-	15	2	14	4969.6062	0.001
16	3	14	-	16	2	15	4979.1858	0.0006
4	2	2	-	3	1	3	4987.0288	-0.0001
17	3	15	-	17	2	16	4990.5508	0.0014
10	0	10	-	9	0	9	4991.832	-0.001
10	2	9	-	9	2	8	4999.1263	-0.0014
10	4	7	-	9	4	6	5001.1708	-0.0009

10	4	6	-	9	4	5	5001.1708	-0.0021
10	3	8	-	9	3	7	5001.5808	0.0002
10	3	7	-	9	3	6	5001.7443	-0.001
18	3	16	-	18	2	17	5003.8791	-0.0002
10	2	8	-	9	2	7	5007.7404	-0.0001
19	3	17	-	19	2	18	5019.3607	0.0018
15	1	14	-	14	2	13	5021.3165	-0.0014
20	3	18	-	20	2	19	5037.1687	-0.0028
10	1	9	-	9	1	8	5039.9058	0.0006
21	3	19	-	21	2	20	5057.5051	0.005
22	3	20	-	22	2	21	5080.5258	0.0009
18	1	18	-	17	2	15	5106.1276	0.0003
23	3	21	-	23	2	22	5106.426	0.0031
24	3	22	-	24	2	23	5135.3698	0.0035
25	3	23	-	25	2	24	5167.522	0.0003
26	3	24	-	26	2	25	5203.044	-0.005
12	0	12	-	11	1	11	5244.8165	0.0004
9	1	9	-	8	0	8	5307.138	-0.0006
20	2	18	-	19	3	17	5326.436	0.0032
6	5	2	-	7	4	3	5381.7228	-0.0022
6	5	1	-	7	4	4	5381.7228	-0.0023
5	2	4	-	4	1	3	5419.6566	-0.0003
21	2	20	-	20	3	17	5428.9782	-0.0011
11	0	11	-	10	0	10	5489.03	0.0018
11	2	10	-	10	2	9	5498.6723	-0.0017
11	5	6	-	10	5	5	5501.1391	0.003
11	5	7	-	10	5	6	5501.1391	0.003
11	4	8	-	10	4	7	5501.3949	-0.0004
11	4	7	-	10	4	6	5501.3949	-0.0028
11	3	9	-	10	3	8	5501.9211	-0.0002
11	3	8	-	10	3	7	5502.191	0.0017
5	2	3	-	4	1	4	5504.7805	-0.0007
11	2	9	-	10	2	8	5510.1067	-0.0002
11	1	10	-	10	1	9	5543.3153	-0.0019
16	1	15	-	15	2	14	5582.8914	-0.0002
10	1	10	-	9	0	9	5769.7755	-0.0011
13	0	13	-	12	1	12	5779.5993	-0.0002
9	6	4	-	10	5	5	5854.826	0.0136
9	6	3	-	10	5	6	5854.826	0.0136
5	5	0	-	6	4	3	5881.8822	-0.0025
5	5	1	-	6	4	2	5881.8822	-0.0025
6	2	5	-	5	1	4	5898.8829	-0.0006
22	2	21	-	21	3	18	5899.7323	-0.0014

12	1	12	-	11	1	11	5947.0138	0.004
12	0	12	-	11	0	11	5985.6858	-0.0043
12	2	11	-	11	2	10	5998.1158	-0.0002
12	3	10	-	11	3	9	6002.3062	0.0016
12	3	9	-	11	3	8	6002.7187	-0.0021
12	2	10	-	11	2	9	6012.8939	0.0007
6	2	4	-	5	1	5	6027.4869	-0.0008
12	1	11	-	11	1	10	6046.544	-0.0092
17	1	16	-	16	2	15	6147.5465	-0.0006
11	1	11	-	10	0	10	6229.901	-0.0012
14	0	14	-	13	1	13	6314.9985	-0.0001
7	2	6	-	6	1	5	6373.965	0.001
13	1	13	-	12	1	12	6441.9241	0.0024
13	0	13	-	12	0	12	6481.7927	-0.0004
13	2	12	-	12	2	11	6497.446	0.0018
13	1	12	-	12	1	11	6549.5905	-0.0015
7	2	5	-	6	1	6	6555.4712	-0.0011
12	1	12	-	11	0	11	6687.884	0.0003
18	1	17	-	17	2	16	6715.1122	0.0000
8	2	7	-	7	1	6	6844.9201	0.0015
15	0	15	-	14	1	14	6850.577	-0.0004
22	4	18	-	22	3	19	6858.3786	-0.0097
20	4	16	-	20	3	17	6876.2173	0.0057
18	4	14	-	18	3	15	6888.5291	0.0000
17	4	13	-	17	3	14	6893.0771	-0.0019
16	4	12	-	16	3	13	6896.7654	0.0017
18	4	15	-	18	3	16	6899.5225	0.0071
15	4	11	-	15	3	12	6899.7152	-0.0016
17	4	14	-	17	3	15	6900.9585	-0.0009
14	4	10	-	14	3	11	6902.0573	0.0007
16	4	13	-	16	3	14	6902.3006	0.0000
15	4	12	-	15	3	13	6903.5221	0.0044
13	4	9	-	13	3	10	6903.8868	0.0004
14	4	11	-	14	3	12	6904.5948	-0.003
12	4	8	-	12	3	9	6905.2955	-0.0005
13	4	10	-	13	3	11	6905.5348	-0.0001
11	4	8	-	11	3	9	6906.9838	-0.0005
10	4	6	-	10	3	7	6907.1553	0.0003
10	4	7	-	10	3	8	6907.5097	-0.0006
9	4	5	-	9	3	6	6907.7268	-0.0005
9	4	6	-	9	3	7	6907.9203	0.0012
8	4	4	-	8	3	5	6908.1342	0.0054
8	2	6	-	7	1	7	7089.1117	0.0002

13	1	13	-	12	0	12	7144.1144	-0.0008
9	2	8	-	8	1	7	7311.7752	0.0009
16	0	16	-	15	1	15	7385.9124	0.0022
14	1	14	-	13	0	13	7599.0137	0.0036
9	2	7	-	8	1	8	7628.8327	0.0022
10	2	9	-	9	1	8	7774.5648	-0.0004

$\Delta\nu$  is the difference between measure and calculated frequencies.

**Table C.1.2.** BnBz-g  $^{13}\text{C}1$  isotopologous assigned rotational transitions.

J'	Ka'	Kc'	-	J''	Ka''	Kc''	$\nu_{\text{Exp}}$ /MHz	$\nu^a$ /MHz
4	1	4	-	3	0	3	2942.4232	0.0129
5	1	5	-	4	0	4	3421.7053	0.0027
6	1	6	-	5	0	5	3897.1534	-0.0111
2	2	1	-	1	1	0	3949.3490	-0.0024
2	2	0	-	1	1	1	3957.7411	0.0033
7	1	7	-	6	0	6	4368.9842	0.0013
3	2	2	-	2	1	1	4440.8438	-0.0080
8	1	8	-	7	0	7	4837.3836	-0.0007
4	2	2	-	3	1	3	4978.9824	0.0118
9	1	9	-	8	0	8	5302.6262	-0.0084
5	2	4	-	4	1	3	5411.3304	0.0018
5	2	3	-	4	1	4	5496.5139	0.0004
10	1	10	-	9	0	9	5765.0444	0.0067
6	2	5	-	5	1	4	5890.3251	0.0073
6	2	4	-	5	1	5	6019.0096	-0.0067
11	1	11	-	10	0	10	6224.9320	0.0003
7	2	6	-	6	1	5	6365.1541	-0.0040
3	3	1	-	2	2	0	6422.4874	-0.0083
3	3	0	-	2	2	1	6422.5542	0.0054

<sup>a</sup> $\Delta\nu$  is the difference between measure and calculated frequencies.

**Table C.1.3.** BnBz-g  $^{13}\text{C}2$  isotopologous assigned rotational transitions.

J'	Ka'	Kc'	-	J''	Ka''	Kc''	$\nu_{\text{Exp}}$ /MHz	$\nu^a$ /MHz
4	1	4	-	3	0	3	2942.1605	0.0011
8	0	8	-	7	1	7	3111.3041	-0.0096
5	1	5	-	4	0	4	3420.7351	0.0017
6	1	6	-	5	0	5	3895.4884	-0.0037
2	2	0	-	1	1	1	3964.513	0.0107
10	0	10	-	9	1	9	4167.5109	-0.0035

7	1	7	-	6	0	6	4366.6205	0.0003
3	2	1	-	2	1	2	4472.0401	0.0108
8	1	8	-	7	0	7	4834.3388	-0.0024
12	0	12	-	11	1	11	5231.2687	0.0115
9	1	9	-	8	0	8	5298.9204	0.0021
5	2	4	-	4	1	3	5415.8607	-0.0119
5	2	3	-	4	1	4	5500.6406	-0.0103
10	1	10	-	9	0	9	5760.6484	-0.0028
6	2	4	-	5	1	5	6022.2238	-0.0008
11	1	11	-	10	0	10	6219.8812	0.0065

<sup>a</sup> $\Delta\nu$  is the difference between measure and calculated frequencies.

**Table C.1.4.** Assigned rotational transitions of the <sup>13</sup>C3 isotopologue of BnBz-g.

J'	Ka'	Kc'	-	J''	Ka''	Kc''	$\nu_{\text{Exp}}$ /MHz	$\nu^a$ /MHz
9	0	9	-	8	1	8	3631.7923	-0.0115
6	1	6	-	5	0	5	3884.0255	0.0000
10	0	10	-	9	1	9	4159.9957	0.0102
3	2	2	-	2	1	1	4432.5120	0.0024
3	2	1	-	2	1	2	4457.8506	-0.0031
8	1	8	-	7	0	7	4820.0344	0.0042
4	2	2	-	3	1	3	4968.7210	-0.0072
5	2	4	-	4	1	3	5398.8609	0.0081
5	2	3	-	4	1	4	5484.3058	-0.0028
10	1	10	-	9	0	9	5743.4490	0.0034
6	2	4	-	5	1	5	6004.8725	0.0053
11	1	11	-	10	0	10	6201.2146	-0.0026
7	2	6	-	6	1	5	6348.4865	-0.0108
3	3	0	-	2	2	1	6412.7562	0.0034

<sup>a</sup> $\Delta\nu$  is the difference between measure and calculated frequencies.

**Table C.1.5.** Assigned rotational transitions of the <sup>13</sup>C4 isotopologue of BnBz-g.

J'	Ka'	Kc'	-	J''	Ka''	Kc''	$\nu_{\text{Exp}}$ /MHz	$\nu^a$ /MHz
4	1	4	-	3	0	3	2927.3237	0.0036
5	1	5	-	4	0	4	3402.9968	0.0001
6	1	6	-	5	0	5	3874.9332	-0.0024
2	2	1	-	1	1	0	3942.4336	0.0082
2	2	0	-	1	1	1	3950.5928	0.0054
10	0	10	-	9	1	9	4133.2450	0.0001
7	1	7	-	6	0	6	4343.3127	-0.0008

3	2	2	-	2	1	1	4429.9906	-0.0031
8	1	8	-	7	0	7	4808.3446	-0.0007
4	2	2	-	3	1	3	4962.9159	-0.0047
9	1	9	-	8	0	8	5270.2838	0.0009
5	2	4	-	4	1	3	5392.9415	0.0020
10	1	10	-	9	0	9	5729.4182	0.0046
6	2	5	-	5	1	4	5868.3337	0.0048
6	2	4	-	5	1	5	5993.5099	-0.0004
11	1	11	-	10	0	10	6186.0522	-0.0068
7	2	6	-	6	1	5	6339.6823	0.0031
3	3	1	-	2	2	0	6412.1384	-0.0148
3	3	0	-	2	2	1	6412.2094	0.0059

<sup>a</sup> $\Delta\nu$  is the difference between measure and calculated frequencies.

**Table C.1.6.** BnBz-g <sup>13</sup>C5 isotopologous assigned rotational transitions.

J'	Ka'	Kc'	-	J''	Ka''	Kc''	$\nu_{\text{Exp}}$ /MHz	$\nu^a$ /MHz
8	0	8	-	7	1	7	3077.6029	0.0076
5	1	5	-	4	0	4	3400.0700	0.0015
6	1	6	-	5	0	5	3871.1444	-0.0068
2	2	1	-	1	1	0	3944.3828	-0.0101
10	0	10	-	9	1	9	4124.6269	-0.0082
7	1	7	-	6	0	6	4338.6663	0.0027
3	2	2	-	2	1	1	4431.1492	-0.0012
3	2	1	-	2	1	2	4455.8154	0.0051
4	2	2	-	3	1	3	4963.4040	0.0016
9	1	9	-	8	0	8	5263.8797	0.0033
5	2	3	-	4	1	4	5475.5648	0.0052
13	0	13	-	12	1	12	5708.3478	-0.0060
6	2	5	-	5	1	4	5866.9746	-0.0060
6	2	4	-	5	1	5	5992.5460	0.0064
11	1	11	-	10	0	10	6177.8729	0.0007
3	3	1	-	2	2	0	6415.7061	-0.0085
7	2	5	-	6	1	6	6514.6625	0.0105

<sup>a</sup> $\Delta\nu$  is the difference between measure and calculated frequencies.

**Table C.1.7.** BnBz-g <sup>13</sup>C6 isotopologous assigned rotational transitions.

J'	Ka'	Kc'	-	J''	Ka''	Kc''	$\nu_{\text{Exp}}$ /MHz	$\nu^a$ /MHz
5	1	5	-	4	0	4	3400.0701	0.0158
9	0	9	-	8	1	8	3624.0989	0.0002

6	1	6	-	5	0	5	3871.6162	-0.0009
7	1	7	-	6	0	6	4339.4736	0.0005
3	2	2	-	2	1	1	4420.3642	0.0077
3	2	1	-	2	1	2	4446.1731	0.0122
4	2	2	-	3	1	3	4955.9035	0.0025
9	1	9	-	8	0	8	5265.0535	0.0001
5	2	3	-	4	1	4	5470.4421	-0.0001
10	1	10	-	9	0	9	5723.3722	-0.0010
6	2	5	-	5	1	4	5858.5641	0.0018
6	2	4	-	5	1	5	5990.0613	-0.0066
11	1	11	-	10	0	10	6179.1723	0.0000
7	2	6	-	6	1	5	6329.4615	-0.0134
3	3	1	-	2	2	0	6395.5726	-0.0053

<sup>a</sup> $\Delta\nu$  is the difference between measure and calculated frequencies.

**Table C.1.8.** BnBz-g <sup>13</sup>C7 isotopologus assigned rotational transitions.

J'	Ka'	Kc'	-	J''	Ka''	Kc''	$\nu_{\text{Exp}}$ /MHz	$\nu^a$ /MHz
4	1	4	-	3	0	3	2935.2311	-0.0009
5	1	5	-	4	0	4	3412.8930	0.0035
9	0	9	-	8	1	8	3638.5276	-0.0087
6	1	6	-	5	0	5	3886.6788	-0.0001
2	2	0	-	1	1	1	3951.7440	-0.0031
10	0	10	-	9	1	9	4167.5112	0.0058
7	1	7	-	6	0	6	4356.7885	-0.0028
3	2	2	-	2	1	1	4433.2648	0.0010
3	2	1	-	2	1	2	4458.8052	-0.0033
8	1	8	-	7	0	7	4823.4599	0.0012
4	2	3	-	3	1	2	4919.0394	0.0020
4	2	2	-	3	1	3	4970.3976	0.0001
12	0	12	-	11	1	11	5230.6584	-0.0014
9	1	9	-	8	0	8	5286.9574	0.0044
5	2	3	-	4	1	4	5486.7341	0.0006
10	1	10	-	9	0	9	5747.5845	-0.0003
6	2	5	-	5	1	4	5877.9398	-0.0006
6	2	4	-	5	1	5	6008.1011	0.0079
11	1	11	-	10	0	10	6205.6972	-0.0029
3	3	1	-	2	2	0	6412.8928	-0.0110
3	3	0	-	2	2	1	6412.9652	0.0069

<sup>a</sup> $\Delta\nu$  is the difference between measure and calculated frequencies.

**Table C.1.9.** BnBz-g  $^{13}\text{C}8$  isotopologues assigned rotational transitions.

$J'$	$K_a'$	$K_c'$	-	$J''$	$K_a''$	$K_c''$	$\nu_{\text{Exp}} / \text{MHz}$	$\nu^a / \text{MHz}$
8	0	8	-	7	1	7	3118.2336	-0.0027
5	1	5	-	4	0	4	3415.8137	-0.0065
9	0	9	-	8	1	8	3644.4613	-0.0033
6	1	6	-	5	0	5	3891.8541	-0.0030
2	2	1	-	1	1	0	3930.2203	0.0002
10	0	10	-	9	1	9	4172.9364	0.0068
7	1	7	-	6	0	6	4364.3968	-0.0022
3	2	1	-	2	1	2	4445.6538	-0.0004
8	1	8	-	7	0	7	4833.6536	0.0004
4	2	2	-	3	1	3	4957.3466	-0.0022
9	1	9	-	8	0	8	5299.8672	0.0042
5	2	4	-	4	1	3	5392.3530	0.0100
5	2	3	-	4	1	4	5473.4933	-0.0010
10	1	10	-	9	0	9	5763.3047	-0.0016
6	2	5	-	5	1	4	5871.7712	0.0030
11	1	11	-	10	0	10	6224.2933	-0.0006
3	3	1	-	2	2	0	6390.4513	-0.0152
3	3	0	-	2	2	1	6390.5277	0.0126
7	2	5	-	6	1	6	6520.1761	-0.0018

<sup>a</sup> $\Delta\nu$  is the difference between measure and calculated frequencies.

**Table C.1.10.** BnBz-g  $^{13}\text{C}9$  isotopologues assigned rotational transitions.

$J'$	$K_a'$	$K_c'$	-	$J''$	$K_a''$	$K_c''$	$\nu_{\text{Exp}} / \text{MHz}$	$\nu^a / \text{MHz}$
5	1	5	-	4	0	4	3418.6755	-0.0144
6	1	6	-	5	0	5	3893.3019	-0.0006
2	2	1	-	1	1	0	3952.8505	0.0098
2	2	0	-	1	1	1	3961.1178	-0.0100
7	1	7	-	6	0	6	4364.3086	0.0016
3	2	1	-	2	1	2	4468.2820	0.0047
8	1	8	-	7	0	7	4831.9288	0.0046
4	2	2	-	3	1	3	4979.8450	0.0002
9	1	9	-	8	0	8	5296.4204	0.0069
5	2	4	-	4	1	3	5411.8806	0.0021
5	2	3	-	4	1	4	5496.0373	-0.0020
6	2	5	-	5	1	4	5889.9857	0.0002
6	2	4	-	5	1	5	6017.1268	0.0018
11	1	11	-	10	0	10	6217.2218	-0.0049
3	3	1	-	2	2	0	6428.5916	-0.0139

3	3	0	-	2	2	1	6428.6683	0.0110
---	---	---	---	---	---	---	-----------	--------

<sup>a</sup> $\Delta\nu$  is the difference between measure and calculated frequencies.

**Table C.1.11.** BnBz-g <sup>13</sup>C10 isotopologous assigned rotational transitions.

J'	Ka'	Kc'	-	J''	Ka''	Kc''	$\nu_{\text{Exp}}$ /MHz	$\nu^a$ /MHz
4	1	4	-	3	0	3	2932.0592	0.0012
8	0	8	-	7	1	7	3107.9585	-0.0042
5	1	5	-	4	0	4	3409.0917	-0.0002
9	0	9	-	8	1	8	3634.0840	-0.0085
6	1	6	-	5	0	5	3882.2518	-0.0012
2	2	1	-	1	1	0	3939.8552	-0.0069
2	2	0	-	1	1	1	3948.3674	0.0140
10	0	10	-	9	1	9	4162.5119	0.0156
7	1	7	-	6	0	6	4351.7344	0.0014
3	2	2	-	2	1	1	4429.2487	-0.0027
8	1	8	-	7	0	7	4817.7649	0.0004
9	1	9	-	8	0	8	5280.6191	-0.0016
5	2	4	-	4	1	3	5395.3479	-0.0020
5	2	3	-	4	1	4	5481.6149	-0.0046
10	1	10	-	9	0	9	5740.6112	-0.0022
6	2	5	-	5	1	4	5872.0738	0.0013
6	2	4	-	5	1	5	6002.4145	-0.0082
11	1	11	-	10	0	10	6198.0925	0.0029
3	3	0	-	2	2	1	6407.4955	0.0058

<sup>a</sup> $\Delta\nu$  is the difference between measure and calculated frequencies.

**Table C.1.12.** BnBz-g <sup>13</sup>C11 isotopologous assigned rotational transitions.

J'	Ka'	Kc'	-	J''	Ka''	Kc''	$\nu_{\text{Exp}}$ /MHz	$\nu^a$ /MHz
4	1	4	-	3	0	3	2924.3233	-0.0016
8	0	8	-	7	1	7	3096.0981	0.0019
5	1	5	-	4	0	4	3399.8061	0.0037
9	0	9	-	8	1	8	3620.5256	-0.0062
6	1	6	-	5	0	5	3871.4185	0.0005
10	0	10	-	9	1	9	4147.2377	0.0002
7	1	7	-	6	0	6	4339.3668	0.0043
3	2	2	-	2	1	1	4420.2775	0.0004
3	2	1	-	2	1	2	4445.7805	-0.0023

11	0	11	-	10	1	10	4675.8204	0.0029
8	1	8	-	7	0	7	4803.8609	-0.0067
9	1	9	-	8	0	8	5265.2046	-0.0007
5	2	3	-	4	1	4	5469.2368	0.0000
10	1	10	-	9	0	9	5723.6876	0.0018
6	2	4	-	5	1	5	5988.3513	0.0009
11	1	11	-	10	0	10	6179.6547	0.0000

<sup>a</sup> $\Delta\nu$  is the difference between measure and calculated frequencies.

**Table C.1.13.** BnBz-g <sup>13</sup>C12 isotopologous assigned rotational transitions.

J'	Ka'	Kc'	-	J''	Ka''	Kc''	$\nu_{\text{Exp}}$ /MHz	$\nu^a$ /MHz
5	1	5	-	4	0	4	3401.0475	-0.0022
6	1	6	-	5	0	5	3873.2278	-0.0021
7	1	7	-	6	0	6	4341.9103	0.0000
9	1	9	-	8	0	8	5269.6334	-0.0017
10	1	10	-	9	0	9	5729.2056	0.0062
11	1	11	-	10	0	10	6186.3011	0.0011
9	0	9	-	8	1	8	3605.6347	-0.0067
10	0	10	-	9	1	9	4130.3235	0.0050
12	0	12	-	11	1	11	5184.9627	0.0022
5	2	4	-	4	1	3	5386.5162	0.0119
6	2	5	-	5	1	4	5862.0736	-0.0039
7	2	6	-	6	1	5	6333.6789	-0.0118
3	2	1	-	2	1	2	4447.5262	-0.0017
4	2	2	-	3	1	3	4955.3958	0.0007
5	2	3	-	4	1	4	5467.7077	-0.0071
6	2	4	-	5	1	5	5984.7407	0.0065
7	2	5	-	6	1	6	6506.7467	-0.0031
3	3	0	-	2	2	1	6401.2992	0.0049

<sup>a</sup> $\Delta\nu$  is the difference between measure and calculated frequencies.

**Table C.1.14.** BnBz-g <sup>13</sup>C13 isotopologous assigned rotational transitions.

J'	Ka'	Kc'	-	J''	Ka''	Kc''	$\nu_{\text{Exp}}$ /MHz	$\nu^a$ /MHz
4	1	4	-	3	0	3	2927.7835	0.0074
8	0	8	-	7	1	7	3094.4223	-0.0061
5	1	5	-	4	0	4	3404.2070	-0.0013
6	1	6	-	5	0	5	3876.8942	0.0027
2	2	0	-	1	1	1	3944.1292	-0.0117
7	1	7	-	6	0	6	4346.0081	0.0043

3	2	2	-	2	1	1	4424.3153	0.0008
11	0	11	-	10	1	10	4672.8209	-0.0006
8	1	8	-	7	0	7	4811.7662	0.0038
4	2	2	-	3	1	3	4958.2151	0.0050
9	1	9	-	8	0	8	5274.4190	-0.0023
5	2	4	-	4	1	3	5388.8139	0.0035
5	2	3	-	4	1	4	5472.0038	0.0056
10	1	10	-	9	0	9	5734.2661	-0.0055
6	2	5	-	5	1	4	5864.9645	0.0118
6	2	4	-	5	1	5	5990.6103	-0.0055
11	1	11	-	10	0	10	6191.6393	0.0018
7	2	6	-	6	1	5	6337.0403	-0.0007
3	3	1	-	2	2	0	6401.0970	-0.0105
7	2	5	-	6	1	6	6514.3789	0.0045
12	1	12	-	11	0	11	6646.8676	-0.0055

<sup>a</sup> $\Delta\nu$  is the difference between measure and calculated frequencies.

**Table C.1.15.** BnBz-g <sup>13</sup>C14 isotopologues assigned rotational transitions.

J'	Ka'	Kc'	-	J''	Ka''	Kc''	$\nu_{\text{Exp}}$ /MHz	$\nu^a$ /MHz
4	1	4	-	3	0	3	2935.1177	0.0094
5	1	5	-	4	0	4	3412.5281	0.0016
6	1	6	-	5	0	5	3886.0867	-0.0008
2	2	1	-	1	1	0	3945.5572	0.0043
10	0	10	-	9	1	9	4163.0675	0.0067
7	1	7	-	6	0	6	4355.9795	-0.0015
3	2	1	-	2	1	2	4460.7256	-0.0073
11	0	11	-	10	1	10	4693.5328	-0.0066
8	1	8	-	7	0	7	4822.4346	-0.0026
4	2	2	-	3	1	3	4971.9763	0.0032
9	1	9	-	8	0	8	5285.7249	-0.0013
5	2	4	-	4	1	3	5402.0832	-0.0028
5	2	3	-	4	1	4	5487.9456	0.0025
10	1	10	-	9	0	9	5746.1538	-0.0024
6	2	5	-	5	1	4	5879.1943	-0.0020
6	2	4	-	5	1	5	6008.9123	-0.0048
11	1	11	-	10	0	10	6204.0703	-0.0005
7	2	6	-	6	1	5	6352.1376	0.0115
3	3	1	-	2	2	0	6416.7778	-0.0128
3	3	0	-	2	2	1	6416.8531	0.0085
7	2	5	-	6	1	6	6535.2279	0.0020

<sup>a</sup> $\Delta\nu$  is the difference between measure and calculated frequencies.

**Table C.2.1.** Experimentally assigned rotational transitions of BnBz-t.

J'	Ka'	Kc'	-	J''	Ka''	Kc''	$\nu_{\text{Exp}}/\text{MHz}$	$\nu^a/\text{MHz}$
6	0	6	-	5	1	5	1723.7485	-0.0019
7	0	7	-	6	1	6	2215.7216	0.0029
6	3	4	-	7	2	5	2250.8365	-0.0040
13	1	12	-	13	0	13	2270.2589	-0.0022
5	1	4	-	4	1	3	2272.2076	-0.0043
6	3	3	-	7	2	6	2287.3981	-0.0081
11	1	10	-	10	2	9	2296.3149	-0.0017
3	1	3	-	2	0	2	2350.4486	0.0002
14	1	13	-	14	0	14	2487.7990	0.0048
6	1	6	-	5	1	5	2603.3367	-0.0038
10	4	7	-	11	3	8	2636.3611	-0.0044
10	4	6	-	11	3	9	2644.1355	-0.0007
6	0	6	-	5	0	5	2656.8038	-0.0009
6	2	5	-	5	2	4	2665.5720	0.0042
6	3	4	-	5	3	3	2668.3730	0.0054
6	3	3	-	5	3	2	2668.5016	-0.0107
6	2	4	-	5	2	3	2675.6738	-0.0030
14	2	12	-	14	1	13	2705.8201	0.0010
15	2	13	-	15	1	14	2707.5447	0.0050
8	0	8	-	7	1	7	2711.4568	-0.0012
13	2	11	-	13	1	12	2719.1465	-0.0050
6	1	5	-	5	1	4	2725.8113	0.0006
5	3	2	-	6	2	5	2727.9768	-0.0052
4	1	4	-	3	0	3	2754.6441	0.0000
17	2	15	-	17	1	16	2763.4201	0.0064
11	2	9	-	11	1	10	2782.5085	-0.0035
10	2	8	-	10	1	9	2827.8675	-0.0007
12	1	11	-	11	2	10	2850.3864	-0.0009
9	2	7	-	9	1	8	2879.0296	0.0005
8	2	6	-	8	1	7	2933.4682	0.0004
16	1	15	-	16	0	16	2984.2870	-0.0014
7	2	5	-	7	1	6	2988.7199	-0.0022
14	5	10	-	15	4	11	3009.6420	0.0012
14	5	9	-	15	4	12	3011.0926	0.0043
7	1	7	-	6	1	6	3036.1968	-0.0042
6	2	4	-	6	1	5	3042.4718	-0.0005
9	4	6	-	10	3	7	3087.4880	-0.0032
5	2	3	-	5	1	4	3092.6026	-0.0035
7	0	7	-	6	0	6	3095.3084	-0.0001
7	2	6	-	6	2	5	3109.0909	0.0026

7	3	5	-	6	3	4	3113.5593	-0.0041
7	3	4	-	6	3	3	3113.8913	0.0023
7	2	5	-	6	2	4	3125.1738	-0.0012
4	2	2	-	4	1	3	3137.2654	-0.0022
5	1	5	-	4	0	4	3149.6879	-0.0007
4	3	2	-	5	2	3	3159.9791	-0.0028
4	3	1	-	5	2	4	3170.1560	0.0034
3	2	1	-	3	1	2	3174.8929	0.0036
7	1	6	-	6	1	5	3178.9255	0.0002
2	2	0	-	2	1	1	3204.2103	0.0007
9	0	9	-	8	1	8	3209.3915	0.0020
17	1	16	-	17	0	17	3261.0787	-0.0013
2	2	1	-	2	1	2	3265.2275	-0.0001
3	2	2	-	3	1	3	3296.0504	-0.0003
4	2	3	-	4	1	4	3337.2563	0.0016
5	2	4	-	5	1	5	3388.9211	-0.0015
13	1	12	-	12	2	11	3410.8411	-0.0017
6	2	5	-	6	1	6	3451.1504	0.0004
13	5	9	-	14	4	10	3459.9746	-0.0013
13	5	8	-	14	4	11	3460.8162	0.0018
8	1	8	-	7	1	7	3468.6225	0.0012
7	2	6	-	7	1	7	3524.0348	-0.0022
8	0	8	-	7	0	7	3531.9412	0.0006
6	1	6	-	5	0	5	3536.3949	0.0001
8	4	5	-	9	3	6	3536.8230	0.0000
8	4	4	-	9	3	7	3539.2175	0.0019
8	2	7	-	7	2	6	3552.2650	-0.0025
18	1	17	-	18	0	18	3554.7319	-0.0116
8	6	2	-	7	6	1	3556.6029	-0.0033
8	6	3	-	7	6	2	3556.6029	-0.0033
8	5	4	-	7	5	3	3557.0356	-0.0029
8	5	3	-	7	5	2	3557.0356	-0.0029
8	3	6	-	7	3	5	3558.9439	0.0031
8	3	5	-	7	3	4	3559.5927	0.0015
8	2	6	-	7	2	5	3576.1991	-0.0012
8	2	7	-	8	1	8	3607.6882	0.0049
3	3	1	-	4	2	2	3609.0648	0.0049
3	3	0	-	4	2	3	3613.4238	0.0049
8	1	7	-	7	1	6	3631.4531	-0.0017
9	2	8	-	9	1	9	3702.1798	0.0004
10	0	10	-	9	1	9	3707.8992	-0.0007
10	2	9	-	10	1	10	3807.5961	-0.0031
19	1	18	-	19	0	19	3863.2363	0.0051

9	1	9	-	8	1	8	3900.5621	0.0004
12	5	8	-	13	4	9	3909.2335	-0.0041
12	5	7	-	13	4	10	3909.7023	-0.0013
7	1	7	-	6	0	6	3915.7910	-0.0001
11	2	10	-	11	1	11	3923.9900	-0.0024
9	0	9	-	8	0	8	3966.5519	-0.0007
14	1	13	-	13	2	12	3976.8386	-0.0012
7	4	4	-	8	3	5	3984.7748	0.0036
7	4	3	-	8	3	6	3985.9668	-0.0005
9	2	8	-	8	2	7	3995.0569	-0.0008
9	6	3	-	8	6	2	4001.3787	-0.0055
9	6	4	-	8	6	3	4001.3787	-0.0055
9	5	5	-	8	5	4	4001.9703	0.0025
9	5	4	-	8	5	3	4001.9703	0.0025
9	3	7	-	8	3	6	4004.5003	-0.0014
9	3	6	-	8	3	5	4005.6928	0.0010
9	2	7	-	8	2	6	4028.8487	-0.0015
12	2	11	-	12	1	12	4051.3764	0.0007
9	1	8	-	8	1	7	4083.2877	-0.0012
2	2	1	-	1	1	0	4113.3258	0.0000
2	2	0	-	1	1	1	4134.0524	-0.0003
20	1	19	-	20	0	20	4184.2663	0.0071
13	2	12	-	13	1	13	4189.7278	0.0013
11	0	11	-	10	1	10	4205.4223	0.0001
23	3	20	-	23	2	21	4269.7013	-0.0091
8	1	8	-	7	0	7	4289.1029	-0.0008
10	1	10	-	9	1	9	4331.9912	-0.0006
14	2	13	-	14	1	14	4338.9729	-0.0030
22	3	19	-	22	2	20	4347.6982	-0.0118
11	5	7	-	12	4	8	4357.5821	-0.0045
11	5	6	-	12	4	9	4357.8342	0.0008
10	0	10	-	9	0	9	4399.0699	-0.0021
6	4	3	-	7	3	4	4431.6677	0.0001
6	4	2	-	7	3	5	4432.2123	0.0011
10	2	9	-	9	2	8	4437.4129	0.0012
10	6	4	-	9	6	3	4446.2141	-0.0194
10	6	5	-	9	6	4	4446.2141	-0.0194
10	5	6	-	9	5	5	4446.9978	-0.0047
10	5	5	-	9	5	4	4446.9978	-0.0050
10	3	8	-	9	3	7	4450.2459	0.0063
10	3	7	-	9	3	6	4452.2743	-0.0002
10	2	8	-	9	2	7	4483.1464	0.0001
21	1	20	-	21	0	21	4515.4142	0.0033

20	3	17	-	20	2	18	4529.5961	0.0037
10	1	9	-	9	1	8	4534.3061	-0.0009
3	2	2	-	2	1	1	4537.3637	0.0010
15	1	14	-	14	2	13	4547.4042	0.0014
3	2	1	-	2	1	2	4600.1238	-0.0006
19	3	16	-	19	2	17	4627.4597	-0.0057
9	1	9	-	8	0	8	4657.7254	0.0005
16	2	15	-	16	1	16	4669.6396	0.0028
12	0	12	-	11	1	11	4700.5189	0.0006
18	3	15	-	18	2	16	4726.0563	0.0021
11	1	11	-	10	1	10	4762.8909	0.0009
10	5	6	-	11	4	7	4805.1568	-0.0048
10	5	5	-	11	4	8	4805.2856	0.0005
17	3	14	-	17	2	15	4822.6503	-0.0008
11	0	11	-	10	0	10	4829.5149	0.0009
17	2	16	-	17	1	17	4850.6467	0.0048
5	4	2	-	6	3	3	4877.7786	-0.0004
5	4	1	-	6	3	4	4877.9993	0.0029
11	6	5	-	10	6	4	4891.1617	-0.0005
11	6	6	-	10	6	5	4891.1617	-0.0005
11	5	7	-	10	5	6	4892.1652	0.0104
11	5	6	-	10	5	5	4892.1652	0.0098
11	3	9	-	10	3	8	4896.1368	-0.0023
11	3	8	-	10	3	7	4899.4304	-0.0040
16	3	13	-	16	2	14	4914.8415	0.0012
11	2	9	-	10	2	8	4939.0194	-0.0010
4	2	3	-	3	1	2	4951.1328	-0.0001
11	1	10	-	10	1	9	4984.3778	0.0010
15	3	12	-	15	2	13	5000.5918	0.0095
10	1	10	-	9	0	9	5023.1639	0.0000
18	2	17	-	18	1	18	5041.7328	0.0019
4	2	2	-	3	1	3	5078.1045	0.0005
16	1	15	-	15	2	14	5121.4110	-0.0086
13	3	10	-	13	2	11	5146.8501	0.0018
13	0	13	-	12	1	12	5191.9570	-0.0002
12	1	12	-	11	1	11	5193.2443	0.0005
23	1	22	-	23	0	23	5198.3754	-0.0117
12	3	9	-	12	2	10	5205.6903	0.0011
19	2	18	-	19	1	19	5242.5671	0.0071
9	5	4	-	10	4	7	5252.1138	-0.0270
9	5	5	-	10	4	6	5252.1138	0.0304
11	3	8	-	11	2	9	5254.7213	0.0000
12	0	12	-	11	0	11	5257.9870	0.0007

10	3	7	-	10	2	8	5294.3072	-0.0002
12	2	11	-	11	2	10	5320.6263	-0.0006
4	4	0	-	5	3	3	5323.3419	-0.0478
4	4	1	-	5	3	2	5323.3419	0.0246
9	3	6	-	9	2	7	5325.1810	0.0018
12	6	6	-	11	6	5	5336.1827	0.0044
12	6	7	-	11	6	6	5336.1827	0.0044
12	5	8	-	11	5	7	5337.4376	0.0013
12	5	7	-	11	5	6	5337.4376	-0.0001
12	4	9	-	11	4	8	5339.6056	-0.0014
12	4	8	-	11	4	7	5339.7264	-0.0033
12	3	10	-	11	3	9	5342.1715	-0.0044
12	3	9	-	11	3	8	5347.2766	-0.0016
8	3	5	-	8	2	6	5348.3372	-0.0004
5	2	4	-	4	1	3	5354.6578	-0.0078
7	3	4	-	7	2	5	5364.9472	0.0002
6	3	3	-	6	2	4	5376.2337	0.0008
5	3	2	-	5	2	3	5383.3984	0.0010
11	1	11	-	10	0	10	5386.9827	0.0008
4	3	1	-	4	2	2	5387.5509	0.0004
3	3	0	-	3	2	1	5389.6636	0.0009
3	3	1	-	3	2	2	5391.1145	0.0014
4	3	2	-	4	2	3	5391.8898	0.0010
5	3	3	-	5	2	4	5393.4772	-0.0001
6	3	4	-	6	2	5	5396.2740	-0.0031
7	3	5	-	7	2	6	5400.7532	0.0007
8	3	6	-	8	2	7	5407.4256	-0.0001
9	3	7	-	9	2	8	5416.8692	-0.0004
10	3	8	-	10	2	9	5429.6957	-0.0018
12	1	11	-	11	1	10	5433.3565	0.0027
11	3	9	-	11	2	10	5446.5522	-0.0015
12	3	10	-	12	2	11	5468.1009	-0.0017
13	3	11	-	13	2	12	5495.0179	-0.0011
14	3	12	-	14	2	13	5527.9773	0.0008
15	3	13	-	15	2	14	5567.6368	-0.0012
5	2	3	-	4	1	4	5569.1619	0.0005
16	3	14	-	16	2	15	5614.6444	-0.0007
13	1	13	-	12	1	12	5623.0504	0.0011
17	3	15	-	17	2	16	5669.6081	-0.0007
14	0	14	-	13	1	13	5678.7721	0.0000
13	0	13	-	12	0	12	5684.6819	-0.0008
17	1	16	-	16	2	15	5697.6385	-0.0046
8	5	4	-	9	4	5	5698.4553	-0.0020

8	5	3	-	9	4	6	5698.4553	-0.0266
18	3	16	-	18	2	17	5733.1014	0.0002
6	2	5	-	5	1	4	5748.0183	-0.0031
12	1	12	-	11	0	11	5750.7123	0.0005
13	2	12	-	12	2	11	5761.4003	0.0001
13	5	9	-	12	5	8	5782.8595	0.0008
13	5	8	-	12	5	7	5782.8595	-0.0022
13	4	10	-	12	4	9	5785.5703	0.0028
13	4	9	-	12	4	8	5785.7940	0.0087
13	3	11	-	12	3	10	5788.3148	-0.0015
13	3	10	-	12	3	9	5795.9201	-0.0042
19	3	17	-	19	2	18	5805.6503	0.0034
13	1	12	-	12	1	11	5881.0832	0.0006
20	3	18	-	20	2	19	5887.7180	0.0015
21	3	19	-	21	2	20	5979.7259	0.0053
14	1	14	-	13	1	13	6052.3097	-0.0019
12	6	7	-	13	5	8	6071.9054	0.0126
12	6	6	-	13	5	9	6071.9054	0.0070
6	2	4	-	5	1	5	6074.7513	-0.0005
14	0	14	-	13	0	13	6109.8665	0.0023
13	1	13	-	12	0	12	6115.7752	0.0004
7	2	6	-	6	1	5	6131.2991	0.0001
7	5	3	-	8	4	4	6144.3824	0.0058
7	5	2	-	8	4	5	6144.3824	-0.0036
15	0	15	-	14	1	14	6160.2905	0.0000
14	4	11	-	13	4	10	6231.7565	0.0055
14	4	10	-	13	4	9	6232.1246	0.0042
14	3	12	-	13	3	11	6234.5205	0.0018
14	3	11	-	13	3	10	6245.4955	-0.0052
18	1	17	-	17	2	16	6274.7021	0.0000
14	1	13	-	13	1	12	6327.4009	0.0038
15	1	15	-	14	1	14	6481.0472	0.0039
14	1	14	-	13	0	13	6483.4023	-0.0013
8	2	7	-	7	1	6	6504.6413	0.0000
15	0	15	-	14	0	14	6533.8322	0.0022
7	2	5	-	6	1	6	6596.5881	0.0016
16	0	16	-	15	1	15	6636.1376	0.0021
3	3	1	-	2	2	0	6724.2662	0.0001
3	3	0	-	2	2	1	6724.5594	0.0001
15	1	15	-	14	0	14	6854.5819	-0.0008
9	2	8	-	8	1	7	6868.2438	-0.0004
17	0	17	-	16	1	16	7106.1987	-0.0010
8	2	6	-	7	1	7	7136.5858	0.0000

4	3	2	-	3	2	1	7168.1342	0.0016
4	3	1	-	3	2	2	7169.6049	0.0012
10	2	9	-	9	1	8	7222.3701	0.0031
16	1	16	-	15	0	15	7230.0207	0.0040
11	4	7	-	11	3	8	7530.3525	0.0052
10	4	6	-	10	3	7	7535.8626	0.0051
11	4	8	-	11	3	9	7537.9357	-0.0017
9	4	5	-	9	3	6	7539.7933	0.0029
10	4	7	-	10	3	8	7540.2145	-0.0035
8	4	4	-	8	3	5	7542.5236	-0.0006
8	4	5	-	8	3	6	7543.7111	0.0032
7	4	3	-	7	3	4	7544.3683	0.0029
7	4	4	-	7	3	5	7544.9054	0.0004
6	4	2	-	6	3	3	7545.5536	-0.0038
17	1	17	-	16	0	16	7610.1286	0.0016
5	3	3	-	4	2	2	7610.8759	0.0006
5	3	2	-	4	2	3	7615.3094	0.0052

<sup>a</sup> $\Delta\nu$  is the difference between measure and calculated frequencies.

**Table C.2.2.** Assigned rotational transitions of the <sup>13</sup>C1 BnBz-t isotopologe.

J'	Ka'	Kc'	-	J''	Ka''	Kc''	$\nu_{\text{Exp}}$ /MHz	$\nu^a$ /MHz
7	1	7	-	6	0	6	3902.6168	0.0048
8	1	8	-	7	0	7	4274.9753	-0.0157
3	2	1	-	2	1	2	4582.3192	0.0008
9	1	9	-	8	0	8	4642.6944	0.0050
10	1	10	-	9	0	9	5007.1772	-0.0018
11	1	11	-	10	0	10	5369.9888	0.0029
6	2	5	-	5	1	4	5727.3747	0.0005
12	1	12	-	11	0	11	5732.6097	-0.0033
13	1	13	-	12	0	12	6096.4663	0.0053
7	2	6	-	6	1	5	6109.6850	-0.0003

<sup>a</sup> $\Delta\nu$  is the difference between measure and calculated frequencies.

**Table C.2.3.** Assigned rotational transitions of the <sup>13</sup>C2 BnBz-t isotopologe.

J'	Ka'	Kc'	-	J''	Ka''	Kc''	$\nu_{\text{Exp}}$ /MHz	$\nu^a$ /MHz
6	1	6	-	5	0	5	3514.4588	0.0078
2	2	1	-	1	1	0	4091.8464	0.0028
8	1	8	-	7	0	7	4262.6058	0.0062
3	2	2	-	2	1	1	4512.7562	0.0004

3	2	1	-	2	1	2	4574.2011	-0.0056
10	1	10	-	9	0	9	4992.1501	-0.0035
11	1	11	-	10	0	10	5353.6194	-0.0023
12	1	12	-	11	0	11	5714.8870	0.0031
13	1	13	-	12	0	12	6077.3289	-0.0049

<sup>a</sup> $\Delta\nu$  is the difference between measure and calculated frequencies.

**Table C.3.** Cartesian coordinates of 14 carbons in BnBz-g obtained through Kraitchman's substitution equations with their Costain errors. They are compared with theoretical results(re).

	<i>re</i>	<i>rs</i>		<i>re</i>	<i>rs</i>		<i>re</i>	<i>rs</i>	
	<i>a</i>	<i>a</i>	$\pm$ err.	<i>b</i>	<i>b</i>	$\pm$ err.	<i>c</i>	<i>c</i>	$\pm$ err.
C(1)	0.7701	0.7021	0.0030	0.7184	0.6818	0.0030	-0.6029	-0.6048	0.0035
C(2)	2.0696	2.0441	0.0008	0.1717	0.1539	0.0111	-0.1293	-0.1122	0.0152
C(3)	2.9589	2.9030	0.0006	1.0466	1.0683	0.0016	0.4952	0.5301	0.0033
C(4)	4.1815	4.1420	0.0004	0.5839	0.6292	0.0027	0.9569	0.9994	0.0017
C(5)	4.5226	4.5321	0.0004	-0.7557	-0.6880	0.0025	0.7994	0.8110	0.0021
C(6)	3.6381	3.6799	0.0005	-1.6313	-1.5861	0.0011	0.1790	0.1327	0.0137
C(7)	2.4140	2.4399	0.0007	-1.1715	-1.1532	0.0015	-0.2857	-0.3111	0.0054
C(8)	-1.2931	-1.2425	0.0014	0.2012	0.1536	0.0109	-1.6833	-1.7117	0.0010
C(9)	-2.3291	-2.2974	0.0009	0.0071	0.0235	0.0924	-0.6143	-0.6232	0.0035
C(10)	-2.9714	-2.8642	0.0006	-1.2224	-1.2792	0.0013	-0.4766	-0.3726	0.0046
C(11)	-3.9138	-3.8021	0.0004	-1.4201	-1.4584	0.0011	0.5240	0.6288	0.0027
C(12)	-4.2237	-4.2018	0.0004	-0.3850	-0.3542	0.0047	1.3987	1.4134	0.0012
C(13)	-3.5891	-3.6565	0.0005	0.8450	0.8839	0.0019	1.2673	1.1751	0.0015
C(14)	-2.6463	-2.7066	0.0006	1.0409	1.0626	0.0016	0.2664	0.1696	0.0100

**Table C.4.** Cartesian coordinates of four carbons in BnBz-t obtained through Kraitchman's substitution equations with their Costain errors. They are compared with theoretical results(re).

	<i>re</i>	<i>rs</i>		<i>re</i>	<i>rs</i>		<i>re</i>	<i>rs</i>	
	<i>a</i>	<i>a</i>	$\pm$ err.	<i>b</i>	<i>b</i>	$\pm$ err.	<i>c</i>	<i>c</i>	$\pm$ err.
C(10)	-4.1215	-3.0258	0.0037	0.7573	0.0000	0.0496	1.2029	1.2230	0.0092
C(14)	-3.0108	-3.0258	0.0037	-0.0768	0.0000	0.0496	-1.2007	-1.2230	0.0092
C(11)	-3.0109	-4.1476	0.0015	-0.0767	-0.7065	0.0085	1.2007	1.2312	0.0049
C(13)	-4.1214	-4.1476	0.0015	0.7572	0.7065	0.0085	-1.2031	-1.2312	0.0049

**Table C.5.** List of computationally identified BnBz dimers at the B3LYP-D3(BJ)/def2-TZVP level of theory with their relative energies, rotational constants, abundances, dipole moments, and quartic centrifugal distortion constants.

	$\Delta E^a$ / kJ mol <sup>-1</sup>	$P^b$ / %	A / MHz	B / MHz	C / MHz	$ \mu_a ,  \mu_b ,  \mu_c $ / Debye	$\Delta_J$ / kHz	$\Delta_K$ / kHz	$\Delta_{JK}$ / kHz	$\delta_J$ / kHz	$\delta_K$ / kHz
BnBz- <i>tg</i> -1	0.00	7%	203.7	126.6	110.6	0,3,0,4	0.002819	0.006571	0.005787	-0.000131	-0.011157
BnBz- <i>tg</i> -2	0.49	6%	201.2	122.9	111.9	0.4,2,5,0,9	0.002903	0.016992	-0.003318	-0.00013	-0.008315
BnBz- <i>tg</i> -3	1.03	5%	195.8	132.6	113.6	1.8,0,1,0,1	0.002328	0.006491	0.000492	0.000295	-0.003172
BnBz- <i>g</i> <sup>+</sup> <i>g</i> <sup>-</sup> -4	1.95	4%	198.3	130.0	115.0	1.4,0,0,3	0.003655	0.014885	-0.007105	0.000572	-0.005346
BnBz- <i>g</i> <sup>+</sup> <i>g</i> <sup>-</sup> -5	3.20	3%	211.5	122.2	110.3	0.8,2,7,0,2	0.002527	0.014395	-0.003628	0.000447	-0.005502
BnBz- <i>g</i> <sup>+</sup> <i>g</i> <sup>-</sup> -6	3.38	3%	208.7	114.3	104.4	2,3,0,1,0,9	0.003974	0.021209	-0.011192	0.000832	-0.005914
BnBz- <i>tt</i> -7	3.62	3%	156.6	147.5	113.4	0.4,2,2,0,3	0.008105	-0.013514	0.007938	0.002503	0.03234
BnBz- <i>tg</i> -8	3.85	2%	251.5	102.1	98.2	2,2,0,5,0,5	0.002717	0.035651	0.018211	0.00102	-0.278171
BnBz- <i>g</i> <sup>+</sup> <i>g</i> <sup>-</sup> -9	3.88	2%	183.1	122.5	108.4	0,3,2,0,3	0.003156	0.01054	-0.00327	0.000744	0.012063
BnBz- <i>tt</i> -10	3.92	2%	183.3	140.8	116.5	0,5,1,7,0,4	0.007087	0.021332	-0.017768	0.001894	-0.002353
BnBz- <i>g</i> <sup>+</sup> <i>g</i> <sup>-</sup> -11	4.27	2%	198.2	124.6	113.5	2,3,1,1	0.004237	0.021257	-0.009866	-0.000051	-0.00399
BnBz- <i>tg</i> -12	4.57	2%	253.0	91.5	88.7	0,8,0,1,0,1	0.002415	0.040744	-0.011814	-0.000094	0.020653
BnBz- <i>g</i> <sup>+</sup> <i>g</i> <sup>-</sup> -13	4.63	2%	304.6	81.6	75.6	0,8,0,1,0,1	0.000753	0.029034	-0.001282	0.000029	-0.002614
BnBz- <i>g</i> <sup>+</sup> <i>g</i> <sup>-</sup> -14	4.63	2%	304.6	81.6	75.6	0,1,1,7,2,8	0.000753	0.029034	-0.001282	0.000029	-0.002614
BnBz- <i>g</i> <sup>+</sup> <i>g</i> <sup>-</sup> -15	4.75	2%	223.2	110.7	105.7	1,5,0,2,0,4	0.002893	0.017952	0.002872	-0.00032	0.011144
BnBz- <i>g</i> <sup>+</sup> <i>g</i> <sup>-</sup> -16	4.91	2%	228.8	100.4	91.2	1,4,1,2,0,9	0.003194	0.020634	0.029837	-0.00029	0.007757
BnBz- <i>g</i> <sup>+</sup> <i>g</i> <sup>-</sup> -17	4.97	2%	172.2	139.6	113.8	1,1,1,1,3	0.00889	0.01511	-0.020507	0.000536	-0.012254
BnBz- <i>tt</i> -18	4.98	2%	327.6	79.2	71.7	0,2,1,1,2,9	0.00047	0.029268	0.002767	0.000061	0.001933
BnBz- <i>g</i> <sup>+</sup> <i>g</i> <sup>-</sup> -19	5.16	2%	220.4	116.2	107.1	0,4,1,5,0,6	0.002254	0.017184	0.000865	-0.000191	0.006475
BnBz- <i>tg</i> -20	5.17	2%	192.3	124.3	113.3	2,2,1,3,0,3	0.004016	0.032858	-0.009039	0.000341	-0.003788
BnBz- <i>tt</i> -21	5.22	2%	208.0	100.1	89.3	0,0,2,9	0.001129	0.019928	0.010099	0.000064	-0.013653
BnBz- <i>tt</i> -22	5.31	2%	317.3	79.9	73.7	1,2,1,0,3	0.000604	0.030398	0.000373	0.000035	-0.034867
BnBz- <i>g</i> <sup>+</sup> <i>g</i> <sup>-</sup> -23	5.37	2%	231.3	110.3	105.0	0,0,0	0.002296	0.003295	0.010937	0.000288	0.007339
BnBz- <i>g</i> <sup>+</sup> <i>g</i> <sup>-</sup> -24	5.42	1%	157.8	150.7	115.0	2,2,1,5,1	0.018802	0.038533	-0.053898	-0.00048	-0.117778
BnBz- <i>g</i> <sup>+</sup> <i>g</i> <sup>-</sup> -25	5.43	1%	198.3	121.0	112.0	0,1,3,2,0,6	0.003102	0.034448	-0.007874	0.000077	-0.005982
BnBz- <i>g</i> <sup>+</sup> <i>g</i> <sup>-</sup> -26	5.50	1%	183.8	124.8	116.8	0,1,2,0,1	0.003161	0.020445	-0.002734	0.000405	-0.015868
BnBz- <i>g</i> <sup>+</sup> <i>g</i> <sup>-</sup> -27	5.58	1%	219.8	114.4	100.0	1,2,0,8,1,2	0.002454	0.024104	-0.005531	0.000329	0.003327
BnBz- <i>g</i> <sup>+</sup> <i>g</i> <sup>-</sup> -28	5.71	1%	204.3	122.5	106.0	1,5,0,3,0,1	0.003915	0.02371	-0.009423	0.000255	-0.002176
BnBz- <i>g</i> <sup>+</sup> <i>g</i> <sup>-</sup> -29	6.00	1%	204.3	113.6	96.3	0,0,2,1	0.005154	0.070538	-0.014564	0.000865	0.004778

BnBz-gg <sup>+</sup> -30	6.04	1%	192.9	128.7	113.6	1.3,0.5,0	0.006374	0.050165	-0.019419	0.002124	-0.004839
BnBz-tg-31	6.17	1%	224.2	109.2	107.4	0,3,0	0.001767	0.008426	0.001383	-0.000347	0.051702
BnBz-gg <sup>-</sup> -32	6.76	1%	200.9	120.3	103.7	2.9,0.6,1	0.002452	0.009696	0.001675	0.000234	-0.005491
BnBz-tg-33	7.12	1%	207.6	113.5	99.2	0.3,2.8,0.4	0.002964	0.015069	0.007405	0.000223	-0.003607
BnBz-gg <sup>-</sup> -34	7.27	1%	263.6	91.1	82.9	2.6,0.6,1.4	0.003204	0.065288	-0.015869	-0.000176	-0.002622
BnBz-tt-35	7.41	1%	199.4	114.8	97.1	0.4,0.4,0	0.009316	0.076018	-0.031801	0.002693	-0.00429
BnBz-tg-36	7.62	1%	188.5	130.4	103.7	1,0.6,3.3	0.00547	0.020804	-0.010082	0.001126	0.001334
BnBz-tg-37	7.68	1%	255.9	98.4	91.7	2.4,0.5,1	0.001209	0.03857	0.015841	0.00008	-0.026124
BnBz-tt-38	7.78	1%	151.3	144.9	105.8	0.1,0.3,0.1	0.004765	-0.017926	0.015564	0.000574	0.108161
BnBz-gg <sup>+</sup> -39	8.02	1%	163.6	141.0	108.2	0.6,2.1,1.1	0.013781	0.010685	-0.02176	-0.0004	0.00078
BnBz-tg-40	8.13	1%	265.6	99.8	89.3	1.1,1.6,0.6	0.000787	-0.016068	0.036461	0.000139	0.018961
BnBz-gg <sup>+</sup> -41	8.26	1%	173.8	137.4	124.6	0.4,0.5,0	0.004782	0.021353	-0.008546	0.000938	0.000663
BnBz-tg-42	8.36	1%	211.1	118.7	97.4	0.3,2.1,0.5	0.002789	0.020905	0.006529	0.000218	0.012891
BnBz-tg-43	8.41	1%	206.0	116.3	87.6	3.2,1,1.5	0.004067	-0.024744	0.048938	0.000664	0.024938
BnBz-gg <sup>+</sup> -44	8.47	1%	167.8	137.6	102.7	2.9,1.5,1.3	0.009997	-0.004673	-0.003609	0.000967	0.008347
BnBz-gg <sup>-</sup> -45	8.61	1%	207.8	114.9	95.7	0.3,2.7,0.3	0.001923	0.014185	0.006018	0.000386	-0.011039
BnBz-tg-46	8.70	1%	195.2	120.6	95.0	0.5,0.4,0	0.00205	-0.004754	0.012995	0.00038	-0.002827
BnBz-tg-47	8.82	1%	179.4	135.7	103.3	1.2,0.7,0.1	0.010802	0.018872	-0.027282	0.001985	-0.016091
BnBz-tg-48	8.86	1%	219.2	116.6	102.4	0.1,1.5,0.1	0.008492	-0.006905	0.020096	-0.002987	0.045399
BnBz-tt-49	9.09	1%	182.3	114.8	94.3	0.6,0.1,0.1	0.007055	0.050813	-0.016166	0.002154	-0.006126
BnBz-tt-50	9.19	0%	197.9	118.0	104.0	1.9,0.2,1.3	0.002097	0.004254	0.008159	0.000065	-0.008232
BnBz-tt-51	9.19	0%	267.6	99.0	88.7	3,0.1,0.9	0.001135	-0.029139	0.059852	0.000111	0.030038
BnBz-tg-52	9.24	0%	265.7	96.6	88.0	2.4,1.5,1.2	0.001774	-0.022132	0.052125	0.000052	0.031995
BnBz-gg <sup>-</sup> -53	9.27	0%	209.8	101.1	97.9	2,0.2,0.3	0.013275	0.135141	-0.075331	0.003085	0.062795
BnBz-tt-54	9.39	0%	150.7	140.5	115.8	2.5,0.1,1.4	0.007366	0.004664	-0.008637	0.000329	-0.007832
BnBz-gg <sup>-</sup> -55	9.40	0%	171.9	139.1	106.4	0.1,2.4,0	0.033808	0.073848	-0.10311	-0.000901	-0.090838
BnBz-gg <sup>+</sup> -56	9.63	0%	212.5	109.4	94.9	1.9,0.4,1	0.001741	0.017893	0.002364	0.000363	-0.000978
BnBz-tg-57	9.76	0%	150.3	144.2	123.9	2.7,1,1.6	0.042571	0.060339	-0.094151	-0.000385	-0.136381
BnBz-tg-58	9.79	0%	270.7	98.2	88.9	0,0,0	0.000831	-0.009976	0.02744	0.000176	0.015628
BnBz-tt-59	9.91	0%	212.3	97.3	86.5	2.1,0,0.7	0.002315	0.029227	0.014241	0.000199	-0.014411
BnBz-gg <sup>-</sup> -60	9.98	0%	230.6	107.0	98.0	0,0,0	0.001836	0.015021	0.005108	0.000459	-0.026732
BnBz-tt-61	10.06	0%	250.9	93.4	89.9	1.5,0.1,0.8	0.002248	0.024849	0.00312	0.000293	-0.007322
BnBz-tt-62	10.17	0%	261.6	88.2	84.7	0.1,0.4,3.3	0.003019	0.020255	0.054076	-0.000578	-0.133459
BnBz-tg-63	10.29	0%	201.5	111.0	86.5	0.7,0.4,3.2	0.002627	0.01087	0.003614	0.000208	0.005423
BnBz-tt-64	10.38	0%	292.9	93.0	87.6	0.4,3,0.5	0.003363	0.105709	0.005068	0.000658	0.029815

BnBz- tg-65	10.45	0%	230.4	106.9	92.5	1,0,8,0,1	0.001581	0.007331	0.014045	-0.000062	0.013548
BnBz- tt-66	10.48	0%	198.9	110.1	88.3	0,3,2,1,2,9	0.003059	0.012568	0.007251	0.000651	0.006955
BnBz- gg-67	10.78	0%	205.3	114.7	85.4	0,5,0,6,0,2	0.001721	0.005643	0.018378	0.000627	0.010387
BnBz- gg-68	11.11	0%	268.3	94.9	88.4	0,1,1,4,2,7	0.002033	-0.289698	0.384323	0.000514	-0.107343
BnBz- tt-69	11.12	0%	267.3	89.1	81.2	0,3,1,9,3	0.00375	0.090391	0.009035	0.000753	0.03088
BnBz- gg-70	11.25	0%	189.8	126.4	106.2	2,3,0,5,2,4	0.003194	0.006206	0.002593	0.000346	-0.001926
BnBz- gg-71	11.25	0%	176.3	133.7	119.1	0,9,0,7,2,4	0.066337	0.349089	-0.192326	-0.01779	-0.241682
BnBz- gg-72	11.26	0%	196.7	121.0	111.0	0,8,1,4,1	0.002858	0.010308	-0.000137	-0.000255	-0.002428
BnBz- tt-73	11.42	0%	180.8	112.1	98.3	0,5,1,4,0,2	0.004267	0.021916	-0.000477	0.000656	-0.008551
BnBz- tg-74	11.50	0%	206.7	109.1	81.7	1,9,0,2,0	0.002128	0.013066	0.005173	0.000698	0.005651
BnBz- tg-75	11.54	0%	257.4	97.2	87.4	2,4,0,1	0.003028	0.036093	0.001041	0.000758	0.020549
BnBz- gg-76	11.80	0%	259.1	92.8	90.4	1,9,0,3,0,3	0.002086	0.011068	0.010462	0.00016	0.044511
BnBz- gg-77	11.88	0%	157.4	129.9	111.7	0,1,4,0	0.00372	-0.005182	0.008273	0.000345	-0.000126
BnBz- tt-78	12.10	0%	206.2	108.8	82.5	0,9,1,9,1,7	0.001762	0.010465	0.006578	0.000583	0.006247
BnBz- gg-79	12.21	0%	209.6	103.0	82.2	2,4,0,3,0,9	0.011673	0.14511	-0.062275	0.002305	0.002117
BnBz- gg-80	12.28	0%	158.7	111.4	85.9	0,0,0	0.006338	0.022088	-0.008829	0.00196	0.004404
BnBz- gg-81	12.33	0%	195.9	113.3	89.2	0,7,2,1,9	0.001495	0.004492	0.026456	0.000237	0.007886
BnBz- gg-82	12.37	0%	215.4	100.4	80.5	0,1,0,3,3,8	0.011041	0.155591	-0.068533	0.002171	-0.000272
BnBz- tg-83	12.39	0%	313.3	83.7	79.6	0,2,0,4,3,3	0.002105	0.011997	0.013291	0.000106	0.009782
BnBz- gg-84	12.58	0%	166.2	113.5	92.6	1,0,3,0	0.00457	0.01651	-0.000323	0.001246	0.001597
BnBz- gg-85	12.59	0%	188.8	121.0	90.5	2,5,1,7,0,5	0.002699	0.00793	0.005898	-0.00021	0.008147
BnBz- tg-86	12.60	0%	150.5	139.4	114.8	0,7,1,4,2,7	0.004239	-0.013305	0.011568	-0.000196	0.037043
BnBz- gg-87	12.66	0%	251.8	96.0	82.1	1,1,0,9,0,9	0.002502	0.022307	0.008733	0.000496	0.006647
BnBz- tg-88	12.71	0%	193.5	98.5	77.4	1,9,1,5,0,9	0.002499	0.007658	0.004347	0.000388	0.006389
BnBz- tg-89	12.90	0%	199.3	108.5	86.9	0,5,1,7,1,5	0.003077	0.012571	-0.000537	0.000633	-0.002186
BnBz- gg-90	13.04	0%	197.3	105.7	83.5	0,2,5,0	0.001833	-0.010579	0.027261	0.000153	0.005734
BnBz- gg-91	13.21	0%	191.8	120.5	102.4	0,9,1,0,3	0.005334	0.079414	-0.023277	-0.000899	0.011466
BnBz- gg-92	13.25	0%	163.3	128.1	103.9	0,2,1,5,1,1	0.008423	0.011324	-0.015678	0.003267	-0.005027
BnBz- tg-93	13.25	0%	158.4	130.9	97.9	1,1,1,8,0,3	0.006605	-0.020002	0.015391	0.000916	0.009427
BnBz- tt-94	13.32	0%	203.3	110.8	83.8	0,3,2,8,1,7	0.00202	0.009424	0.004892	0.000532	0.006494
BnBz- gg-95	13.45	0%	180.7	125.6	95.4	0,6,1,7,0,8	0.008551	0.009884	-0.014616	0.00321	-0.00399
BnBz- gg-96	13.48	0%	166.2	143.7	101.9	0,5,1,3,3	0.0085	0.010647	-0.017945	0.000029	-0.020496
BnBz- gg-97	13.51	0%	230.4	99.7	82.0	1,1,0,3,0,7	0.003282	0.027061	0.008721	0.001048	0.014546
BnBz- gg-98	13.60	0%	307.2	76.4	69.0	0,8,2,4,0,2	0.000933	0.046849	-0.001528	0.000126	0.002186
BnBz- tg-99	13.75	0%	184.8	109.0	87.0	0,2,0,5,0	0.006461	0.005497	-0.000155	0.001412	0.010964

BnBz- tg-100	13.79	0%	307.3	76.7	74.8	2,0,9,0,4	0.001784	0.050597	-0.00376	-0.000097	-0.022306
BnBz- tg-101	13.88	0%	188.8	121.0	90.5	0,9,1,9,1,8	0.0027	0.00788	0.005888	-0.000212	0.008165
BnBz- gg- 102	13.95	0%	230.7	93.6	85.2	1,2,0,1,0,5	0.002896	0.034821	-0.003878	0.000148	0.009879
BnBz- g <sup>-</sup> g <sup>-</sup> - 103	13.97	0%	221.1	86.4	73.8	0,9,0,7,0,3	0.004366	0.077819	-0.023146	0.001028	0.005318
BnBz- gg <sup>-</sup> - 104	14.06	0%	270.9	72.7	65.5	0,7,0,1,0,1	0.001178	0.060934	-0.00549	0.000202	-0.002162
BnBz- gg <sup>-</sup> - 105	14.18	0%	189.7	101.7	85.6	0,3,0,5,0,1	0.003995	0.017228	0.004896	0.001174	0.010259
BnBz- tg-106	14.21	0%	218.6	95.7	78.8	0,5,0,4,0,4	0.00346	0.042195	-0.010045	0.001266	0.007844
BnBz- tg-107	14.24	0%	214.1	109.7	84.9	2,4,0,3,0,9	0.001105	0.006318	0.009248	0.000168	0.005285
BnBz- tg-108	14.30	0%	180.2	105.5	83.5	3,2,2,0,7	0.011717	0.041814	-0.028086	0.00338	0.011959
BnBz- tg-109	14.39	0%	285.2	71.1	63.6	0,2,7,1,8	0.000875	0.043263	-0.000336	0.000159	-0.000281
BnBz- gg <sup>-</sup> - 110	14.50	0%	268.7	75.8	74.1	0,4,1,8,0,7	0.003844	0.165061	-0.03378	0.000305	0.004331
BnBz- gg <sup>-</sup> - 111	14.59	0%	205.4	109.3	86.1	2,9,2,3,0,1	0.001152	0.009335	0.00947	0.000197	0.00118
BnBz- gg <sup>-</sup> - 112	14.72	0%	285.4	71.2	63.7	0,7,0,6,0,5	0.00085	0.042764	-0.000388	0.000167	-0.002408
BnBz- tg-113	14.73	0%	220.9	82.8	71.4	0,3,1,2,2,7	0.003624	0.071128	-0.019113	0.000929	0.008912
BnBz- gg <sup>+</sup> - 114	14.74	0%	330.7	73.4	69.3	0,1,2,1,7	0.001071	0.034846	0.000206	0.000126	0.001392
BnBz- gg <sup>+</sup> - 115	14.87	0%	273.8	72.4	64.6	0,4,2,2,1,8	0.001161	0.060434	-0.005595	0.000202	0.000481
BnBz- gg <sup>+</sup> - 116	14.95	0%	202.3	117.4	95.1	0,4,0,8,3,1	0.002625	0.018078	0.003334	0.000005	0.008422
BnBz- gg <sup>+</sup> - 117	16.02	0%	168.8	125.1	119.3	0,5,2,4,0,4	0.006326	0.047226	-0.019011	-0.002373	0.025353
BnBz- tg-118	16.92	0%	235.8	84.9	73.1	1,4,1,7,1,8	0.004733	0.104125	-0.026604	0.001235	0.001877
BnBz- tg-119	16.94	0%	164.9	134.4	99.3	0,2,0,4,0,1	0.008836	-0.002309	-0.005008	0.001527	0.002977
BnBz- tg-120	17.16	0%	159.9	105.9	82.0	0,5,2,3,1,5	0.011366	0.054436	-0.021487	0.003534	-0.00054
BnBz- tg-121	17.21	0%	177.6	99.8	84.7	1,7,0,3,0	0.003924	0.029031	-0.007623	0.00097	-0.009191
BnBz- tg-122	17.94	0%	248.6	83.3	74.0	1,2,0,7,0,7	0.002757	0.068476	-0.015758	0.000552	-0.000822
BnBz- gg <sup>-</sup> - 123	18.60	0%	198.0	110.8	83.3	0,1,0,7,1,2	0.001909	-0.001223	0.017059	0.000422	0.00951
BnBz- tg-124	18.67	0%	176.1	112.6	83.2	0,3,2,8,0,9	0.003539	0.008402	0.018466	-0.000257	0.019225
BnBz- tg-125	18.82	0%	196.5	124.2	106.6	1,0,8,1,3	0.003844	-0.003288	0.022202	-0.000532	0.010933
BnBz- gg <sup>-</sup> - 126	19.24	0%	152.4	103.6	75.7	0,2,6,0	0.01499	0.013233	-0.027386	0.002611	-0.004137
BnBz- tg-127	19.57	0%	148.5	128.3	93.8	1,5,1,0,3	0.012934	-0.082233	0.072408	0.004388	0.181964

BnBz-  
 $g^+g^-$ -  
 128      21.64      0%      166.4      97.8      67.4      0.5,2,2,0,9      0.009622      -0.000332      -0.008688      0.003445      0.004574

**Table C.6.** List of assigned dimer transitions.

J'	Ka'	Kc'	-	J''	Ka''	Kc''	$\nu_{\text{Exp}} / \text{MHz}$	$\nu^a / \text{MHz}$
6	5	2	-	5	4	1	2135.3150	0.0045
10	0	10	-	9	1	9	2204.1670	-0.0059
10	1	10	-	9	0	9	2207.2136	-0.0131
6	6	1	-	5	5	0	2301.2283	-0.0005
6	6	0	-	5	5	1	2301.2283	-0.0011
10	2	9	-	9	1	8	2311.4660	0.0077
7	5	3	-	6	4	2	2366.3848	0.0080
7	5	2	-	6	4	3	2366.8047	-0.0103
11	0	11	-	10	1	10	2421.8730	-0.0027
11	2	10	-	10	1	9	2515.3223	0.0105
7	6	2	-	6	5	1	2532.7488	0.0033
7	6	1	-	6	5	2	2532.7488	-0.0029
8	5	3	-	7	4	4	2598.2039	0.0150
9	4	6	-	8	3	5	2623.1138	-0.0006
12	0	12	-	11	1	11	2639.2519	0.0216
12	1	12	-	11	0	11	2640.0103	-0.0045
9	4	5	-	8	3	6	2686.5968	-0.0032
7	7	1	-	6	6	0	2698.5662	-0.0109
7	7	0	-	6	6	1	2698.5662	-0.0109
12	2	11	-	11	1	10	2723.6195	-0.0014
10	4	7	-	9	3	6	2822.9889	-0.0115
9	5	5	-	8	4	4	2825.0399	-0.0134
13	0	13	-	12	1	12	2856.4029	0.0014
13	1	13	-	12	0	12	2856.7855	-0.0053
13	1	12	-	12	2	11	2922.2589	0.0164
8	7	2	-	7	6	1	2930.1178	0.0015
8	7	1	-	7	6	2	2930.1178	0.0011
9	6	4	-	8	5	3	2995.1521	-0.0142
9	6	3	-	8	5	4	2995.3381	0.0076
11	4	8	-	10	3	7	3011.6629	-0.0091
10	5	6	-	9	4	5	3050.3061	0.0081
10	5	5	-	9	4	6	3062.4453	-0.0086
14	0	14	-	13	1	13	3073.4825	0.0043
14	1	14	-	13	0	13	3073.6691	-0.0003

13	3	11	-	12	2	10	3077.0852	-0.0054
8	8	1	-	7	7	0	3095.9206	0.0010
8	8	0	-	7	7	1	3095.9206	0.0010
14	1	13	-	13	2	12	3141.9319	-0.0036
14	2	13	-	13	1	12	3149.0350	-0.0170
9	7	3	-	8	6	2	3161.5632	0.0015
9	7	2	-	8	6	3	3161.5632	-0.0013
14	2	12	-	13	3	11	3172.8082	-0.0030
11	4	7	-	10	3	8	3210.3733	0.0003
10	6	5	-	9	5	4	3225.6717	-0.0004
10	6	4	-	9	5	5	3226.2481	0.0037
14	3	12	-	13	2	11	3268.3387	-0.0048
11	5	7	-	10	4	6	3270.0797	-0.0011
15	0	15	-	14	1	14	3290.4923	-0.0150
15	1	15	-	14	0	14	3290.6092	0.0088
11	5	6	-	10	4	7	3297.4695	-0.0124
9	8	1	-	8	7	2	3327.4636	-0.0068
9	8	2	-	8	7	1	3327.4636	-0.0068
15	1	14	-	14	2	13	3360.3948	-0.0013
15	2	14	-	14	1	13	3364.2201	0.0065
10	7	3	-	9	6	4	3392.8412	-0.0073
10	7	4	-	9	6	3	3392.8412	0.0071
11	6	6	-	10	5	5	3455.2158	0.0025
11	6	5	-	10	5	6	3456.9076	-0.0054
15	3	13	-	14	2	12	3466.5841	-0.0013
12	5	8	-	11	4	7	3481.5730	0.0109
9	9	0	-	8	8	1	3493.2533	-0.0032
9	9	1	-	8	8	0	3493.2533	-0.0032
12	4	8	-	11	3	9	3499.4860	0.0078
12	5	7	-	11	4	8	3537.1989	0.0025
16	2	15	-	15	1	14	3580.1690	0.0026
16	2	14	-	15	3	13	3635.5901	-0.0021
16	3	14	-	15	2	13	3670.9214	0.0124
13	5	9	-	12	4	8	3681.9828	-0.0002
12	6	7	-	11	5	6	3683.1034	0.0199
17	0	17	-	16	1	16	3724.5196	0.0136
17	1	17	-	16	0	16	3724.5196	-0.0079
10	9	2	-	9	8	1	3724.8171	0.0023
10	9	1	-	9	8	2	3724.8171	0.0023
13	5	8	-	12	4	9	3784.9486	0.0035
11	8	4	-	10	7	3	3790.3232	0.0025
11	8	3	-	10	7	4	3790.3232	0.0013
17	1	16	-	16	2	15	3795.5082	-0.0134

17	2	16	-	16	1	15	3796.5668	-0.0016
12	7	6	-	11	6	5	3854.3996	-0.0016
12	7	5	-	11	6	6	3854.5994	0.0029
17	2	15	-	16	3	14	3859.3501	-0.0009
16	4	13	-	15	3	12	3864.7357	-0.0024
14	5	10	-	13	4	9	3869.7104	-0.0116
17	3	15	-	16	2	14	3879.8038	-0.0036
10	10	0	-	9	9	1	3890.5831	-0.0045
10	10	1	-	9	9	0	3890.5831	-0.0045
13	6	7	-	12	5	8	3918.6548	0.0026
18	4	14	-	17	5	13	3938.7901	0.0068
18	1	18	-	17	0	17	3941.5047	0.0013
18	0	18	-	17	1	17	3941.5047	0.0116
11	9	3	-	10	8	2	3956.3186	-0.0046
11	9	2	-	10	8	3	3956.3186	-0.0046
18	1	17	-	17	2	16	4012.6781	-0.0046
18	2	17	-	17	1	16	4013.2224	0.0019
12	8	5	-	11	7	4	4021.4992	-0.0036
12	8	4	-	11	7	5	4021.4992	-0.0087
18	2	16	-	17	3	15	4080.2550	-0.0012
13	7	7	-	12	6	6	4084.3383	0.0022
13	7	6	-	12	6	7	4084.9170	0.0014
18	3	15	-	17	4	14	4102.3734	0.0038
11	10	1	-	10	9	2	4122.1491	-0.0016
11	10	2	-	10	9	1	4122.1491	-0.0016
14	6	9	-	13	5	8	4128.4644	0.0074
14	6	8	-	13	5	9	4151.2772	-0.0058
19	1	19	-	18	0	18	4158.4805	-0.0009
19	0	19	-	18	1	18	4158.4805	0.0039
12	9	4	-	11	8	3	4187.7437	0.0004
12	9	3	-	11	8	4	4187.7437	0.0003
16	5	12	-	15	4	11	4209.8427	0.0094
19	1	18	-	18	2	17	4229.7420	0.0057
19	2	18	-	18	1	17	4230.0046	-0.0047
19	4	15	-	18	5	14	4232.3829	0.0137
13	8	6	-	12	7	5	4252.4488	0.0253
13	8	5	-	12	7	6	4252.4488	0.0058
11	11	0	-	10	10	1	4287.9103	-0.0019
11	11	1	-	10	10	0	4287.9103	-0.0019
19	2	17	-	18	3	16	4299.4194	0.0080
19	3	17	-	18	2	16	4305.8182	-0.0023
14	7	8	-	13	6	7	4313.2878	-0.0041
14	7	7	-	13	6	8	4314.8370	-0.0036

15	5	10	-	14	4	11	4322.6224	-0.0010
15	6	10	-	14	5	9	4341.5769	0.0024
12	10	2	-	11	9	3	4353.6948	0.0198
12	10	3	-	11	9	2	4353.6948	0.0198
17	5	13	-	16	4	12	4367.3121	0.0069
20	0	20	-	19	1	19	4375.4604	0.0026
20	1	20	-	19	0	19	4375.4604	0.0003
15	6	9	-	14	5	10	4387.2021	0.0036
19	4	16	-	18	3	15	4418.1700	-0.0192
13	9	5	-	12	8	4	4419.0318	0.0023
13	9	4	-	12	8	5	4419.0318	0.0019
20	1	19	-	19	2	18	4446.7429	0.0074
20	2	19	-	19	1	18	4446.8767	0.0035
20	2	18	-	19	3	17	4517.5377	0.0016
12	11	2	-	11	10	1	4519.4786	-0.0003
12	11	1	-	11	10	2	4519.4786	-0.0003
20	3	18	-	19	2	17	4521.0244	-0.0040
15	7	9	-	14	6	8	4540.7149	0.0057
20	3	17	-	19	4	16	4571.7493	-0.0056
13	10	3	-	12	9	4	4585.1332	0.0024
13	10	4	-	12	9	3	4585.1332	0.0024
21	0	21	-	20	1	20	4592.4177	-0.0195
21	1	21	-	20	0	20	4592.4177	-0.0205
16	5	11	-	15	4	12	4622.0205	-0.0134
21	1	20	-	20	2	19	4663.7424	0.0337
21	2	20	-	20	1	19	4663.7424	-0.0349
19	5	15	-	18	4	14	4675.8173	-0.0061
12	12	1	-	11	11	0	4685.2291	-0.0006
12	12	0	-	11	11	1	4685.2291	-0.0006
15	8	8	-	14	7	7	4713.0517	-0.0018
15	8	7	-	14	7	8	4713.2406	-0.0046
17	6	12	-	16	5	11	4734.4289	-0.0018
21	3	19	-	20	2	18	4736.9436	-0.0079
13	11	3	-	12	10	2	4751.0168	0.0025
13	11	2	-	12	10	3	4751.0168	0.0025
16	7	10	-	15	6	9	4765.6707	0.0005
21	3	18	-	20	4	17	4797.2516	0.0004
22	1	22	-	21	0	21	4809.4166	0.0012
22	0	22	-	21	1	21	4809.4166	0.0017
14	10	4	-	13	9	5	4816.4824	-0.0016
14	10	5	-	13	9	4	4816.4824	-0.0015
21	4	18	-	20	3	17	4825.0922	-0.0153
20	5	16	-	19	4	15	4835.3348	0.0158

15	9	7	-	14	8	6	4880.9795	0.0014
15	9	6	-	14	8	7	4880.9795	-0.0049
16	8	8	-	15	7	9	4942.9725	0.0052
22	2	20	-	21	3	19	4952.2977	0.0029
22	3	20	-	21	2	19	4953.2867	-0.0029
14	11	4	-	13	10	3	4982.4942	-0.0007
14	11	3	-	13	10	4	4982.4942	-0.0007
17	7	10	-	16	6	11	5004.8042	-0.0096
23	1	23	-	22	0	22	5026.3955	0.0046
23	0	23	-	22	1	22	5026.3955	0.0048
22	4	19	-	21	3	18	5035.3444	0.0033
15	10	5	-	14	9	6	5047.6944	-0.0008
15	10	6	-	14	9	5	5047.6944	-0.0007
13	13	1	-	12	12	0	5082.5404	0.0008
13	13	0	-	12	12	1	5082.5404	0.0008
23	1	22	-	22	2	21	5097.6322	0.0067
23	2	22	-	22	1	21	5097.6322	-0.0100
16	9	8	-	15	8	7	5111.5129	0.0090
16	9	7	-	15	8	8	5111.5129	-0.0118
14	12	3	-	13	11	2	5148.3432	0.0007
14	12	2	-	13	11	3	5148.3432	0.0007
17	8	10	-	16	7	9	5170.8772	-0.0101
17	8	9	-	16	7	10	5172.2107	0.0225
22	5	18	-	21	4	17	5181.4340	0.0121
15	11	5	-	14	10	4	5213.8971	0.0029
15	11	4	-	14	10	5	5213.8971	0.0029
20	6	15	-	19	5	14	5224.0776	0.0125
18	7	11	-	17	6	12	5237.5400	-0.0021
23	3	20	-	22	4	19	5238.9950	0.0019
24	1	24	-	23	0	23	5243.3676	0.0028
24	0	24	-	23	1	23	5243.3676	0.0029
23	4	20	-	22	3	19	5248.1457	0.0060
23	4	19	-	22	5	18	5275.7010	-0.0041
16	10	6	-	15	9	7	5278.7186	-0.0011
16	10	7	-	15	9	6	5278.7186	-0.0005
24	1	23	-	23	2	22	5314.5812	0.0020
24	2	23	-	23	1	22	5314.5812	-0.0061
21	6	16	-	20	5	15	5368.4118	-0.0102
15	12	4	-	14	11	3	5379.8435	0.0022
15	12	3	-	14	11	4	5379.8435	0.0022
24	2	22	-	23	3	21	5386.3061	-0.0023
18	8	11	-	17	7	10	5397.9278	-0.0024
18	8	10	-	17	7	11	5400.9766	0.0056

19	7	13	-	18	6	12	5407.8174	-0.0034
16	11	5	-	15	10	6	5445.1799	-0.0018
24	3	21	-	23	4	20	5457.4461	0.0099
25	0	25	-	24	1	24	5460.3408	0.0040
25	1	25	-	24	0	24	5460.3408	0.0040
24	4	21	-	23	3	20	5462.5395	-0.0031
14	14	1	-	13	13	0	5479.8431	0.0021
14	14	0	-	13	13	1	5479.8431	0.0021
17	10	8	-	16	9	7	5509.5050	0.0003
17	10	7	-	16	9	8	5509.5050	-0.0017
25	1	24	-	24	2	23	5531.5340	0.0021
25	2	24	-	24	1	23	5531.5340	-0.0018
15	13	3	-	14	12	2	5545.6616	0.0010
15	13	2	-	14	12	3	5545.6616	0.0010
18	9	10	-	17	8	9	5571.2027	0.0054
18	9	9	-	17	8	10	5571.3545	-0.0126
20	7	14	-	19	6	13	5601.9043	0.0062
25	2	23	-	24	3	22	5603.2206	-0.0116
16	12	5	-	15	11	4	5611.2723	-0.0014
16	12	4	-	15	11	5	5611.2723	-0.0014
19	8	12	-	18	7	11	5622.8608	-0.0043
17	11	7	-	16	10	6	5676.3206	-0.0026
17	11	6	-	16	10	7	5676.3206	-0.0026
26	0	26	-	25	1	25	5677.3084	0.0017
26	1	26	-	25	0	25	5677.3084	0.0016
25	4	22	-	24	3	21	5677.9210	-0.0010
15	14	2	-	14	13	1	5711.4166	0.0025
15	14	1	-	14	13	2	5711.4166	0.0025
18	10	9	-	17	9	8	5739.9940	0.0015
18	10	8	-	17	9	9	5739.9940	-0.0051
26	1	25	-	25	2	24	5748.4822	-0.0018
26	2	25	-	25	1	24	5748.4822	-0.0038
16	13	4	-	15	12	3	5777.1696	-0.0031
16	13	3	-	15	12	4	5777.1696	-0.0031
17	12	6	-	16	11	5	5842.6127	-0.0032
17	12	5	-	16	11	6	5842.6127	-0.0032
20	8	13	-	19	7	12	5844.5746	0.0135
15	15	1	-	14	14	0	5877.1327	-0.0006
15	15	0	-	14	14	1	5877.1327	-0.0006
26	4	23	-	25	3	22	5893.8819	-0.0037
27	1	27	-	26	0	26	5894.2747	0.0002
27	0	27	-	26	1	26	5894.2747	0.0002
18	11	8	-	17	10	7	5907.2789	-0.0012

18	11	7	-	17	10	8	5907.2789	-0.0014
16	14	3	-	15	13	2	5942.9664	-0.0020
16	14	2	-	15	13	3	5942.9664	-0.0020
26	4	22	-	25	5	21	5958.8094	-0.0023
27	2	26	-	26	1	25	5965.4338	-0.0028
27	1	26	-	26	2	25	5965.4338	-0.0018
19	10	10	-	18	9	9	5970.1197	0.0058
19	10	9	-	18	9	10	5970.1197	-0.0138
17	13	5	-	16	12	4	6008.6274	-0.0025
17	13	4	-	16	12	5	6008.6274	-0.0025
20	9	12	-	19	8	11	6028.0683	0.0000
20	9	11	-	19	8	12	6029.1207	0.0136
18	12	7	-	17	11	6	6073.8415	0.0007
18	12	6	-	17	11	7	6073.8415	0.0007
16	15	2	-	15	14	1	6108.7072	-0.0007
16	15	1	-	15	14	2	6108.7072	-0.0007
28	0	28	-	27	1	27	6111.2466	0.0066
28	1	28	-	27	0	27	6111.2466	0.0066
19	11	9	-	18	10	8	6138.0026	-0.0063
19	11	8	-	18	10	9	6138.0026	-0.0069
17	14	4	-	16	13	3	6174.4880	-0.0030
17	14	3	-	16	13	4	6174.4880	-0.0030
18	13	6	-	17	12	5	6240.0043	-0.0082
18	13	5	-	17	12	6	6240.0043	-0.0082
16	16	1	-	15	15	0	6274.4179	0.0018
16	16	0	-	15	15	1	6274.4179	0.0018
19	12	8	-	18	11	7	6304.9117	-0.0064
19	12	7	-	18	11	8	6304.9117	-0.0065
17	15	3	-	16	14	2	6340.2690	0.0028
17	15	2	-	16	14	3	6340.2690	0.0028
18	14	5	-	17	13	4	6405.9702	0.0030
18	14	4	-	17	13	5	6405.9702	0.0030
17	17	1	-	16	16	0	6671.6914	0.0029
17	17	0	-	16	16	1	6671.6914	0.0029

---

<sup>a</sup> $\Delta\nu$  is the difference between measure and calculated frequencies.